amU
Aix Marseille Université

NNT : 2024AIXM0001

THÈSE DE DOCTORAT

Soutenue à AMU — Aix-Marseille Université
le 14 Novembre 2024 par

Mattia DICORATO

Stability and turbulent transport of JET pedestal plasmas in different ELMy regimes

Discipline
Physique et Sciences de la Matière

Spécialité
Energie, Rayonnement et Plasma

École doctorale
ED 352

Laboratoire/Partenaires de recherche
Physique des Interactions Ioniques et Moléculaires (PIIM) - AMU - CNRS, UMR7345
IRFM - CEA Cadarache, F13108 Saint-Paul-Lez-Durance, France

Composition du jury

Costanza F. MAGGI CCFE, UKAEA	Rapporteuse
Moritz J. PUESCHEL DIFFER	Rapporteur
Stephan BRUNNER SPC, EPFL	Examinateur
Laure VERMARE LPP, CNRS	Présidente du jury
Xavier GARBET CEA Cadarache & NTU	Directeur de thèse
Magali MURAGLIA PIIM, AMU & CNRS	Co-directrice de thèse
Yann CAMENEN PIIM, AMU & CNRS	Co-encadrant
Jeronimo GARCIA CEA Cadarache	Invité

PIIM Physique des Interactions Ioniques et Moléculaires
cnrs
cea

Affidavit

I, undersigned, Mattia Dicorato, hereby declare that the work presented in this manuscript is my own work, carried out under the scientific supervision of Xavier Garbet and Magali Muraglia, in accordance with the principles of honesty, integrity and responsibility inherent to the research mission. The research work and the writing of this manuscript have been carried out in compliance with both the french national charter for Research Integrity and the Aix-Marseille University charter on the fight against plagiarism.

This work has not been submitted previously either in this country or in another country in the same or in a similar version to any other examination body.

Marseille, January 20, 2025



This work is licensed under Creative Commons Attribution-NonCommercial-NoDerivatives 4.0 International Public License

Liste de publications et participation aux conférences

Liste des publications et/ou brevets réalisées dans le cadre du projet de thèse:

1. **M. Dicorato**, M. Muraglia, Y. Camenen, J. Garcia, X. Garbet, D. R. Hatch, G. Merlo, E. de la Luna, Ž. Štancar, L. Garzotti, V.K. Zotta, F. Rimini, D. Frigione, JET Contributors, and the EUROfusion Tokamak Exploitation Team, *Turbulent transport mechanisms and their impact on the pedestal top of JET plasmas with small-ELMs*, Plasma Phys. Control. Fusion 66 125002, 10.1088/1361-6587/ad867b (2024).

2. **M. Dicorato**, M. Muraglia, Y. Camenen, J. Garcia, X. Garbet, D. Frigione, L. Garzotti, P. Lomas, F. Rimini, C. Sozzi, and D. Van Eester, *Gyrokinetic Stability Analysis of JET Pedestal Top Plasmas with Small-ELMs*, Phys.: Conf. Ser. 2397 012007, 10.1088/1742-6596/2397/1/012007 (2022).

3. J. Garcia, E. de la Luna, M. Sertoli, F. J. Casson, S. Mazzi, Ž. Štancar, G. Szepesi, D. Frigione, L. Garzotti, F. Rimini, D. van Eester, P. Lomas, C. Sozzi, N. Aiba, **M. Dicorato**, A. Mariani, R. Coelho, L. Frasinetti, G. T. A. Huijsmans, F. Liu, JET Contributors, *New H-mode regimes with small ELMs and high thermal confinement in the Joint European Torus*, Phys. Plasmas, 29 (3): 032505. 10.1063/5.0072236 (2022).

Participation aux conférences et écoles d'été au cours de la période de thèse:

1. *Turbulent transport at the pedestal top of small-ELMs plasmas at JET: key mechanisms and their impact*, 50th EPS Conference on Plasma Physics, 8-12 July 2024, Salamanca, Spain. Oral.

2. *Gyrokinetic Simulations of JET Pedestal Top Plasmas in Different ELMy Regimes*, European Fusion Theory Conference, 2-5 October 2023, Padova, Italy. Poster.

3. *Gyrokinetic simulations of JET pedestal top plasmas in small-ELM regime*, US Transport Task Force Workshop, May 2-5 2023, Madison (WI), USA. Poster.

4. *Gyrokinetic Stability Analysis of JET Pedestal Top in Small-ELM Regime*, Joint Varenna-Lausanne International Workshop "Theory of Fusion Plasmas", 12-16 September 2022, Varenna, Italy. Poster.

Abstract

One key challenge for future fusion reactors is the development of tokamak plasma regimes that ensure confinement compatible with fusion performance requirements, while maintaining edge dynamics that satisfy plasma-facing component tolerated heat and particle loads. A critical factor influencing both confinement and edge dynamics is the radial transport of particles and heat driven by plasma microturbulence, which arises from micro-instabilities such as ion and electron temperature gradient (ITG and ETG) modes, and trapped-electron modes (TEM).

In high confinement mode (H-mode), the plasma edge is characterized by reduced turbulence, leading to the formation of a pressure pedestal. The pedestal plays a dual role, defining the boundary for core plasma profiles and determining the stability of edge-localized modes (ELMs), which affect plasma-facing component fluxes. The EPED model is commonly used to predict pedestal height and width based on constraints from peeling-ballooning magnetohydrodynamic modes and kinetic-ballooning mode (KBM) limits. However, the role of turbulent transport mechanisms in shaping the pedestal remains poorly understood.

This thesis is motivated by the discovery of new H-mode regimes with small-ELMs at the JET tokamak, referred to as baseline small-ELMs (BSE). The distinct pedestal structures in BSE regimes, compared to type-I ELM regimes, are not explained by the EPED model. This work aims to enhance understanding of turbulent transport in BSE regimes through a comparative analysis with a type-I ELMy H-mode discharge, using gyrokinetic modeling with the GENE code.

Stability analyses at the pedestal top positions in the two regimes reveal that, at ion scales, the type-I ELM regime is dominated by hybrid ITG-KBM and KBM modes, while the BSE regime is dominated by hybrid ITG-TEM modes, linked to lower plasma β due to reduced density. Electromagnetic effects weakly influence the microinstability spectra in both regimes. These differences in ion-scale stability suggest distinct roles for turbulent transport in each regime. At electron scales, multiple ETG branches are destabilized in both regimes, with toroidal-ETG in BSE regimes sensitive to impurity stabilization.

To investigate the mechanisms responsible for turbulence saturation, non-linear simulations of hybrid ITG-TEM turbulence in the BSE regime focus on key mechanisms in edge turbulent transport: the interplay of electromagnetic effects with equilibrium $\boldsymbol{E} \times \boldsymbol{B}$ shearing. Ion-scale turbulence shows strong electromagnetic stabilization, with enhanced mesoscale modes. A comparison of zonal flow activity in electrostatic and electromagnetic simulations reveals a significant enhancement in the latter, suggesting its role in electromagnetic stabilization. Analyses of heat turbulence spectra indicate that transport carried by mesoscale modes is negligible due to transport-unfavorable cross-phases.

Despite the evidence of strong nonlinear mechanisms, good agreement is found between nonlinear and linear cross-phases for modes with the highest transport contribution,

motivating tests of quasi-linear models to reproduce nonlinear heat flux spectra. Promising agreement is obtained, supporting the use of quasi-linear models for plasma edge conditions.

Finally, electron heat transport driven by slab-ETG turbulence is shown to be insensitive to electromagnetic effects and $\boldsymbol{E} \times \boldsymbol{B}$ shearing. Stiff electron heat transport with respect to the temperature gradient is demonstrated, suggesting its role in limiting the electron temperature pedestal height in BSE regimes.

These findings advance our understanding of key transport mechanisms at the pedestal top in the new BSE regimes, emphasizing the competition between stabilizing electromagnetic effects and equilibrium $\boldsymbol{E} \times \boldsymbol{B}$ shearing in hybrid ITG-TEM turbulence, as well as the role of electron-scale transport driven by ETG turbulence.

Keywords: plasma, tokamak, H-mode, small-ELMs, pedestal, turbulent transport, gyro-kinetic simulations

Résumé

Un défi majeur pour les futurs réacteurs à fusion est le développement de régimes plasma assurant un confinement compatible avec les exigences de performance, tout en maintenant des dynamiques de bord qui respectent les charges thermiques et particulaires tolérées par les composants exposés au plasma. Un facteur clé influençant le confinement et les dynamiques de bord est le transport radial des particules et de la chaleur, généré par la microturbulence du plasma, liée à des micro-instabilités telles que les modes dues au gradient de température ionique et électronique (ITG et ETG), ainsi que les modes d'électrons piégés (TEM).

En mode de confinement élevé (H-mode), le bord du plasma est caractérisé par une turbulence réduite, formant un piédestal de pression. Ce piédestal définit la frontière des profils du plasma central et influence la stabilité des modes localisés au bord (ELMs), impactant les flux vers les parois. Le modèle EPED est utilisé pour prédire la hauteur et la largeur du piédestal, basé sur les limites des modes magnétohydrodynamiques "peeling-ballooning" et des modes cinétiques-ballooning (KBM). Cependant, le rôle des mécanismes de transport turbulent dans la formation du piédestal reste mal compris.

Cette thèse s'appuie sur la découverte de nouveaux régimes H-mode avec de petits ELMs dans le tokamak JET, appelés "baseline small-ELM" (BSE). Les structures du piédestal dans les régimes BSE, contrairement aux régimes à ELMs de type I, ne sont pas expliquées par le modèle EPED. Ce travail vise à approfondir la compréhension du transport turbulent dans les régimes BSE par une analyse comparative avec un H-mode à ELMs de type I, en utilisant des simulations gyrocinétiques avec le code Gene.

Les analyses de stabilité au sommet du piédestal montrent qu'aux échelles ioniques, le régime à ELMs de type I est dominé par des modes hybrides ITG-KBM, tandis que le régime BSE est dominé par des modes hybrides ITG-TEM, liés à une plus faible densité du plasma. Les effets électromagnétiques influencent peu les spectres de microinstabilités dans les deux régimes. Ces différences suggèrent des rôles distincts du transport turbulent. Aux échelles électroniques, plusieurs branches ETG sont déstabilisées dans les deux régimes, avec une sensibilité des ETG toroïdaux à la stabilisation par impuretés dans les régimes BSE.

Pour explorer les mécanismes de saturation de la turbulence, des simulations non linéaires de turbulence ITG-TEM dans le régime BSE se concentrent sur le rôle des effets électromagnétiques et du cisaillement d'équilibre $\boldsymbol{E} \times \boldsymbol{B}$. La turbulence ionique présente une forte stabilisation électromagnétique, avec une déstabilisation des modes à grande-échelle. L'activité des flux zonaux dans les simulations électromagnétiques augmente par rapport aux simulations électrostatiques, suggérant son rôle dans la stabilisation électromagnétique. Malgré d'importants mécanismes non linéaires, un bon accord est trouvé entre les phases croisées linéaires et non linéaires pour les modes contribuant le plus au transport. Cela justifie des tests de modèles quasi-linéaires pour reproduire les spectres de flux de chaleur non linéaire, donnant des comparaisons satisfaisantes.

Enfin, le transport thermique électronique induit par la turbulence ETG est démontré

comme insensible aux effets électromagnétiques et au cisaillement $\boldsymbol{E} \times \boldsymbol{B}$. Le transport thermique électronique rigide en fonction du gradient de température semble limiter la hauteur du piédestal de température électronique dans les régimes BSE.

Ces résultats améliorent la compréhension des mécanismes de transport au sommet du piédestal dans les régimes BSE, en soulignant la compétition entre les effets stabilisants électromagnétiques et le cisaillement d'équilibre $\boldsymbol{E} \times \boldsymbol{B}$ dans la turbulence ITG-TEM, ainsi que le rôle du transport à échelle électronique induit par la turbulence ETG.

Mots clés: plasma, tokamak, mode H, small-ELMs, piédestal, transport turbulent, simulations gyrocinétiques

Résumé (Version étendue)

L'un des principaux défis dans l'exploitation des futurs réacteurs à fusion est le développement de régimes de plasma de tokamak qui garantissent un confinement compatible avec les exigences de performance de la fusion et une dynamique de bord satisfaisant les contraintes des composants en contact avec le plasma pour les charges thermiques et particulaires tolérées. Un facteur critique influençant à la fois le confinement et la dynamique de bord est le transport radial de particules et de chaleur, provoqué par la turbulence du plasma, résultant des micro-instabilités telles que les modes de gradient de température des ions et des électrons (ITG et ETG), ainsi que les modes d'électrons piégés (TEM).

En particulier, la région du bord du plasma caractéristique du mode de confinement élevé (H-mode) est marquée par une forte réduction de la turbulence du plasma, conduisant à la formation d'un piédestal dans les profils de pression, jouant un double rôle fondamental. D'une part, il définit la limite pour les profils de plasma du cœur, d'autre part, il détermine les frontières d'instabilité des modes localisés au bord (ELMs), et par conséquent, les flux sur les composants en contact avec le plasma. Actuellement, le modèle EPED est le plus largement utilisé pour prédire la hauteur et la largeur du piédestal de pression, en se basant sur des contraintes imposées par des modes magnétohydrodynamiques (MHD) couplés peeling-ballooning, combinés avec des limites de modes cinétiques-ballooning (KBM) issues des processus de transport. Malgré des progrès dans la compréhension des processus physiques déterminant la structure du piédestal, le rôle des mécanismes de transport turbulents reste l'un des moins compris.

Cette thèse est motivée par la découverte, lors des campagnes expérimentales 2019-2020 au tokamak JET au Royaume-Uni, de nouveaux régimes H-mode avec des dynamiques de petits ELMs, appelés "baseline small-ELMs" (BSE). Ces régimes se caractérisent notamment par des structures de piédestal distinctes par rapport

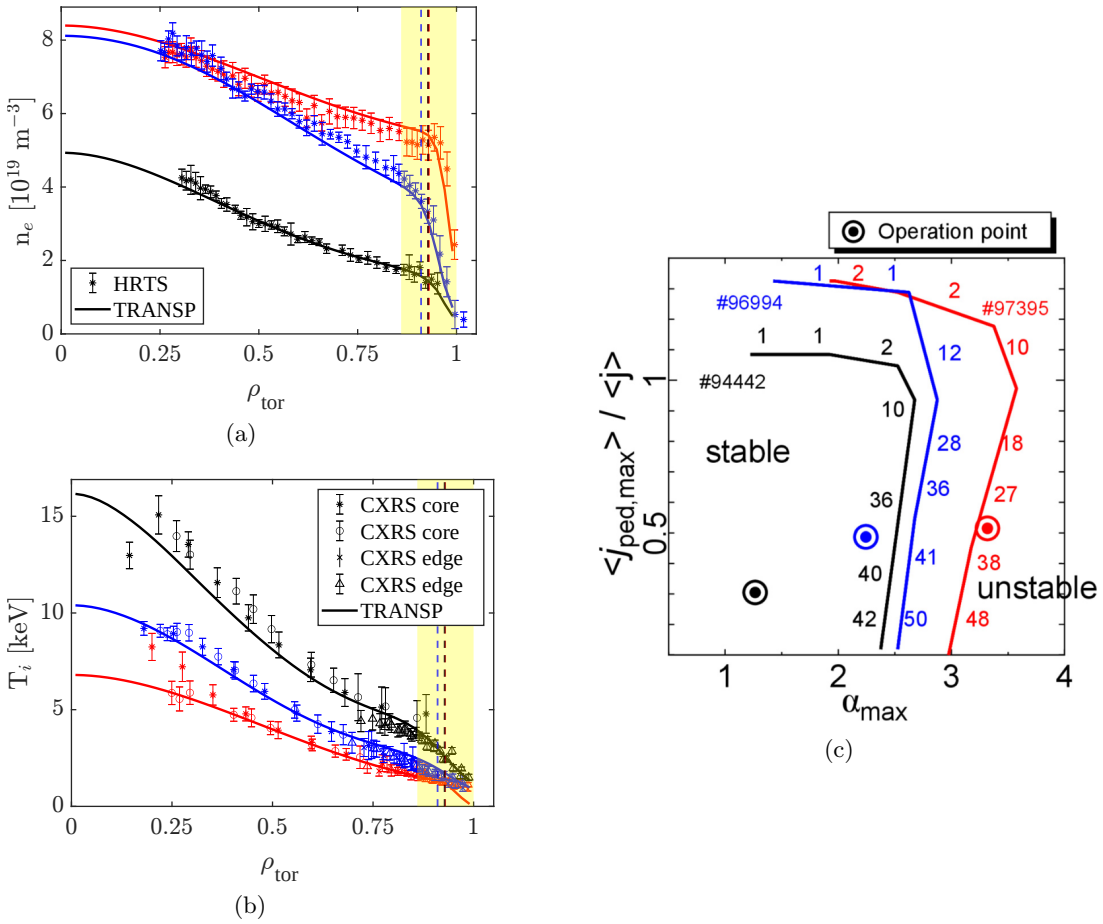

Figure 1.: (a-b) Profils expérimentaux en fonction du rayon toroïdal normalisé ρ_{tor} de densité n_e et de température ionique T_i pour trois décharges JET : #97395-Type-I ELMs (rouge), #96994-BSE (bleu), et #94442-BSE (noir). (c) Diagramme de stabilité peeling-ballooning pour les trois décharges en fonction de la densité de courant au bord normalisée par rapport à la densité de courant moyenne dans le volume $j_{\text{ped,max}}/\langle j \rangle$ et du gradient de pression maximal normalisé $\alpha_{\text{max}} = -2\mu_0 q^2 R/B^2 \, \mathrm{d}p/\mathrm{d}r \, |_{\text{max}}$ (source [1]).

au H-mode standard avec des ELMs de type-I. Le chapitre 2 est donc consacré à la description des conditions expérimentales et à la caractérisation des profils expérimentaux de deux décharges représentatives en régimes BSE et d'une décharge avec ELMs de type-I considérées dans ce travail de thèse. Il est particulièrement notable que les régimes BSE sont accessibles via une optimisation des sources particulaires. Les structures distinctes du piédestal sont montrées dans les figures 1a-1b, où sont reportés les profils radiaux expérimentaux de densité n_e et de température ionique T_i pour deux décharges BSE (#94442-#96994) et une décharge H-mode avec ELMs de type-I (#97395). On note en particulier que les piédestaux de densité électronique sont plus larges et plus bas dans les décharges BSE ($n_{e,\text{top}} \sim 1.45 - 3.5 \cdot 10^{19}\,\text{m}^{-3}$) par rapport à la décharge avec ELMs de type-I ($n_{e,\text{top}} \sim 5.4 \cdot 10^{19}\,\text{m}^{-3}$). De plus, les piédestaux de température ionique sont plus élevés dans les régimes BSE comparés aux ELMs de type-I. Pour discerner les mécanismes physiques responsables du déclenchement des ELMs, la stabilité du piédestal vis-à-vis de la limite de stabilité "peeling-ballooning" (P-B), comme montré dans la figure 1c, est calculée. Cette analyse révèle que, tandis que le piédestal du régime ELMs de type-I est instable vis-à-vis du P-B, le piédestal BSE reste stable, n'atteignant pas les gradients critiques de pression et de courant nécessaires pour l'instabilité P-B. À la lumière de ces résultats, la structure du piédestal des régimes BSE reste inexpliquée dans le cadre des hypothèses du modèle EPED, indiquant potentiellement un manque d'informations physiques. Enfin, le profil radial du champ électrique radial E_r sera estimé à partir des profils en utilisant l'équation de l'équilibre des forces radiales. Cela permettra d'estimer la dérivée radiale des flux de plasma $\boldsymbol{E} \times \boldsymbol{B}$, c'est-à-dire le taux de cisaillement $\gamma_{\boldsymbol{E}\times\boldsymbol{B}}$, un facteur clé dans la régulation de la turbulence.

L'objectif de cette thèse est de mieux comprendre les mécanismes de transport turbulent dans la région du piédestal des régimes BSE à travers une analyse comparative avec une décharge H-mode standard à ELMs de type-I. Pour évaluer la responsabilité potentielle du transport dans la limitation de la hauteur du piédestal, l'analyse se concentrera autour de la position du sommet du piédestal, qui a été

quantitativement définie comme la position radiale correspondant à la hauteur du piédestal de la pression du piédestal électronique. L'étude est menée au moyen de modélisation gyrocinétique interprétative en utilisant la version locale du code GENE. Le système d'équations gyrocinétiques et les hypothèses physiques sous-jacentes utilisées pour les dériver, ainsi que les principales méthodes numériques employées pour les résoudre, seront introduits dans le chapitre 3.

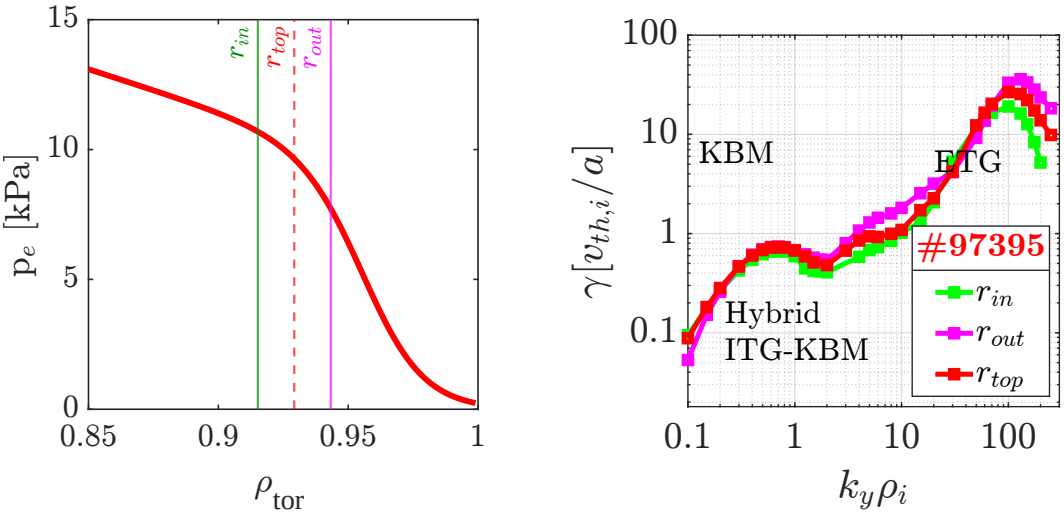

(a) #97395-Type-I ELMs

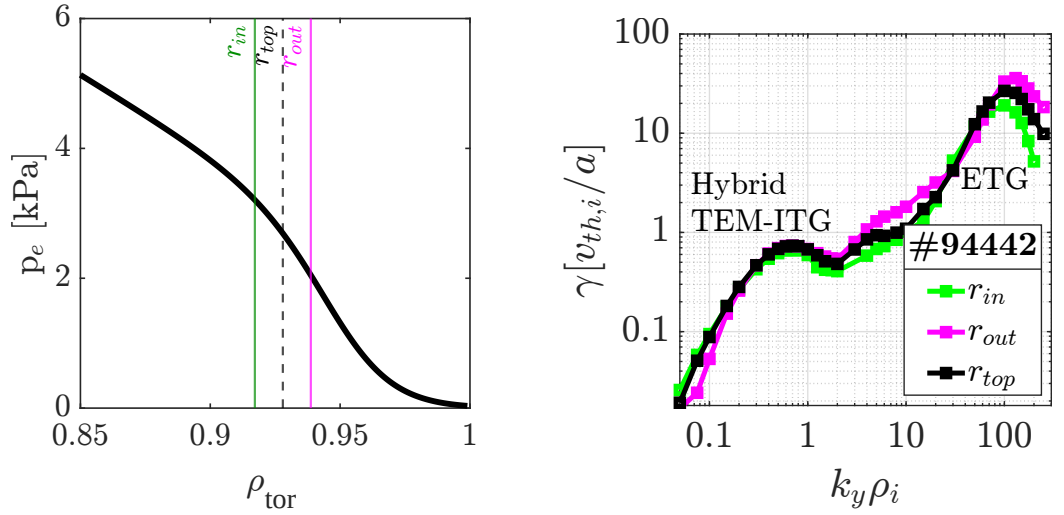

(b) #94442-BSE

Figure 2.: Profils radiaux de la pression électronique au bord et positions radiales sélectionnées (gauche), taux de croissance linéaire γ correspondant en fonction du nombre d'onde binormal $k_y\rho_i$ (droite) pour la décharge (a) #97395-Type-I ELMs, (b) #94442-BSE.

Pour évaluer l'impact des différences dans la structure du piédestal sur la stabilité à travers les différents régimes à ELMs, des simulations gyrocinétiques linéaires sont présentées dans le chapitre 4. Les résultats obtenus à trois positions rapprochées près du sommet du piédestal dans les deux régimes à ELMs sont résumés dans la figure 2, où les spectres des taux de croissance γ des micro-instabilités en fonction du nombre d'onde binormal $k_y\rho_i$ sont rapportés. Ces analyses révèlent qu'à l'échelle ionique, alors que le régime à ELMs de type-I est dominé par des modes hybrides ITG-KBM et KBM, la décharge BSE est caractérisée par des modes hybrides ITG-TEM. Dans le premier cas, les résultats sont cohérents avec la compréhension actuelle selon laquelle les limites KBM combinées aux limites P-B jouent un rôle déterminant dans les piédestaux du H-mode à ELMs de type-I. Une étude dédiée attribue l'origine de cette différence à la faible valeur du rapport de la pression thermique à la pression magnétique du plasma, due à la densité plus faible caractéristique du régime BSE. Les spectres des micro-instabilités pour des paramètres de référence au sommet du piédestal seront également comparés avec des simulations dans la limite électrostatique, montrant des effets électromagnétiques faibles. Fait intéressant, la déstabilisation des modes micro-tearing (MTM), récemment considérés comme un mécanisme clé pour le transport dans les piédestaux de JET-ILW, est exclue dans ces décharges, même dans les analyses de modes sous-dominants, indiquant que d'autres mécanismes sont responsables du transport de chaleur électronique. Cependant, compte tenu de la sensibilité des résultats à la localisation radiale de l'analyse, ce mécanisme ne peut être exclu dans l'ensemble du piédestal. Au-delà de l'échelle ionique, les spectres des micro-instabilités révèlent la déstabilisation de plusieurs branches des modes ETG toroïdaux et slab, ces derniers s'étendant jusqu'à des échelles très fines, pour les deux régimes à ELMs. Ces résultats sont cohérents avec d'autres études des piédestaux de JET. Notamment, les branches ETG-toroïdales dans les régimes BSE, contrairement à celles dans les régimes à ELMs de type-I, sont sensibles à la stabilisation par les impuretés. En outre, les spectres des micro-instabilités pour des paramètres de référence sont comparés avec des simulations dans la limite électrostatique, montrant des effets électromagnétiques

faibles. L'analyse de stabilité a ainsi fourni des preuves de différentes instabilités à l'échelle ionique au sommet du piédestal des deux régimes à ELMs, indiquant potentiellement des rôles distincts des processus de transport turbulents.

Dans le chapitre 5, pour obtenir des informations sur les principaux mécanismes responsables de la saturation de la turbulence, des simulations gyrocinétiques non linéaires locales très complexes sont menées, en se concentrant sur la décharge de référence BSE. En s'appuyant sur des études disponibles sur le transport turbulent de bord, le rôle de deux mécanismes clés dans le transport turbulent de bord est considéré : les effets électromagnétiques et leur interaction avec le cisaillement $\boldsymbol{E} \times \boldsymbol{B}$ à l'équilibre. Les traces temporelles du flux de chaleur ionique résultant des simulations de la turbulence à l'échelle ionique sont montrées dans la figure 3a. En particulier, les résultats obtenus en incluant les effets électromagnétiques (EM) sont comparés à ceux obtenus en adoptant la limite électrostatique (ES_l). Ces résultats révèlent des niveaux de flux de chaleur significativement plus élevés dans le régime électrostatique ES_l par rapport au régime électromagnétique EM, indiquant un mécanisme de stabilisation électromagnétique. Ces résultats étendent l'observation de la stabilisation électromagnétique, typiquement trouvée dans les simulations de turbulence du cœur, à la turbulence de bord caractérisée par des gradients raides et la faible valeur du rapport de la pression thermique à la pression magnétique du plasma des régimes BSE. Pour caractériser les deux régimes de turbulence, les spectres de Fourier de la turbulence du potentiel électrostatique sont analysés, montrant la présence de modes à grande-échelle dans le cas EM, en cohérence avec des études précédentes, qui sont absents dans le cas ES_l. Compte tenu des faibles effets électromagnétiques observés dans les simulations linéaires, la déstabilisation des modes à grande-échelle est attribuée à des mécanismes non linéaires, soutenant ainsi des preuves de processus non linéaires dominants dans la turbulence électromagnétique. L'activité des flux zonaux auto-générés par la turbulence est également comparée dans les cas ES_l et EM pour évaluer son rôle dans la stabilisation électromagnétique. Une différence remarquable dans les spectres du taux de cisaillement zonal est observée, avec une augmentation à grande

échelle dans le cas EM. Bien que les preuves suggèrent que l'autorégulation des flux zonaux joue un rôle plus significatif dans le cas EM comparé au cas ES_l, une conclusion définitive sur son rôle décisif dans la stabilisation électromagnétique ne peut être tirée. De plus, les spectres de flux de chaleur obtenus dans des simulations avec différents cisaillements $\boldsymbol{E} \times \boldsymbol{B}$ à l'équilibre sont comparés, soulignant son rôle ambivalent dans le cas EM, où un taux de cisaillement plus élevé entraîne des flux de chaleur plus élevés, suggérant une compétition entre les mécanismes d'auto-organisation et le cisaillement à l'équilibre. De plus, il est démontré que les modes à grande-échelle, bien que fortement excités dans les spectres de Fourier, ne transportent pas significativement la chaleur. Ce mécanisme est exploré plus en détail en examinant les déphasages croisés des fluctuations du potentiel avec la densité et la température, montrant que les modes à grande-échelle présentent des déphasages croisés défavorables au transport. Le mécanisme non linéaire dans le cas EM, impliquant le transfert d'énergie et l'augmentation des fluctuations des modes à grande-échelle tout en modifiant simultanément les déphasages croisés pour les rendre défavorables au transport, est suggéré comme contribuant à la stabilisation électromagnétique, avec ces modes jouant potentiellement le rôle de réservoirs d'énergie.

En outre, des simulations de turbulence pilotée par les modes ETG, retenant la branche slab-ETG du régime BSE, sont menées pour évaluer quantitativement le transport de chaleur des électrons Q_e. Les résultats obtenus démontrent leur insensibilité aux effets EM et au cisaillement $\boldsymbol{E} \times \boldsymbol{B}$ à l'équilibre. Au lieu de cela, un transport de chaleur des électrons rigide par rapport au gradient logarithmique normalisé de la température électronique, $1/L_{T_e}$, est montré dans la figure 3b, qui atteint des niveaux de transport pertinents expérimentalement. Ces résultats mettent en évidence le rôle de la turbulence à l'échelle des électrons dans le transport de chaleur dans le canal des électrons pour les régimes BSE, représentant potentiellement un mécanisme qui limite la hauteur du piédestal de température des électrons.

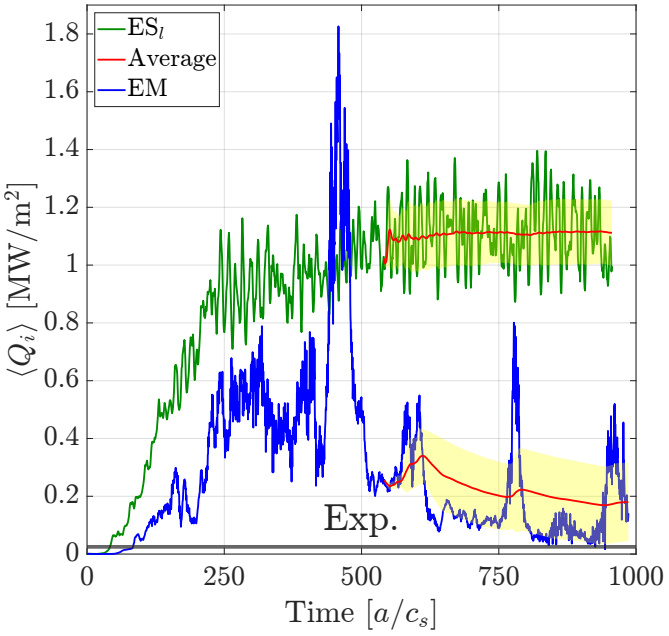

(a)

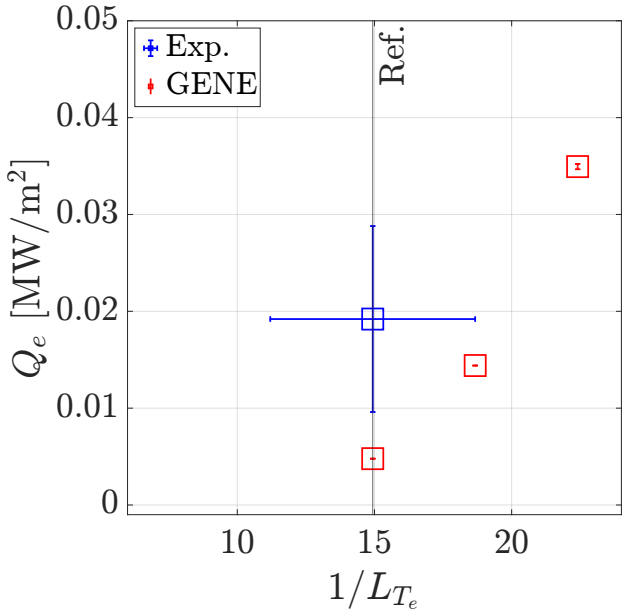

(b)

Figure 3.: Simulations non linéaires GENE à la position du sommet du piédestal avec un taux de cisaillement à l'équilibre $\gamma_{\boldsymbol{E}\times\boldsymbol{B}} = 0.45$ pour la décharge #94442-BSE. (a) Échelle ionique : traces temporelles du flux de chaleur ionique pour les cas ES$_l$ et EM avec moyenne glissante (rouge) et variance correspondante (jaune). (b) Échelle électronique : flux de chaleur électronique moyenné dans le temps (rouge) comparé à la valeur expérimentale issue du calcul d'équilibre de puissance (bleu). La surface de la surface de flux est $V' = 108.27\,\mathrm{m}^2$.

En dépit de preuves de mécanismes non linéaires forts à l'échelle ionique, un bon accord est trouvé entre les résultats non linéaires et les déphasages croisés dominants obtenus linéairement pour les modes ayant les déphasages les plus favorables au transport. Ce résultat motive l'application de la théorie quasi-linéaire pour reproduire le flux de chaleur non linéaire à l'échelle ionique. Les spectres sont construits en testant différentes règles de saturation et en utilisant les flux linéaires des simulations GENE. Les résultats obtenus avec la meilleure règle de saturation testée sont montrés dans la figure 4, où les spectres des flux de chaleur quasi-linéaires et non linéaires sont comparés. Les spectres sont normalisés avec le maximum des spectres de flux de chaleur ionique, et l'aire sous les spectres est rapportée dans la légende. Bien que le pic des spectres quasi-linéaires soit décalé par rapport à celui des spectres non linéaires, un accord remarquable pour les flux totaux normalisés de chaleur ionique et électronique, Q_i et Q_e, est obtenu. Des résultats prometteurs ont été obtenus concernant l'accord entre les spectres des flux de chaleur non linéaires et les modèles quasi-linéaires de base testés, suggérant leur applicabilité potentielle tout en mettant également en évidence des domaines critiques nécessitant un développement supplémentaire, tels que la capture des pics des spectres de flux.

Les conclusions contribuent à étendre notre compréhension des mécanismes clés de transport au sommet du piédestal dans les nouveaux régimes BSE, en soulignant particulièrement l'importance de la compétition entre les effets stabilisants électromagnétiques et le cisaillement $\boldsymbol{E} \times \boldsymbol{B}$ à l'équilibre pour la turbulence hybride ITG-TEM, ainsi que le rôle du transport à l'échelle des électrons induit par la turbulence ETG. Ces résultats confirment que le transport turbulent dans le piédestal est électromagnétique et multi-échelle, avec des mécanismes de turbulence sous-jacents ayant une influence non triviale sur les différents canaux de transport.

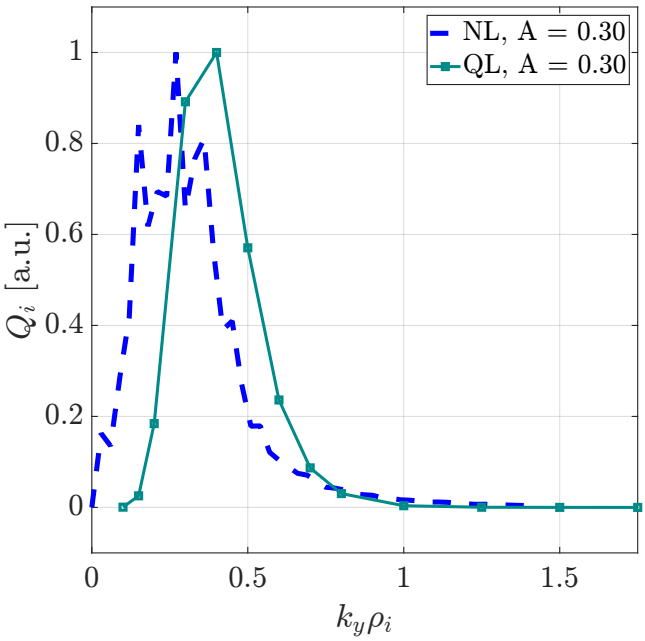

(a)

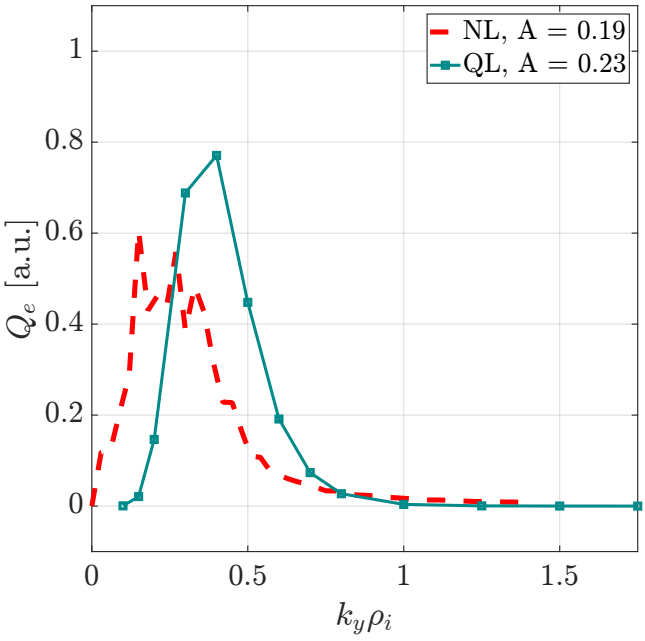

(b)

Figure 4.: Comparaison des spectres de flux de chaleur non linéaires et quasi-linéaires en fonction du nombre d'onde binormal $\hat{k}_y$ des simulations EM GENE: (a) ions et (b) électrons. Les spectres sont normalisés par le pic du flux de chaleur ionique. L'aire sous la courbe est indiquée dans la légende, A.

Acknowledgments

The time has finally come to write these words, after more than three years since the beginning of this PhD journey. I would like to start by expressing my gratitude to the institutions that welcomed me and provided the funding: the PIIM Laboratory and the ISFIN Institute at Aix-Marseille University, the IRFM-CEA Cadarache, and EUROfusion.

Surely, I am thankful to my official and unofficial supervisors: Xavier, Magali, Yann, and Jeronimo. To my thesis director, Xavier, thank you for giving me the freedom to follow my instincts while always providing essential support and guidance, which were crucial in interpreting the (sometimes cryptic) results we got. I am grateful for the time you always found for me, despite your busy agenda and the physical distance, and for all the "frontal lectures" you imparted me at CEA – I really enjoyed and will never forget. Thank you to my thesis co-director, Magali, for all the meetings and the physics questions raised during these years, which allowed me to take a deeper and more critical look at the results, always pushing me to learn and go further. I also extend my thanks to Yann for the time dedicated to my thesis, particularly for the technical support with gyrokinetic simulations using the GKW and Gene codes, and for the invaluable feedback on my work; I greatly enjoyed co-supervising Pierre's master project with you. Your organization, meticulousness, and dedication have been exemplary and have contributed to my professional growth. Lastly, I am grateful to Jeronimo for involving me in this fascinating international research project on new experimental results of small-ELMs regimes obtained at JET. Our discussions helped me better focus my modeling analysis and finally reach the main results of my thesis.

I am also grateful to David Hatch for welcoming me to the Institute for Fusion Studies (IFS) at the University of Texas in Austin, including me in his team, and introducing me to Gabriele Merlo. My visiting period was not only an enjoyable first-time experience in the U.S., but also essential in achieving the main results of my thesis. Thank you both for your contributions to the analysis and technical support. I hope we will have more opportunities to collaborate in the future.

I would like to thank the members of the examination committee for agreeing to evaluate my thesis: Laure Vermare, Costanza Maggi, M. J. Pueschel, Stephan Brunner, and of course, Xavier, Magali, Yann, and Jeronimo. I appreciate your comments, questions, and the examination discussion, which have helped improve the content of this thesis.

I am also thankful for participating in the JET Pedestal Task working group, organized by Samuli Saarelma and Lorenzo Frassinetti. This opportunity allowed me to stay updated on the advancements in pedestal modeling of JET experimental results and also provided valuable feedback on my work. Special thanks to Elena de la Luna for her experimental insights and support in finalizing the paper and thesis, providing plots of experimental waveforms.

I extend my gratitude to Paola Mantica and Alberto Mariani from ISTP-CNR in Milan, supervisors of my master's thesis, for introducing me to the world of gyrokinetic simula-

tions for tokamak turbulence and leading me to this PhD project. I really appreciated your feedback and encouragement throughout these years.

I am grateful to all the colleagues and friends I shared these three years with, especially Martino and Federica, who were with me from the beginning to the end of this journey. Thanks to Daniele and Surabhi for all the advices regarding the PhD adventure. To my office and corridor mates, Alodie, Anass, Matisse, Julien, Akbar, Emanuele, and Emil thank you for always being available for help and discussions about life and work. I also thank the CEA colleagues Virginia, Olivier, Raffael, and Yann for the engaging discussions during coffee breaks and lunches. Special thanks to Samuele for the physics discussions around simulation results and for his support and encouragement, especially during the paper and thesis drafting.

Beyond the lab, I am grateful to my friends in Marseille for the wonderful moments that helped me maintain a healthy work-life balance (even though I struggled to achieve it). Thank you, Paco, Mattheus, Matthieu, Ana, Jack, Chiara, Concetta, Federica, Lara, and Gianluca.

I thank my friends from Italy, who, despite the distance, always stayed close and warmly welcomed me whenever I returned in Italy. Thanks to Lau, Albi, Norbi, Richi, Chicco, Chiara, Gaia, Ele, Eli, Samu, and Silvia.

Finally, I thank my family. I know how difficult it is for you to be distant from me, and all the support and encouragement you have always given to me means a lot. Thank you to Bianca for being there, believing in me every day, and supporting me since we met.

Contents

Affidavit 2

Liste de publications et participation aux conférences 3

Abstract 4

Résumé 6

Résumé (Version étendue) 8

Acknowledgments 18

Contents 20

List of Figures 23

List of Tables 28

1. Introduction 30
- 1.1. The energy crisis and fusion energy . . . 30
  - 1.1.1. Nuclear fusion reactions . . . 32
  - 1.1.2. Thermonuclear plasma . . . 34
  - 1.1.3. Lawson criterion . . . 35
- 1.2. Charged particles motion in an electromagnetic field . . . 36
  - 1.2.1. Single-particle drifts . . . 36
  - 1.2.2. Diamagnetic drift . . . 38
- 1.3. The tokamak device . . . 39
  - 1.3.1. Magnetic equilibrium . . . 39
  - 1.3.2. The JET tokamak . . . 41
- 1.4. Tokamak plasma regimes and the pedestal . . . 42
  - 1.4.1. Pedestal physics . . . 43
- 1.5. Brief overview of turbulent transport . . . 45
  - 1.5.1. Microinstabilities . . . 46
  - 1.5.2. Microturbulence . . . 50
- 1.6. Thesis objectives and outline . . . 53

2. Description of JET shots: type-I ELMs vs. small-ELMs 55
- 2.1. Experimental conditions . . . 55
- 2.2. Plasma profiles . . . 59
  - 2.2.1. Time-averaged radial profiles . . . 59
  - 2.2.2. Magnetic equilibrium . . . 65
  - 2.2.3. Electron pressure pedestal fit . . . 67

2.3. Equilibrium flow shearing rate . . . 68
2.4. Physical input parameters . . . 71

3. The gyrokinetic theory and numerical methods 73
3.1. Introduction to kinetic theory . . . 73
3.2. Gyrokinetic system of equations . . . 75
3.3. Field-aligned coordinates . . . 81
3.3.1. Operators in field-aligned coordinate . . . 82
3.4. Numerical resolution of the gyrokinetic equations . . . 83
3.4.1. Time integration: Runge-Kutta scheme and eigenvalue solver . . . 83
3.4.2. Phase-space discretization and boundary conditions . . . 84
3.4.3. Parallelization . . . 87

4. Pedestal top stability: type-I ELMs vs. small-ELMs 88
4.1. Local gyrokinetic modeling in the pedestal region . . . 89
4.2. Stability across the pedestal top position . . . 90
4.3. Detailed analysis of modes at the pedestal top . . . 94
4.3.1. Sub-dominant modes . . . 94
4.3.2. Modes identification: transport fingerprints and normalized parallel electric field . . . 95
4.3.3. Kinetic-ballooning modes threshold: scan $(\beta_e, 1/L_{T_i})$ . . . 97
4.3.4. The impact of electromagnetic effects . . . 98
4.3.5. The impact of impurities . . . 99
4.4. Linear insights for the importance of non-linear mechanisms . . . 103
4.4.1. Shearing rate comparison with linear spectra . . . 104
4.4.2. Multi-scale criterion . . . 105

5. Turbulent transport at the pedestal top 106
5.1. Ion-scale turbulence: electromagnetic effects vs. equilibrium $\boldsymbol{E} \times \boldsymbol{B}$ shear flow . . . 107
5.1.1. Time traces of fluxes . . . 108
5.1.2. Comparison of turbulence regimes: Fourier spectra . . . 112
5.1.3. Assessing the importance of Zonal Flows vs. $\boldsymbol{E} \times \boldsymbol{B}$ flow shear in saturation . . . 113
5.1.4. Heat flux spectra . . . 116
5.1.5. Analysis of cross-phases . . . 118
5.2. Electron-scale turbulence: stiff ETG transport . . . 120
5.2.1. The role of electromagnetic effects and equilibrium $\boldsymbol{E} \times \boldsymbol{B}$ shear flow 122
5.2.2. The impact of adiabatic ions modelled with $\lambda = Z_{\text{eff}} T_e/T_i$ . . . 123
5.2.3. Stiffness study of ETG transport: comparison with experimental transport level . . . 124
5.3. Basic application of quasi-linear theory . . . 125
5.3.1. Quasi-linear expression of fluxes . . . 125
5.3.2. Heat flux spectra comparison: quasi-linear vs. non-linear . . . 130
5.3.3. Heat flux ratio Q_e/Q_i: sensitivity scan to input parameters . . . 132

6. Conclusions **134**
6.1. Results summary 135
6.2. Discussion and future work 137

Bibliography **139**

Appendix **162**

A. Normalization and diagnostics in GENE **163**
A.1. Normalization 163
A.2. Diagnostics 164

B. Dispersion relations of ITG and ETG modes with impurities **166**
B.1. Linear electrostatic gyrokinetic equation 166
B.1.1. Field-aligned coordinates 166
B.1.2. Linear response 168
B.2. Quasi-neutrality 168
B.3. Dispersion relations 168
B.3.1. ETG with impurity 168
B.3.2. ITG with impurity 172

List of Figures

1. (a-b) Profils expérimentaux en fonction du rayon toroïdal normalisé ρ_{tor} de densité n_e et de température ionique T_i pour trois décharges JET : #97395-Type-I ELMs (rouge), #96994-BSE (bleu), et #94442-BSE (noir). (c) Diagramme de stabilité peeling-ballooning pour les trois décharges en fonction de la densité de courant au bord normalisée par rapport à la densité de courant moyenne dans le volume $j_{\text{ped,max}}/\langle j \rangle$ et du gradient de pression maximal normalisé $\alpha_{\text{max}} = -2\mu_0 q^2 R/B^2 \, \mathrm{d}p/\mathrm{d}r \, |_{\text{max}}$ (source [1]). 9
2. Profils radiaux de la pression électronique au bord et positions radiales sélectionnées (gauche), taux de croissance linéaire γ correspondant en fonction du nombre d'onde binormal $k_y \rho_i$ (droite) pour la décharge (a) #97395-Type-I ELMs, (b) #94442-BSE. 11
3. Simulations non linéaires GENE à la position du sommet du piédestal avec un taux de cisaillement à l'équilibre $\gamma_{\boldsymbol{E}\times\boldsymbol{B}} = 0.45$ pour la décharge #94442-BSE. (a) Échelle ionique : traces temporelles du flux de chaleur ionique pour les cas ES_l et EM avec moyenne glissante (rouge) et variance correspondante (jaune). (b) Échelle électronique : flux de chaleur électronique moyenné dans le temps (rouge) comparé à la valeur expérimentale issue du calcul d'équilibre de puissance (bleu). La surface de la surface de flux est $V' = 108.27\,\text{m}^2$. 15
4. Comparaison des spectres de flux de chaleur non linéaires et quasi-linéaires en fonction du nombre d'onde binormal $\hat{k}_y$ des simulations EM GENE: (a) ions et (b) électrons. Les spectres sont normalisés par le pic du flux de chaleur ionique. L'aire sous la courbe est indiquée dans la légende, A. . . 17

1.1. Global primary energy consumption by source from 1800 to 2022. (a) Absolute consumption measured in terawatt-hours. (b) Share of energy consumption by sources. Adapted from source [3]. 31
1.2. (a) Cross section as a function of the kinetic energy in the center of mass for the fusion reactions D−T, D−D (total), and D−^{3}He. (b) Velocity averaged cross-section $\langle \sigma_f v \rangle$ as a function of the temperature. Data source [12]. 33
1.3. Sketches of tokamak and stellarator devices. Source: Max–Planck Institut für Plasmaphysik. 35
1.4. Trajectory of a charged particle in a uniform and stationary magnetic field $\boldsymbol{B}$. The particle position $\boldsymbol{x}$, guiding-center $\boldsymbol{X}_{gc}$, and Larmor radius $\boldsymbol{\rho}_L$ are indicated. 37
1.5. Gyro-orbit of positive charged particles in the presence of a density gradient $\boldsymbol{\nabla} n$, with a net drift velocity $\boldsymbol{v}^*$ arising. Adapted from source [18]. 38
1.6. Sketch of tokamak field line and nested flux surfaces. 39

1.7. Radial profiles of (a) electron density and (b) electron temperature for L-mode and H-mode confinement regimes of DIII-D tokamak plasmas. Source [34]. 43
1.8. Illustrations of the driving mechanisms of the (left) drift-wave and (right) interchange instability. The dark and light areas represent regions with higher and lower density, respectively. The equilibrium profile is perturbed with an oscillation. Source [63]. 46
1.9. Sketch of basic physical mechanism of (left) parallel-velocity gradient instability (right) reconnection with magnetic islands formation (adapted from source [68]). 47
1.10. Radial profiles of (a) radial electric field E_r, (b) corresponding shearing rate $\omega_{E\times B}$, and (c) main ion pressure gradient $\boldsymbol{\nabla} p_i$ for L-, I-, and H-mode confinement regimes of ASDEX-U tokamak plasmas. Source [103]. 51
1.11. Basic mechanism of $\boldsymbol{E}\times\boldsymbol{B}$ shear decorrelation of turbulent eddies reducing the radial correlation length L_r. Turbulent eddies are schematically represented as circles. Inspired from source [103]. 52

2.1. Time traces of relevant engineering and plasma parameters for the type-I ELM discharge #97395 and the small-ELM discharges #94442 and #96994: (a) P_{IN} the total input power, and $P_{\mathrm{RAD}}^{\mathrm{bulk}}$ the bulk radiated power; (b) f_{GW}, the ratio of the line-averaged electron density to the Greenwald density, along with the gas flow rate; (c) $\beta_N \equiv \beta/(I_p a B_{\mathrm{tor}})$; (d) H_{98}, the thermal energy enhancement factor relative to the IPB98$(y,2)$ scaling law; (e)–(g) BeII line emission from the inner divertor. 57
2.2. (a) f_{ELM} ELM frequency, W_{MHD} total stored plasma energy, and Beryllium II line emission from the inner divertor. (b) Peeling-ballooning stability diagram using the MINERVA-DI code [121] (which solves the extended Frieman–Rotenberg equation and includes rotation and diamagnetic effects, using the Sauter formula for the bootstrap current model [122, 123]) for the three discharges #97395, #96994, and #94442 as function of the edge current density normalized to the volume-averaged current density $j_{\mathrm{ped,max}}/\langle j\rangle$ and maximum normalized pressure gradient $\alpha_{\mathrm{max}} = -(2\mu_0 q^2 R/B^2)\cdot \mathrm{d}p/\mathrm{d}r\,|_{\mathrm{max}}$. Adapted from source [1]. 58
2.3. Time averaged radial profiles as function of the normalized toroidal radius ρ_{tor}: type-I ELM #97395 $t = 11.95 - 11.98\,\mathrm{s}$ (red), BSE #96994 $t = 12.4 - 12.6\,\mathrm{s}$ (blue), and BSE #94442 $t = 11.35 - 11.45\,\mathrm{s}$ (black). (a). Electron density, n_e. (b) Electron temperature, T_e. (c) Ion temperature, T_i. (d) Toroidal angular frequency ω_{tor}. (e) Be density, n_{Be}. (f) Ni density, n_{Ni}. 61
2.4. The modified hyperbolic tangent (*mtanh*) fit (see Sec. 2.2.3 for its definition) of the electron density and temperature pedestal profiles obtained from TRANSP simulations is shown for three discharges: (a) #97395–type-I ELMs, (b) #96994–BSE, and (c) #94442–BSE. The pedestal widths (w) with their relative uncertainties, the fit parameter (p), and the pedestal heights are reported. 62

2.5. Radial profiles of the normalized gradients of (a) electron density n_e (b) deuterium density n_D (c) electron temperature T_e, and (d) ion temperature T_i. Vertical lines indicate the pedestal top positions. 64
2.6. Equilibrium flux-surfaces from EFIT++ reconstruction (green), and interpolated with GENE at the pedestal top position of the three discharges, red blue and black flux-surfaces respectively: (a) #97395-Type-I ELM (b) #96994-BSE and (c) #94442-BSE. 66
2.7. Radial profiles of (a) safety factor q, (b) magnetic shear $\hat{s}$, and (c) electron beta β_e. 67
2.8. Electron pressure radial profile (points) computed from TRANSP electron density and temperature profiles, and *mtanh* fit line (green) for the three discharges. Vertical lines indicate the pedestal top position r_{top}, corresponding to the pedestal height h_1 coefficient from the fit, and two other positions at $r_{\text{top}} \pm (p - r_{\text{top}})/2$ where p is a coefficient from the fit. 68
2.9. Radial electric field profiles of the three discharges (a) #97395-Type-I ELMs, (b) #96994-BSE, and (c) #94442-BSE. The contributions to the radial electric field (red) from toroidal rotation (solid line) and the diamagnetic term (dashed line) are shown. The vertical line indicates the pedestal top position. 70

3.1. Illustration of the particle coordinate $\boldsymbol{x}$, the guiding-center coordinate $\boldsymbol{X}_{gc}$. The magnetic field is oriented in the z direction $\boldsymbol{B} = B\hat{\boldsymbol{z}}$. This figure corresponds to the (x, y) projection of Fig. 1.4. 75
3.2. Sketch of the flux-tube domain. The non-orthogonal straight-field-aligned coordinates (x, y, z), respectively radial, bi-normal, and parallel, are shown. Adapted from source [155]. 81
3.3. Discretization of a shaped flux surface by varying the distribution of discretization points n_z as a function of the parameter k (or `edge_opt` in GENE input parameters: (a) with standard distribution, i.e. $k = 0$ (b) with $k = 3.0$. 86

4.1. Electron pressure pedestals radial profiles for the three discharges, highlighting the three radial locations across the pedestal top position: r_{in}, r_{top}, and r_{out}. This figure is analog to Fig. 2.8. 90
4.2. Linear growth rate γ and mode frequency ω as function of the binormal wavenumber $k_y\rho_i$ at the three selected radial locations. Positive (negative) real frequency represents mode propagating in the ion (electron) diamagnetic drift $\omega^*_{i(e)}$ direction. 91
4.3. Representative normalized ballooning mode structures of the electrostatic potential $|\phi_1|$ and parallel vector potential $\left|A_{1\parallel}\right|$ as function of the parallel coordinate z for four binormal wavenumber $\hat{k}_y$ at the pedestal top position for the three discharges. 93
4.4. Linear growth rates γ and mode frequency ω as function of the binormal wavenumber $\hat{k}_y$ for the type-I ELM #97395 and BSE #94442 discharges. The sub-dominant modes are obtained with eigenvalue computation. . . . 94

4.5. (a-b) Transport fingerprints and (c) normalized parallel electric field of the most unstable modes at the pedestal top position of the three discharges. 96
4.6. Linear growth rate γ and real frequency ω spectra as a function of β_e and $1/L_{T_i}$ for the $\hat{k}_y = 0.1$ mode at the pedestal top of the three discharges. The vertical lines indicate the experimental reference β_e values. 97
4.7. Linear growth rates γ and real frequency ω as function of the binormal wavenumber $\hat{k}_y$ at the pedestal top of the three discharges: reference input parameters (EM) are compared with electrostatic-limit (ES$_l$). 99
4.8. Linear growth rates γ and real frequency ω as function of the binormal wavenumber $\hat{k}_y$ at the pedestal top of the three discharges. Spectra with reference input parameters (w/ imp.) are compared with spectra obtained: without kinetic impurities (w/o imp.), including only one kinetic impurity (only Ni or only Be), and for BSE discharges, electron-scale (from $\hat{k}_y \sim 2.0$) simulations with adiabatic ions (a-Ions) with/without $\lambda = Z_{\rm eff}T_e/T_i$ parameter. 100
4.9. Linear growth rates γ and real frequency ω as function of the binormal wavenumber $\hat{k}_y$ at the pedestal top of the three discharges: reference input parameters (w/ λ_D) are compared with neglecting the laplacian in the Poisson equation (w/o λ_D). 103
4.10. Linear growth rates γ as function of the binormal wavenumber $\hat{k}_y$ at the pedestal top of the three discharges. The value of the total shearing rate $\gamma_{\boldsymbol{E}\times\boldsymbol{B},tot}$ (solid) and the one only due to the toroidal rotation $\gamma_{\boldsymbol{E}\times\boldsymbol{B},rot}$ (dashed) are shown as horizontal lines for comparison. 104
4.11. Linear $\hat{k}_y$ spectra of $\gamma/k_y[v_{{\rm th},i}/a\rho_i]$ at the pedestal top for the three discharges. 105

5.1. Time traces of electron (red) and ion (blue) heat, and electron particle (green) fluxes in Gyro-Bohm units for the pedestal top parameters of #97395-Type-I ELM discharge. (a) ES$_l$ with $\gamma_{\boldsymbol{E}\times\boldsymbol{B}} = 0.6$. (b) EM with $\gamma_{\boldsymbol{E}\times\boldsymbol{B}} = 0.6$. 109
5.2. Time traces of electron (red) and ion (blue) heat, and electron particle (green) fluxes in Gyro-Bohm units for the pedestal top parameters of #94442-BSE discharge. (a) ES$_l$ with $\gamma_{\boldsymbol{E}\times\boldsymbol{B}} = 0.3$. (b) ES$_l$ with $\gamma_{\boldsymbol{E}\times\boldsymbol{B}} = 0.45$. (c) EM with $\gamma_{\boldsymbol{E}\times\boldsymbol{B}} = 0.3$. (d). EM with $\gamma_{\boldsymbol{E}\times\boldsymbol{B}} = 0.45$ 110
5.3. Fourier spectra of field-line averaged, and time averaged electrostatic potential $\phi^2_{\hat{k}_x,\hat{k}_y}$ for discharge #94442-BSE: (a) ES$_l$ case, (b) EM case. . . 112
5.4. Time averaged zonal flows shearing rate spectra: ES$_l$ (red) vs. EM (blue) for the simulations with $\gamma_{\boldsymbol{E}\times\boldsymbol{B}} = 0.45$. 113
5.5. Normalized ion (blue) and electron (red) heat flux spectra (lin-log scales) as a function of the binormal wavenumber $\hat{k}_y$ for the discharge #94442-BSE: (a) $\gamma_{\boldsymbol{E}\times\boldsymbol{B}} = 0.45$, ES$_l$ vs. EM; (b) EM, $\gamma_{\boldsymbol{E}\times\boldsymbol{B}} = 0.3/0.45$; (c) ES: $\gamma_{\boldsymbol{E}\times\boldsymbol{B}} = 0.3/0.45$. In (a) and (b) insets with a zoom at low $\hat{k}_y$ are shown (lin-lin scales). 116
5.6. Normalized ion (blue) and electron (red) heat flux spectra as a function of the binormal wavenumber $\hat{k}_y$ for the discharge #97395-Type-ELMs for the ES$_l$ case. 117

5.7. Time averaged histograms of cross-phases α between the electrostatic potential ϕ_1 and fluctuating quantities $(n_1, T_{\parallel 1}, T_{\perp 1})$ for each k_y mode: (a,b) for electrons and deuterium in the ES_l simulation; (b,c) for electrons and deuterium in the EM simulation. White stars indicate the dominant cross-phases for each $\hat{k}_y$ mode from linear simulations of discharge #94442-BSE with $\gamma_{\boldsymbol{E}\times\boldsymbol{B}} = 0$. 118
5.8. Normalized electron heat flux spectra as a function of the binormal wavenumber $\hat{k}_y$ for the sensitivity scan: (a) $\beta = [0.75, 1, 1.5, 2.0]\beta_{\text{ref}}$, (b) $\gamma_{\boldsymbol{E}\times\boldsymbol{B}} = [0.3, 0.45, 0.6]$. 122
5.9. Normalized electron heat flux spectra as a function of the binormal wavenumber $\hat{k}_y$ for different values of $1/L_{T_e}$: (a) [(b)] without [with] including the $\lambda = T_e/T_i Z_{\text{eff}}$ parameter in the ion adiabatic response, and Z_{eff} in the collisional operator. 123
5.10. Electron heat flux Q_e as function of the normalized logarithmic gradient $1/L_{T_e}$: including (and not) λ and Z_{eff} in red (green). One case with reduced normalized logarithmic density gradient $1/L_{n_e} = 0.8(1/L_{n_e})_{\text{ref}}$ is shown in magenta. The experimental inferred electron heat transport is shown in blue. For reference, the flux-surface area is $V' = 108.27\,\text{m}^2$. . . . 124
5.11. Comparison of the three saturation rules ML (magenta), ML-mod (green), and QuaLiKiz (grey) computed from linear GENE simulations. For each spectrum, the area below the curve is reported in the legend. (a) For the ES_l settings the non-linear $|\phi|^2$ spectrum is shown in dashed blue for discharge #94442-BSE with $\gamma_{\boldsymbol{E}\times\boldsymbol{B}} = 0.45$. 127
5.12. Comparison of the inverse effective perpendicular wavenumber $1/\langle k_\perp^2 \rangle$ from linear GENE simulations as function of $\hat{k}_y$: ES_l (green), EM considering only ϕ_1 (blue), and EM considering the three fields $(\phi_1, A_{1\parallel}, B_{1\parallel})$ (magenta). 128
5.13. Normalized linear heat fluxes for the electron (red) and deuterium (blue) as function of the binormal wavenumber $\hat{k}_y$ for: (a) ES_l, and (b) EM. . . 129
5.14. Comparison of non-linear (with $\gamma_{\boldsymbol{E}\times\boldsymbol{B}} = 0.45$) and quasi-linear (using the three saturation rules) heat flux spectra as function of $\hat{k}_y$ from ES_l GENE simulations: (a) ion, and (b) electron heat flux. The spectra are normalized with the peak of the ion heat flux. For each spectrum, the area below the curve is reported in the legend. 130
5.15. Comparison of non-linear (with $\gamma_{\boldsymbol{E}\times\boldsymbol{B}} = 0.45$) and quasi-linear (using the three saturation rules) heat flux spectra as function of $\hat{k}_y$ from EM GENE simulations: (a) ion, and (b) electron heat flux. The spectra are normalized with the peak of the ion heat flux. For each spectrum, the area below the curve is reported in the legend. 131
5.16. Contours of electron to ion heat flux ratio Q_e/Q_i from quasi-linear calculations using ML-mod saturation rule and GENE EM linear simulations: (a) $(1/L_{n_e}, 1/L_{T_i})$, and (b) $(1/L_{n_e}, 1/L_{T_e})$ parameters scan. The solid magenta line corresponds to the experimental value of Q_e/Q_i. The vertical and horizontal orange lines are in correspondence of the reference values of $(1/L_{n_e}, 1/L_{T_i})$ (see Table 2.5). 132

List of Tables

1.1. Typical parameters of thermonuclear plasma in different confinement approaches. . . . 34
1.2. Maximum values of main engineering parameters achieved in the JET tokamak. The heating systems are: the neutral beam injection (NBI), and the ion cyclotron resonance heating (ICRH). The current drive is the lower hybrid (LH) system. . . . 41
1.3. Properties of *standard* micro-instabilities: kinetic ballooning mode (KBM), micro-tearing mode (MTM), ion temperature gradient (ITG) mode, trapped electron mode (TEM), and electron temperature gradient (ETG) mode. The real frequency ω sign is positive (negative) in the ion(electron)-diamagnetic direction. The normalized inverse scale length is $L_X^{-1} = -\,\mathrm{d}\log(X)/\mathrm{d}r$ with r a normalized radial coordinate. . . . 49

2.1. Main engineering parameters for the three selected JET shots: plasma current I_p, toroidal magnetic field B_{tor}, average triangularity δ, safety factor q_{95}, $H_{98}(y,2)$ energy confinement enhancement factor relative to the IPB98$(y,2)$ scaling law [28], ICRH power P_{ICRH}, NBI power P_{NBI}, edge gas puff particle sources $\Gamma_e(\sigma)$, the measured effective charge $Z_{\mathrm{eff}} = \sum_i n_i Z_i^2/n_e$, and time window of averaging t. . . . 56
2.2. Electron and ion heat flux across the surface at the pedestal top positions from TRANSP power balance calculation. . . . 63
2.3. Measured effective charge Z_{eff} for the three discharges. . . . 65
2.4. Toroidal rotation, diamagnetic, and neoclassical term contribution to the shearing rate at the pedestal top position for the three discharges. . . . 71
2.5. Local parameters for the three discharges, at the three selected radii. The reference values are: $n_{\mathrm{ref}} = n_e$ $[10^{19}\,\mathrm{m}^{-3}]$, $T_{\mathrm{ref}} = T_i$ [keV], L_{ref} [m], B_{ref} [T], and the toroidal angular velocity ω_{ref} $[\mathrm{rad\,s}^{-1}]$. . . . 72

4.1. Properties of *standard* microinstabilities: kinetic ballooning mode (KBM), microtearing mode (MTM), ion temperature gradient (ITG) mode, trapped electron mode (TEM), and electron temperature gradient (ETG) mode. The *transport fingerprints* (derived from a combination of analytical arguments and numerical simulations as reported in Ref. [76]), and normalized parallel electric field $\hat{E}_{\parallel}$ are defined in the text. . . . 96

5.1. Set of ion-scale simulations performed at the pedestal top positions. . . . 107
5.2. Flux-tube resolutions for the non-linear simulations at the ion-scale. The parameters are: number of radial and bi-normal modes, parallel resolution, parallel-velocity resolution, magnetic-moment resolution, radial, bi-normal and velocity domain size. . . . 108

5.3. Averaged heat fluxes in the electron Q_e and ion Q_i channels in the time windows corresponding to turbulence saturated phases. For comparison, the experimentally inferred fluxes, calculated from power balance in TRANSP, are reported. Notice: N.C. indicates a not converged simulation. The flux surface area is $V' = 108.27\,\mathrm{m}^2$. 111
5.4. Shearing rate vs. equilibrium $\boldsymbol{E} \times \boldsymbol{B}$ shearing comparison. The ratio between the zonal flows shearing rate ω_{ZF} and the peak of growth rate at the ion-scale γ_{lin}, corresponding to the spectra discussed in Chapter 4. . . 114
5.5. Set of electron-scale simulations performed at the pedestal top position of discharge #94442-BSE. 120
5.6. Flux-tube resolutions for the converged non-linear simulations at the electron-scale for discharge #94442-BSE. The parameters are: number of radial and bi-normal modes, parallel resolution, parallel-velocity resolution, magnetic-moment resolution, radial, bi-normal, parallel velocity and magnetic moment domain size. 121

1. Introduction

Contents

1.1. The energy crisis and fusion energy . . . 30
1.1.1. Nuclear fusion reactions . . . 32
1.1.2. Thermonuclear plasma . . . 34
1.1.3. Lawson criterion . . . 35
1.2. Charged particles motion in an electromagnetic field . . . 36
1.2.1. Single-particle drifts . . . 36
1.2.2. Diamagnetic drift . . . 38
1.3. The tokamak device . . . 39
1.3.1. Magnetic equilibrium . . . 39
1.3.2. The JET tokamak . . . 41
1.4. Tokamak plasma regimes and the pedestal . . . 42
1.4.1. Pedestal physics . . . 43
1.5. Brief overview of turbulent transport . . . 45
1.5.1. Microinstabilities . . . 46
1.5.2. Microturbulence . . . 50
1.6. Thesis objectives and outline . . . 53

The purpose of this chapter is to introduce the reader to the motivations behind the search for new energy sources, and to provide the basic concepts of nuclear fusion research in the realm of magnetically confined plasmas. The main concepts relevant to the content of this thesis are introduced: the tokamak device, the issue of plasma confinement, and turbulent transport processes, with a focus on the mechanisms occurring in the edge plasma region called *pedestal*. This will allow us to highlight the main open questions and thereby introduce the objectives of this thesis work.

1.1. The energy crisis and fusion energy

The quality of life in contemporary society is directly linked to reliable access to energy resources [2]. The technological advancements and industrial growth over the past two centuries have largely depended on the discovery and utilization of new, and abundant energy sources such as fossil fuels, nuclear fission, and renewables (including e.g. solar, wind, hydropower).

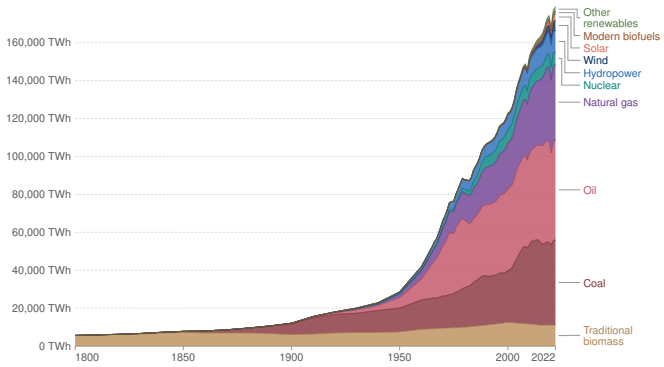

(a)

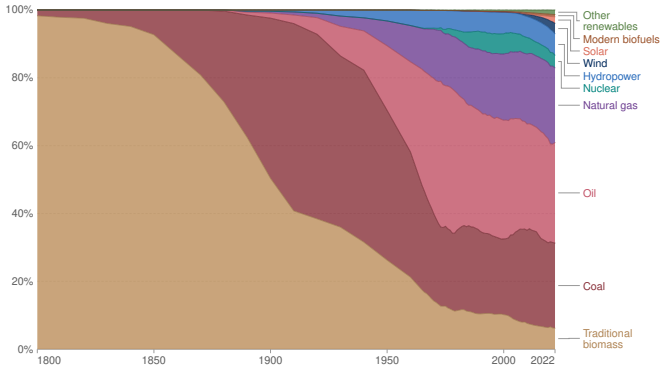

(b)

Figure 1.1.: Global primary energy consumption by source from 1800 to 2022. (a) Absolute consumption measured in terawatt-hours. (b) Share of energy consumption by sources. Adapted from source [3].

The primary energy, including electricity, transport, and heating, yearly consumed from 1800 to 2022, along with the corresponding share of energy sources, is shown in Fig. 1.1. We observe that energy consumption increased during the 20th century, and it will continue to rise due to global population growth and an increase in per capita consumption in developing countries. Currently, fossil fuels – coal, oil, and natural gas – represent the primary energy source, providing approximately 80% of the energy consumed in 2022.

In recent years, there has been growing concern over the sustainability of energy sources and their impact on climate change. Energy produced from fossil fuels releases toxic substances and carbon dioxide CO_2 into the atmosphere, which, being a greenhouse gas, contributes to global warming [4]. Additionally, fossil fuel reserves are expected to be depleted in the coming decades. For these reasons, there is a need for long-term alternative energy sources that can satisfy the continuous growth in consumption and environmental sustainability requirements.

In this context, nuclear energy emerges as one of the most promising solutions to meet the global energy demand, alongside renewable resources. The energy released by nuclear reactions is equivalent to the mass defect between the reacting atomic nuclei and the products, as described by Einstein's equation $E = \Delta mc^2$. As a consequence of this

formula, nuclear energy is a high-density energy source compared to, for example, the chemical energy released by combustion reactions. Specifically, nuclear energy can be released through two different types of nuclear reactions: fission and fusion.

Nuclear fission is the process in which heavy atomic nuclei, such as uranium or plutonium, absorb a neutron and split into lighter nuclei, releasing energy and additional neutrons. These neutrons can then trigger further fission reactions, resulting in a self-sustaining chain reaction. The technology used in nuclear fission power plants is mature and well-established, playing a significant role in the low-carbon energy mix. The main disadvantages are: the production of highly radioactive waste that requires specialized storage facilities for very long periods (ranging from 10^3 to 10^6 years), the risk of nuclear accidents with harmful environmental consequences, and the risk of nuclear proliferation.

Nuclear fusion, on the other hand, is the process in which two light atomic nuclei, such as isotopes of deuterium, fuse to form a heavier nucleus and release energy. The concept of nuclear fusion reactions was proposed in the early 1900s and was hypothesized to be the process behind energy production in stars [5]. In the 1930s, there were two breakthroughs: the achievement of the first fusion reaction in the laboratory by E. Rutherford [6, 7], and the publication of the *proton-proton chain* by H. Bethe to explain the fusion reaction cycles through which stars convert hydrogen into helium [8]. From that point onward, intense research began to harness nuclear fusion reactions for energy production on Earth. There are several advantages of this technology. Firstly, the elements suitable for use as fuels, i.e., deuterium (^{2}H or D) and tritium (^{3}H or T) (see Sec. 1.1.1), are abundant on Earth. Deuterium can be extracted at low cost from seawater, which contains one deuterium atom for every 6700 hydrogen atoms. Rough estimates of reserves and consumption in fusion power plants suggest that the available deuterium could last for billions of years [9]. Tritium, however, is not naturally occurring as it is a radioactive element with a half-life of about twelve years. For this reason, tritium in future fusion power plants will be obtained by breeding with the lithium isotope ^{6}Li. The fuel limit for D−T fusion reactions is therefore tied to the limits of ^{6}Li reserves. Estimates of ^{6}Li reserves and consumption in fusion power plants indicate that they should be sufficient for about 20 000 years [9]. Another advantage is the low environmental impact. Fusion reactions do not emit CO_2 or other harmful substances. However, the neutrons produced by fusion reactions cause neutron activation of the materials used in the reactor. This activation results in radioactive materials that need to be stored for a short time on the order of 100 years. Finally, another significant advantage is the intrinsic safety of fusion reactions, which, not relying on chain reactions, make the process easy to control externally.

We have thus seen that energy production from fusion reactions would represent a highly attractive source compared to those used today. However, there are several challenges—scientific, technological, and economic—that must be considered [10].

1.1.1. Nuclear fusion reactions

We now turn to the introduction of the main fusion reactions considered for use on Earth. In this regard, it is useful to introduce the *reaction rate* $\mathcal{R}$, which is the number of fusion

reactions between two species σ per unit volume and time [9, 11].

$$\begin{aligned}\mathcal{R} &= n_{\sigma_1} n_{\sigma_2} \int\int \mathrm{d}^3\boldsymbol{v}_{\sigma_1} \mathrm{d}^3\boldsymbol{v}_{\sigma_2}\, f_{\sigma_1}(\boldsymbol{v}_{\sigma_1}) f_{\sigma_2}(\boldsymbol{v}_{\sigma_2}) |\boldsymbol{v}_{\sigma_1} - \boldsymbol{v}_{\sigma_2}| \sigma_f(|\boldsymbol{v}_{\sigma_1} - \boldsymbol{v}_{\sigma_2}|) \\ &\equiv n_{\sigma_1} n_{\sigma_2} \langle \sigma_f v \rangle\end{aligned}$$

where n_σ is the number density, $\boldsymbol{v}_\sigma$ the velocity, f_σ the distribution function, σ_f the fusion cross-section between the two species as a function of the relative velocity, and $\langle \sigma_f v \rangle$ the velocity-averaged cross-section. If we assume that the species are in thermodynamic equilibrium, and thus have Maxwellian distribution functions, the corresponding velocity-averaged cross-section can be evaluated knowing the cross-section σ_f. The fusion cross-section measures the probability of two nuclei fusing as a function of their kinetic energy. This includes various phenomena, from Coulomb electrostatic repulsion to quantum mechanical effects, such as tunneling effects, and the attractive *strong nuclear force* responsible for the fusion of nuclei. The most promising fusion reactions to be used in

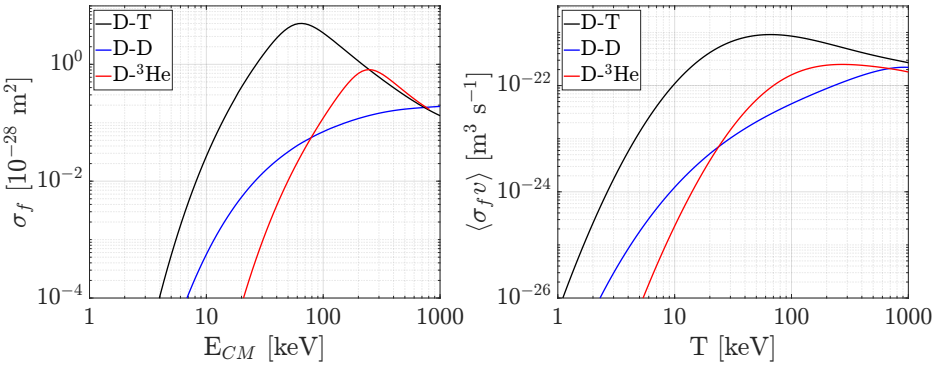

Figure 1.2.: (a) Cross section as a function of the kinetic energy in the center of mass for the fusion reactions D−T, D−D (total), and D−^{3}He. (b) Velocity averaged cross-section $\langle \sigma_f v \rangle$ as a function of the temperature. Data source [12].

nuclear fusion power plants are

$$\begin{aligned}\mathrm{D} + \mathrm{T} &\longrightarrow {}^4\mathrm{He}\,(3.5\,\mathrm{MeV}) + n\,(14.1\,\mathrm{MeV}) \\ \mathrm{D} + \mathrm{D} &\longrightarrow \begin{cases} {}^3\mathrm{He}\,(0.82\,\mathrm{MeV}) + n\,(2.45\,\mathrm{MeV}) \\ \mathrm{T}\,(1.01\,\mathrm{MeV}) + \mathrm{H}\,(3.02\,\mathrm{MeV}) \end{cases} \\ \mathrm{D} + {}^3\mathrm{He} &\longrightarrow {}^4\mathrm{He}\,(3.6\,\mathrm{MeV}) + \mathrm{H}\,(14.7\,\mathrm{MeV})\end{aligned}$$

whose corresponding velocity-averaged cross-sections $\langle \sigma_f v \rangle$ as a function of the temperature of the reacting nuclei are shown in Fig. 1.2. By convention, the temperatures are expressed in units of energy electron-volts (eV), related to the temperature in kelvin (K) via the Boltzmann constant $k_\mathrm{B} \approx 1.381 \cdot 10^{-23}\,\mathrm{J\,K^{-1}}$, and the conversion in joules, $1\,\mathrm{eV} = 1.6022 \cdot 10^{-19}\,\mathrm{J}$. It can be observed that the D−T reaction has the lowest energy threshold and the highest values of the velocity-averaged cross-section, making it the leading candidate for use in first-generation fusion power plants. In recent years, there has also

Table 1.1.: Typical parameters of thermonuclear plasma in different confinement approaches.

	Gravitational	Magnetic	Inertial
Temperature (keV)	1.5–5	10	2.5
Density (m^{-3})	10^{32}	10^{20}	10^{27}
Pressure (Pa)	$2 \cdot 10^{16}$	10^{5}	10^{14}
Size (m)	$1.3 \cdot 10^{8}$	10	10^{-3}

been growing interest in the proton-boron fusion reaction $^{11}\mathrm{B} + {}^{1}\mathrm{H} \longrightarrow 3\,{}^{4}\mathrm{He}\,(8.7\,\mathrm{MeV})$ for its potential in advanced fusion applications [13, 14], with the main advantages being its aneutronic nature, which avoids material activation, and the availability of readily accessible fuel.

1.1.2. Thermonuclear plasma

We have just realized that for fusion reactions to occur, nuclei must have energies between 1 keV and 100 keV, corresponding to temperatures between 10^7 K and 10^9 K. The lower bound corresponds to temperatures comparable to those in the core of the Sun (15 MK$\sim$1.5 keV). At these temperatures, light atoms are completely ionized, i.e. electrons are stripped from their orbitals. The matter is thus in a gaseous state composed of positively charged nuclei of light atoms and electrons, and is macroscopically neutral, known as *plasma*.

No material can withstand and contain a plasma at thermonuclear temperatures. In stars, these plasmas are confined by the gravitational attraction resulting from their enormous mass. On Earth, two different approaches are pursued: inertial confinement and magnetic confinement.

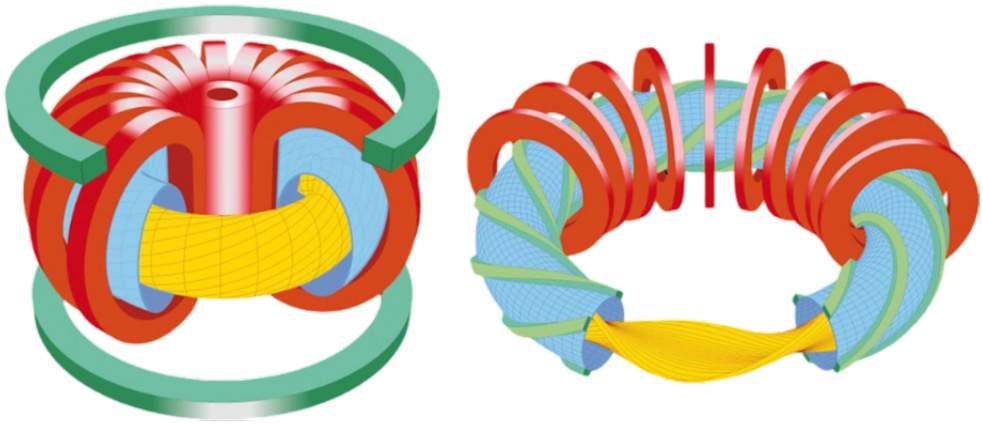

Figure 1.3.: Sketches of tokamak and stellarator devices. Source: Max–Planck Institut für Plasmaphysik.

In the inertial confinement fusion (ICF) approach [15], a D−T fuel pellet is compressed to high densities and heated using high-energy lasers or ion beams. This process leads to an implosion resulting in energy release.

In the magnetic confinement fusion (MCF) approach, since the motion of charged particles immersed in a magnetic field is constrained to helical trajectories around magnetic field lines and freely stream along the field line direction (see Sec. 1.2 for details), the goal is to create a magnetic field configuration that forms a *magnetic cage*. The most advanced devices are the tokamak and stellarator, shown in Fig. 1.3. The toroidal configuration allows the field lines to close, thus avoiding losses parallel to the field lines.

In Table 1.1 the main parameters of thermonuclear plasmas corresponding to the different methods of confinement are compared.

1.1.3. Lawson criterion

Regardless of the confinement method, the goal of a fusion power plant is to produce more energy than is required to heat the plasma to initiate fusion reactions. To this end, the fusion power gain factor Q is defined as the ratio of the fusion power output to the power used to heat the plasma. The break-even point is achieved at $Q = 1$. Ignition occurs when $Q \to \infty$, representing a self-sustaining fusion reaction without external heating. For electricity production, instead of the *fusion* power gain factor, a *reactor* gain factor should be considered. This needs to take into account additional terms, such as the power used to operate the reactor (e.g., for the coils, pumping, and heating systems), and the efficiency of turbines cycle in converting heat into electricity. These factors tend to reduce the reactor gain factor compared to the fusion power gain factor. In general,

the objective of a fusion power plant is to achieve $Q \gg 1$, where the majority of heating is provided by self-heating from fusion-born particles.

A simplified energy balance calculation allows for the derivation of the Lawson criterion [16] for the self-sustainment of nuclear fusion reactions in a thermonuclear plasma. This criterion can be formulated as a lower bound for the *triple product* [9, 11, 17]

$$nT\tau_E > 3 \cdot 10^{21}\,\mathrm{m}^{-3}\,\mathrm{keV\,s}$$

with n the number density, T the temperature, and τ_E the energy confinement time defined as the ratio between the energy stored in the plasma and the power losses. This represents an estimate in ideal conditions, assuming a pure plasma with constant density and temperature. More realistic conditions contribute to increasing this lower bound. To satisfy this condition, within ICF, the aim is to maximize the density, requiring a very short energy confinement time $\tau_E \sim 100\,\mathrm{ns}$. In MCF, however, macroscopic plasma stability limits the maximum achievable plasma pressure, thus requiring a higher energy confinement time of the order $\tau_E \sim 1\,\mathrm{s}$. Specifically, τ_E is determined by various transport processes, the dominant of which are conductive losses due to microturbulence, introduced in Sec. 1.5.2. Ultimately, a better understanding of turbulent transport processes in magnetized plasmas is crucial for optimizing current experiments and designing future fusion reactors.

1.2. Charged particles motion in an electromagnetic field

As previously mentioned, thanks to the properties of charged particle motion in electromagnetic fields, it is possible to design appropriate configurations or devices capable of confining plasma and keeping it away from material walls. We now aim to discuss the motion of charged particles and some of the velocity drifts perpendicular to the magnetic field that can occur. These drifts can arise both in single-particle motion and when treating plasma as a fluid [18]. This will allow us to introduce some of the typical quantities that characterize a magnetized plasma, which will be used in this thesis work.

1.2.1. Single-particle drifts

The equation of motion for a particle σ with charge q_σ and mass m_σ in the presence of electromagnetic fields $\boldsymbol{E}$ and $\boldsymbol{B}$ is generally determined by the Lorentz force

$$m_\sigma \frac{\mathrm{d}\boldsymbol{v}_\sigma}{\mathrm{d}t} = q_\sigma \left(\boldsymbol{E} + \boldsymbol{v}_\sigma \times \boldsymbol{B}\right) . \tag{1.1}$$

At this stage, only the equilibrium electromagnetic fields are considered, neglecting the plasma's self-generated electromagnetic fields. This assumption allows to study the net particle motion as a superposition of motions corresponding to simpler configurations, thus allowing us to derive the most fundamental aspects of the motion [11, 17–19]. First, considering only the presence of a uniform magnetic field $\boldsymbol{B}$ in Eq. 1.1, the resulting particle motion is a helical trajectory around the magnetic field lines, as shown in Fig. 1.4. It is thus possible to define several quantities associated with this *gyro-motion*: the frequency of gyration around the magnetic field line, i.e., the cyclotron frequency (or

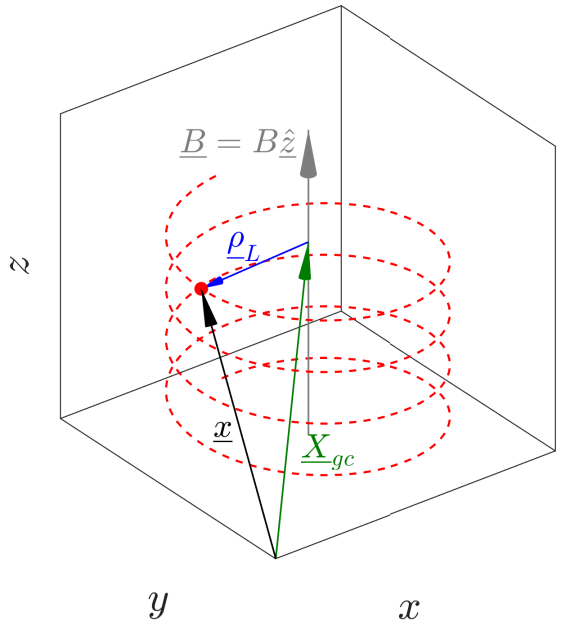

Figure 1.4.: Trajectory of a charged particle in a uniform and stationary magnetic field $\boldsymbol{B}$. The particle position $\boldsymbol{x}$, guiding-center $\boldsymbol{X}_{gc}$, and Larmor radius $\boldsymbol{\rho}_L$ are indicated.

Larmor frequency) $\Omega_{c,\sigma}$, and the gyration radius, i.e., the Larmor radius $\rho_{L,\sigma}$

$$\Omega_{c,\sigma} = \frac{q_\sigma B}{m_\sigma} \qquad \rho_{L,\sigma} = \frac{v_{\perp,\sigma}}{\Omega_{c,\sigma}} = \frac{m_\sigma v_{\perp,\sigma}}{q_\sigma B}$$

where $v_{\perp,\sigma}$ represents the velocity of the particle in the direction perpendicular to the magnetic field $\boldsymbol{B}$. Specifically, the particle position $\boldsymbol{x}$ can be decomposed into the guiding-center position $\boldsymbol{X}_{gc}$, corresponding to the center of the gyro-orbit, and the Larmor radius, as shown in Fig. 1.4. It is important to note that, since the cyclotron frequency depends on the charge, electrons and ions spiral in opposite directions.

If now we also consider the superposition of a uniform electric field $\boldsymbol{E}$, the particles undergo a drift velocity perpendicular to both fields, given by

$$\boldsymbol{v}_{\boldsymbol{E}\times\boldsymbol{B}} = \frac{\boldsymbol{E}\times\boldsymbol{B}}{B^2}\,.$$

This velocity, called the $\boldsymbol{E}\times\boldsymbol{B}$ drift, represents one of the guiding-center drifts. This velocity is the same for all charged particles, as it is independent of both mass and charge.

Finally, let us consider spatial inhomogeneities in the magnetic field, which determine additional guiding-center drifts. In fact, in the presence of a curved magnetic field, a particle is subjected to a centrifugal force, which results in a drift velocity. Furthermore, when there is a variation in the magnetic field strength, the Lorentz force changes throughout a gyro-orbit, leading to a force directed opposite to the gradient of the magnetic field (i.e. a mirror force), causing a particle drift. The drifts due to the

curvature of the magnetic field lines and the gradient of the magnetic field strength are given by

$$\begin{aligned} \boldsymbol{v}_{\mathrm{c},\sigma} &= \frac{m_\sigma v_{\parallel,\sigma}^2}{q_\sigma B^2} \boldsymbol{B} \times (\hat{\boldsymbol{b}} \cdot \boldsymbol{\nabla}) \hat{\boldsymbol{b}} \underset{\beta \ll 1}{\approx} \frac{m_\sigma v_{\parallel,\sigma}^2}{q_\sigma B} \frac{\boldsymbol{B} \times \boldsymbol{\nabla} B}{B^2} \\ \boldsymbol{v}_{\nabla B,\sigma} &= \frac{m_\sigma v_{\perp,\sigma}^2}{2 q_\sigma B} \frac{\boldsymbol{B} \times \boldsymbol{\nabla} B}{B^2} \end{aligned} \tag{1.2}$$

where $(\hat{\boldsymbol{b}} \cdot \boldsymbol{\nabla}) \hat{\boldsymbol{b}}$ represents the field line curvature, and $v_\parallel$ is the velocity parallel to the magnetic field. It is important to note that in this case, the drifts depend on the particle's charge, leading to charge separation. In the following section, we will discuss the relevance of these drifts in the magnetic configuration of the tokamak device.

1.2.2. Diamagnetic drift

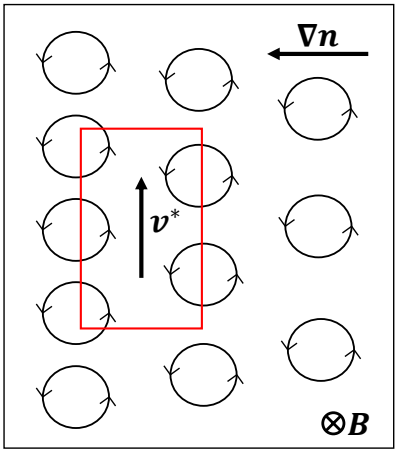

Figure 1.5.: Gyro-orbit of positive charged particles in the presence of a density gradient $\boldsymbol{\nabla} n$, with a net drift velocity $\boldsymbol{v}^*$ arising. Adapted from source [18].

We introduce now the *macroscopic* drift, known as the diamagnetic drift, which results from the combination of the cyclotron motion of individual particles in the presence of a density or temperature gradient perpendicular to the magnetic field. The situation for ions is schematically represented in Fig. 1.5. Due to the varying plasma density in the horizontal direction, in a vertical cross-section of the plasma, indicated by the red box, there are more particles gyrating in the upward direction than in the downward direction, thus determining a net drift velocity v_σ^*, even though the guiding centers are not displaced. A similar effect is caused by the temperature gradient, as it modifies the Larmor radius. The diamagnetic drift velocity is generally given by

$$v_\sigma^* = -\frac{\boldsymbol{\nabla} p_\sigma \times \boldsymbol{B}}{q_\sigma n_\sigma B^2}$$

where p_σ, n_σ, and q_σ are the pressure, density, and charge of the plasma species σ, respectively. The name of this drift comes from the associated diamagnetic current, which acts to reduce the background magnetic field.

1.3. The tokamak device

The tokamak is an axisymmetric toroidal device and the most advanced for the magnetic confinement of thermonuclear plasmas. The main component of the magnetic field is in the toroidal direction $\boldsymbol{B}_\varphi$, and it is generated by the external toroidal field coils. A purely toroidal magnetic field is insufficient to ensure plasma confinement due to plasma particle drifts associated with the in-homogeneity, $\boldsymbol{\nabla} B$, and curvature of the field [11, 17, 18] (see Sec. 1.2). These drifts in the vertical direction, opposite for particles with opposite charges, would cause charge separation and consequently an electric field, resulting in an $\boldsymbol{E} \times \boldsymbol{B}$ outward drift that leads to the loss of confinement. This problem is overcome by twisting the magnetic field lines by introducing a poloidal component of the magnetic field $\boldsymbol{B}_\theta$. This component is generated by a toroidal current induced by the central solenoid via Faraday's law.

1.3.1. Magnetic equilibrium

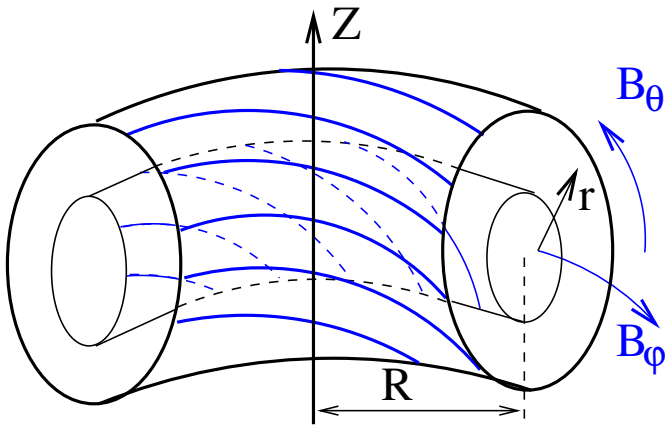

Figure 1.6.: Sketch of tokamak field line and nested flux surfaces.

Due to the geometrical configuration, the magnetic field lines in a tokamak trace nested *magnetic surfaces*, as shown in Fig. 1.6. The magnetic field is conveniently described in the cylindrical coordinate system (R, Z, φ), with R as the radial direction, Z as the vertical direction, and φ as the toroidal angle, as shown in Fig. 1.6. Since the magnetic field is divergence-free and in a tokamak is axisymmetric, meaning it does not depend on the φ coordinate, it can be written as [20]

$$\boldsymbol{B}(R, Z) = \boldsymbol{B}_\varphi + \boldsymbol{B}_\theta = F(\psi)\boldsymbol{\nabla}\varphi + \boldsymbol{\nabla}\varphi \times \boldsymbol{\nabla}\psi$$

where two scalar functions, $F(\psi)$ and $\psi(R, Z)$, have been introduced. It can be verified that the function $\psi(R, Z)$ is linked with the flux of the poloidal magnetic field component through a surface spanning from the magnetic axis to a radial location

$$\psi = \frac{\psi_{\mathrm{pol}}}{2\pi} = \frac{1}{2\pi}\int_S \boldsymbol{B}_\theta \cdot \mathrm{d}\boldsymbol{S}\,.$$

Similarly, a toroidal flux can be defined, which is the flux of the toroidal magnetic field through a surface cutting a poloidal plane (R, Z) as

$$\psi_{\text{tor}} = \int_S \boldsymbol{B}_\varphi \cdot \mathrm{d}\boldsymbol{S}\,.$$

Since the fluxes just defined are constant on the magnetic surfaces, i.e., $\boldsymbol{B}\cdot\boldsymbol{\nabla}\psi = \boldsymbol{B}\cdot\boldsymbol{\nabla}\psi_{\text{tor}} = 0$, the magnetic surfaces are also called *flux surfaces* and can be labeled with ψ or ψ_{tor}, thus being a convenient choice as radial coordinates.

The global equilibrium of the plasma at the lowest order is described by the MHD force-balance equation, which prescribes the balance between the magnetic force and the plasma pressure force [21]

$$\boldsymbol{j}\times\boldsymbol{B} = \boldsymbol{\nabla}p\,,$$

combined with the Ampère's law $\boldsymbol{\nabla}\times\boldsymbol{B} = \mu_0\boldsymbol{j}$. As a consequence of the force-balance equation, we have $\boldsymbol{B}\cdot\boldsymbol{\nabla}p = 0$ and $\boldsymbol{j}\cdot\boldsymbol{\nabla}p = 0$, meaning that the pressure is constant on the magnetic surfaces, and the current also lies on these surfaces. It follows that both pressure and current are *flux functions*, i.e., $p(\psi)$ and $j(\psi)$. To characterize the magnetic field lines, we introduce the *safety factor*, which provides a measure of the twist of a magnetic field line

$$q(\psi) = \frac{\mathrm{d}\psi_{\text{tor}}}{\mathrm{d}\psi_{\text{pol}}} = \frac{\mathrm{d}\varphi}{\mathrm{d}\theta}$$

where θ is the poloidal angle. For rational values, the safety factor represents the number of toroidal revolutions a magnetic field line needs to make to complete a single poloidal turn. It is of particular interest because high values of q determine the stability of MHD modes [21, 22]. Since this parameter is associated with the plasma current $\boldsymbol{j}$, stability considerations determine the maximum current that can be used in the tokamak. Associated with the safety factor, the *magnetic shear* is defined as its normalized radial derivative

$$\hat{s} = \frac{r}{q}\frac{\mathrm{d}q}{\mathrm{d}r}$$

with r being a radial coordinate. This parameter is important for the study of microinstabilities (see Sec. 1.5) because both negative and high positive magnetic shear improve stability [23].

Finally, we introduce the plasma beta parameter β, which is determined by the ratio of plasma pressure to magnetic pressure [11]

$$\beta = \frac{p}{B^2/2\mu_0}\,.$$

This parameter provides a measure of the efficiency of the magnetic field in confining the plasma pressure p. It plays a significant role in the stability, since high values of beta can lead to MHD instabilities [21, 22]. In the context of this thesis, the role of β will be associated with electromagnetic effects in turbulent transport. Specifically, it will be shown that the Ampere's equation for the magnetic field fluctuations is proportional to the plasma β, thus representing the coupling parameter for the electromagnetic effects.

Table 1.2.: Maximum values of main engineering parameters achieved in the JET tokamak. The heating systems are: the neutral beam injection (NBI), and the ion cyclotron resonance heating (ICRH). The current drive is the lower hybrid (LH) system.

Parameter	Value
Major radius (R)	2.96 m
Minor radius (a)	1.25 m
Plasma volume	100 m^3
Toroidal magnetic field (B)	4 T
Plasma current (I_p) X-point	6.0 MA
NBI power (P_{NBI})	34 MW
ICRH power (P_{ICRH})	22 MW
LH power (P_{LH})	7 MW

1.3.2. The JET tokamak

The world's largest tokamak experiment is the Joint European Torus (JET) tokamak, located in Culham, UK, which was designed to operate with the D – T fuel mix. It has been operated since 1983, with the last plasma produced on December 18, 2023. It is currently in the decommissioning phase. The JET tokamak featured a D-shaped poloidal cross-section, and it was upgraded from a limiter configuration to a divertor configuration in 1993 which led to a significantly improved plasma performance. This resulted in the record fusion power of 16 MW and $Q \sim 0.67$ obtained during the deuterium-tritium first experimental campaign (DTE1) in 1997. Initially designed with carbon plasma-facing components (C-wall), it was upgraded in 2011 to an ITER-like wall (ILW) consisting of beryllium and tungsten in the divertor. This upgrade facilitated experiments supporting future ITER operations in terms of scientific and technical challenges [24]. The main engineering parameters of JET are provided in Table 1.2, which also details the available heating systems and their maximum power.

The discharges considered in this thesis (see Chapter 2) were obtained during experimental campaigns with deuterium plasmas performed in JET-ILW. These campaigns aimed to develop plasma regimes that achieve high core plasma performance while ensuring edge plasma conditions and dynamics that, when extrapolated to a reactor-scale fusion power plant like ITER, are compatible with the thermal and particle loads sustainable by plasma-facing components [25, 26]. This led to the discovery of new plasma regimes at JET, as reported in Ref. [1, 27]. These new regimes, achieved by operating with low or no gas injection, are obtained under plasma conditions that align with the ITER baseline scenario. These include a safety factor at the flux surface containing 95% of the poloidal flux, $q_{95} = 3.2$, a normalized plasma beta $\beta_N \equiv \beta/(I_p a B_t) = 1.8 - 2$, and an energy confinement enhancement factor relative to the IPB98$(y, 2)$ scaling law [28], $H_{98} \sim 1$. However, it is important to note, as shown in Chapter 2, that these regimes are characterized by a lower density compared to the predicted ITER baseline scenario, posing challenges to their compatibility with divertor detachment operation, which is required in ITER and future fusion reactors.

These regimes are the starting point of the research conducted in this thesis, which

focuses on characterizing the impact of turbulent transport (see Sec. 1.5) in the pedestal (see Sec. 1.4) of these new regimes.

1.4. Tokamak plasma regimes and the pedestal

As previously mentioned, for the MCF approach to be successful, it is necessary to maximize the energy confinement time τ_E to achieve the ignition condition. Due to the high complexity of the turbulent transport phenomena that limit τ_E, a complete theoretical model is not yet available. Experimentally, therefore, efforts have been dedicated to characterizing τ_E through empirical scaling laws (see e.g. Ref. [11]) based on various parameters, e.g. the plasma current I_p, the atomic mass A, the toroidal magnetic field strength B_t, the major radius R, the minor radius a, the averaged plasma density $\langle n \rangle$, and input power P. Specifically, it was realized that a single empirical law able to capture all experimental results does not exist. This leads to the definition of the different plasma confinement regimes.

The main confinement modes achieved by externally heating the plasma are the low confinement mode (L-mode) and high-confinement mode (H-mode). The H-mode regime was first discovered in 1982 in the ASDEX tokamak in Garching, Germany [29]. This discovery represented a significant breakthrough in fusion research, as the H-mode has an energy confinement time approximately twice that of the L-mode ($\tau_{E,\text{H-mode}} \sim 2\tau_{E,\text{L-mode}}$). This advancement made it feasible to conceive a tokamak reactor for energy production of reasonable dimensions.

Experimentally, access to the H-mode is achieved by applying a plasma heating power above a certain threshold, P_{L-H}, which depends on various parameters such as plasma density, magnetic field, and magnetic configuration. Although H-mode regimes are now routinely accessed in tokamaks worldwide, the physical understanding of the mechanisms underlying the L-H transition is incomplete and continue to be an active area of research [30]. The L-H transition is associated with a spontaneous reduction of turbulent transport just inside the last closed magnetic flux surface (LCFS), due to the formation of an edge transport barrier (ETB) [31]. This results in a steepening of the temperature and density profiles, leading to the formation of the so-called *pedestal*.

Figure 1.7 shows radial profiles of the electron density and temperature obtained at the DIII-D tokamak in both L-mode and H-mode, where the steepening of edge profiles is evident. This region is typically fitted using a hyperbolic tangent function with appropriate linear terms [32, 33]. The advantage of this approach is that the fit parameters provide quantities directly related to pedestal characteristics (e.g., height, width), allowing for quantitative comparisons. This method will be utilized in Chapter 2 to quantitatively define the pedestal top position in the various discharges analyzed in this thesis. In addition to the formation of the pedestal, there are other typical features common to plasmas in the H-mode regime. Firstly, around the position of the ETB, a reduction in density fluctuation amplitude is observed, indicative of reduced turbulence. Furthermore, at the same time as the formation of the ETB and in its proximity, a steepening of the radial electric field E_r takes place, such that the associated $\boldsymbol{E} \times \boldsymbol{B}$ sheared flows can play a determining role in quenching turbulence [35, 36] (see Sec. 1.5.2 for further discussion).

Finally, another common feature of H-mode is the destabilization of edge-localized

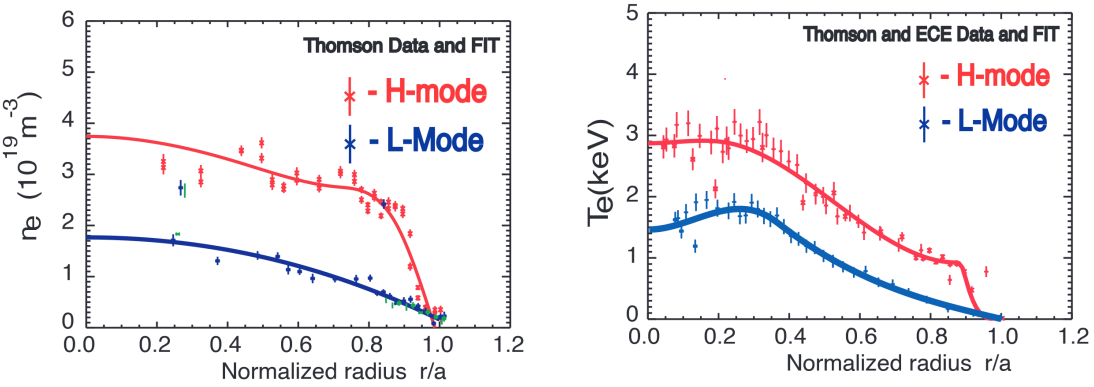

(a) (b)

Figure 1.7.: Radial profiles of (a) electron density and (b) electron temperature for L-mode and H-mode confinement regimes of DIII-D tokamak plasmas. Source [34].

modes (ELMs) [37–39], which appear as spontaneous, periodic relaxations of the pedestal, leading to the release of plasma energy and particles to the first wall and divertor. There are various types of ELMs, categorized by their frequency f_{ELM} and energy released per ELM, ΔW.

The most common ELMs are type-I ELMs, which result in the expulsion of particles and energy at levels that could irreparably damage the plasma-facing components of reactor-scale devices such as ITER. For this reason, research has focused on developing plasma regimes that maintain high confinement while having small or no ELMs [40, 41]. Specifically, recent experimental campaigns have been conducted at JET with this goal, leading to the development of regimes with small-ELMs [1], which are the subject of this thesis. In particular, as described in Chapter 2, these regimes are also characterized by pedestal structures different from those typically obtained in type-I ELM regimes. This features motivates the dedicated modeling of the transport processes to clarify their potential different role. This will be the subject of this thesis.

1.4.1. Pedestal physics

We now proceed briefly introducing the various factors that play a role in determining and regulating the pedestal dynamics, which is characterized by phenomena spanning several different spatio-temporal scales. This introduction aims to clarify the role of turbulent transport, which has been the focus of investigation in this thesis.

The importance of the pedestal region in plasma profiles is primarily connected to its role as a boundary for the stiff core profiles, where an increase in heating power does not lead to a significant steepening in gradients (with internal transport barriers being an exception). For this reason, the pedestal height determines the overall energy confinement time and, consequently, the fusion power. Additionally, the pedestal profiles strongly influence edge dynamics, such as ELM features, thus affecting the heat and particle fluxes toward plasma-facing components—an essential consideration for reactor-scale devices, as mentioned earlier. For these reasons, significant efforts have been devoted to the experimental characterization and understanding of the pedestal structure, specifically

focusing on the height, width, and gradients of density, temperature, and pressure profiles.

From a theoretical perspective, the pedestal dynamics, and thus its structure, are determined by the self-consistent interaction of heat and particle sources, MHD limits [21], and transport phenomena (see Sec. 1.5 for an introduction on turbulent transport). Therefore, pedestal modeling must incorporate several physical models that span different spatio-temporal scales.

Starting with the role of sources, the conditions in the divertor and the region beyond the LCFS, gas fuelling, and pumping strongly influence the particle sources and thus the pedestal structure [42]. In this context, the presence of metallic walls and the resulting impurity content can also be decisive factors [43]. As for heat sources, the heat flowing from the core represents the main source for the pedestal. A quantitative understanding of these sources is crucial for comparison with theoretical models.

Regarding the role of MHD stability, it is believed that, for the most common ELMy H-mode operations, kink-peeling modes [44], ballooning modes [45], and the coupled peeling-ballooning (P-B) modes [45] (driven by pressure gradients and current density) are responsible for the ELM crash. These instabilities determine the pedestal height and maximum gradients between each pedestal recovery [46–48]. In the context of this thesis, P-B stability boundaries for the analyzed discharges will be presented in Chapter 2.

Regarding transport processes, although the formation of the ETB is associated with the stabilization of instabilities (also known as modes) that cause turbulent transport, since the transport associated with neoclassical processes [49] is not always sufficient to explain the experimentally inferred transport, a residual turbulent transport must be present. Specifically, turbulent transport mechanisms are thought to be responsible for the inter-ELM time evolution of the density and temperature pedestal profiles, depending on the heat and particle sources, thus determining the limits of pedestal gradients and heights during the recovery phase. Identifying the nature of these mechanisms through experimental measurements and numerical simulations remains an active area of research [50]. In Sec. 1.5, the main mechanisms responsible for turbulent transport will be introduced.

The stability limits imposed by the models described above, namely MHD and transport, can be combined to develop a predictive model for the pedestal structure. In this context, the most widely used model for predicting pedestal height and width for a given pedestal density is the EPED model [46]. This model consists of two main constraints, which together provide a predictive framework: (1) the P-B stability boundary at the critical normalized pressure gradient $\alpha_{\text{crit}} = -2\mu_0 R q^2/(B^2) \cdot \mathrm{d}p/\mathrm{d}r$ constrains the edge pressure gradient $\mathrm{d}p/\mathrm{d}r$; (2) the second constraint derives from transport considerations, attributing it to kinetic-ballooning modes (see Sec. 1.5), which constrain the pedestal width to $w = c_1\sqrt{\beta_{\theta,\text{ped}}}$, with c_1 calibrated based on DIII-D experimental data [46, 48]. However, discrepancies have been observed between EPED model predictions and experimental results, particularly in JET-ILW [42, 51], where ELMs were triggered before the P-B boundary was reached, highlighting the need for further advancements in theoretical understanding to address the model's limitations.

Despite the progress made in understanding the physical processes that determine the pedestal structure [50, 52–56], the role of turbulent transport mechanisms in limiting the pedestal gradients remains likely the least understood. The objective of this thesis thus fits within this gap in understanding. Starting from plasma discharges obtained at JET-

ILW, which feature small and high-frequency ELM dynamics compared to standard type-I ELMs and exhibit different pedestal structures, a turbulence analysis will be conducted to better understand and compare the potentially distinct roles and mechanisms governing turbulent transport.

1.5. Brief overview of turbulent transport

We now turn to the final section of this introductory chapter, which aims to introduce the main concepts related to turbulent transport, focusing on the general aspects relevant to this thesis.

Building on what was mentioned earlier, the main processes limiting plasma confinement in the MCF approach (once large-scale plasma stability is ensured) making it challenging to meet the Lawson criterion, are due to turbulence phenomena. To be precise, several processes are responsible for the radial, or cross-field, transport of particles and heat, thus limiting the plasma confinement time. The goal of transport theory is to investigate and understand these phenomena, and ultimately, to control them. At the most basic level, Coulomb collisions between particles, confined in a toroidal magnetic field, are responsible for the radial diffusion of particles, known as *neoclassical transport* [49, 57]. However, estimates of radial transport due to neoclassical processes are typically insufficient to explain the experimentally inferred radial fluxes of particles and heat, thus requiring the involvement of other processes.

The processes responsible for the missing transport are due to plasma turbulence [58–60], driven by instabilities that develop on microscopic scales, with characteristic wavelengths perpendicular to the magnetic field on the order of the ion and electron Larmor radius [61]. Heated confined plasmas deviate from thermodynamic equilibrium, making free-energy sources available, such as density or temperature gradients [62], which feed these instabilities. The resulting turbulence manifests as chaotic fluctuations in electromagnetic fields, as well as in density, temperature, and current densities. Essentially, the cross-field transport of particles and heat can be governed by two regimes: (1) in the *electrostatic regime*, where $\boldsymbol{E} \times \boldsymbol{B}$ advection, driven by electromagnetic fluctuations, transports particles, heat and momentum; (2) in the *electromagnetic regime*, if magnetic fluctuations are strong enough to locally disrupt the magnetic flux surfaces, magnetic islands can be created enhancing the plasma mixing and resulting in radial heat transport.

In the following, we will first introduce the physical mechanisms driving microinstabilities, namely the drift-wave, interchange, parallel-velocity gradient, and tearing mechanisms. These will allow us to present the main microinstabilities, along with their features and dependencies on plasma parameters. Additionally, it should be noted that in the context of this thesis, these microinstabilities will be addressed using a reduced kinetic theory, introduced in Chapter 3, which allows us to account for mechanisms such as Landau resonances, finite-Larmor radius effects, and collisions. Subsequently, aspects related to turbulence development, self-regulation, and saturation mechanisms will be briefly introduced.

1.5.1. Microinstabilities

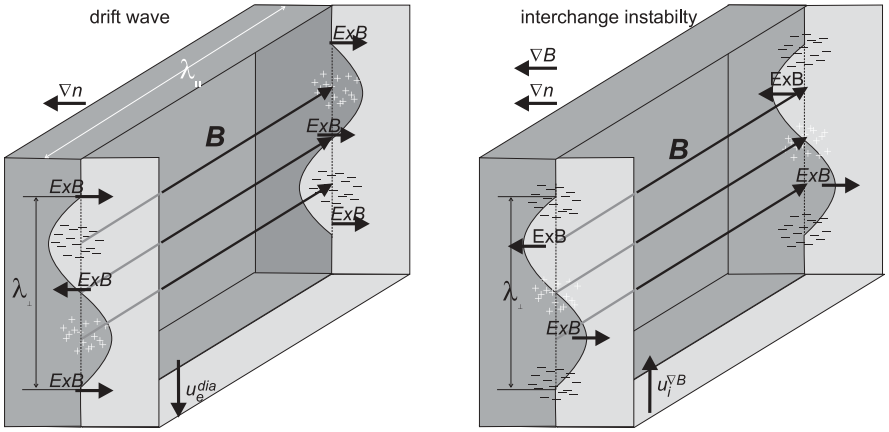

Figure 1.8.: Illustrations of the driving mechanisms of the (left) drift-wave and (right) interchange instability. The dark and light areas represent regions with higher and lower density, respectively. The equilibrium profile is perturbed with an oscillation. Source [63].

Drift-wave mechanism To describe the drift-wave mechanism, consider a plasma in a uniform magnetic field with a density gradient, as shown on the left of Fig. 1.8. Let us consider an initial three-dimensional perturbation of the equilibrium density, characterized by parallel and perpendicular wavenumbers with respect to the background magnetic field, such that $k_{\parallel} \neq 0$ and $k_{\perp} \gg k_{\parallel}$, meaning the perturbation is elongated along the magnetic field line.

A key factor in the instability is the different inertia of ions and electrons along the magnetic field line. Due to the higher mobility of electrons, they respond more quickly to the density gradient, creating positive (negative) charges along the field line in regions of positive (negative) density perturbations. This charge accumulation generates an electric field in the plane perpendicular to the magnetic field, directed from the region of higher density to lower density. The presence of this electric field leads to the $\boldsymbol{E} \times \boldsymbol{B}$ drift, which advects the background density.

Assuming electrons respond instantly to the density perturbation (i.e., they are adiabatic), the electric potential and density perturbations are in phase. In this case, the $\boldsymbol{E} \times \boldsymbol{B}$ drift shifts the density perturbation downward while keeping its amplitude constant, making the drift-wave stable. However, it becomes unstable if the electron response to the density gradient along the field line is delayed, due to factors such as electron-ion collisions or Landau damping. In this case, the electric potential perturbation lags behind the density perturbation, allowing the $\boldsymbol{E} \times \boldsymbol{B}$ drift to amplify the initial density perturbation.

Modes belonging to this category include the slab-ion-temperature-gradient (slab-ITG) mode, the slab-electron-temperature-gradient (slab-ETG) mode, and collisional drift-wave [62, 64, 65].

Interchange mechanism To describe the interchange mechanism, consider a plasma in a magnetic field with finite curvature in the presence of a density gradient, as shown on the right of Fig. 1.8. Unlike the drift-wave mechanism, the interchange instability is two-dimensional, as all the fundamental dynamics occur in the plane orthogonal to the magnetic field. Here, we consider a density perturbation with $k_{\parallel} = 0$. Due to the curvature drift (see Eq. 1.2) in the vertical direction and the fact that particles with opposite charges drift in opposite directions, charge separation occurs. This results in an electric field and an associated $\boldsymbol{E} \times \boldsymbol{B}$ drift.

This drift amplifies the initial density perturbation only if $\boldsymbol{\nabla} B \cdot \boldsymbol{\nabla} n > 0$, which is referred to as the *bad curvature region*; in contrast, if $\boldsymbol{\nabla} B \cdot \boldsymbol{\nabla} n < 0$, the initial perturbation is damped, and this region is called the *good curvature region*. In a tokamak, due to the dependence of the magnetic field on the major radius, $B \sim 1/R$, the bad curvature region corresponds to the low-field side of the torus, while the high-field side is the good curvature region.

This category includes the toroidal-ion-temperature-gradient (toroidal-ITG) mode, which is a primary candidate for explaining ion heat transport in the core of fusion plasmas [66]. In this case, the basic mechanisms depicted on the right of Fig. 1.8 should consider $\boldsymbol{\nabla} T_i$ instead of $\boldsymbol{\nabla} n$. Since the curvature drift (see Eq. 1.2) depends on thermal particle energy via $v_{\parallel,\sigma}$, the hotter plasma drifts faster than the cooler plasma, leading to the same amplification described above. A similar mechanism at the electron scale and involving $\boldsymbol{\nabla} T_e$ is responsible for the toroidal-electron-temperature-gradient (toroidal-ETG) mode [67].

This category also includes trapped-electron modes (TEM), where the charge separation is due to the toroidal precession of electrons trapped on the low-field side. Finally, kinetic-ballooning modes (KBM) also belong to this category, where electromagnetic effects, and thus fluctuations in the vector potential, play a crucial role.

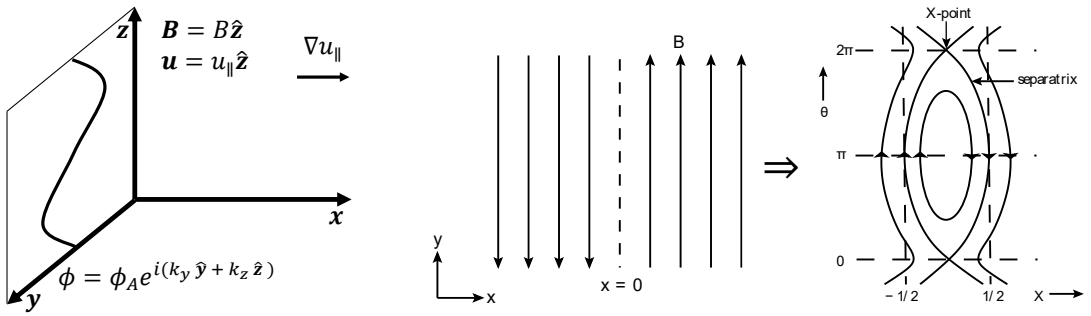

Figure 1.9.: Sketch of basic physical mechanism of (left) parallel-velocity gradient instability (right) reconnection with magnetic islands formation (adapted from source [68]).

Parallel velocity gradient mechanism Another class of instability is driven by the radial gradient of parallel velocity to the magnetic field, $\boldsymbol{\nabla} u_{\parallel}$, also known as parallel sheared velocity. This radial variation of $u_{\parallel}$ represents a departure from thermodynamic equilibrium, and so a free energy source. In tokamak plasmas, such gradients can arise, for instance, through the neutral beam injection (NBI) heating system, which transfers

momentum to the plasma, establishing a mean velocity that differs from one magnetic surface to another.

To describe the basic physical mechanism [69], consider a plasma in a uniform magnetic field $\boldsymbol{B} = B\hat{\boldsymbol{z}}$, with cold ions and electrons at thermodynamic equilibrium. Now, assume a parallel velocity $\boldsymbol{u}_\parallel = u_\parallel(x)\hat{\boldsymbol{z}}$ that varies radially along $\hat{\boldsymbol{x}}$, with $\boldsymbol{\nabla}_x u_\parallel > 0$. Consider an initial perturbation of the electrostatic potential $\phi = \phi_A e^{i(k_y\hat{\boldsymbol{y}}+k_z\hat{\boldsymbol{z}})}$, resulting in an electric field $\boldsymbol{E} = -i(k_y\hat{\boldsymbol{y}} + k_z\hat{\boldsymbol{z}})\phi$. This setup is shown on the left of Fig. 1.9.

Focusing on the motion parallel to the magnetic field, ions are accelerated by the parallel electric field $E_\parallel \propto -ik_z\phi$. Simultaneously, due to the electric field along $\hat{\boldsymbol{y}}$, there is an $\boldsymbol{E}\times\boldsymbol{B}$ drift resulting in a radial velocity, $u_x \propto -ik_y\phi$. As ions move along $\hat{\boldsymbol{x}}$, they experience a second acceleration (or deceleration) along $\hat{\boldsymbol{z}}$, since $u_\parallel(x)$ and $\boldsymbol{\nabla}_x u_\parallel > 0$. Two situations can occur: (1) if the two accelerations along $\hat{\boldsymbol{z}}$ due to $E_\parallel$ and $\boldsymbol{\nabla}_x u_\parallel$ act in the same direction, the system remains stable; (2) however, if the accelerations are in opposite directions, and the opposing velocity change due to $\boldsymbol{\nabla}_x u_\parallel$ exceeds that from $E_\parallel$, an instability can occur. This is called the Parallel Velocity Gradient (PVG) instability [69, 70], which operates similarly to the Kelvin-Helmholtz instability in fluids.

Since, in the JET tokamak, the torque from NBI heating is significant, leading to strong toroidal plasma rotation accompanied by radial shear, this effect can provide a significant additional drive for the micro-instability.

Tearing mechanism Finally, there are instabilities that drive the growth of magnetic field perturbations, fed by free energy sources such as the radial gradient of equilibrium toroidal current density, or the electron temperature gradient for micro-tearing modes (MTM) [11, 71, 72]. The physical mechanism of this instability is related to the self-reinforcement of magnetic perturbations via a current density that arises from the electric field established through charge separation (see [11, 72] for further details). This process can eventually lead to the reconnection of magnetic field lines, altering the magnetic topology and forming magnetic islands, as depicted in the right of Fig. 1.9.

MTMs, in particular, can result in small-scale magnetic islands on the scale of the ion Larmor radius, contributing to transport processes.

We have seen that various physical mechanisms, fed by different free-energy sources available in the plasma, can lead to a wide range of microinstabilities in tokamaks. Regarding the pedestal, it is important to remember that it is a region characterized by steep pressure gradients, meaning that potentially all the discussed instabilities can be present. To distinguish these instabilities, some key features of the modes introduced so far are summarized in Table 1.3. In particular, the classification is made according to the length scales at which they develop (where k_y is the effective poloidal wave number), the driving parameters, and the direction of rotation. Thus, we have

- **Ion-temperature gradient (ITG) mode** [62, 65] This electrostatic instability develops on the ion scale, propagates in the ion diamagnetic direction, and is driven by the logarithmic ion temperature gradient $L_{T_i}^{-1}$, while being stabilized by the logarithmic density gradient L_n^{-1}. The instability threshold can be expressed in terms of the parameter $\eta_i = L_n/L_{T_i}$. It primarily drives heat transport in the ion channel [66]. In some modeling studies, ITG modes have been found to be unstable

Table 1.3.: Properties of *standard* micro-instabilities: kinetic ballooning mode (KBM), micro-tearing mode (MTM), ion temperature gradient (ITG) mode, trapped electron mode (TEM), and electron temperature gradient (ETG) mode. The real frequency ω sign is positive (negative) in the ion(electron)-diamagnetic direction. The normalized inverse scale length is $L_X^{-1} = -\,\mathrm{d}\log(X)/\mathrm{d}r$ with r a normalized radial coordinate.

	Scale	Drive	sgn(ω)
KBM	$k_y\rho_i \sim 0.1$	L_p^{-1}, $q^2\beta_e$	> 0
MTM	$k_y\rho_i \sim 0.1$	$L_{T_e}^{-1}$, β_e	< 0
ITG	$0.1 < k_y\rho_i \leq 1$	$L_{T_i}^{-1}$	> 0
TEM	$k_y\rho_i > 0.1$	$L_{T_e}^{-1}$, $L_{n_e}^{-1}$	< 0
ETG	$k_y\rho_i > 1$	$L_{T_e}^{-1}$	< 0

in the pedestal of JET-ILW [73–75], and it is believed that they can be stabilized at sufficiently high equilibrium $\boldsymbol{E} \times \boldsymbol{B}$ shearing [76], discussed later.

- **Trapped-electron mode (TEM)** [77, 78] This electrostatic instability develops across ion and electron scales, propagates in the electron diamagnetic direction, and can be driven by the logarithmic electron temperature and density gradients, $L_{T_e}^{-1}$ and L_n^{-1}. It is stabilized by collisionality and drives both particle and heat transport in the electron channel. In modeling work, these modes have been found to be unstable in the pedestal, e.g., in ASDEX-U [79, 80]. In the pedestal region, it is believed to be stabilized by equilibrium $\boldsymbol{E} \times \boldsymbol{B}$ shearing [76].

- **Kinetic-ballooning mode (KBM)** [81, 82] This electromagnetic instability develops on the ion scale, propagates in the ion diamagnetic direction, and is driven by the logarithmic pressure gradient L_p^{-1} and $q^2\beta_e$. It drives both particle and heat transport in all channels. Similar to ideal MHD ballooning modes, above the critical β threshold, the growth rate increases rapidly with β. These modes have been experimentally identified in tokamaks [83] and in numerical modeling [84], supporting their potential role in controlling inter-ELM pedestal evolution.

- **Micro tearing mode (MTM)** [71, 72] This electromagnetic instability develops on the ion scale, propagates in the electron diamagnetic direction, and is driven by the logarithmic electron temperature gradient $L_{T_e}^{-1}$. It primarily drives heat transport in the electron channel. Recent studies have proposed MTMs as key mechanisms in determining electron heat transport in tokamaks [85–90], and in the pedestals of JET-ILW [73, 91] and MAST [92].

- **Electron-temperature gradient (ETG) mode** [67, 78, 93, 94] This electrostatic instability develops on the electron scale, propagates in the electron diamagnetic direction, and is driven by the logarithmic electron temperature gradient $L_{T_e}^{-1}$, and stabilized by the logarithmic density gradient L_n^{-1}. The instability threshold can be expressed in terms of the parameter $\eta_e = L_n/L_{T_e}$. It primarily drives heat transport

in the electron channel [95, 96]. Recently, ETG modes have been proposed to significantly contribute to electron heat transport in the pedestal of JET-ILW [97, 98] and DIII-D [99]. However, due to the hyperfine scale at which they develop, experimental validation remains very limited [100] and challenging.

Finally, we note that in the presence of the strong driving normalized gradients typical of the pedestal region, a clear distinction between these modes will not always be possible. Indeed, it will be seen that ion-scale instabilities may assume a more *hybrid* character, i.e., exhibiting features belonging to different instabilities.

In the context of this thesis, the goal is first to compare the stability of JET plasma pedestals obtained in different ELMy regimes and characterized by different pedestal structures, as described in Chapter 2. To this end, numerical simulations will be performed, whose main advantage is that more realistic physical conditions can be considered compared to analytical treatments, which soon become intractable without introducing approximations and simplifications. The results of this analysis will be presented in Chapter 4, where the instabilities found will be categorized, taking into account the characteristics discussed here and other criteria introduced there.

1.5.2. Microturbulence

The reason we are interested in the instabilities is that they generally interact and eventually saturate into a state of microturbulence, determining the overall properties of turbulent transport. In fact, many of the microinstabilities present in tokamaks are typically unstable, thus accumulating energy, which is then redistributed through nonlinear couplings. In the context of this thesis, as mentioned earlier, turbulence will be studied using a statistical approach via a kinetic model, introduced in Chapter 3, where plasma dynamics are represented by the time evolution of the distribution function in phase space, i.e., in space and velocity [101]. Microturbulence manifests as fluctuations of the distribution function and self-generated electromagnetic fields. In this context, the nonlinear interaction leading to energy transfer occurs through two mechanisms [102]: *wave–wave interaction* and *wave–particle interaction*.

The first category includes phenomena like *three-wave coupling*, which arises from quadratic nonlinearities, and links two modes with wavenumbers and frequencies $(\boldsymbol{k}, \omega_{\boldsymbol{k}})$ and $(\boldsymbol{k'}, \omega_{\boldsymbol{k'}})$ with a third mode such that $\boldsymbol{k} = \boldsymbol{k'} + \boldsymbol{k''}$ and $\omega_{\boldsymbol{k}} = \omega_{\boldsymbol{k'}} + \omega_{\boldsymbol{k''}}$. Generally, two main situations can be distinguished depending on where the energy is transferred. In the case of *local* interactions, i.e. those occurring between nearby modes $\boldsymbol{k} \approx \boldsymbol{k'} \approx \boldsymbol{k''}$, a direct energy cascade may occur, transferring energy toward larger $\boldsymbol{k}$ down to the dissipative scale; alternatively, an inverse energy cascade toward smaller $\boldsymbol{k}$ can lead to the formation of large-scale structures. This latter case corresponds to *non-local* interactions, i.e. those occurring between distant modes $\boldsymbol{k} \approx \boldsymbol{k'} \gg \boldsymbol{k''}$, which can result in the excitation or damping of large structures by smaller ones.

The second category includes phenomena like the *nonlinear Landau resonance*, where energy transfer occurs through a resonant interaction between two waves $(\boldsymbol{k}, \omega_{\boldsymbol{k}})$ and $(\boldsymbol{k'}, \omega_{\boldsymbol{k'}})$ and a particle with velocity $\boldsymbol{v}$ under the condition $\omega_{\boldsymbol{k}} - \omega_{\boldsymbol{k'}} = (\boldsymbol{k} - \boldsymbol{k'}) \cdot \boldsymbol{v}$.

A quantitative study that accounts for these dynamics requires the use of numerical simulations, which will be introduced in Chapter 3.

In the following, some of the main saturation mechanisms of magnetized plasma

turbulence, which are expected to play a major role in both the triggering and sustainment of transport barriers, are introduced.

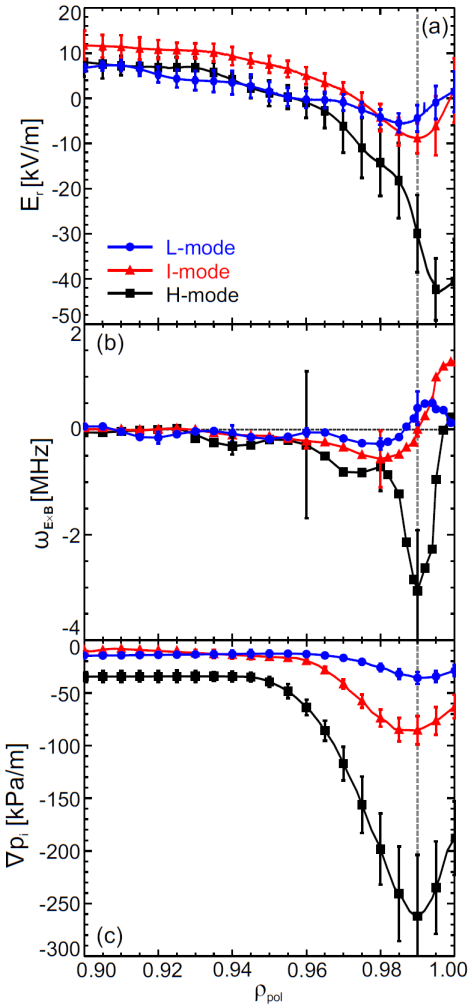

Figure 1.10.: Radial profiles of (a) radial electric field E_r, (b) corresponding shearing rate $\omega_{E\times B}$, and (c) main ion pressure gradient $\boldsymbol{\nabla} p_i$ for L-, I-, and H-mode confinement regimes of ASDEX-U tokamak plasmas. Source [103].

Radial electric field As mentioned earlier, the transition between L-H confinement regimes is accompanied by a modification of the radial electric field E_r in the edge region, where a negative well develops at the location of the edge transport barrier. The equation for the radial electric field is derived from the MHD radial force balance, yielding [104]

$$E_r = \frac{1}{n_i Z_i e} \boldsymbol{\nabla} p_i - v_{i\varphi} B_\theta + v_{i\theta} B_\varphi$$

where n_i is the ion density, $Z_i e$ is the ion charge, $p_i = n_i T_i$ is the pressure, T_i is the temperature, $v_{i\varphi}$ is the toroidal rotation velocity, $v_{i\theta}$ is the poloidal rotation velocity, and B_φ and B_θ are the toroidal and poloidal components of the magnetic field, respectively.

Representative radial profiles of E_r obtained at the ASDEX-U tokamak for different confinement modes are shown in Fig. 1.10. The corresponding shearing rate $\omega_{\boldsymbol{E}\times\boldsymbol{B}} = r/q\ \partial[(qE_r)/(rB)]/\partial r$ [105], and diamagnetic term $\boldsymbol{\nabla} p_i$ are also shown.

Theoretical efforts have thus been devoted to understanding the mechanisms linking turbulence suppression with the strong radial gradients (i.e., shearing) of the $\boldsymbol{E}\times\boldsymbol{B}$ plasma flow [35, 36]. This model would explain the sustainment mechanisms for the edge transport barrier and consequently the pedestal in pressure profiles. It was first shown that $\boldsymbol{E}\times\boldsymbol{B}$ shearing reduces the radial extent of turbulent eddies [106] and also decorrelates and alters the phase between pressure and potential fluctuations [35], resulting in reduced radial transport of particles and heat.

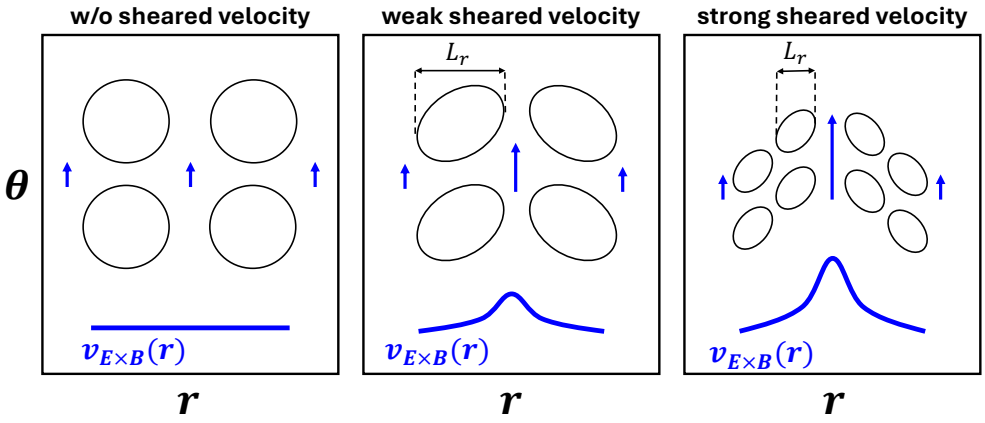

Figure 1.11.: Basic mechanism of $\boldsymbol{E}\times\boldsymbol{B}$ shear decorrelation of turbulent eddies reducing the radial correlation length L_r. Turbulent eddies are schematically represented as circles. Inspired from source [103].

A schematic representation of the decorrelation mechanism associated with $\boldsymbol{E}\times\boldsymbol{B}$ shear is shown in Fig. 1.11. If the background flow is radially constant, the turbulent eddies are not distorted. However, in the presence of a radially varying background flow, due to the different flow velocities, the turbulent eddies become distorted. If the shearing rate is sufficiently high, the turbulent vortices will eventually break into smaller structures, thus reducing the radial correlation length over which turbulence can develop.

In Chapter 2, where the experimental results obtained at JET are discussed, an estimate of the shearing rate will be provided. The inclusion of this effect in the numerical modeling carried out in this thesis will be discussed in Chapter 3. This effect on the turbulence at the pedestal top of the analyzed discharges will be addressed in Chapter 5.

Zonal flows In addition to the background, or mean, $\boldsymbol{E}\times\boldsymbol{B}$ plasma flow discussed previously, turbulence itself can generate sheared plasma flows: the zonal flows [107]. They are electrostatic potential fluctuations with toroidal and predominantly poloidal symmetry, i.e., $n = m = 0$, where n and m are the toroidal and poloidal mode numbers, with a finite radial wavenumber and finite frequency. Due to their symmetry properties, they cannot directly access the free energy in the density and temperature gradients and are not subject to Landau damping, with collisions being the main damping process. Their excitation mechanism is purely due to nonlinear interactions, such as three-wave

coupling, which transfer energy from finite n drift-wave modes to the $n = 0$ mode. Moreover, since zonal flows are parallel to the flux surfaces, they do not cause cross-field transport of particles and heat.

These zonal flows create a radially varying electric field, leading to a sheared $\boldsymbol{E} \times \boldsymbol{B}$ plasma flow in the poloidal direction. As a result, zonal flows produce a complex spatio-temporal $\boldsymbol{E} \times \boldsymbol{B}$ shearing pattern that tends to distort turbulent convective cells, eventually breaking them into smaller structures and thus reducing the turbulence radial correlation length. Through this decorrelation process, similar to the effect of a mean shear flow discussed earlier, zonal flows can effectively suppress microturbulence, representing an important self-regulation mechanism.

In Chapter 5, dedicated to the study of turbulence, an analysis of zonal flow activity will be presented.

Impact of electromagnetic effects Finally, electromagnetic effects introduced by finite plasma β can also be crucial, particularly in the edge pedestal region where the steep gradients lower the critical threshold β_{crit} for electromagnetic effects to become significant. As mentioned previously, new instabilities driven by β, such as KBM and MTM, can arise. Beyond that, even electrostatic instabilities can be modified by finite-β, such as toroidal-ITG β stabilization [108, 109] before the KBM onset, or toroidal-ETG β destabilization [110]. More interestingly and importantly, electromagnetic effects have been shown to influence saturation mechanisms [111, 112], even for predominantly electrostatic modes, often having a greater impact than found in linear studies [113, 114]. Recently, the nonlinear electromagnetic stabilization observed in ITG-driven turbulence regimes has been linked to increased coupling with zonal flows in finite-β cases [115].

Regarding turbulence simulations in the plasma edge, the strong enhancement of electromagnetic effects compared to linear instability has been reported in several studies, e.g., Ref. [116–119]. As identified in those works, nonlinear electromagnetic effects contribute to the excitation of MHD-like large-scale or *mesoscale* modes of the electric potential, even below the linear MHD threshold.

Motivated by these results, dedicated analyses will be discussed in Chapter 4 and Chapter 5, where the stability and turbulence of the pedestals in the JET discharges analyzed in this thesis will be studied.

1.6. Thesis objectives and outline

As highlighted throughout this introduction, the pedestal region is crucial both for achieving the high fusion performance required in a fusion device, representing the boundary of stiff core profiles, and for developing plasma regimes that avoid ELMs of sizes that could damage the plasma-facing components. For these reasons, advancing our understanding of the mechanisms regulating pedestal dynamics and its structure is of critical importance. The most widely used model for predicting pedestal pressure height and width is the EPED model, based on the combination of constraints from peeling-ballooning MHD modes and KBM limits. Among the various mechanisms influencing the pedestal, the role of turbulent transport remains one of the least understood.

This thesis is motivated by the recent discovery at the JET tokamak of new H-mode plasma regimes characterized by high thermal confinement and featuring small-ELM

dynamics, referred to as baseline small-ELMs (BSE), which are desirable and potentially applicable to reactor-scale devices such as ITER. Although significant progress has been made in understanding the pedestal, the pedestal structures of the new BSE regimes remain unexplained by the EPED model, unlike the pedestals of standard H-mode plasmas with type-I ELMs. This suggests that additional mechanisms may regulate the pedestal in these regimes, warranting further investigation. The aim of this thesis is to better understand the role of turbulent transport mechanisms in the pedestal of BSE regimes through a comparative local gyrokinetic modeling analysis with a standard H-mode discharge featuring type-I ELMs. This study will allow us to identify the main differences in turbulent transport processes between the two ELMy regimes, thereby expanding our understanding of pedestal turbulent transport across different plasma regimes. The gyrokinetic theoretical framework and local version of the GENE code will be introduced in Chapter 3.

The main experimental conditions of the selected JET discharges in BSE regimes will be compared with a reference standard H-mode with type-I ELMs in Chapter 2. The P-B boundary stability analysis will reveal that while the pedestal in the type-I ELM regime is P-B unstable, the BSE pedestals remain stable, not reaching the critical pressure and current gradients required for the P-B onset. The experimental pedestal profiles will then be analyzed in preparation for the gyrokinetic modeling, and the main differences will be highlighted. Finally, the radial electric field will be reconstructed from the rotation, temperature, and ion density profiles, providing estimates for the equilibrium $\boldsymbol{E} \times \boldsymbol{B}$ shearing rate.

The stability analysis around three closely spaced radial locations near the pedestal top in the different ELMy plasma regimes will be compared in Chapter 4, providing new insights into potential differences in the underlying mechanisms. It will be shown that ion-scale instabilities are indeed dominated by different modes depending on the ELMy regime. At the electron scale, both regimes will be found to be dominated by ETG modes. By focusing on the impact of parameters that differ most between the two ELMy regimes, the origins of the main emerging differences will be identified and reconducted to specific physical effects.

Turbulence simulations will be conducted in Chapter 5 to gain insights into the main physical mechanisms responsible for turbulence saturation, particularly in the new BSE regime. Recognizing the importance of electromagnetic effects and equilibrium $\boldsymbol{E} \times \boldsymbol{B}$ shearing in pedestal turbulence, special attention will be given to assessing their interplay and role in saturation. Single-scale ion and electron simulations will be performed, providing estimates of heat flux levels to be compared with experimental values. Finally, basic quasi-linear models will be developed to reproduce the nonlinear heat flux spectra and assess their validity.

In the concluding Chapter 6, the results obtained in this thesis will be summarized allowing for the discussion of potential future developments in light of remaining and emerging open questions.

2. Description of JET shots: type-I ELMs vs. small-ELMs

Contents

2.1. Experimental conditions 55
2.2. Plasma profiles 59
2.2.1. Time-averaged radial profiles 59
2.2.2. Magnetic equilibrium 65
2.2.3. Electron pressure pedestal fit 67
2.3. Equilibrium flow shearing rate 68
2.4. Physical input parameters 71

In this chapter, the plasma discharges obtained at JET, which have been the subject of the gyrokinetic modeling performed in this thesis, will be described. Specifically, three discharges reported in Ref. [1, 27] have been selected. These discharges are characterized by different edge-localized mode types, and in particular different pedestal structures. This chapter is organized as follows: in Sec. 2.1 the experimental results are introduced; in Sec. 2.2 the plasma radial profiles, with a focus on the pedestal region, and the magnetic equilibria are presented; the equilibrium flow calculation are described in Sec. 2.3; and in Sec. 2.4 the local physical parameters for the gyrokinetic modelling are summarized. The study of turbulent transport mechanisms occurring in the pedestals of selected discharges will be the subject of the following chapters.

2.1. Experimental conditions

As discussed in Chapter 1, experimental campaigns were conducted at JET in 2019-2020 aimed at developing H-mode regimes that combined good energy confinement with moderated heat and particle loads on the plasma-facing components, thereby avoiding type-I ELMs. This led to the development of new H-mode regimes with small-ELMs under conditions relevant to the baseline scenario planned for ITER [120]. These regimes were subsequently termed baseline small-ELM (BSE) regimes [1].

In this work, following Ref. [1], two representative discharges in the BSE regime, #94442 and #96994, were analyzed and compared with a standard H-mode discharge with type-I ELM, #97395. It should be noted that access to BSE regimes is achieved by optimizing the externally applied edge particle sources, either by removing them or by substituting gas injection with pellets.

Table 2.1.: Main engineering parameters for the three selected JET shots: plasma current I_p, toroidal magnetic field B_{tor}, average triangularity δ, safety factor q_{95}, $H_{98}(y,2)$ energy confinement enhancement factor relative to the IPB98$(y,2)$ scaling law [28], ICRH power P_{ICRH}, NBI power P_{NBI}, edge gas puff particle sources $\Gamma_e(\sigma)$, the measured effective charge $Z_{\text{eff}} = \sum_i n_i Z_i^2/n_e$, and time window of averaging t.

	#97395	#96994	#94442
Main ion	D	D	D
I_p [MA]	3	3	3
B_{tor} [T]	2.8	2.8	2.8
δ	0.23	0.23	0.23
q_{95}	3.2	3.2	3.2
$H_{98}(y,2)$	~ 1	~ 1	~ 1
P_{ICRH} [MW]	4	4	4
P_{NBI} [MW]	28	28	17
Γ_e(D) $[10^{22}\,\text{s}^{-1}]$	2.5	0.4	0
Γ_e(Ne) $[10^{22}\,\text{s}^{-1}]$	0	0.8	0
D Pacing pellets [Hz]	0	45	0
Z_{eff}	1.4	2.4	3.1
ELMs type	type-I	small	small
t [s]	11.95-11.98	12.4-12.6	11.35-11.45

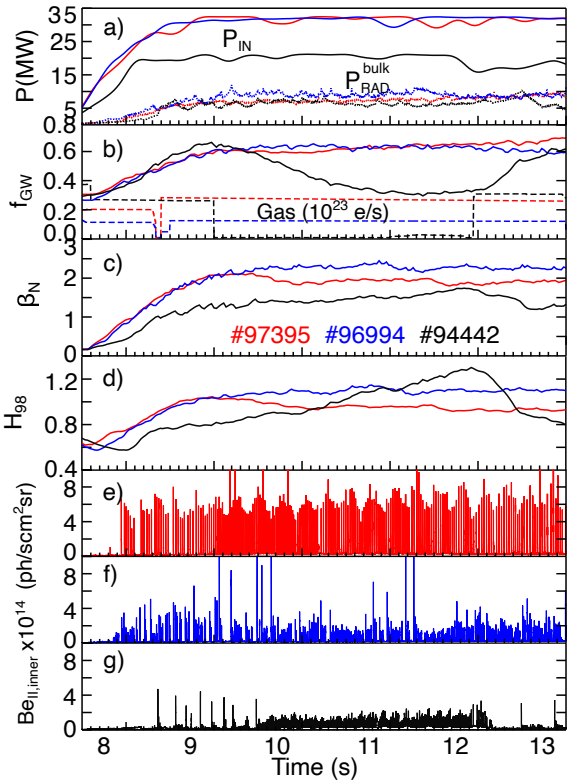

Figure 2.1.: Time traces of relevant engineering and plasma parameters for the type-I ELM discharge #97395 and the small-ELM discharges #94442 and #96994: (a) P_{IN} the total input power, and $P_{\mathrm{RAD}}^{\mathrm{bulk}}$ the bulk radiated power; (b) f_{GW}, the ratio of the line-averaged electron density to the Greenwald density, along with the gas flow rate; (c) $\beta_N \equiv \beta/(I_p a B_{\mathrm{tor}})$; (d) H_{98}, the thermal energy enhancement factor relative to the IPB98$(y,2)$ scaling law; (e)–(g) BeII line emission from the inner divertor.

The main engineering and plasma parameters of the three considered discharges are given in Table 2.1, and the time traces of selected engineering and physical parameters are compared in Fig. 2.1. Panel (a) shows the total input power (P_{IN}) and the radiated power from the plasma bulk, excluding the divertor region ($P_{\mathrm{RAD}}^{\mathrm{bulk}}$). In panel (b), the ratio of the line-average electron density to the Greenwald density (f_{GW}) is shown along with the deuterium gas injection rate. In panels (c) and (d), the normalized beta defined as $\beta_N \equiv \beta/(I_p a B_{\mathrm{tor}})$ and the energy enhancement factor H_{98} are displayed, which are indicative of the performance of these discharges. All three discharges were performed in a favorable configuration, i.e., with the main ion ∇B-drift pointing towards the X-point. They are characterized by the same plasma shape, high plasma current $I_p = 3\,\mathrm{MA}$, toroidal magnetic field $B_{\mathrm{tor}} = 2.8\,\mathrm{T}$, safety factor value at the flux surface containing 95 % of the poloidal flux $q_{95} = 3.2$, and low triangularity $\delta = 0.23$. As reported in Table 2.1 and Fig. 2.1, the three discharges are predominantly heated by NBI with a minor fraction of ICRH. Specifically, the BSE discharge #96994 was heated with the same mix as the type-I ELM discharge #97395 $P_{\mathrm{NBI}} = 28\,\mathrm{MW}$ and $P_{\mathrm{ICRH}} = 4\,\mathrm{MW}$, while #94442 had the same ICRH but reduced NBI power $P_{\mathrm{NBI}} = 17\,\mathrm{MW}$.

Regarding the edge particle sources, (see Fig. 2.1 panel (b) for the deuterium gas injection rates) the type-I ELM discharge #97395 was fueled with deuterium gas puff at a flux rate of $\Gamma_e(\mathrm{D}) = 2.5 \cdot 10^{22}\,\mathrm{s}^{-1}$, while the BSE discharge #96994 was fueled by a mixture of deuterium gas puff at a reduced flux rate of $\Gamma_e(\mathrm{D}) = 0.4 \cdot 10^{22}\,\mathrm{s}^{-1}$, with the addition of deuterium pacing pellets at a frequency of $f = 45\,\mathrm{Hz}$ and Neon impurity injection with $\Gamma_e(\mathrm{Ne}) = 0.8 \cdot 10^{22}\,\mathrm{s}^{-1}$. The BSE discharge #94442, on the other hand, was achieved without edge particle sources, with NBI as the sole external particle source. It is worth to note that the BSE discharges have a confinement enhancement factor relative to the IPB98$(y, 2)$ scaling law $H_{98} \sim 1$ (see Fig. 2.1 panel (d)), thereby meeting the scaling required for the ITER baseline scenario with $Q = 10$ operation.

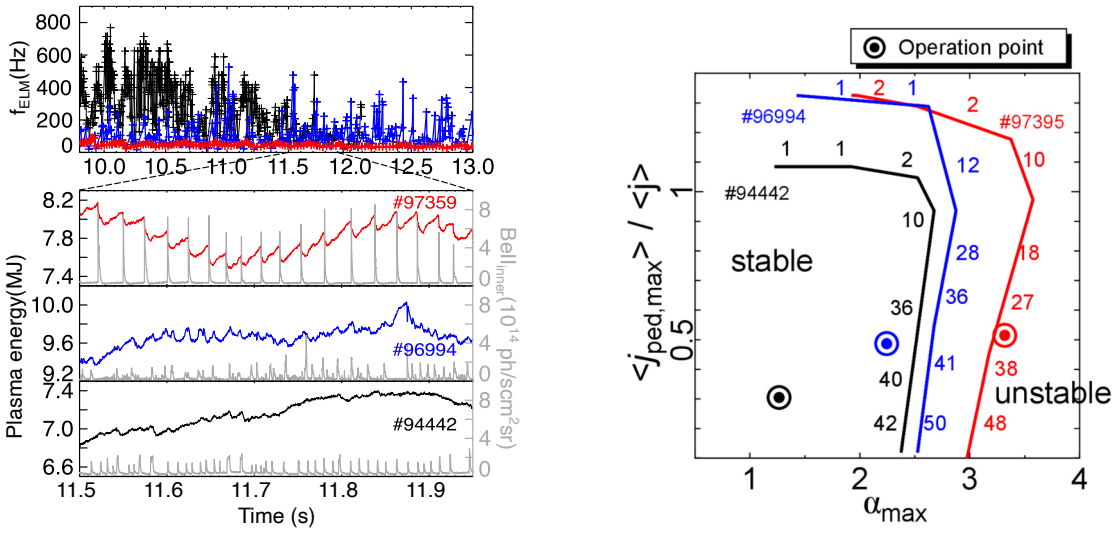

(a) (b)

Figure 2.2.: (a) f_{ELM} ELM frequency, W_{MHD} total stored plasma energy, and Beryllium II line emission from the inner divertor. (b) Peeling-ballooning stability diagram using the MINERVA-DI code [121] (which solves the extended Frieman–Rotenberg equation and includes rotation and diamagnetic effects, using the Sauter formula for the bootstrap current model [122, 123]) for the three discharges #97395, #96994, and #94442 as function of the edge current density normalized to the volume-averaged current density $j_{\mathrm{ped,max}}/\langle j \rangle$ and maximum normalized pressure gradient $\alpha_{\mathrm{max}} = -(2\mu_0 q^2 R/B^2) \cdot \mathrm{d}p/\mathrm{d}r\,|_{\mathrm{max}}$. Adapted from source [1].

The plasma regimes thus obtained exhibit different edge dynamics, characterized by different types of ELMs, as it can be inferred from panels (e–g) in Fig. 2.1, where the BeII line emission from the inner divertor are compared, and in Fig. 2.2a where the plasma stored energy time traces are shown. Notably, discharge #97395 develops regular type-I ELMs with a frequency of $f_{\mathrm{ELM}} = 45\,\mathrm{Hz}$, resulting in a plasma energy loss per ELM relative to the total stored energy of $\Delta W_{\mathrm{ELM}}/W_{\mathrm{MHD}} = 2.2\%$. The two BSE regimes reveal different ELM dynamics. The BSE discharge #96994 is characterized by a compound ELM behavior, with relatively long periods of fast and small ELMs up to an ELM frequency of $f_{\mathrm{ELM}} = 400\,\mathrm{Hz}$, separated by isolated large ELMs, resulting in a reduced

average energy expelled per ELM of $\Delta W_{\mathrm{ELM}}/W_{\mathrm{MHD}} = 0.8\%$. During the stationary phase with the removal of the edge particle source, the BSE discharge #94442 develops only small-ELMs at high frequencies in the range of $f_{\mathrm{ELM}} = 100 - 600\,\mathrm{Hz}$. The ELM size is reduced to the point where the decrease in the stored energy associated with a single ELM stands within the noise level of the W_{MHD} signal (approximately 30 kJ), leading to an estimated maximum energy expelled by each ELM of $\Delta W_{\mathrm{ELM}}/W_{\mathrm{MHD}} = 0.6\%$. It should be noted that in this case, the small-ELMs are so weak that they do not produce any practically measurable perturbation of the density or temperature pedestal.

To discern the physical mechanism responsible for ELM onset, the stability of the pedestals against finite-n MHD peeling-ballooning (P-B) instabilities was characterized as a first step. Indeed, P-B modes are typically responsible for limiting the pedestal height in H-mode plasma regimes with type-I ELMs [124]. The results obtained are reported in Fig. 2.2b, where it is noted that discharge #97395 with type-I ELMs is at the P-B boundary as expected; the two BSE discharges, however, remain stable against P-B instabilities. These results leave the mechanisms determining the small-ELMs unexplained.

Motivated by these results, this thesis focuses on investigating the turbulent transport mechanisms at play in the edge region of these discharges to elucidate their potentially different roles in determining the different pedestal structures. The results of this analysis and the main differences across the different ELMy regimes will be presented in Chapter 4, dedicated to the study of microinstabilities, and Chapter 5, dedicated to the study of microturbulence.

We now proceed with the description of the experimental profiles, which constitute the starting point for the modeling.

2.2. Plasma profiles

2.2.1. Time-averaged radial profiles

Experimental measurements and radial profiles obtained in TRANSP simulations [125] for the three discharges as a function of the normalized toroidal radius $\rho_{\mathrm{tor}} = \sqrt{\Phi/\Phi_{\mathrm{max}}}$ (where Φ and Φ_{max} are the toroidal magnetic flux and its value at the separatrix, respectively) are shown in Fig. 2.3. In this case, the TRANSP code has been used for the interpretation of tokamak plasma discharges starting from the experimental measurements (see, e.g. Ref. [126] for an introduction on transport codes and their use). The electron density and temperature profiles were obtained using high-resolution Thomson scattering (HRTS) diagnostics [127], while the ion temperature and rotation profiles were obtained using core and edge charge-exchange recombination spectroscopy (CXRS) diagnostics [128–130]. Note that the experimental measurements of the ion temperature in the pedestal, i.e. in the range $0.9 \lesssim \rho_{\mathrm{tor}} \lesssim 1.0$, of discharge #97395 with type-I ELM were considered unsatisfactory. Since experimental measurements indicate $T_e \sim T_i$ up to the pedestal top, the ion temperature in the pedestal was assumed to be equal to the electron temperature in the TRANSP run. This assumption is justified by the high collisionality. The impurity density profiles were obtained in TRANSP assuming the presence of nickel and beryllium with profiles proportional to the electron density, and rescaled to match the experimentally measured effective charge Z_{eff}. Although tungsten (W) represents an intrinsic impurity in JET-ILW, its presence was initially neglected

since its density was very small compared to the Be density. For more details regarding the TRANSP simulations, the reader is referred to Ref. [131].

The purpose of the subsequent modeling will be to characterize the microturbulence at the pedestal top once the pedestal is fully developed. For this reason, the experimental profiles have been averaged over appropriate time-windows, depending on the ELM types. For the type-I ELM discharge #97395, the experimental profiles were averaged over a very narrow time window just before an ELM representing the maximum recovery of the pedestal before the new collapse. Regarding the BSE discharges #94442 and #96994, since the small-ELMs are very frequent and of low intensity, they cause density and temperature perturbations in the pedestal that remain within the measurement uncertainty. For this reason, the experimental profiles of the BSE discharges are temporally averaged over several small-ELMs cycles.

The pedestal region is highlighted in yellow, and the vertical lines indicate the position of the pedestal top, defined as the radial position corresponding to the pedestal height of the electron pressure profile. This position is selected as described later in Sec. 2.2.3. From Fig. 2.3, the differences between the density and temperature structures of the pedestals in different regimes become evident.

Regarding the electron density compared in Fig. 2.3a, it is noted that the BSE discharges develop a wider and lower pedestal ($n_{e,\text{top}} \sim 1.45 - 3.5 \cdot 10^{19}\,\text{m}^{-3}$) compared to the type-I ELM discharge ($n_{e,\text{top}} \sim 5.4 \cdot 10^{19}\,\text{m}^{-3}$). The electron temperature pedestals, shown in Fig. 2.3b, are wider in the BSE regimes, with the value at the pedestal top remaining similar across the different regimes. In particular, a quantitative estimation of the electron density and temperature pedestal widths has been calculated by performing a modified hyperbolic tangent (mtanh) fit (see Sec. 2.2.3 for the definition) to the pedestal profiles, as shown in Fig. 2.4 for the three discharges. The width derived from the fit parameter w and the associated error, calculated as half of the 95% confidence interval derived from the fit, are reported. The ion temperature pedestals in Fig. 2.3c are higher in the BSE regimes, resulting in a lower $T_e/T_i \sim 0.5$. Regarding the toroidal rotation frequency shown in Fig. 2.3d, the discharge #94442-BSE reaches higher values at the pedestal compared to the other two discharges.

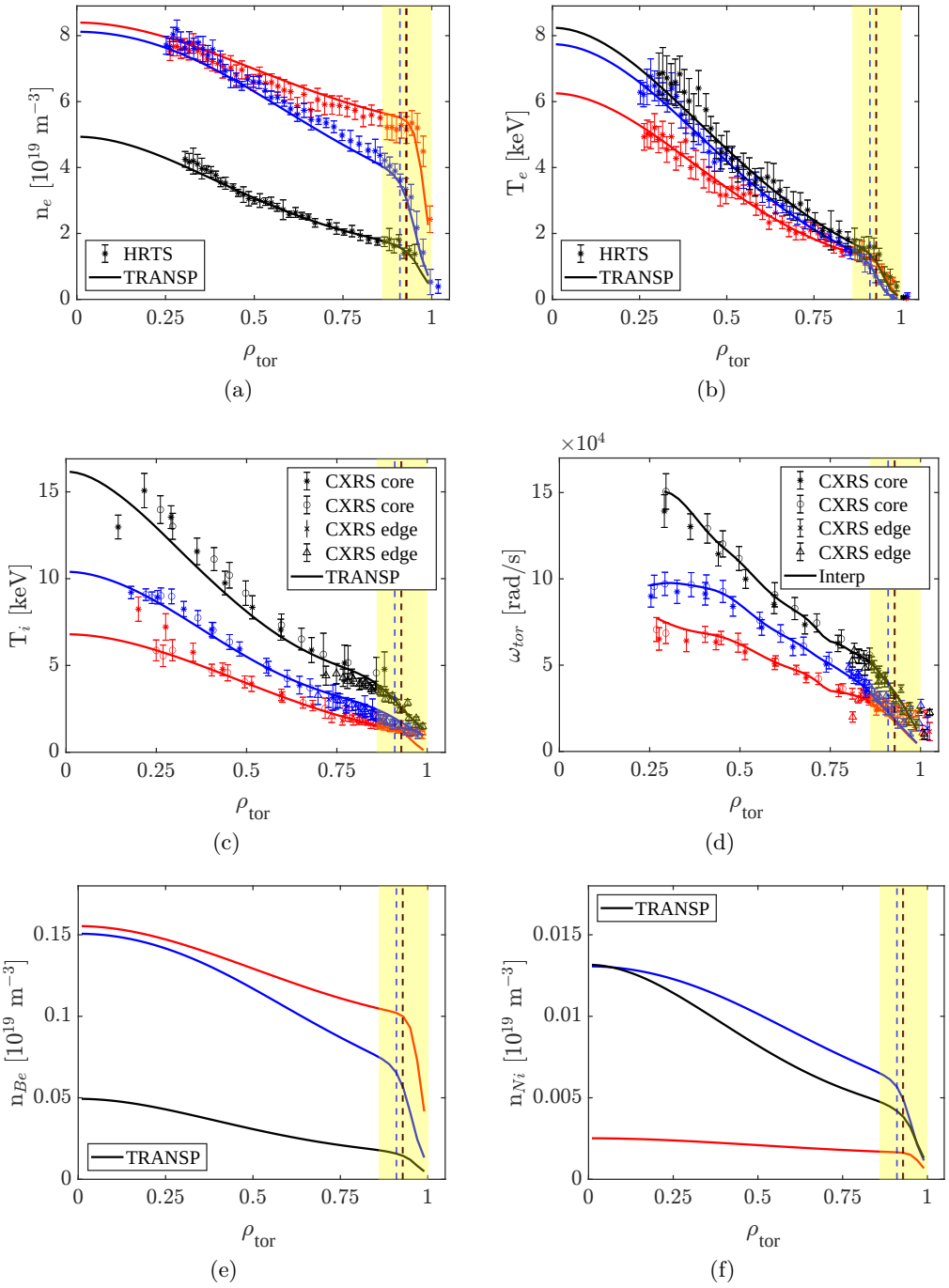

Figure 2.3.: Time averaged radial profiles as function of the normalized toroidal radius ρ_{tor}: type-I ELM #97395 $t = 11.95 - 11.98$ s (red), BSE #96994 $t = 12.4 - 12.6$ s (blue), and BSE #94442 $t = 11.35 - 11.45$ s (black). (a). Electron density, n_e. (b) Electron temperature, T_e. (c) Ion temperature, T_i. (d) Toroidal angular frequency ω_{tor}. (e) Be density, n_{Be}. (f) Ni density, n_{Ni}.

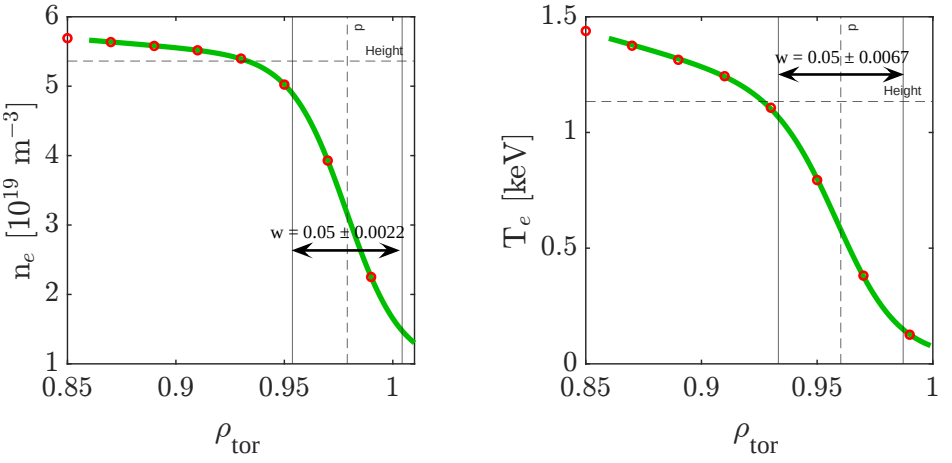

(a)

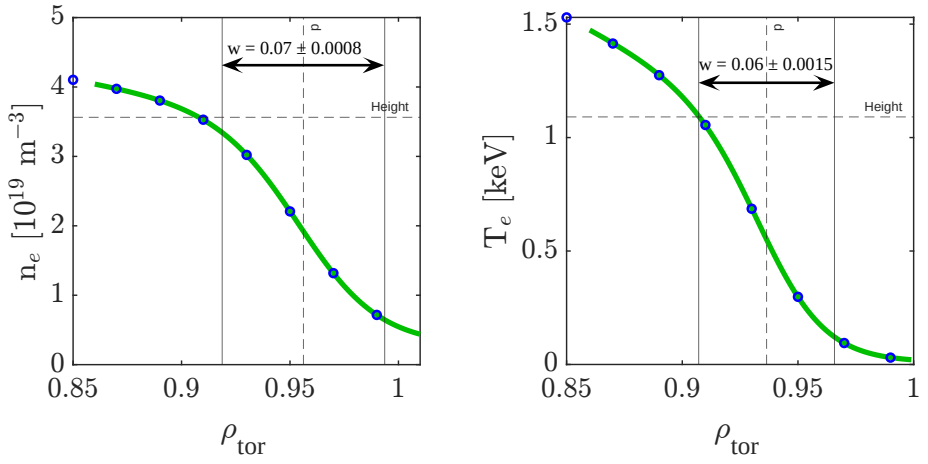

(b)

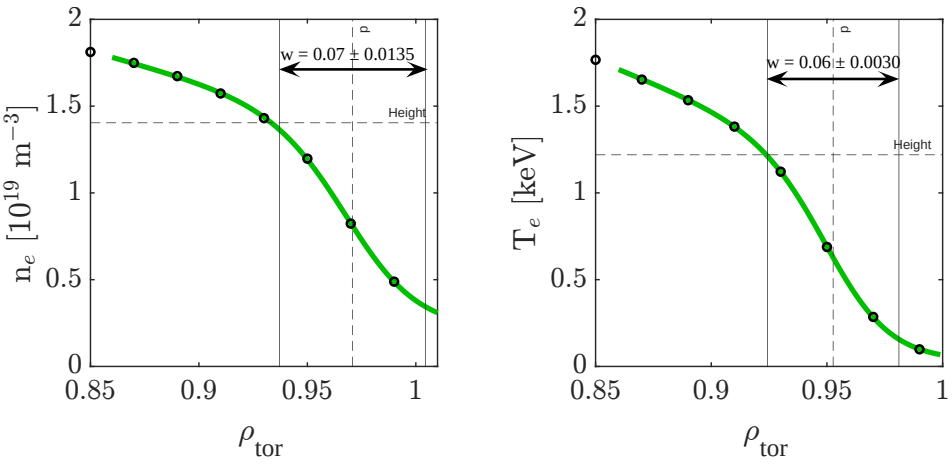

(c)

Figure 2.4.: The modified hyperbolic tangent (*mtanh*) fit (see Sec. 2.2.3 for its definition) of the electron density and temperature pedestal profiles obtained from TRANSP simulations is shown for three discharges: (a) #97395–type-I ELMs, (b) #96994–BSE, and (c) #94442–BSE. The pedestal widths (w) with their relative uncertainties, the fit parameter (p), and the pedestal heights are reported.

Table 2.2.: Electron and ion heat flux across the surface at the pedestal top positions from TRANSP power balance calculation.

Discharge	Q_e [MW/m^2]	Q_i [MW/m^2]
#94442-BSE	0.0192	0.025
#97395-Type-I ELMs	0.076	0.062

Within the TRANSP analysis, ion and electron power balance calculations were performed to estimate the radial transport. The calculations were carried out to match the measured radiated power. The values obtained at the pedestal top positions are reported in Table 2.2. Note that these values, being derived from experimental measurements, are characterized by high uncertainties of $\sim 50\%$. Therefore, in this thesis, they will be used just as indicative values for comparison with simulation results.

Starting from the TRANSP experimental profiles, the quantities necessary for the subsequent gyrokinetic modeling are computed by performing cubic spline interpolation with tension using the INTERPOS package [132]. In Fig. 2.5, the radial profiles of the normalized logarithmic gradients are shown, defined for a generic quantity X as

$$L_X^{-1} = -\frac{1}{X}\frac{\mathrm{d}X}{\mathrm{d}\rho_{\mathrm{tor}}}\,.$$

We emphasize that this quantity does not represent the inverse gradient scale length, but rather a normalized inverse gradient scale length, as the radial coordinate ρ_{tor} is dimensionless. Firstly, we note that the positions of the pedestal top, indicated by the vertical lines, coincide with the locations where the normalized gradients start to increase, compared to the flat values of the core and outer core up to $\rho_{\mathrm{tor}} \sim 0.8$. In the pedestal region, there is a sharp increase in the normalized gradients, indicating a potential difference in stability according to the radial position of analysis. This will motivate the selection of different radial positions (see Sec. 2.2.3) for carrying out the gyrokinetic investigation.

Focusing on the normalized density gradients in Fig. 2.5a, although the density gradients are similar across the various regimes, the BSE regimes reach values approximately three times higher than the type-I ELM regime due to the lower density achieved. A similar trend is observed for the normalized electron temperature gradients in Fig. 2.5c, resulting in a 50% higher value at the pedestal top for the BSE regimes compared to the type-I ELM. Meanwhile, the higher and less steep ion temperature obtained in the pedestals of BSE regimes results in a lower gradient compared to the type-I ELM regime, as shown in Fig. 2.5d.

Note that the density profiles and corresponding normalized gradient of the main ion deuterium in Fig. 2.5b are obtained from the electron density profiles and those of the

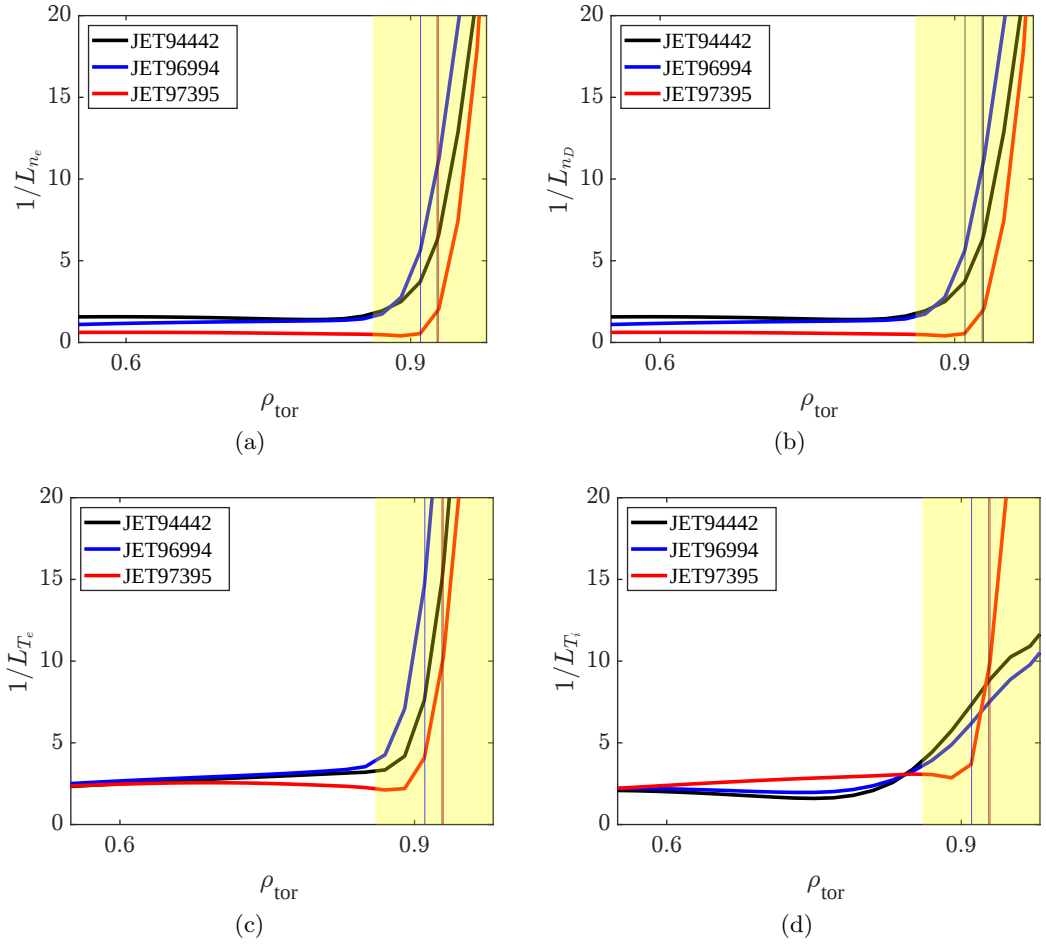

Figure 2.5.: Radial profiles of the normalized gradients of (a) electron density n_e (b) deuterium density n_D (c) electron temperature T_e, and (d) ion temperature T_i. Vertical lines indicate the pedestal top positions.

Table 2.3.: Measured effective charge Z_{eff} for the three discharges.

	#97395	#96994	#94442
Z_{eff}	1.4	2.4	3.1

two impurities, Be and Ni, by imposing quasi-neutrality

$$\sum_{\sigma} q_\sigma n_\sigma = 0\,,$$
$$\frac{\mathrm{d}}{\mathrm{d}\rho_{\text{tor}}} \sum_{\sigma} q_\sigma n_\sigma = 0\,.$$

The two impurities are considered fully stripped, i.e., $q_{\text{Be}} = 4$ and $q_{\text{Ni}} = 28$, consistent with the experimentally measured ion effective charge $Z_{\text{eff}} = \sum_i n_i Z_i^2 / n_e$, as reported in Table 2.3. Considering the ionization energies of the two elements [133] and the temperatures reached at the pedestal top (e.g., for #94442 $T_{i,\text{top}} \sim 2.6\,\text{keV}$), this assumption is well satisfied for Beryllium, while for Nickel a more realistic charge would be around $q_{\text{Ni}} \sim 26$. Finally, we note that the effective charge values reveal the higher impurity concentration in the BSE regimes compared to the type-I ELM regime. The impact of impurities on instabilities will be characterized in Chapter 4.

2.2.2. Magnetic equilibrium

In this thesis work, realistic magnetic equilibria have been used to carry out the gyrokinetic modeling. This choice is motivated by the fact that flux surfaces in the edge plasma region can assume complex shaping, thus impacting the stability and transport [134].

The magnetic equilibria and safety factor profiles were reconstructed using an iterative approach within the TRANSP runs (as described in Ref. [131]) employing the EFIT++ code [135, 136] which solves the Grad-Shafranov equilibrium equation [137] with constraints from magnetic measurements and pressure profiles.

The magnetic equilibria, i.e., poloidal flux contours, of the three discharges are shown in Fig. 2.6. It is thus evident that the three discharges have the same plasma shape, as mentioned previously. Based on these equilibria, the geometric coefficients that enter the gyrokinetic equation are calculated using the interface to the TRACER module [138]. In the next chapter, an introduction to gyrokinetic theory and the GENE code will be provided. The interpolated flux surfaces at the pedestal top positions computed in GENE are thus shown in Fig. 2.6, showing an excellent agreement with the input equilibria.

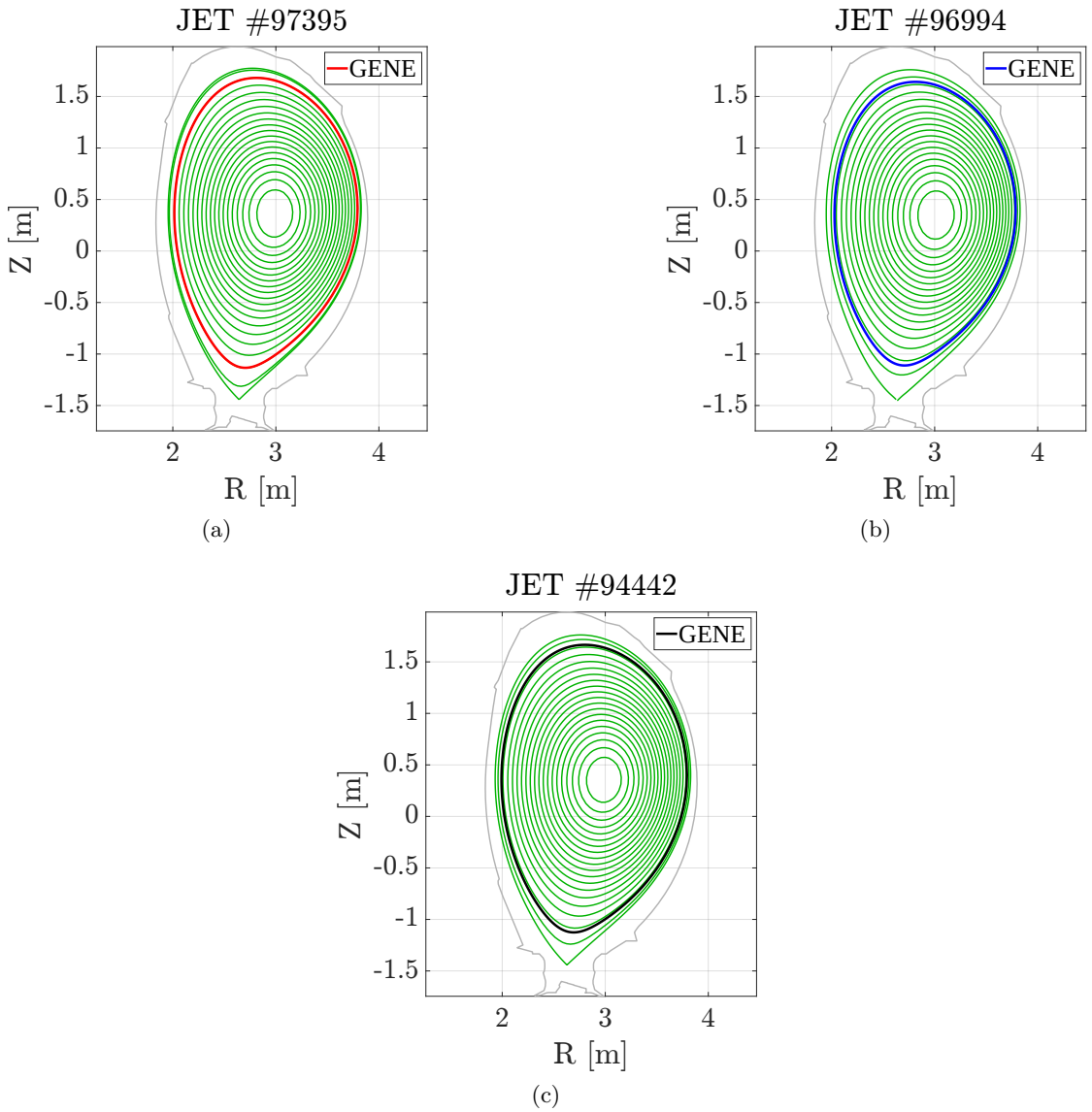

Figure 2.6.: Equilibrium flux-surfaces from EFIT++ reconstruction (green), and interpolated with GENE at the pedestal top position of the three discharges, red blue and black flux-surfaces respectively: (a) #97395-Type-I ELM (b) #96994-BSE and (c) #94442-BSE.

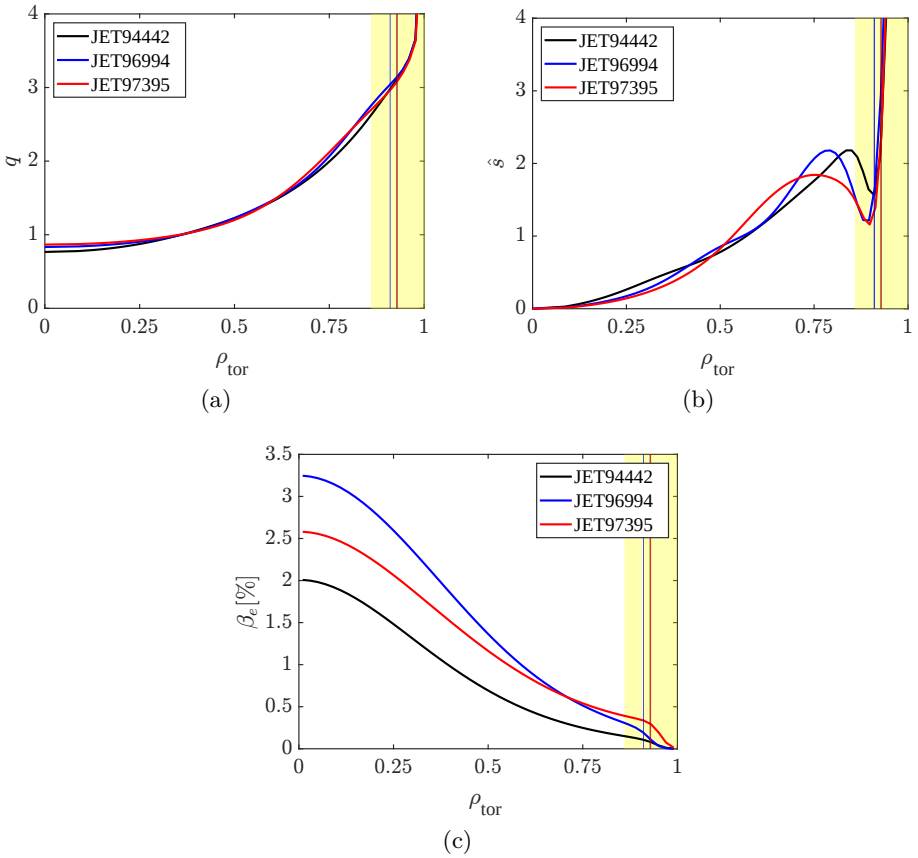

Figure 2.7.: Radial profiles of (a) safety factor q, (b) magnetic shear $\hat{s}$, and (c) electron beta β_e.

Finally, the safety factor, magnetic shear, and electron plasma beta profiles of the three discharges are compared in Fig. 2.7. We note that the safety factor and magnetic shear profiles are very similar across the three discharges corresponding to the same baseline scenario. The electron beta profiles were obtained from the TRANSP electron density and temperature profiles shown in Figs. 2.3a and 2.3b to compute the electron thermal pressure, and then by applying the definition $\beta_e = 8\pi p_e/B^2$, with B being the magnetic field on axis.

It is observed that β_e at the pedestal is significantly lower for the BSE regimes compared to the type-I ELM. Since electromagnetic effects are introduced via finite-β, this difference in β depending on the regime will result in significant differences in the stability of the pedestal depending on the plasma regime, and also in the saturation of the nonlinear turbulence regime. These effects will be discussed in the following chapters.

2.2.3. Electron pressure pedestal fit

As previously introduced, the purpose of the investigation is to compare the turbulent transport mechanisms occurring around the pedestal top position across different plasma regimes. This will elucidate the transport mechanisms and their impact on pedestals characterized by different structures.

To this end, the pedestal top position has been quantitatively defined across the different discharges as the radial position corresponding to the pedestal height of the electron pressure. The pedestal parameters, including the pedestal height, were thus calculated by fitting the pedestal profiles in the radial domain $\rho_{\text{tor}} = [0.85, 1]$ using the 5-parameter modified hyperbolic tangent analytical function [33, 42]

$$\text{mtanh}(r) = \frac{h_1 - h_0}{2}\left(\frac{(1+sx)e^x - e^{-x}}{e^x + e^{-x}} + 1\right) + h_0$$
$$\text{with } x = \frac{p - r}{(w/2)}$$

where r is the radial coordinate, h_1 is the pedestal height, h_0 the offset in the scrape-off layer, $s > 0$ a parameter linked with the derivative inside the pedestal top, p a parameter related to the steepest gradient position, and w the pedestal width.

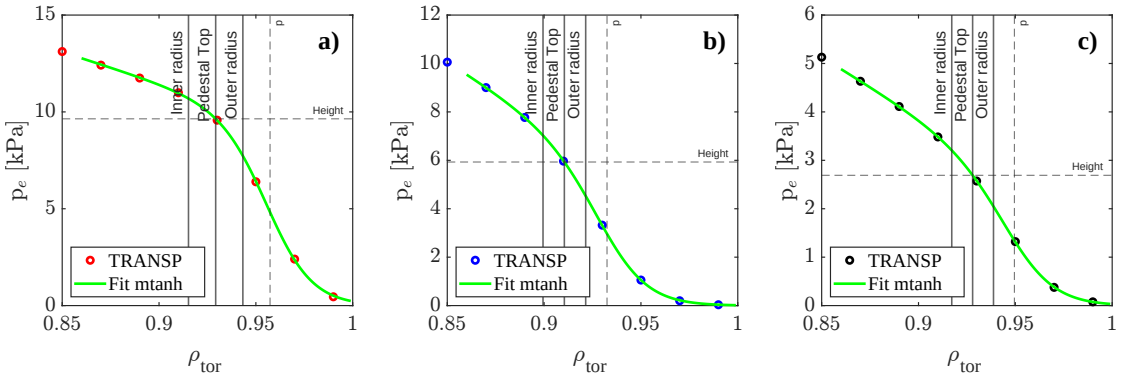

(a) #97395-Type-I ELM (b) #96994-BSE (c) #94442-BSE

Figure 2.8.: Electron pressure radial profile (points) computed from TRANSP electron density and temperature profiles, and *mtanh* fit line (green) for the three discharges. Vertical lines indicate the pedestal top position r_{top}, corresponding to the pedestal height h_1 coefficient from the fit, and two other positions at $r_{\text{top}} \pm (p - r_{\text{top}})/2$ where p is a coefficient from the fit.

The results of the fit for the three discharges are shown in Fig. 2.8. As observed in Fig. 2.5, across a relatively narrow radial extension within the pedestal region, a sharp increase in the logarithmic gradients is observed. To evaluate the potential dependence of the modeling results on slight variations of the radial positions in the analysis, two additional radial positions across the pedestal top position have been selected to conduct the local gyrokinetic analysis. These positions are $r_{\text{top}} \pm (p - r_{\text{top}})/2$ and are shown in Fig. 2.8 as vertical lines.

2.3. Equilibrium flow shearing rate

In the previous chapter, particularly in Sec. 1.5.2, we have discussed the impact of the equilibrium radial electric field shear on turbulence saturation. In the next chapter, in Sec. 3.2, its inclusion in the GENE code will be presented. In particular, in δf codes, the

equilibrium radial electric field is not treated self-consistently in the model and must be imposed externally. Therefore, to consistently include its effect in simulations, we need to estimate its value from experimental profiles of pressure and toroidal velocity, as explained below.

The externally imposed equilibrium $\boldsymbol{E}\times\boldsymbol{B}$ shear flow is included in GENE by providing the normalized parameter

$$\gamma_{E\times B}\frac{L_{\mathrm{ref}}}{c_{\mathrm{ref}}} = \texttt{ExBrate} = -\frac{\rho_{\mathrm{tor},0}}{|q|}\frac{\mathrm{d}|\Omega_{\mathrm{tor}}|}{\mathrm{d}\rho_{\mathrm{tor}}}\frac{L_{\mathrm{ref}}}{c_{\mathrm{ref}}}\,.$$

In general terms, the $\boldsymbol{E}\times\boldsymbol{B}$ shearing rate can be written as

$$\gamma_{E\times B} = \frac{\rho_{\mathrm{tor}}}{q}\frac{\mathrm{d}}{\mathrm{d}\rho_{\mathrm{tor}}}\frac{E_r}{B_\theta R}\,. \tag{2.1}$$

Following Ref. [139], the radial electric field E_r formula is derived, and considerations will be made to reconcile the formalism with the ones used in GENE. Starting from the ideal MHD Ohm's law and by inserting the radial force balance equation $\boldsymbol{J}_0\times\boldsymbol{B}_0 = \boldsymbol{\nabla}P_0$ (with $P_0 = p_{e,0}+p_{i,0}$), we obtain

$$0 = n_{i,0}q_i(\boldsymbol{E}_0+\bar{\boldsymbol{V}}_i\times\boldsymbol{B}_0) - \boldsymbol{\nabla}p_{i,0} \quad\Longrightarrow\quad 0 = \boldsymbol{E}_0+\bar{\boldsymbol{V}}_i\times\boldsymbol{B}_0 - \frac{1}{n_{i,0}q_i}\frac{\mathrm{d}p_{i,0}}{\mathrm{d}\psi_0}$$

where $\boldsymbol{E}_0 \equiv -\boldsymbol{\nabla}\Phi_0(\psi_0)$ is the lowest order electrostatic electric field, and $2\pi\psi_0$ is the poloidal magnetic flux. By taking the radial projection of the last equation, the toroidal rotation frequency is obtained

$$\Omega_{\mathrm{tor}} \equiv \bar{\boldsymbol{V}}_i\cdot\boldsymbol{\nabla}\varphi = -\left(\frac{\mathrm{d}\Phi_0}{\mathrm{d}\psi_0}+\frac{1}{n_{i,0}q_i}\frac{\mathrm{d}p_{i,0}}{\mathrm{d}\psi_0}-q\bar{\boldsymbol{V}}_i\cdot\boldsymbol{\nabla}\theta\right)$$

with φ being the toroidal angle. For completeness, we notice that the lowest order radial electric field is given by

$$E_r \equiv -\frac{\mathrm{d}\Phi_0}{\mathrm{d}\psi_0}|\boldsymbol{\nabla}\psi_0|\,. \tag{2.2}$$

Rearranging the equation, the terms that contribute to the radial electric field are made explicit, keeping them in units of a rotation frequency to be consistent with GENE formalism

$$\frac{\mathrm{d}\Phi_0}{\mathrm{d}\psi_0} = -\Omega_{\mathrm{tor}} - \frac{1}{n_{i,0}q_i}\frac{\mathrm{d}p_{i,0}}{\mathrm{d}\psi_0} + q\bar{\boldsymbol{V}}_i\cdot\boldsymbol{\nabla}\theta\,.$$

In particular, the toroidal rotation frequency Ω_{tor} is available from experimental measurements.

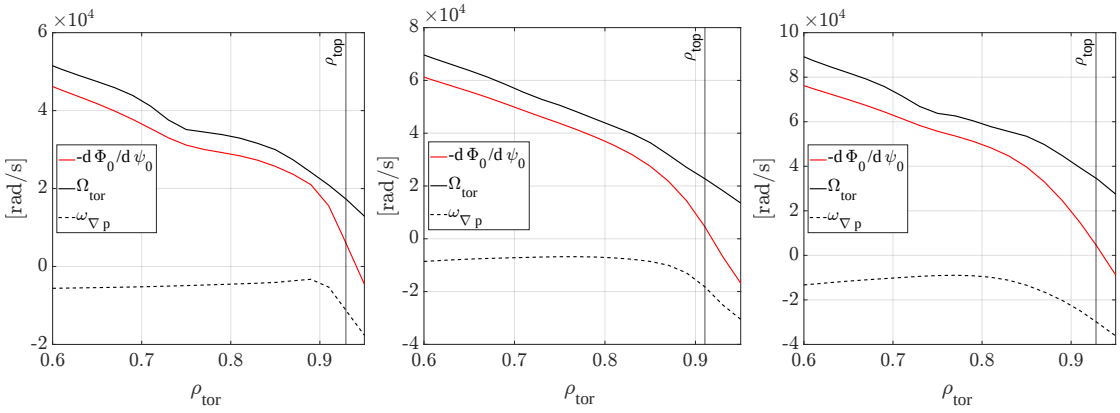

(a) #97395-Type-I ELM (b) #96994-BSE (c) #94442-BSE

Figure 2.9.: Radial electric field profiles of the three discharges (a) #97395-Type-I ELMs, (b) #96994-BSE, and (c) #94442-BSE. The contributions to the radial electric field (red) from toroidal rotation (solid line) and the diamagnetic term (dashed line) are shown. The vertical line indicates the pedestal top position.

For the remaining terms, two different formulations can be considered

1. Firstly, by neglecting the poloidal rotation $\bar{\boldsymbol{V}}_i \cdot \boldsymbol{\nabla}\theta$, the term due to the ion pressure gradient, the so-called diamagnetic term, is defined as

$$\omega_{\mathrm{diam},\boldsymbol{\nabla}p} = \frac{1}{n_{i,0} q_i} \frac{\mathrm{d}p_{i,0}}{\mathrm{d}\psi_0}$$

such that the equation for the radial electric field reads

$$\frac{\mathrm{d}\Phi_0}{\mathrm{d}\psi_0} = -\Omega_{\mathrm{tor}} - \omega_{\mathrm{diam},\boldsymbol{\nabla}p}\,.$$

The radial profiles obtained for the three discharges are shown in Fig. 2.9, along with the rotation frequency terms and the diamagnetic term. We note that the radial electric field profile follows the trend of the rotation profile up to $\rho_{\mathrm{tor}} \sim 0.85$ just before the pedestal. Entering the pedestal region, where the pressure gradient becomes significant, the contribution of the diamagnetic term determines the steepening of the radial electric field.

2. Secondly, by estimating the poloidal rotation, which could play a role especially at the edge, as derived from the neoclassical theory (see, e.g., [49, 140]), the diamagnetic and poloidal rotation terms can be rearranged as

$$\omega_{\mathrm{NC}} = \frac{1}{q_i}\left[(1 - k_{\mathrm{neo}})\frac{\mathrm{d}T_i}{\mathrm{d}\psi_0} + \frac{T_i}{n_i}\frac{\mathrm{d}n_i}{\mathrm{d}\psi_0}\right]$$

with k_{neo} a dimensionless coefficient depending on the collisionality regime (e.g.

Table 2.4.: Toroidal rotation, diamagnetic, and neoclassical term contribution to the shearing rate at the pedestal top position for the three discharges.

	#97395	#96994	#94442
$\partial\Omega_{\mathrm{tor}}/\partial\rho_{\mathrm{tor}}$	0.31	0.24	0.29
$\partial\omega_{\mathrm{diam},\boldsymbol{\nabla}p}/\partial\rho_{\mathrm{tor}}$	0.55	0.39	0.29
$\partial\omega_{\mathrm{NC}}/\partial\rho_{\mathrm{tor}}$	0.62	0.40	0.34

see [49, 140]), such that the equations for the radial electric field reads

$$\frac{\mathrm{d}\Phi_0}{\mathrm{d}\psi_0} = -\Omega_{\mathrm{tor}} - \omega_{\mathrm{NC}}\,.$$

The value entering as input parameter to the GENE simulations is given by the radial derivative of $\mathrm{d}\Phi_0/\mathrm{d}\psi_0$, determining a value with large uncertainty. The values of the terms contributing to the shearing rate, namely due to the toroidal rotation, diamagnetic term, and neoclassical term, obtained at the pedestal top for the three discharges are given in Table 2.4. We observe that the values of the contributions from the diamagnetic term $\omega_{\mathrm{diam},\boldsymbol{\nabla}p}$ and the neoclassical term ω_{NC} are compatible with each other, considering the large uncertainty associated with these parameters. Therefore, it was decided to use the the diamagnetic term as the nominal value to compute the shearing rate. Additionally, we note that the contribution from toroidal rotation constitutes approximately 50% of the $\boldsymbol{E}\times\boldsymbol{B}$ shearing rate, highlighting the importance of the diamagnetic term in the pedestal region.

2.4. Physical input parameters

Finally, for completeness, we provide all the local physical parameters, necessary for the gyrokinetic modelling, used in the simulations presented in the following chapters. Specifically, the parameters for the three discharges at the three previously selected radial positions are reported in Table 2.5. In particular, the selected reference plasma parameters at the radial locations of analysis are the ion temperature $T_{\mathrm{ref}} = T_i$, the electron density $n_{\mathrm{ref}} = n_e$, and for the macroscopic length, an average minor radius defined as $L_{\mathrm{ref}} = \sqrt{\Phi_{\mathrm{LCFS}}/\pi B_{\mathrm{ref}}}$, where Φ_{LCFS} is the toroidal magnetic flux at the last closed flux surface. For a discussion regarding the normalizations introduced in GENE, see Appendix A. The main geometric parameters are the reference magnetic field on axis $B_{\mathrm{ref}} = B_0$, the safety factor q, and the magnetic shear $\hat{s} = (\rho_{\mathrm{tor}}/q)\ \mathrm{d}q/\mathrm{d}\rho_{\mathrm{tor}}$. The electron-ion collisional frequency is given by $\nu_{e,i} = 4\pi n_{0,i} e^4 \ln(\Lambda)(2T_{0,e})^{-3/2} m_e^{-1/2}$ with $\ln(\Lambda)$ being the Coulomb logarithm, and the dimensionless electron collisionality is $\nu_e^* = 16qZ^2Rn_{0,i}T_{\mathrm{ref}}^2\nu_c/\left(3\sqrt{\pi}\epsilon^{3/2}L_{\mathrm{ref}}n_{\mathrm{ref}}T_e^2\right)$ where $\nu_c = \pi\ln(\Lambda)e^4 n_{\mathrm{ref}}L_{\mathrm{ref}}/\left(2^{3/2}T_{\mathrm{ref}}^2\right)$ [141]. The rotation parameters are the toroidal angular velocity ω_{ref}, the normalized parallel flow shearing rate $\gamma_{\mathrm{pfs}} = \rho_{\mathrm{tor}}/q\ \mathrm{d}\Omega_{\mathrm{tor}}/\mathrm{d}\rho_{\mathrm{tor}}\ L_{\mathrm{ref}}/c_{\mathrm{ref}}$ as the driving term, and in non-linear simulations, the equilibrium $\boldsymbol{E}\times\boldsymbol{B}$ shearing rate $\gamma_{E\times B}$ including the diamagnetic term as discussed in Sec. 2.3.

Table 2.5.: Local parameters for the three discharges, at the three selected radii. The reference values are: $n_{\text{ref}} = n_e$ [$10^{19}\,\text{m}^{-3}$], $T_{\text{ref}} = T_i$ [keV], L_{ref} [m], B_{ref} [T], and the toroidal angular velocity ω_{ref} [$\text{rad}\,\text{s}^{-1}$].

	ρ_{tor}	n_{ref}	n_{D}/n_e	n_{Be}/n_e	n_{Ni}/n_e	Z_{eff}	T_{ref}	T_e/T_i	$1/L_{n_e}$	$1/L_{T_e}$
r_{in}	0.915	5.5	0.92	1.8%	0.03%	1.4	1.30	0.93	0.71	5.16
r_{top}	0.929	5.4	0.92	1.8%	0.03%	1.4	1.19	0.93	2.00	10.2
r_{out}	0.943	5.2	0.92	1.8%	0.03%	1.4	0.97	0.93	5.03	18.3
	$1/L_{T_i}$	L_{ref}	B_{ref}	$q/\hat{s}$	β_e	ν_e^*	$\nu_{e,i}$	ω_{ref}	γ_{pfs}	$\gamma_{E\times B}$
r_{in}	4.49	1.21	2.86	2.97/1.84	0.30%	0.23	0.56	$2.0 \cdot 10^4$	0.27	0.68
r_{top}	9.95	1.21	2.86	3.06/2.05	0.29%	0.28	0.67	$1.7 \cdot 10^4$	0.31	0.85
r_{out}	18.6	1.21	2.86	3.17/2.4	0.23%	0.39	0.94	$1.4 \cdot 10^4$	0.36	0.82

(a) Type-I ELM - #97395

	ρ_{tor}	n_{ref}	n_{D}/n_e	n_{Be}/n_e	n_{Ni}/n_e	Z_{eff}	T_{ref}	T_e/T_i	$1/L_{n_e}$	$1/L_{T_e}$
r_{in}	0.899	3.6	0.88	1.9%	0.16%	2.44	2.08	0.57	3.77	9.83
r_{top}	0.910	3.5	0.88	1.9%	0.16%	2.44	1.95	0.53	5.68	14.89
r_{out}	0.920	3.25	0.88	1.8%	0.16%	2.44	1.81	0.46	8.43	21.8
	$1/L_{T_i}$	L_{ref}	B_{ref}	$q/\hat{s}$	β_e	ν_e^*	$\nu_{e,i}$	ω_{ref}	γ_{pfs}	$\gamma_{E\times B}$
r_{in}	5.47	1.22	2.79	2.97/1.67	0.22%	0.29	0.71	$2.5 \cdot 10^4$	0.25	0.57
r_{top}	6.21	1.22	2.79	3.0/1.63	0.19%	0.36	0.88	$2.3 \cdot 10^4$	0.24	0.66
r_{out}	6.99	1.22	2.79	2.08/1.64	0.14%	0.50	1.22	$2.0 \cdot 10^4$	0.29	0.72

(b) BSE - #96994

	ρ_{tor}	n_{ref}	n_{D}/n_e	n_{Be}/n_e	n_{Ni}/n_e	Z_{eff}	T_{ref}	T_e/T_i	$1/L_{n_e}$	$1/L_{T_e}$
r_{in}	0.917	1.53	0.88	1.0%	0.27%	3.14	2.84	0.46	4.45	9.94
r_{top}	0.928	1.45	0.86	1.0%	0.27%	3.14	2.59	0.44	6.24	14.9
r_{out}	0.938	1.33	0.86	1.0%	0.27%	3.14	2.35	0.40	8.91	22.0
	$1/L_{T_i}$	L_{ref}	B_{ref}	$q/\hat{s}$	β_e	ν_e^*	$\nu_{e,i}$	ω_{ref}	γ_{pfs}	$\gamma_{E\times B}$
r_{in}	7.9	1.21	2.86	3.01/2.19	0.10%	0.13	0.33	$3.7 \cdot 10^4$	0.26	0.56
r_{top}	8.77	1.21	2.86	3.1/2.21	0.08%	0.16	0.40	$3.4 \cdot 10^4$	0.29	0.61
r_{out}	9.58	1.21	2.86	3.17/2.33	0.06%	0.22	0.55	$3.1 \cdot 10^4$	0.35	0.65

(c) BSE - #94442

3. The gyrokinetic theory and numerical methods

Contents

3.1. Introduction to kinetic theory . . . 73
3.2. Gyrokinetic system of equations . . . 75
3.3. Field-aligned coordinates . . . 81
3.3.1. Operators in field-aligned coordinate . . . 82
3.4. Numerical resolution of the gyrokinetic equations . . . 83
3.4.1. Time integration: Runge-Kutta scheme and eigenvalue solver . . . 83
3.4.2. Phase-space discretization and boundary conditions . . . 84
3.4.3. Parallelization . . . 87

In this thesis, the investigation of turbulent transport processes in the pedestal region is conducted within a kinetic-reduced theory known as the gyrokinetic framework. The goal of this chapter is to present the gyrokinetic system of equations and the numerical methods used to solve them. The chapter is organized as follows: in Sec. 3.1, the kinetic theory is introduced; in Sec. 3.2, the gyrokinetic orderings are discussed, and the system of equations is provided; in Sec. 3.3, the field-aligned coordinate system is introduced, and the differential operators are explicitly defined; in Sec. 3.4, the discretization of equations and the main numerical methods employed in the GENE code [142] are described.

3.1. Introduction to kinetic theory

The kinetic theory aims to describe plasma dynamics, in a statistical sense, by introducing the single-particle distribution function $f_\sigma(\boldsymbol{x}, \boldsymbol{v}, t)$ for each plasma species σ, as a function of the six-dimensional phase space coordinates $(\boldsymbol{x}, \boldsymbol{v})$ and time t. The interest in this model lies in its ability to consistently describe physical phenomena involving velocity space dynamics, including collective phenomena such as the generation of plasma waves, and their resonances with particles, e.g. Landau resonance, or effects associated with finite Larmor radius (FLR).

The spatio-temporal evolution of f_σ is given by the Vlasov-Landau-Maxwell system of equations [101, 104]

$$\frac{\partial f_\sigma}{\partial t} + \boldsymbol{v} \cdot \boldsymbol{\nabla} f_\sigma + \frac{q_\sigma}{m_\sigma} (\boldsymbol{E} + \boldsymbol{v} \times \boldsymbol{B}) \cdot \frac{\partial f_\sigma}{\partial \boldsymbol{v}} = \left(\frac{\partial f_\sigma}{\partial t} \right)_{\text{coll}} \tag{3.1}$$

where q_σ and m_σ are respectively the species charge and mass, and the right-hand side term represents the collisional operator. Magnetically confined plasma of fusion interest typically have high temperature and low density such that collisions can be approximated

by two particles interaction. The velocity moments of f_σ are directly associated with fluid quantities, e.g. the density n_σ, and mean velocity $\boldsymbol{u}_\sigma$, providing the sources of the self-consistently generated electromagnetic fields given by the Maxwell equations

$$\begin{aligned}
\boldsymbol{\nabla}\cdot\boldsymbol{E} &= 4\pi\sum_\sigma q_\sigma n_\sigma = \sum_\sigma q_\sigma \int \mathrm{d}\boldsymbol{v}\, f_\sigma(\boldsymbol{x},\boldsymbol{v},t)\\
\boldsymbol{\nabla}\cdot\boldsymbol{B} &= 0\\
\boldsymbol{\nabla}\times\boldsymbol{E} &= -\frac{1}{c}\frac{\partial \boldsymbol{B}}{\partial t}\\
\boldsymbol{\nabla}\times\boldsymbol{B} &= \frac{1}{c}\frac{\partial \boldsymbol{E}}{\partial t} + \frac{4\pi}{c}\sum_\sigma q_\sigma \boldsymbol{u}_\sigma = \frac{1}{c}\frac{\partial \boldsymbol{E}}{\partial t} + \frac{4\pi}{c}\sum_\sigma q_\sigma \int \mathrm{d}\boldsymbol{v}\, \boldsymbol{v} f_\sigma(\boldsymbol{x},\boldsymbol{v},t)\,.
\end{aligned}$$

In what follows, the electromagnetic fields will be expressed using the scalar and vector potential ϕ and $\boldsymbol{A}$, through the equations

$$\boldsymbol{E} = -\boldsymbol{\nabla}\phi - \frac{1}{c}\frac{\partial \boldsymbol{A}}{\partial t} \quad \text{and} \quad \boldsymbol{B} = \boldsymbol{\nabla}\times\boldsymbol{A}\,.$$

This system of equations describes plasma phenomena spanning disparate temporal and spatial scales. Temporally, for instance, from Langmuir waves, which are plasma oscillations resulting from the restoring Coulomb force caused by an initial plasma charge separation, with frequencies on the order of $\omega_{p,e} = \sqrt{n_e e^2/(m_e\varepsilon_0)} \sim 1\cdot 10^{10}\,\mathrm{Hz}$, up to transport time scales of $t \sim 1\cdot 10^{-1}\,\mathrm{s}$. Spatially, from the Debye length at a spatial scale of $\lambda_{\mathrm{D,e}} \sim 1\cdot 10^{-4}\,\mathrm{m}$, which is the length beyond which the rearrangement of charges results in shielding of the electrostatic potential, causing the plasma to be quasi-neutral up to the machine size of $L \sim 1\,\mathrm{m}$.

In the context of this thesis, we are interested in the description of magnetized plasma turbulence occurring on spatial scales of the order of the Larmor radius and with frequencies on the order of the diamagnetic frequency, called micro-turbulence. For this task, the kinetic equations are inadequate, because it would require simulating the plasma dynamics across a multiple hierarchy of spatio-temporal scales, which is prohibitive even on the most powerful supercomputers.

For this reason, reduced models have been developed by introducing a set of orderings such that only the spatial and temporal scales relevant for micro-turbulence are retained. To this end, the gyrokinetic theory provides the theoretical framework to derive the appropriate set of equations. The development of this theory is made possible by the presence of a strong magnetic field confining the plasma, which results in the cyclotron motion of the particles around the magnetic field lines being much faster than the dynamics of interest. As a consequence, the fast gyro-motion dynamics can be decoupled, reducing the phase space dimension from six to five (three space, two velocity). In this way, only the gyro-centers dynamics are resolved, while the dependence on the gyro-phase is removed. Compared to the guiding center dynamics, the gyro-center ones retains the electromagnetic perturbations effect into the gyro-motion determining the plasma polarization and magnetization. This results in the *gyrokinetic* Vlasov-Maxwell system of equations [143].

3.2. Gyrokinetic system of equations

Earlier papers on the derivation of linearized gyrokinetic equations date back to the late 1970s [144]. A significant advancement was made by Frieman and Chen [145], who discussed the nonlinear problem. In these works, the equations were obtained using the $\epsilon \sim \rho_L/L$ (with L a macroscopic scale length) expansion approach. A comprehensive derivation employing asymptotic expansions can be found in the review by Abel and co-workers [146]. An alternative derivation, upon which much of the modern literature is based, was developed using Lagrangian and Hamiltonian Lie-transform perturbation methods, following the pioneering work of Littlejohn [147]. The advantage of the Lagrangian and Hamiltonian formalism lies in providing a systematic procedure for derivation, preserving conservation laws, symmetries, and invariants of the system. Two exhaustive reviews regarding the application of mathematical methods and complete derivation are respectively the works of Cary and Brizard [148] and Brizard and Hahm [143]. In what follows, the equations will be briefly introduced by following the modern derivation as in Ref. [143], i.e., adopting the Lie-transform derivation.

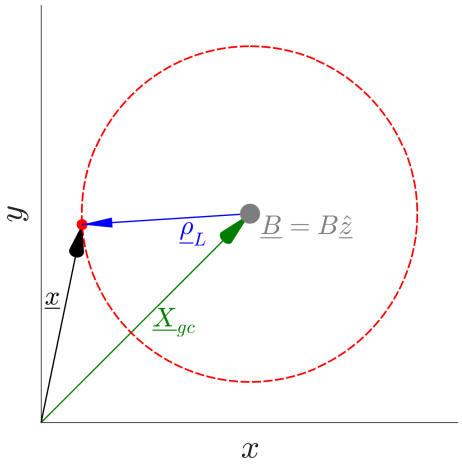

Figure 3.1.: Illustration of the particle coordinate $\boldsymbol{x}$, the guiding-center coordinate $\boldsymbol{X}_{gc}$. The magnetic field is oriented in the z direction $\boldsymbol{B} = B\hat{\boldsymbol{z}}$. This figure corresponds to the (x, y) projection of Fig. 1.4.

The main idea behind the modern derivation involves introducing an appropriate set of phase space coordinates, called gyrocenter coordinates $\bar{\boldsymbol{Z}}$, obtained through a near-identity transformation using the Lie transform from the guiding-center coordinates $\boldsymbol{Z} = (\boldsymbol{X}, v_\parallel, \mu, \theta)$, with $\boldsymbol{X} = \boldsymbol{x} - \boldsymbol{\rho}$, $v_\parallel = \boldsymbol{v} \cdot \hat{\boldsymbol{b}}$, and $\mu = m_\sigma v_\perp^2/(2B)$ (see Fig. 3.1). The gyrocenter coordinates are constructed to ensure the exact conservation of the magnetic moment $\bar{\mu}$, which renders the gyro-phase conjugate variable $\bar{\theta}$ ignorable. This procedure ensures that the distribution function in terms of gyrocenter coordinates is independent of $\bar{\theta}$, reducing the phase space from 6D to 5D. The complete derivation of gyrokinetic equations is not presented here; only the final equations are provided.

Gyrokinetic orderings The approximations upon which gyrokinetic theory is based reflect the experimentally measured microturbulence features [149] and some fundamental plasma properties [143]. The orderings, as reported in Ref. [143], are here summarized.

- **Equilibrium quantities spatio-temporal scales.** The background equilibrium quantities are assumed to be slowly varying in space

$$\rho_\sigma \boldsymbol{\nabla} \log F_0 \sim \rho_\sigma \boldsymbol{\nabla} \log B \sim \epsilon_B \ll 1$$

  and constant in time. Their evolution in time scales of the order of the confinement time, is therefore much larger than those of typical turbulent fluctuations.

- **Typical frequencies lower than the gyro-frequencies.** The typical frequency spectra of the turbulent fluctuations cover a broad range of scales with the mean frequency being of the same order of the diamagnetic drift frequency $\omega^*_\sigma \sim v_{\mathrm{th},\sigma}/L$ and therefore much lower than the cyclotron frequencies Ω_σ

$$\frac{\omega}{\Omega_\sigma} \sim \epsilon_\omega \ll 1\,.$$

- **Small amplitude fluctuations**. The typical amplitudes of the turbulent fluctuations, e.g. in the perturbed distribution function f_1 of the single-particle distribution function $f_\sigma = F_{0\sigma} + f_{1\sigma}$, densities n_1, are small compared to the mean equilibrium values n_0. This ordering can be expressed in terms of the dimensionless expansion parameter $\epsilon_\delta \ll 1$

$$\frac{f_{1\sigma}}{F_{0\sigma}} \sim e\frac{\phi_1}{T_\sigma} \sim e\frac{v_\parallel A_{1\parallel}}{T_\sigma} \sim \frac{B_{1\parallel}}{B} \sim \epsilon_\delta \ll 1$$

  where F_0 is the background Maxwellian, e the electric charge, ϕ_1 the perturbed electrostatic potential, $v_\parallel$, $A_{1\parallel}$ and $B_{1\parallel}$ respectively the velocity, perturbed parallel vector potential, and perturbed magnetic field parallel to the background magnetic field $\boldsymbol{B}_0$.

- **Spatial scales anisotropy.** The fast particle motion along the magnetic field lines determine a typical parallel correlation length of the turbulence fluctuations to be comparable to macroscopic scale length L; while typical perpendicular correlation length are of the order of few Larmor radii. These determine the orderings of the parallel and perpendicular wavelengths to be

$$k_\perp \rho_\sigma \sim k_\parallel L \sim 1 \quad \Rightarrow \quad \frac{k_\parallel}{k_\perp} \sim \epsilon_\parallel \ll 1$$

  following from $\rho_\sigma/L \sim \epsilon$.

Finally, all the different ordering parameters introduced $\epsilon_\delta, \epsilon_\parallel, \epsilon_\omega, \epsilon_B$ are assumed to be of the same size ϵ.

Gyrokinetic Vlasov equation The gyrokinetic Vlasov equation describing the spatio-temporal evolution of the single-particle distribution function as a function of gyrocenter

coordinates $F_\sigma(\bar{\boldsymbol{X}}, \bar{v}_\parallel, \bar{\mu}, t)$ in the 5D phase space is thus given by

$$\frac{\partial F_\sigma}{\partial t} + \dot{\bar{\boldsymbol{X}}} \cdot \boldsymbol{\nabla} F_\sigma + \dot{\bar{v}}_\parallel \frac{\partial F_\sigma}{\partial \bar{v}_\parallel} + \dot{\bar{\mu}} \frac{\partial F_\sigma}{\partial \bar{\mu}} = 0\,. \tag{3.2}$$

The gyrocenter equations of motions are derived via the Euler-Lagrange equations, and at first order in ϵ are given by [150]

$$\dot{\bar{\boldsymbol{X}}} = \bar{v}_\parallel \hat{\boldsymbol{b}} + \frac{B_0}{B_\parallel^*} \left(\boldsymbol{v}_\chi + \boldsymbol{v}_c + \boldsymbol{v}_{\boldsymbol{\nabla} B} \right)\,, \tag{3.3}$$

$$\dot{\bar{v}}_\parallel = -\frac{\dot{\bar{\boldsymbol{X}}}}{m_\sigma \bar{v}_\parallel} \cdot \left(q_\sigma \boldsymbol{\nabla} \bar{\phi}_1 + \frac{q_\sigma}{c} \dot{\bar{A}}_{1\parallel} \hat{\boldsymbol{b}} + \mu \boldsymbol{\nabla} (B_0 + \bar{B}_{1\parallel}) \right)\,, \tag{3.4}$$

$$\dot{\bar{\mu}} = 0\,. \tag{3.5}$$

Several notations have been introduced. In particular, the effective magnetic field $\boldsymbol{B}^*$, containing terms due to magnetic fluctuations, can be written as [150]

$$\boldsymbol{B}^* = B_{0\parallel}^* \hat{\boldsymbol{b}} + \frac{m_\sigma}{q_\sigma} v_\parallel \boldsymbol{\nabla} \times \hat{\boldsymbol{b}} - \hat{\boldsymbol{b}} \times \boldsymbol{\nabla} \bar{A}_{1\parallel}\,.$$

The gyrocenter velocity is given by the parallel streaming along the equilibrium magnetic field, the generalized $\boldsymbol{E} \times \boldsymbol{B}$ drift velocity, the curvature drift, and grad-B drift

$$\begin{aligned} \boldsymbol{v}_\chi &= -c \frac{\boldsymbol{\nabla} \bar{\chi} \times \boldsymbol{B_0}}{B_0^2} \\ \boldsymbol{v}_c &= \frac{v_\parallel^2}{\Omega_\sigma} \left(\boldsymbol{\nabla} \times \hat{\boldsymbol{b}} \right)_\perp = \frac{v_\parallel^2}{\Omega_\sigma} \hat{\boldsymbol{b}} \times \left(\frac{\boldsymbol{\nabla} B_0}{B_0} + \frac{\beta}{2} \frac{\boldsymbol{\nabla} p}{p} \right) \\ \boldsymbol{v}_{\boldsymbol{\nabla} B} &= \frac{\mu c}{q_\sigma B_0} \hat{\boldsymbol{b}} \times \boldsymbol{\nabla} B_0 \end{aligned} \tag{3.6}$$

where the modified gyroaveraged potential is $\bar{\chi} = \bar{\phi}_1 - v_\parallel \bar{A}_{1\parallel}/c + \mu \bar{B}_{1\parallel}/q_\sigma$. The overbars above the fields appearing in the equation of motions indicate the gyroaverages around the gyrocenters position $\bar{\boldsymbol{X}}$. Specifically, the gyroaverage of a quantity A is defined as $\bar{A}(\bar{\boldsymbol{X}}) = (2\pi)^{-1} \int_0^{2\pi} \mathrm{d}\theta\, A(\bar{\boldsymbol{X}} + \bar{\boldsymbol{\rho}})$. If the directions perpendicular to the field line are represented in Fourier space, the gyroaverage reduces to a multiplication by the zeroth-order Bessel function J_0 [151]: $\bar{A}(\bar{\boldsymbol{X}}) = J_0(k_\perp \rho_\sigma) \hat{A}_{\boldsymbol{k}}$. We notice that to get Eq. 3.6 the MHD equilibrium force balance $\boldsymbol{\nabla} p = \boldsymbol{j} \times \boldsymbol{B_0}/c$ and Ampére's law $\boldsymbol{\nabla} \times \boldsymbol{B_0} = 4\pi \boldsymbol{j}/c$ have been used, and the β parameter has been introduced $\beta = 8\pi p / B_0^2$.

Inserting the equations of motion Eqs. 3.3, 3.4, 3.5 into the Vlasov equation Eq. 3.2 yields the so-called full-F gyrokinetic equation. This equation can be simplified, considering the orderings introduced in Sec. 3.2, by adopting the delta-f approximation. Thus, the distribution function is expanded as $F_\sigma = F_{0\sigma} + f_{1\sigma}$, where $F_{0\sigma}$ is the equilibrium static distribution function, and $f_{1\sigma}$ is the perturbed distribution function of order ϵ compared to the equilibrium. The resulting equation can be expanded to various orders

in ϵ. At zeroth order in ϵ, the unperturbed gyrokinetic equation is obtained as

$$v_\parallel \hat{\boldsymbol{b}} \cdot \left[\boldsymbol{\nabla} F_{0\sigma} - \frac{\mu}{m v_\parallel} \boldsymbol{\nabla} B_0 \frac{\partial F_{0\sigma}}{\partial v_\parallel} \right] = 0 \tag{3.7}$$

which imposes constraints on the functional form of the background distribution function $F_{0\sigma}$. The equation at first order in ϵ, incorporating the condition Eq. 3.7, finally reads

$$\begin{aligned} &\frac{\partial f_{1\sigma}}{\partial t} - \frac{q_\sigma}{m_\sigma c} \dot{\bar{A}}_{1\parallel} \frac{\partial F_{0\sigma}}{\partial v_\parallel} + \left[\frac{c\hat{\boldsymbol{b}}}{q_\sigma B^*_\parallel} \times \boldsymbol{\nabla} \left(\mu B_0 + q_\sigma \bar{\chi} \right) + \frac{B_0}{B^*_\parallel} \boldsymbol{v}_c \right] \\ &\quad \cdot \left[\boldsymbol{\nabla} (F_{0\sigma} + f_{1\sigma}) - \frac{1}{m_\sigma v_\parallel} \left(q_\sigma \boldsymbol{\nabla} \bar{\phi}_1 + \mu \boldsymbol{\nabla} (B_0 + \bar{B}_{1\parallel}) \right) \frac{\partial F_{0\sigma}}{\partial v_\parallel} \right] \\ &\quad + v_\parallel \hat{\boldsymbol{b}} \cdot \left[\boldsymbol{\nabla} f_{1\sigma} - \frac{1}{m_\sigma v_\parallel} \left(q_\sigma \boldsymbol{\nabla} \bar{\phi}_1 + \mu \boldsymbol{\nabla} \bar{B}_{1\parallel} \right) \frac{\partial F_{0\sigma}}{\partial v_\parallel} - \frac{1}{m_\sigma v_\parallel} \mu \boldsymbol{\nabla} B_0 \frac{\partial f_{1\sigma}}{\partial v_\parallel} \right] = 0 \,. \end{aligned} \tag{3.8}$$

It's worth noting that the only nonlinear term appearing in the equation is given by the advection of the perturbed distribution function by the generalized $\boldsymbol{E} \times \boldsymbol{B}$ drift velocity $(c/B^*_\parallel \hat{\boldsymbol{b}} \times \boldsymbol{\nabla} \bar{\chi}) \cdot \boldsymbol{\nabla} f_1$. The second order terms in ϵ giving rise to the *parallel nonlinearity* have been neglected in accordance with previous studies where their negligible impact was demonstrated [152].

In this thesis work, Maxwellian distribution functions, representing the thermodynamic equilibrium and solutions of Eq. 3.7, are used for each plasma species

$$F_{0\sigma} = F_{M\sigma} = \frac{n_{0\sigma}}{\pi^{3/2} v^3_{\mathrm{th},\sigma}} \exp\left(- \frac{m_\sigma v_\parallel^2/2 + \mu B_0}{T_{0\sigma}} \right)$$

where $n_{0\sigma}$, $T_{0\sigma}$, and $v_{\mathrm{th},\sigma}$ respectively denote the density, temperature, and thermal velocity of species σ. Thus, the derivatives of the background appearing in the delta-f Eq. 3.8 are given by

$$\begin{aligned} \boldsymbol{\nabla} F_{M\sigma} &= \left[\frac{\boldsymbol{\nabla} n_{0,\sigma}}{n_{0,\sigma}} + \frac{\boldsymbol{\nabla} T_{0,\sigma}}{T_{0,\sigma}} \left(\frac{m_\sigma v_\parallel^2/2 + \mu B_0}{T_{0\sigma}} - \frac{3}{2} \right) - \frac{\boldsymbol{\nabla} B_0}{B_0} \frac{\mu B_0}{T_{0\sigma}} \right] F_{M\sigma} \,, \\ \frac{\partial F_{M\sigma}}{\partial v_\parallel} &= - \frac{m_\sigma v_\parallel}{T_{0\sigma}} F_{M\sigma} \,. \end{aligned}$$

Maxwell's equations To close the system of gyrokinetic equations, the electromagnetic fields must be self-consistently calculated via Maxwell's equations, where the source terms are given by appropriate moments of the perturbed distribution function. The Poisson and Ampère's laws for the fluctuations of the electrostatic potential ϕ_1 and vector potential $\boldsymbol{A}_1$, adopting the Coulomb gauge $\boldsymbol{\nabla} \cdot \boldsymbol{A} = 0$, and neglecting the displacement current, are given by

$$\begin{aligned} -\nabla^2 \phi_1 &= 4\pi \sum_\sigma q_\sigma n_\sigma(\boldsymbol{x}) = 4\pi \sum_\sigma q_\sigma \int \mathrm{d}\boldsymbol{v} \, f_{1\sigma}(\boldsymbol{x}, \boldsymbol{v}) \,, \\ -\nabla^2 \boldsymbol{A}_1 &= \frac{4\pi}{c} \sum_\sigma \boldsymbol{j}_\sigma(\boldsymbol{x}) = \frac{4\pi}{c} \sum_\sigma q_\sigma \int \mathrm{d}\boldsymbol{v} \, \boldsymbol{v} f_{1\sigma}(\boldsymbol{x}, \boldsymbol{v}) \,. \end{aligned}$$

We notice that the charge and current density appearing on the right-hand side of the Maxwell equations are calculated using the particle distribution function, while the gyrokinetic equation Eq. 3.8 provides the distribution function in gyro-center coordinates. It is therefore necessary to connect the two distribution functions. The adopted procedure involves expressing both distribution functions in guiding-center phase space.

First, the particle density and current density are calculated by adopting a coordinate transformation in guiding-center phase space through

$$n_\sigma(\boldsymbol{x}) = \int \mathrm{d}\boldsymbol{v}\, f_{1\sigma}(\boldsymbol{x},\boldsymbol{v}) = \frac{B^*_{0\parallel}}{m_\sigma} \int \mathrm{d}\boldsymbol{X}\mathrm{d}v_\parallel \mathrm{d}\mu\mathrm{d}\theta\, \delta\left(\boldsymbol{X} - (\boldsymbol{x} - \boldsymbol{\rho}_\mathrm{L})\right) f_{1\sigma}(\boldsymbol{Z}) \tag{3.9}$$

$$\boldsymbol{j}_\sigma(\boldsymbol{x}) = q_\sigma \int \mathrm{d}\boldsymbol{v}\, \boldsymbol{v} f_{1\sigma}(\boldsymbol{x},\boldsymbol{v}) = \frac{q_\sigma B^*_{0\parallel}}{m_\sigma} \int \mathrm{d}\boldsymbol{X}\mathrm{d}v_\parallel \mathrm{d}\mu\mathrm{d}\theta\, \delta\left(\boldsymbol{X} - (\boldsymbol{x} - \boldsymbol{\rho}_\mathrm{L})\right) f_{1\sigma}(\boldsymbol{Z})\boldsymbol{v} \tag{3.10}$$

where $B^*_{0\parallel}/m_\sigma$ represents the Jacobian of the change of variables, and the delta Dirac function is formally introduced since the coordinate transformation involves the entire phase space, but the integral is performed only over velocity space, thus ensuring the invariance of the spatial region during the coordinate transformation. The next step involves expressing the guiding-center distribution function by using the pull-back operator on the gyro-center distribution function, which yields for $F_{0\sigma} = F_{M\sigma}$ [150]

$$f_{1\sigma}(\boldsymbol{Z}) = f_{1\sigma}(\bar{\boldsymbol{Z}}) - \left[q_\sigma\left(\phi_1(\boldsymbol{X} + \boldsymbol{\rho}_\mathrm{L}) - \bar{\phi}_1(\boldsymbol{X})\right) - \mu \bar{B}_{1\parallel}(\boldsymbol{X})\right] \frac{F_{0\sigma}}{T_{0\sigma}}\,. \tag{3.11}$$

This transformation introduces two terms containing fluctuations of the electromagnetic fields that describe the effects of polarization and magnetization on the gyro-motion orbit [143]. By inserting Eq. 3.11 into Eqs. 3.9 and 3.10, it is therefore possible to calculate the gyrokinetic Maxwell's equations. Together with the Vlasov equation Eq. 3.8, these equations constitute a closed system.

Collisional operator In the gyrokinetic equations derived so far, interactions among different species of plasma occur via the self-generated electromagnetic fields resulting from collective processes. However, plasma particles can also interact through Coulomb collisions. Although these collisions are not frequent in hot magnetized plasmas, collisional dissipation can play a significant role e.g., affecting the linear growth rates of the instabilities, providing the damping of zonal flows, and so physical dissipation mechanisms necessary for turbulence to reach a quasi-steady state. For these reasons, in this thesis work, the addition of a collisional operator for the description of binary Coulomb collisions has been considered, such that the gyrokinetic Vlasov equation Eq. 3.2 becomes

$$\frac{\partial F_\sigma}{\partial t} + \dot{\bar{\boldsymbol{X}}} \cdot \boldsymbol{\nabla} F_\sigma + \dot{\bar{v}}_\parallel \frac{\partial F_\sigma}{\partial \bar{v}_\parallel} = \sum_{\sigma'} C\left(F_\sigma, F_{\sigma'}\right)\,.$$

In the context of this thesis, a linearized Landau-Boltzmann collisional operator is employed, formally given by [151]

$$C\left(F_\sigma, F_{\sigma'}\right) = \frac{\partial}{\partial \boldsymbol{v}} \cdot \left(\overline{\overline{\boldsymbol{D}}} \cdot \frac{\partial}{\partial \boldsymbol{v}} - \boldsymbol{R}\right) F_\sigma$$

where $\overline{\overline{\boldsymbol{D}}}$ denotes the diffusion tensor, and $\boldsymbol{R}$ represents dynamical friction, providing diffusion and advection mechanisms in velocity space. For further details the reader is referred to Ref. [151].

Sheared equilibrium flows in local simulations In Sec. 1.5.2, we introduced that turbulence saturation is influenced by various mechanisms, notably sheared plasma flows, which play a critical role [36]. The gyrokinetic model includes the physics of small-scale zonal flows, which are self-generated by the turbulence [107]. In the model described so far, the inclusion of the large scale $\boldsymbol{E} \times \boldsymbol{B}$ plasma flows have not been discussed. They are associated with the radial electric field from the radial force balance equation (see Sec. 2.3)

$$E_r = \frac{\boldsymbol{\nabla}_r p_i}{Zen} - v_\theta B_\phi + v_\phi B_\theta$$

where the diamagnetic term from the pressure gradient and the contributions from the poloidal velocity v_θ and toroidal velocity v_ϕ appear. The significant impact of $\boldsymbol{E} \times \boldsymbol{B}$ flow, particularly its radial variation (or flow shear), modifies turbulent structures by reducing their radial correlation length, thereby reducing radial transport. To incorporate this effect into the gyrokinetic model, an advection term from the background $\boldsymbol{E} \times \boldsymbol{B}$ flow is necessary. Firstly, we assume that the radial electric field $\boldsymbol{E}_r$ varies over slower temporal and larger spatial scales compared to those considered in the local gyrokinetic model. These assumptions allow to treat the $\boldsymbol{E} \times \boldsymbol{B}$ flow as uniformly sheared across the flux-tube radial domain, such that the it can be expressed as

$$v_{\boldsymbol{E}\times\boldsymbol{B}} = \gamma_{\boldsymbol{E}\times\boldsymbol{B}} x \,.$$

Here, $\gamma_{\boldsymbol{E}\times\boldsymbol{B}}$ represents the constant shearing rate. We notice that in the GENE coordinate system, this velocity is along the bi-normal direction y. This non-radially-periodic advection term needs to be included into the local gyrokinetic equation employing the spectral representation and thus satisfying periodic radial boundary conditions. In GENE, the *corrected wavevector-remap* method is used, as introduced in Ref. [153], representing an improvement compared to the *standard* wavevector-remap [154].

The normalized shearing rate parameter to set in GENE is

$$\hat{\gamma}_{\boldsymbol{E}\times\boldsymbol{B}} = -\frac{x_0}{|q|}\frac{\mathrm{d}}{\mathrm{d}x}\left(\frac{\mathrm{d}\Phi_0}{\mathrm{d}\psi_0}\right)\frac{L_{\mathrm{ref}}}{c_{\mathrm{ref}}}$$

where ψ_0, represents the poloidal magnetic flux, and $\mathrm{d}\Phi_0/\mathrm{d}\psi_0$, is proportional to the lowest order radial electric field [139], for a discussion regarding the normalizations introduced in GENE, see Appendix A. A detailed derivation of this parameter starting from the experimental profiles was given in Chapter 2, Eqs. 2.1-2.2 in Sec. 2.3.

3.3. Field-aligned coordinates

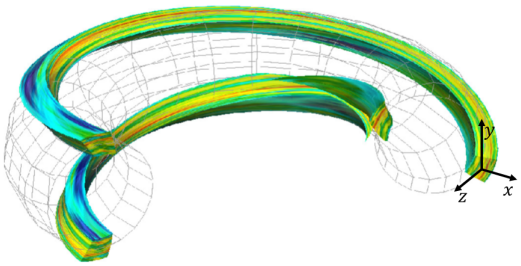

Figure 3.2.: Sketch of the flux-tube domain. The non-orthogonal straight-field-aligned coordinates (x, y, z), respectively radial, bi-normal, and parallel, are shown. Adapted from source [155].

As discussed in Sec. 3.2, the microinstabilities responsible for the development of microturbulence exhibit spatial anisotropy due to the strong magnetic field, characterized by long wavelengths parallel to the background magnetic field and short perpendicular wavelengths ($k_{\parallel} \ll k_{\perp}$). Furthermore, experimental measurements of fluctuations in tokamaks reveal that the correlation lengths of turbulent eddies are indeed short in the direction perpendicular to the field, $\sim 10\rho_{\mathrm{L},i}$, but long in the parallel direction, of the order of the system size. It is possible to exploit these properties to define an appropriate coordinate system, called *field-aligned* [156, 157], which minimizes the number of grid points in the spatial discretization. This is achieved by first reducing the number of points needed to resolve the dynamics in the direction parallel to the field line and then allowing the simulated plasma volume to be reduced to a long and thin flux-tube, as illustrated in Fig. 3.2. Note that the local, or flux-tube, model used in this thesis assumes a complete scale separation between the equilibrium background quantities and fluctuations, corresponding to the limit $\rho_* = \rho_i/a \to 0$ (where a is the minor radius of the plasma).

We start by introducing a system of *straight-field-line* coordinates [20, 157] (Ψ, χ, φ), with Ψ the poloidal flux function serving as the flux surface label, χ as the straight field line poloidal angle, and φ as the toroidal angle. The system of "straight-field-aligned" coordinates [156] (or flux-tube coordinates) used in GENE [142] is defined by [158]

$$\begin{cases} x = C_x(\Psi) - x_0 \\ y = C_y[q(\rho)\chi - \varphi] \\ z = \chi \end{cases} \tag{3.12}$$

where (x, y, z) are the radial, binormal, and parallel coordinates, respectively, and q is the safety factor, representing the number of toroidal revolutions a field line must complete to undergo one poloidal rotation. The factors C_x and C_y are chosen such that the coordinates are lengths, particularly $C_y = x_0/q_0$. Finally, x_0 is the radial position of the center of the simulation domain. In these coordinates, the magnetic field can be

expressed in Clebsch representation as [20, 158]

$$\boldsymbol{B}_0 = \boldsymbol{\nabla}\Psi \times \boldsymbol{\nabla}(q\chi - \varphi) = \frac{1}{\frac{\mathrm{d}C_x}{\mathrm{d}\Psi} C_y} \boldsymbol{\nabla}x \times \boldsymbol{\nabla}y = \mathcal{C}(x)\boldsymbol{\nabla}x \times \boldsymbol{\nabla}y\,.$$

It is evident that the directions $\boldsymbol{\nabla}x$ and $\boldsymbol{\nabla}y$ are orthogonal to the magnetic field, satisfying $\boldsymbol{B}_0 \cdot \boldsymbol{\nabla}x = \boldsymbol{B}_0 \cdot \boldsymbol{\nabla}y = 0$.

3.3.1. Operators in field-aligned coordinate

Having introduced the field-aligned system of coordinates, it is now possible to explicitly calculate the differential and vector operators that appear in the gyrokinetic equation Eq. 3.8. This ultimately allows obtaining a scalar equation that can be discretized and numerically solved.

In particular, the Jacobian and the metric tensor associated with the coordinate system $u^i = (x, y, z)$ are defined by

$$J^{-1} = (\boldsymbol{\nabla}x \times \boldsymbol{\nabla}y) \cdot \boldsymbol{\nabla}z = \frac{\boldsymbol{B}_0 \cdot \boldsymbol{\nabla}z}{\mathcal{C}}$$
$$g = \boldsymbol{\nabla}u^i \cdot \boldsymbol{\nabla}u^j = \begin{pmatrix} g^{xx} & g^{xy} & g^{xz} \\ g^{yx} & g^{yy} & g^{yz} \\ g^{zx} & g^{zy} & g^{zz} \end{pmatrix}.$$

Firstly, note that with these definitions, the B_0^2 term is given by

$$B_0^2 = \boldsymbol{B}_0 \cdot \boldsymbol{B}_0 = \mathcal{C}^2 \left[g^{xx} g^{yy} - (g^{xy})^2 \right].$$

Subsequently, note that the differential and vector operators to be calculated in the gyrokinetic equation are given by parallel derivatives, laplacian, and by vector products appearing into the drift velocities. In practice, the vector expressions to be expanded reduce to

$$\hat{\boldsymbol{b}} \cdot \boldsymbol{\nabla} = \frac{\mathcal{C}}{B_0}(\boldsymbol{\nabla}x \times \boldsymbol{\nabla}y) \cdot \boldsymbol{\nabla}u^i \partial_i = \frac{\mathcal{C}}{B_0 J}\partial_z$$
$$\nabla_\perp^2 = (\boldsymbol{\nabla}x\partial_x + \boldsymbol{\nabla}y\partial_y)^2 = g^{xx}\partial_x^2 + 2g^{xy}\partial_{xy}^2 + g^{yy}\partial_y^2$$
$$\hat{\boldsymbol{b}} \times \boldsymbol{\nabla}A \cdot \boldsymbol{\nabla} = \frac{\mathcal{C}}{B_0}(\boldsymbol{\nabla}x \times \boldsymbol{\nabla}y) \times \boldsymbol{\nabla}A \cdot \boldsymbol{\nabla} =$$
$$= \frac{\mathcal{C}}{B_0}(g^{xi}g^{yj} - g^{yi}g^{xj})\partial_i A \partial_j$$

where a generic scalar quantity A is introduced, and Einstein notation is used. Finally, the terms that appear in the gyrokinetic equation are explicitly calculated by exploiting the orderings $k_\perp \gg k_\parallel$, such that the parallel derivatives ∂_z of the perturbed quantities are negligible compared to the perpendicular ones, and recalling that the equilibrium quantities are independent of y. The final gyrokinetic equations in (x, y, z) coordinates thus obtained can be found, for example, in Ref. [151, 159].

3.4. Numerical resolution of the gyrokinetic equations

Solving the previously introduced system of equations is a formidable task. Analytical solutions, although providing fundamental insights for understanding physical mechanisms, are often achievable only by introducing simplifications, in particular linearization. In order to retain more physical mechanisms and actually simulate microturbulence, the system of equations is thus solved numerically. In this thesis work, the GENE code [141, 142] has been used. In what follows, the numerical techniques employed are briefly described.

3.4.1. Time integration: Runge-Kutta scheme and eigenvalue solver

The gyrokinetic equation Eq. 3.8 for the temporal evolution of the distribution function $f_{1\sigma}$ can be formally rewritten as follows

$$\frac{\partial f_{1\sigma}}{\partial t} = \mathcal{L}[f_{1\sigma}] + \mathcal{N}[f_{1\sigma}] + \mathcal{S}$$

where $\mathcal{L}$ and $\mathcal{N}$ respectively represent the linear and nonlinear operators of the perturbed quantities, while $\mathcal{S}$ denotes the terms independent from the perturbed distribution function $f_{1\sigma}$, which include the gradients of density, temperature, and velocity, providing the sources for microturbulence development.

To characterize the linear instabilities present in the system, the set of gyrokinetic equations is solved by neglecting the nonlinear term $\mathcal{N}$. As a consequence of the axisymmetry of the unperturbed tokamak system, reflected by the translational invariance in the y coordinate, each wavevector k_y represents an exact mode number for linear instabilities, allowing for the equation to be solved for a selected k_y. This enables the computation of the linear spectra of micro-instabilities, namely the real frequencies ω and the growth rate γ, as a function of k_y. Specifically, the linear system can be solved as an initial-value problem, in which the perturbed distribution function is evolved over time using a fourth-order explicit Runge-Kutta scheme. As a result, the system will eventually converge to the most unstable mode, characterized by the highest growth rate γ.

Alternatively, the linear system can be solved as an eigenvalue problem, solved in GENE by interfacing with the PETSc [160] and SLEPc [161, 162] libraries. In this approach, the explicit temporal evolution of the perturbed distribution function is not calculated, but instead, the eigenvalues and eigenvectors associated with the discretization matrix are computed. This method is often computationally more demanding but allows for the calculation of sub-dominant modes as well. In the context of this thesis, which is devoted to the study of turbulence in the pedestal, where the drives of instabilities are very high, it proves particularly useful to investigate sub-dominant instabilities due to their role in nonlinear dynamics.

To simulate microturbulence, the nonlinear term is included in the equation. In this case, the only available option is to solve the system as an initial value problem still using the fourth order Runge-Kutta scheme. Here, an adaptive time-step system is implemented during the simulation to ensure compliance with the Courant-Friedrichs-Lewy (CFL) condition, which is imposed by the nonlinear advection term. For further details, the reader is referred to Ref. [151].

3.4.2. Phase-space discretization and boundary conditions

Perpendicular directions The turbulent structures that develop from microinstabilities are characterized by perpendicular correlation lengths of the order of several ion Larmor radii. As long as the perpendicular box size is sufficiently larger than a few radial correlation lengths, it is then reasonable to assume that the statistical properties of turbulent fluctuations are equal at the boundaries. For practical purposes, *exact* periodicity is assumed in the radial and binormal directions

$$f(x + L_x, y, z) = f(x, y, z)$$
$$f(x, y + L_y, z) = f(x, y, z)$$

where L_x denotes the radial and L_y the bi-normal box size. These conditions allow the perturbed quantities $f_{1\sigma}$, ϕ_1, $A_{1\parallel}$, and $B_{1\parallel}$ to be decomposed in the perpendicular plane (x, y) into a Fourier series

$$f(x, y, z) = \sum_{k_x, k_y} \hat{f}_{k_x,k_y}(z) \exp(ik_x x + ik_y y) \tag{3.13}$$
$$\text{with} \quad \hat{f}_{k_x,k_y}(z) = \frac{1}{L_x L_y} \int_0^{L_x} \int_0^{L_y} \mathrm{d}x\, \mathrm{d}y\, f(x, y, z) \exp(-ik_x x - ik_y y)$$

thus ensuring the periodic boundary conditions by construction. The derivatives along x and y are thus computed in Fourier space as simple products. In numerical simulations, the spectral representation is approximated with a finite number of wave-numbers defined by N_{k_x} and N_{k_y}, including the zero modes. Consequently, grids for the radial and bi-normal wave-numbers are given by $k_x = j_x k_{x,\min}$ where the integer j_x ranges from $-(N_{k_x} - 1)/2$ to $(N_{k_x} - 1)/2$, and $k_y = j_y k_{y,\min} \geq 0$ (by invoking the reality condition $\hat{f}_{k_x,k_y} = \hat{f}^*_{-k_x,-k_y}$) where the integer j_y ranges from 0 to $N_{k_y} - 1$. According to these definitions, the radial and bi-normal box size are respectively given by $L_x = 2\pi/k_{x,\min}$, and $L_y = 2\pi/k_{y,\min}$.

Parallel direction The derivatives appearing in the gyrokinetic equation along the parallel direction z are computed by employing finite difference schemes. To derive the boundary condition along the z direction, we start from the physical boundary condition, which imposes 2π-periodicity along the straight field line angle χ (corresponding to the poloidal angle) given by

$$f(\Psi, \chi, \varphi) = f(\Psi, \chi + 2\pi, \varphi)\,.$$

This condition, in the flux-tube coordinates introduced in Eq. 3.12, translates to the so-called "twist-and-shift" condition [156]

$$f(x, y, z) = f(x, y + 2\pi q(x) C_y(\Psi), z + 2\pi)\,.$$

Using the spectral representation Eq. 3.13, this condition becomes

$$\sum_{k_x,k_y} \hat{f}_{k_x,k_y}(z) \exp(ik_x x + ik_y y) = \sum_{k_x,k_y} \hat{f}_{k_x,k_y}(z + 2\pi) \exp(ik_x x) \exp(ik_y (y + 2\pi q(x) C_y)) \tag{3.14}$$

This condition applies to the boundaries of the domain in z and simultaneously provides a condition that the radial wave-numbers must satisfy. To derive it, the safety factor $q(x)$ is first linearized by expanding it in a Taylor series to the first order

$$q(x) \approx q_0 + \frac{\mathrm{d}q}{\mathrm{d}x} x = q_0 \left(1 + \frac{x}{x_0} \hat{s}\right)$$

where the magnetic shear is defined as $\hat{s} = (x_0/q_0)\, \mathrm{d}q/\mathrm{d}x$. Then, inserting this expansion into Eq. 3.14 and using the definition of $C_y = x_0/q_0$, we obtain

$$\begin{aligned}
&\sum_{k_x,k_y} \hat{f}_{k_x,k_y}(z) \exp(ik_x x + ik_y y) = \\
&\quad = \sum_{k_x,k_y} \hat{f}_{k_x,k_y}(z + 2\pi) \exp(ik_x x) \exp\left[ik_y (y + 2\pi x_0 \left(1 + \frac{x}{x_0}\right) \hat{s})\right] = \\
&\quad = \sum_{k_x,k_y} \hat{f}_{k_x,k_y}(z + 2\pi) \exp(ik_y y) \exp\left[ik_y 2\pi x_0\right] \exp\left[ix(k_x + 2\pi k_y \hat{s})\right] .
\end{aligned}$$

This condition implies that at the domain boundaries in z, the mode k_y, k_x is connected to a mode of the radial grid with $k_x^{'}$ that satisfies the condition

$$k_x^{'} = k_x + 2\pi \hat{s} k_y \,. \tag{3.15}$$

In view of this condition, a requirement for the radial mode grid spacing is given by

$$k_{x,\mathrm{min}} = \frac{2\pi \hat{s}}{\mathcal{K}} k_{y,\mathrm{min}} \tag{3.16}$$

where an integer number $\mathcal{K} \geq 1$ is introduced, which also determines the spacing between the k_x connected modes. The implications of this constraint in the context of simulations towards the plasma edge conducted in this thesis are as follows. Firstly, we note that towards the plasma edge the magnetic shear $\hat{s}$ progressively increases. At the same time, it has been reported [119] that in the plasma edge, turbulent structures assume considerable sizes, requiring larger box sizes compared to those typically used to simulate the plasma core. This implies that, to have a sufficiently low $k_{x,\mathrm{min}}$ to ensure an adequate radial box size L_x, a sufficiently large $\mathcal{K}$ is necessary, which in turn implies that a sufficiently high number of modes N_{k_x} is required. This ensures that sufficient number of k_x modes are connected in order to well represent the structures as function of the z coordinate (see Appendix A for the definition of the ballooning structures). Finally, we notice that the definition Eq. 3.16 prescribes the aspect ratio of the perpendicular dimensions of the flux-tube to be given by the quantization rule:

$$\frac{L_x}{L_y} = \frac{\mathcal{K}}{2\pi \hat{s}} \,.$$

The parallel coordinate z is discretized into a grid of n_z equidistant points covering a poloidal turn, i.e., $L_z = 2\pi$. For magnetic surfaces characteristic of the plasma edge, which are significantly shaped, the previously introduced coordinate z results in an imbalance in the distribution of grid points n_z, unfavorable at the outboard midplane. For this reason, to effectively resolve the typical ballooned turbulence structures, the parallel

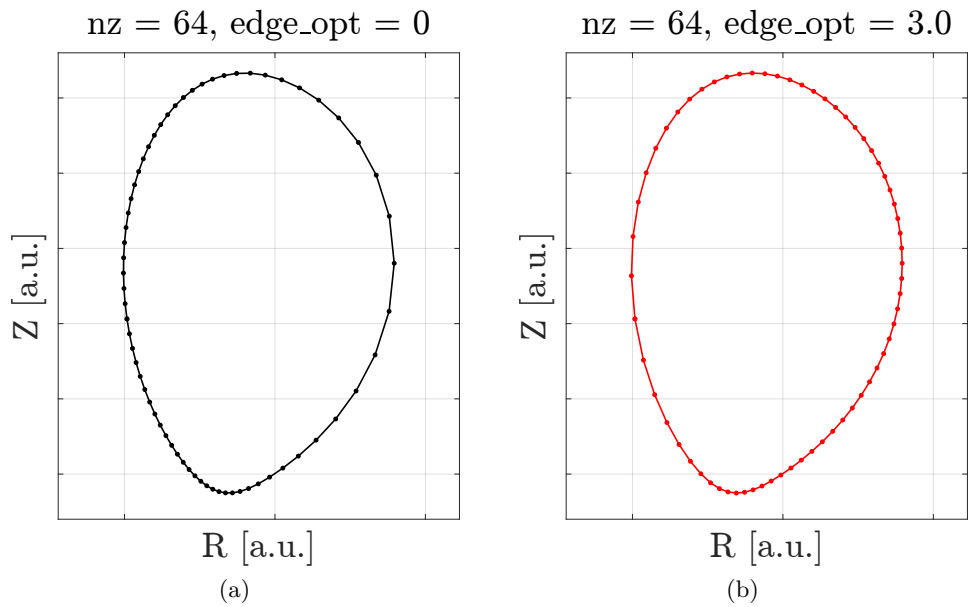

Figure 3.3.: Discretization of a shaped flux surface by varying the distribution of discretization points n_z as a function of the parameter k (or `edge_opt` in GENE input parameters: (a) with standard distribution, i.e. $k = 0$ (b) with $k = 3.0$.

resolution requirements increase. To address this issue in GENE, another coordinate z' has been defined that allows for an improved grid points distribution

$$z' = \frac{\pi}{\operatorname{arcsinh}(k\pi)} \operatorname{arcsinh}(kz)$$

where k is a scaling factor required as input. For example, it is shown in Fig. 3.3, the same flux-surface discretized with $n_z = 64$ with different k resulting in the improved discretization with increasing k. In the nonlinear simulations conducted in this thesis work, this parametrization of the parallel coordinate has been used, allowing for a reduction in the number of grid points n_z determining computationally affordable simulations.

Velocity space In the local approximation used here, the perturbed distribution function $f_{1\sigma}$ is assumed to be smooth and to fall off at high energy, thus decaying for high velocity in the space $(v_\parallel, \mu)$. It is therefore sufficient to choose velocity space domains ensuring that a substantial portion of the perturbed distribution function is contained. Typical choices, based on numerical convergence studies, are $L_{v_\parallel,\max} = 3v_{\text{th}}$ (where $v_{\text{th}} = \sqrt{2T_{0\sigma}/m_\sigma}$), with $-L_{v_\parallel,\max} \leq v_\parallel \leq L_{v_\parallel,\max}$, and $L_\mu = 9T_{0\sigma}/B_0$ with $0 \leq \mu \leq L_\mu$. Velocity space is thus discretized with $n_{v_\parallel}$ and n_μ grid points respectively in an equidistant and a Gauss-Laguerre distribution respectively. Regarding the coordinate $v_\parallel$, it is thus possible to assume that $f_{1\sigma}$ is zero outside the domain and to apply Dirichlet boundary conditions. Derivatives with respect to the μ coordinate are only calculated in the collisional operator, whose numerical scheme based on a finite volume approach assumes that the fluxes across the domain boundary vanish [151]. On the other hand, derivatives with respect to the $v_\parallel$ coordinate are computed employing finite difference

schemes.

3.4.3. Parallelization

We have thus seen how the 5D phase space is discretized, which numerical schemes and boundary conditions are used in the flux-tube version of GENE to solve the system of gyrokinetic equations for each plasma species. Given the high dimensionality of the problem and its nonlinear nature, a very large number of grid points is necessary for discretization (e.g., a standard grid for nonlinear simulations would be $[n_{k_x} \times n_{k_y} \times n_z \times n_\mu \times n_{v_\parallel}] = [128 \times 48 \times 32 \times 16 \times 48] \sim 150$ million points for each plasma species considered.) This implies that to obtain numerical solutions in a reasonable time, it is essential to parallelize the code execution and exploit high-performance computing (HPC). In practice, in GENE, parallelization is achieved by separating the different species and decomposing phase space into different domains, which are then solved by different processors using the Message Passing Interface (MPI), allowing to perform simulations on thousands of CPUs.

4. Pedestal top stability: type-I ELMs vs. small-ELMs

Contents

4.1. Local gyrokinetic modeling in the pedestal region 89
4.2. Stability across the pedestal top position 90
4.3. Detailed analysis of modes at the pedestal top 94
4.3.1. Sub-dominant modes 94
4.3.2. Modes identification: transport fingerprints and normalized parallel electric field 95
4.3.3. Kinetic-ballooning modes threshold: scan $(\beta_e, 1/L_{T_i})$ 97
4.3.4. The impact of electromagnetic effects 98
4.3.5. The impact of impurities 99
4.4. Linear insights for the importance of non-linear mechanisms 103
4.4.1. Shearing rate comparison with linear spectra 104
4.4.2. Multi-scale criterion 105

In Chapter 2, we have seen that new H-mode plasma regimes characterized by small and high-frequency ELMs, as compared to the standard type-I ELMs, were achieved at the JET tokamak. Interestingly, it was found that different pedestal structures were obtained in the various ELMy discharges. In particular, the associated normalized density and temperature gradients were compared and, representing key parameters driving turbulent transport processes, they highlighted the potential different roles played by turbulent transport in the pedestals of different plasma regimes.

The aim of this chapter is, therefore, to characterize the stability around the pedestal top position, in order to clarify the microinstabilities underlying the development of microturbulence. As previously introduced, the framework adopted in this thesis is the gyrokinetic system of equations, numerically solved using the GENE code. The analysis will focus on comparing the stability of the pedestals in different ELMy regimes, with special attention given to clarifying the role of the most different plasma parameters between the two regimes, such as impurities and plasma β. The outcome of this analysis will provide insights into the main physical mechanisms at play in the pedestals of these plasma regimes, laying the groundwork for the nonlinear dynamics study presented in the next chapter.

This chapter is organized as follows: in Sec. 4.1, the local gyrokinetic modeling framework limits and numerical setup at the plasma edge are discussed; in Sec. 4.2, the stability across the pedestal top positions for discharges in the BSE and type-I ELM regimes is compared; Sec. 4.3 focuses on the characterization of modes at the pedestal top positions, firstly computing the sub-dominant modes, followed by the introduction of the concept of *fingerprints*, and subsequently evaluating the sensitivity to relevant input

parameters (e.g., electromagnetic effects), and finally addressing the impact of impurities, particularly on electron-scale modes; the last Sec. 4.4 is dedicated to the application of heuristic linear criteria to evaluate the potential impact of equilibrium $\boldsymbol{E} \times \boldsymbol{B}$ shearing and cross-coupling between ion and electron scales on nonlinear dynamics.

Part of the results presented in this chapter have been reported in Ref. [165]. Additionally, some of the results presented below, obtained using the GENE code, were initially performed with the gyrokinetic GKW code [164] and have been reported in Ref. [163]. Comparable results between the two codes have been obtained.

4.1. Local gyrokinetic modeling in the pedestal region

Before proceeding with the extensive use of the GENE code to characterize transport in the pedestal region, it is important to discuss the limitations of the gyrokinetic theory, specifically its local (or flux-tube) and δf approach employed here. This discussion will provide some considerations for the subsequent analyses.

As discussed in Chapter 3, the derivation of gyrokinetic theory relies on the assumption that the typical amplitudes of turbulent fluctuations are small compared to the mean equilibrium quantities. Additionally, the background equilibrium quantities, such as the distribution function F_0 (and consequently the mean density and temperature), are assumed to vary slowly in space compared to the scales of fluctuations at Larmor radii, $\sim \rho_\sigma$. The validity of both these assumptions becomes questionable in the pedestal region. In fact, large fluctuation amplitudes are experimentally observed near the last closed flux surface [166]. Furthermore, due to the significant variations across a narrow radial region, which result in steep gradients in the density and temperature profiles, the condition $\rho_i/L_{n,T} \ll 1$ may not be consistently satisfied across the entire pedestal.

In addition to these considerations, the local approximation [156] (also known as the flux-tube approximation, introduced in Sec. 3.3) is employed here. This approximation corresponds to the limit $\rho_* = \rho_i/a \to 0$ (where a is the minor radius of the plasma) of the radially global simulations [167, 168], where variations in equilibrium quantities over the typical scales of the turbulence correlation length are neglected.

Motivated by these considerations, the analysis conducted in this thesis has focused on the pedestal top position of the analyzed discharges. This represents the best compromise for performing simulations relevant to pedestal dynamics while remaining within the validity limits of the employed model. Recalling the physical parameters calculated in Sec. 2.4, we find that at the pedestal top position, $\rho_* \sim 1/450$, and the scale length associated with the steepest gradients in the driving parameters is $L_\perp = L_{T_e}$, which gives $\rho_i L_{T_e}^{-1} \sim 1/30$. Although previous works [167, 168] suggest that global effects could already play a role in determining the saturation level of ion-scale turbulence at these values, the local analysis around the pedestal top conducted here provides a reasonable starting point for investigating transport processes in this region. In contrast, for electron-scale dynamics, the validity of the above assumptions is more easily satisfied since $\rho_e = \sqrt{m_e/m_\mathrm{D}}\rho_i \sim \rho_i/60$.

Simulations setup The simulations at the reference plasma parameters (detailed in Sec. 2.4) were performed while retaining full electromagnetic effects, including the perpendicular $A_{1\parallel}$ and parallel $B_{1\parallel}$ magnetic fluctuations. Up to four kinetic species

were included: e, D, Be, and Ni, with multi-species collisions modeled using a linearized Landau-Boltzmann operator. As previously discussed, realistic magnetic equilibria, reconstructed with EFIT++, were used through the TRACER-EFIT module in GENE. In addition, rotation terms, such as centrifugal, Coriolis, and parallel flow shear, were included. This setup corresponds to the model that includes all relevant physics. In the following sections, the impact of various physical terms will be tested.

As we will see, various microinstabilities will be identified in the pedestals of the three analyzed discharges. These modes will exhibit different structures along the parallel coordinate z, necessitating appropriately refined numerical grids for accurate resolution. Given the broad parameter space explored in this thesis, a numerical grid was chosen to ensure the resolution of the most challenging modes to capture, even if this often leads to over-resolving other modes. At this stage, extensive tests involved only the resolution n_z, while the parallel hyperdiffusion was kept fixed at `hyp_z` $= -2.0$. It should be noted that finite hyperdiffusion is required to damp grid-scale oscillations introduced by the central finite difference scheme used in GENE to compute the derivative parallel to the field line [169]. Therefore, the typical grid resolution employed is $[n_{k_x}, n_{k_y}, n_z, n_{v_\parallel}, n_\mu] = [48, 1, 192, 48, 16]$. The reference ballooning angle is set to $k_{x,0} = 0$. To simplify the text, the notation for normalized wavenumbers will be introduced: $\hat{k}_y \equiv k_y \rho_i$ and similarly $\hat{k}_x \equiv k_x \rho_i$.

4.2. Stability across the pedestal top position

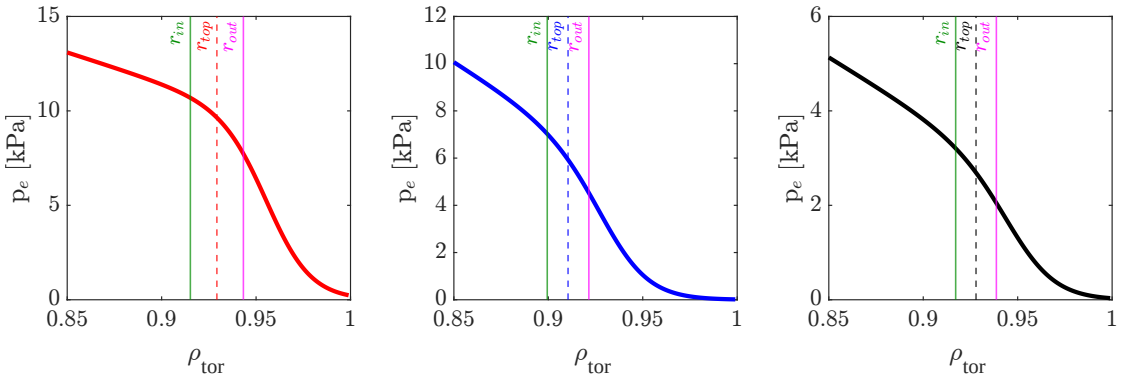

(a) #97395-Type-I ELMs (b) #96994-BSE (c) #94442-BSE

Figure 4.1.: Electron pressure pedestals radial profiles for the three discharges, highlighting the three radial locations across the pedestal top position: r_{in}, r_{top}, and r_{out}. This figure is analog to Fig. 2.8.

As a first investigation, linear initial-value GENE simulations were conducted to calculate the spectra of the most unstable microinstabilities, spanning from ion to electron scales, for the three discharges. This analysis was performed across the pedestal top positions at the three radial locations defined for each discharge (see Sec. 2.4) which are reported in Fig. 4.1. The goal of this analysis is twofold: first, to compare the stability across the different plasma regimes, and second, to evaluate the sensitivity of the results to slight

variations in the radial position. This latter analysis, given the uncertainties associated with experimental measurements, particularly at the plasma edge, simultaneously provides an assessment of the sensitivity of the results to uncertainties in the input parameters.

The normalized growth rate γ and real frequency ω as a function of the binormal wavenumber $\hat{k}_y$ are shown in Fig. 4.2. These quantities are normalized using reference parameters that vary depending on the radial position. The classification of modes will be based on their features as described in Sec. 1.5.1.

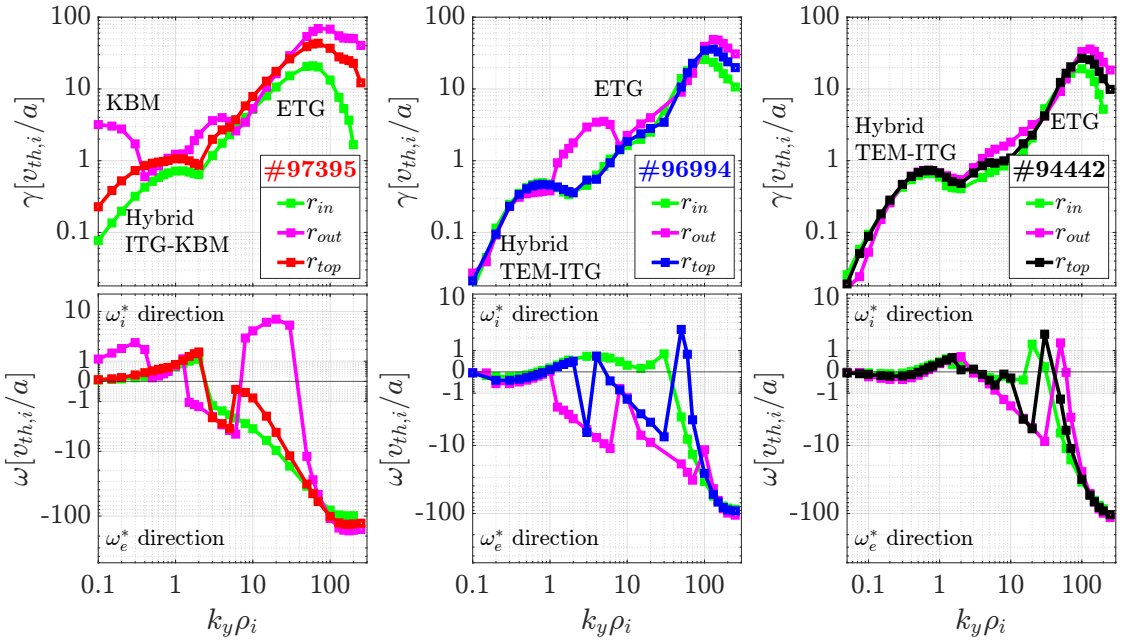

(a) #97395-Type-I ELMs (b) #96994-BSE (c) #94442-BSE

Figure 4.2.: Linear growth rate γ and mode frequency ω as function of the binormal wavenumber $k_y\rho_i$ at the three selected radial locations. Positive (negative) real frequency represents mode propagating in the ion (electron) diamagnetic drift $\omega^*_{i(e)}$ direction.

Focusing on the largest-scale modes, in the wavenumber range $0.1 \lesssim \hat{k}_y \lesssim 2.0$, we observe that while discharge #97395-Type-I ELMs is dominated by modes with positive frequencies and increasing growth rates as a function of radius, both BSE regime discharges reveal a branch of modes with slightly negative frequencies up to $\hat{k}_y \sim 0.8$, which then become slightly positive, with comparable growth rates across all analyzed radii. Based on their features (analyzed in more detail later), these modes in discharge #97395-Type-I ELMs are identified as hybrid ITG-KBM in the two inner radii and KBM at the outer, while in both BSE regimes, they are identified as hybrid TEM-ITG modes at all the radii. In the next section, an analysis will focus on quantifying the KBM threshold at the pedestal top of the three discharges to understand the origin of this difference.

It is also noteworthy that, unlike in other studies [91], in the discharges analyzed here, we do not observe MTM as the most unstable modes. Since MTMs have been proposed as a key mechanism for electron heat transport in JET pedestals [91], to verify whether sub-dominant MTMs are unstable, eigenvalue simulations will be later discussed.

Moving on to intermediate and electron scales, for wavenumbers $\hat{k}_y \gtrsim 2$, both regimes are dominated by negative frequency modes identified as ETG modes. Specifically, two branches can be distinguished according to the extensive classification performed in Ref. [97] for the JET-ILW pedestals: the toroidal-ETG (t-ETG) branch, which dominates at intermediate scales $2.0 \lesssim \hat{k}_y \lesssim 10$, and the slab-ETG (s-ETG) modes, which dominate at finer scales with $\hat{k}_y > 10$. As a reference parameter for ETG stability, we report the ratio of temperature to density normalized logarithmic gradient $\eta_e = L_n/L_{T_e}$ for the three discharges: #97395-Type-I ELMs $\eta_e = 5$, #96994-BSE $\eta_e = 2.4$, and #94442-BSE $\eta_e = 1.7$. These values suggest stronger ETG modes in the type-I ELM regime compared to the BSE regimes. Interestingly, in particular for discharge #97395-Type-I ELMs, a clear separation between ion and electron scales is not evident, since strong t-ETG modes are destabilized even at intermediate scales [97]. As we will see later, the relatively weaker t-ETG modes at the pedestal top positions of the BSE regimes can be partly attributed to the stabilizing role of impurities.

We have thus observed that the different pedestal structures found in the different plasma regimes, i.e., type-I ELMs and BSE, are indeed dominated by different instabilities at the ion scale: hybrid ITG-KBM and KBM in the first case, and hybrid ITG-TEM in the second. This difference already suggests a potentially distinct role played by turbulent transport processes in these regimes. Lastly, it is worth noting that ion-scale hybrid instabilities have been reported in various numerical investigations, such as hybrid ITG-KBM [170], hybrid TEM-ITG [79, 171–173], and hybrid KBM-TEM [174].

We proceed with the characterization of the modes by examining some representative ballooning structures (see Appendix A for the definition) of the normalized electrostatic potential $|\phi_1|$ and parallel vector potential $\left|A_{1\parallel}\right|$, as shown in Fig. 4.3 for the three discharges at the pedestal top positions.

In general, we observe that highly localized structures at the outboard midplane $z = 0$ are obtained at both ion and electron scales. This is particularly evident for the parallel vector potential $\left|A_{1\parallel}\right|$, which develops profiles with very sharp variations. These features are considered to be the main reason for the very high parallel resolution required to accurately resolve these modes. These features justify *a posteriori* the use of the option to redistribute the parallel grid points to concentrate around $z = 0$ (i.e. `edge_opt` in GENE, see Chapter 3).

It is also noted that some mode structures are not symmetric with respect to the $z = 0$ plane. The origin of this asymmetry is associated with the inclusion of rotation terms in the model, as well as the nature of the modes destabilized in steep gradient regions [175]. In particular, ETG modes can peak far from the outboard midplane, as observed in the mode at $\hat{k}_y = 3.0$ in Fig. 4.3b.

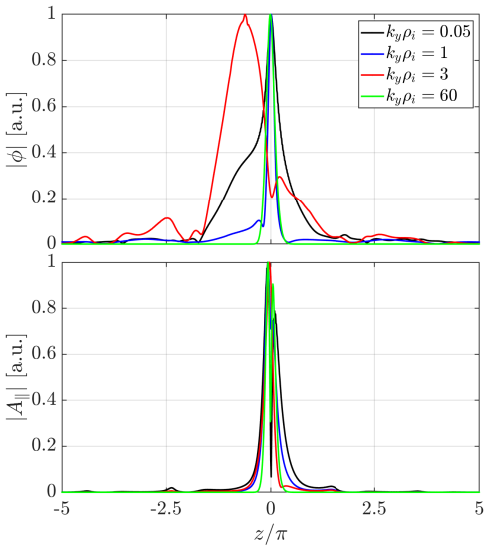

(a) #97395-Type-I ELMs

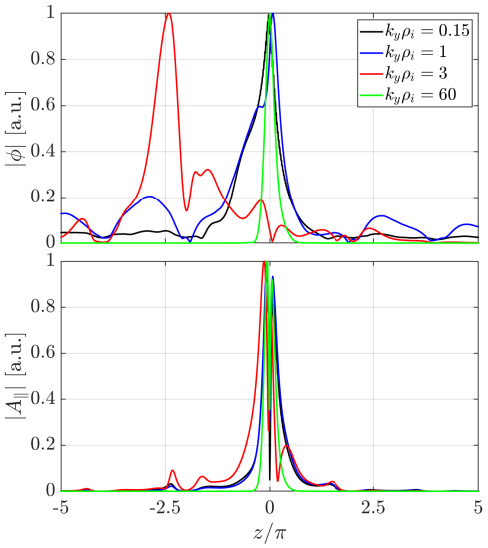

(b) #96994-BSE

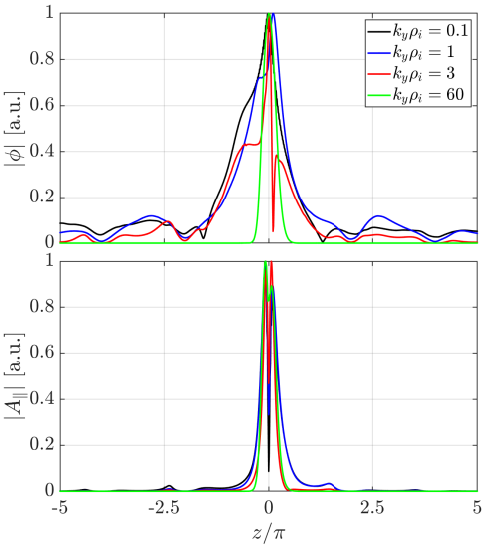

(c) #94442-BSE

Figure 4.3.: Representative normalized ballooning mode structures of the electrostatic potential $|\phi_1|$ and parallel vector potential $\left|A_{1\parallel}\right|$ as function of the parallel coordinate z for four binormal wavenumber $\hat{k}_y$ at the pedestal top position for the three discharges.

4.3. Detailed analysis of modes at the pedestal top

To complete the comparison of the modes governing the pedestal top position in different plasma regimes, a more detailed analysis is carried out in this section. First, we focus on the calculation of sub-dominant modes, which are likely to be destabilized due to the strong driving logarithmic gradients in the pedestal region. Next, a more quantitative distinction of the most unstable modes will be made using the concept of fingerprints [76]. Following this, a targeted sensitivity scan will be conducted to quantify the KBM threshold in the three discharges. Finally, the role of electromagnetic effects and impurities will be investigated.

4.3.1. Sub-dominant modes

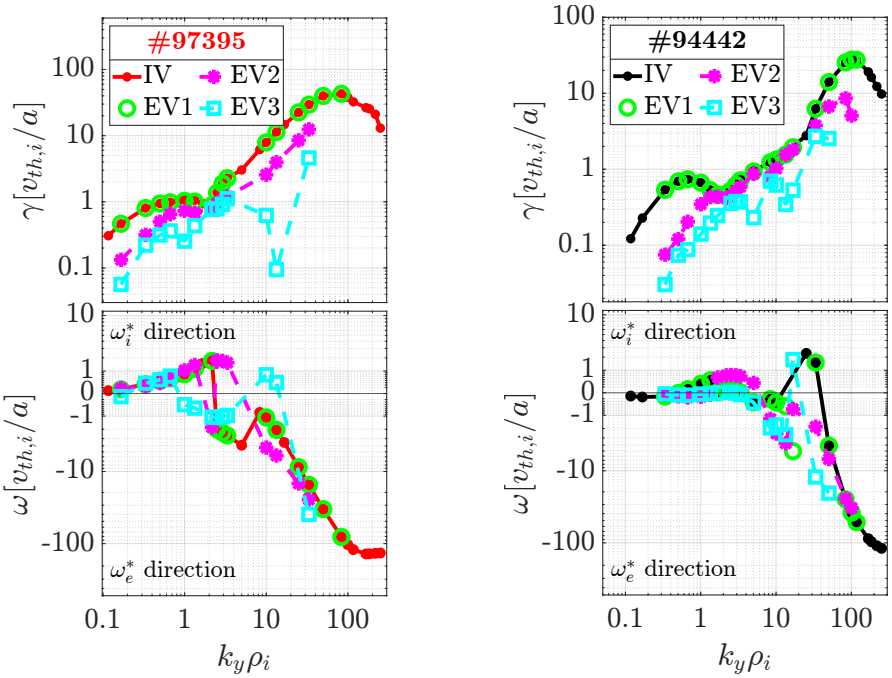

(a) #97395-Type-I ELMs (b) #94442-BSE

Figure 4.4.: Linear growth rates γ and mode frequency ω as function of the binormal wavenumber $\hat{k}_y$ for the type-I ELM #97395 and BSE #94442 discharges. The sub-dominant modes are obtained with eigenvalue computation.

To complete the stability characterization, eigenvalue simulations were performed to resolve the sub-dominant modes at the pedestal top positions. This analysis provides additional insights into the instabilities competing for turbulence development. The spectra of discharges #97395-Type-I ELM and #94442-BSE are shown in Fig. 4.4.

At the ion-scale of the type-I ELM discharge, we observe two sub-dominant branches with positive frequencies and growth rates that roughly peak at the same $\hat{k}_y$ as the most unstable modes. These results indicate that the ion-scale turbulence will be determined by the interplay of several strongly driven modes. In contrast, for the BSE regimes, the

ion-scale sub-dominant modes exhibit much lower growth rates compared to the most unstable mode and peak at slightly higher $\hat{k}_y$. Additionally, the jump in frequencies observed for the most unstable modes at $\hat{k}_y \sim 1.5-2.0$ corresponds to different instability branches, whose spectrum is completed by calculating the sub-dominant modes.

Lastly, it is worth noting that even the two sub-dominant modes identified here do not reveal tearing-parity mode structures, so the presence of MTMs in these cases cannot be confirmed. This suggests that other mechanisms may be responsible for the electron heat transport at the pedestal top of these discharges.

4.3.2. Modes identification: transport fingerprints and normalized parallel electric field

To obtain a quantitative classification and comparison of the modes dominating at the pedestal top of the different plasma regimes, we employ the concept of transport fingerprints [76] as well as compute the normalized parallel electric field $\hat{E}_\parallel$ [91, 176]. The first analysis involves calculating appropriate ratios of the *effective* particle diffusivity D_σ and heat diffusivity χ_σ associated with each $\hat{k}_y$ mode, thereby providing insights into the transport contributions of each mode in the various channels. These features are indeed a direct consequence of the physical mechanisms defining the modes. The second quantity, $\hat{E}_\parallel$, indicates the departure from a predominantly electrostatic mode with $\hat{E}_\parallel = 1$, towards a kinetically modified *ideal* ballooning mode, where $\hat{E}_\parallel \sim 0$ [82, 177].

From GENE linear simulations, the *effective* particle and heat diffusivities for a plasma species σ are calculated as

$$D_\sigma = \frac{\Gamma_\sigma}{n_\sigma} L_{n_\sigma} \qquad \text{and} \qquad \chi_\sigma = \frac{Q_\sigma}{n_\sigma T_\sigma} L_{T_\sigma}$$

where the particle and heat fluxes Γ_σ and Q_σ are defined in Appendix A. The parallel electric field $E_\parallel = -\boldsymbol{\nabla}_\parallel \phi - \partial A_\parallel \big/ \partial t$ as a function of the coordinate along the field line z is computed from $\hat{\phi}(z)$ and $\hat{A}_\parallel(z)$ and then normalized as [91]

$$\hat{E}_\parallel = \frac{\left\langle \left| -\frac{\partial_z \hat{\phi}}{\sqrt{g_{zz}}} + i\omega \hat{A}_\parallel \right| \right\rangle_z}{\left\langle \left| \frac{\partial_z \hat{\phi}}{\sqrt{g_{zz}}} \right| \right\rangle_z + \left\langle \left| i\omega \hat{A}_\parallel \right| \right\rangle_z} \leq 1$$

where $\langle \dots \rangle_z$ indicates the field-line average of the ballooning structures of the fields (see Appendix A for the definition), ω is the complex mode frequency, and g_{zz} is the metric tensor.

The typical values of these quantities for *standard* microinstabilities are summarized in Table 4.1. It is important to note that microinstabilities driven by strong gradients may exhibit characteristics of different *standard* modes, leading to their classification as *hybrid* modes.

Table 4.1.: Properties of *standard* microinstabilities: kinetic ballooning mode (KBM), microtearing mode (MTM), ion temperature gradient (ITG) mode, trapped electron mode (TEM), and electron temperature gradient (ETG) mode. The *transport fingerprints* (derived from a combination of analytical arguments and numerical simulations as reported in Ref. [76]), and normalized parallel electric field $\hat{E}_{\parallel}$ are defined in the text.

	Fingerprints		$\hat{E}_{\parallel}$
	χ_i/χ_e	D_e/χ_e	
KBM	~ 1	$\sim 2/3$	< 1
MTM	~ 0	~ 0	< 1
ITG	≥ 1	$-0.2 - 1$	~ 1
TEM	≥ 1	$-0.2 - 1$	~ 1
ETG	~ 0	~ 0	~ 1

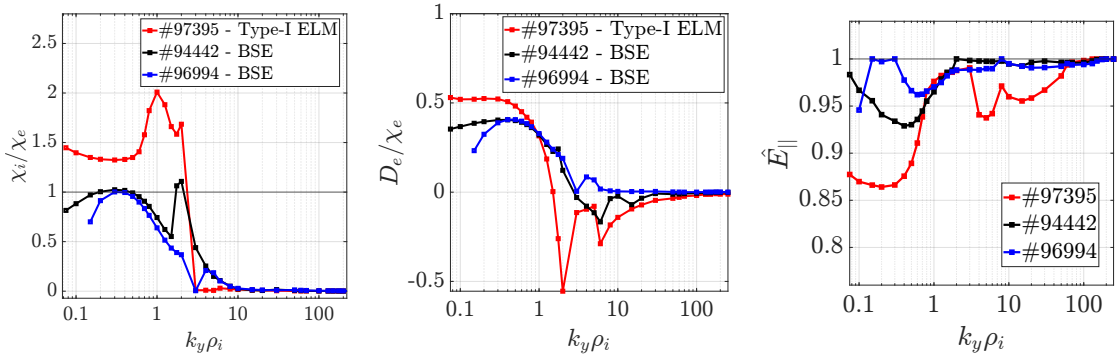

Figure 4.5.: (a-b) Transport fingerprints and (c) normalized parallel electric field of the most unstable modes at the pedestal top position of the three discharges.

The transport fingerprints and normalized parallel electric field values for each mode at the pedestal top positions of the three discharges are shown in Fig. 4.5.

First, it is noted that the fingerprints are very similar for the modes in the two BSE regimes. Specifically, at the ion-scale up to $\hat{k}_y \sim 1$, the modes exhibit $\chi_i/\chi_e \sim 0.6 - 1$ and $D_e/\chi_e \sim 0.3$, indicating a relative effectiveness in transporting electron heat compared to ion heat, along with a non-negligible contribution to particle transport. Scans of the driving parameters (not shown for brevity) indicate that these modes are driven by $1/L_{T_i}$ and $1/L_{T_e}$, are slightly stabilized by $1/L_{n_e}$, and are strongly destabilized by increasing T_e/T_i, which is a threshold parameter for ITG modes. In summary, these modes have been identified as hybrid TEM-ITG. Interestingly, the values of $\hat{E}_{\parallel}$ for the ion-scale modes slightly deviate from unity, suggesting a small departure from being purely electrostatic.

The ion-scale modes in the type-I ELM regime show different fingerprints. Specifically,

χ_i/χ_e is consistently above unity, reaching $\chi_i/\chi_e = 2$ at $\hat{k}_y = 1$, with a corresponding drop in D_e/χ_e and an increase in $\hat{E}_{\parallel}$, indicating a more electrostatic nature. However, the modes around $\hat{k}_y \sim 0.2$ reach $\hat{E}_{\parallel} \sim 0.86$, suggesting a significant departure from purely electrostatic behavior towards kinetic ballooning modes. These characteristics, along with scans of the driving parameters (not shown for brevity), suggest that these are hybrid ITG-KBM and ITG modes.

Finally, for the electron-scale modes starting from $\hat{k}_y \sim 3$, typical characteristics of ETG modes are observed: the fingerprints indicate that transport is predominantly in the electron heat channel χ_e compared to ion heat χ_i and particle transport D_e, while the values of $\hat{E}_{\parallel} \sim 1$ confirm their electrostatic nature.

4.3.3. Kinetic-ballooning modes threshold: scan $(\beta_e, 1/L_{T_i})$

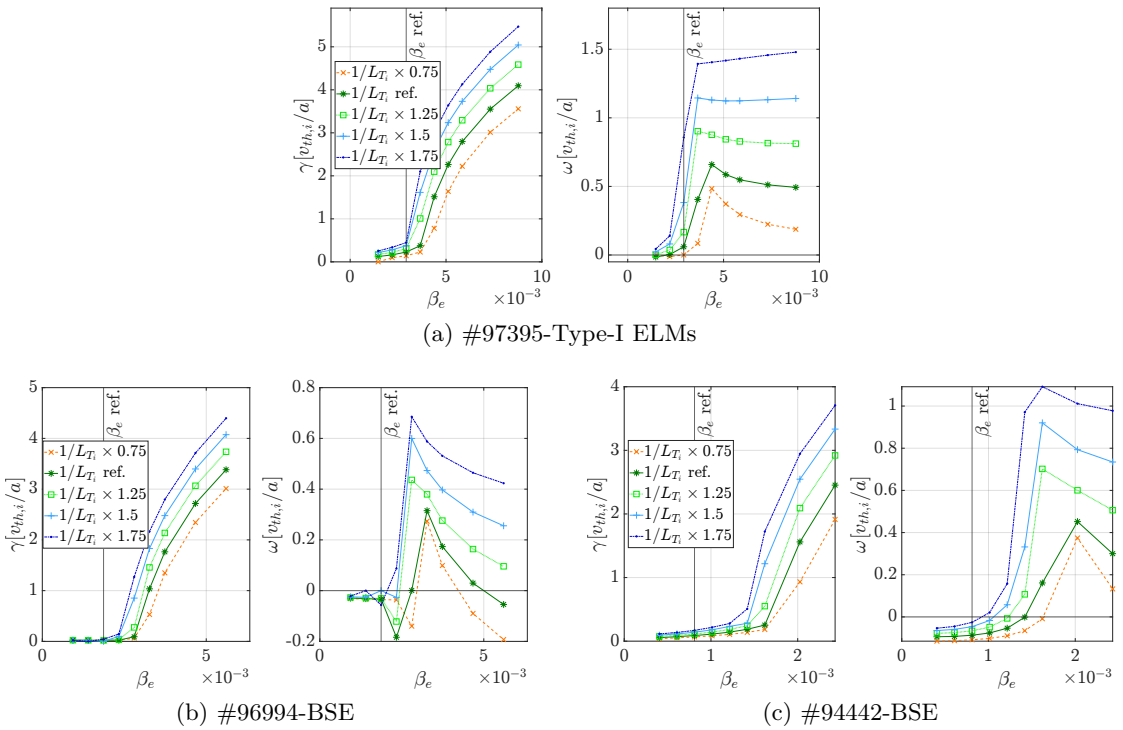

(a) #97395-Type-I ELMs

(b) #96994-BSE

(c) #94442-BSE

Figure 4.6.: Linear growth rate γ and real frequency ω spectra as a function of β_e and $1/L_{T_i}$ for the $\hat{k}_y = 0.1$ mode at the pedestal top of the three discharges. The vertical lines indicate the experimental reference β_e values.

As noted above, one of the main differences in the stability of the two regimes is the presence of KBMs around the pedestal top in discharge #97395-Type-I ELMs, while the BSE regimes are dominated by hybrid ITG-TEM modes. Given the prominent role attributed to KBM-driven transport in the pedestal region [124, 178], we now focus on evaluating the linear KBM threshold. For this purpose, a double scan in the KBM driving parameters $(\beta_e, 1/L_{T_i})$ is conducted over the ranges $\beta_e = [0.5, 0.75, 1.0, 1.25, 1.5, 1.75, 2.0, 2.5, 3.0]\beta_{e,\text{ref}}$ and $1/L_{T_i} = [0.75, 1, 1.25, 1.5, 1.75]1/L_{T_i,\text{ref}}$, using pedestal top parameters and at $\hat{k}_y = 0.1$. The resulting growth rate γ and real frequency for the three discharges

are shown in Fig. 4.6. KBM destabilization is identified by a simultaneous increase in the growth rate and a jump to high, positive real frequencies [176].

The analysis for discharge #97395-Type-I ELMs in Fig. 4.6a reveals that KBM destabilization occurs within a parameter range compatible with experimental uncertainties. Indeed, at the nominal $1/L_{T_i}$, a *pure* KBM appears when β_e is increased by only 50% above the nominal value. Additionally, with a 25% increase in $1/L_{T_i}$ and in β_e, a KBM appears. A different scenario is observed for the two BSE discharges, where the KBM threshold in β_e requires, for the highest $1/L_{T_i}$ tested (i.e., 75% above the nominal value), an increase of at least 50% over the nominal value, making KBM destabilization not compatible within the experimental uncertainties. Moreover, the mode branch preceding KBM destabilization is characterized by marginally positive real frequencies in discharge #97395-Type-I ELMs, whereas a clearly negative frequency branch dominates in both BSE discharges. In general, and consistent with theoretical expectations, the KBM threshold in β_e decreases as $1/L_{T_i}$ increases. The absence of KBM destabilization in the BSE regimes can thus be attributed to the lower β_e observed, due to the lower density at the pedestal top in these regimes.

In conclusion, we find that the KBM threshold in the BSE regimes, unlike in the type-I ELM regime, is somewhat beyond the uncertainty levels associated with the driving parameters (β_e and $1/L_{T_i}$). This suggests that in BSE regimes, KBM-induced transport is not the primary mechanism, indicating instead that transport driven by hybrid TEM-ITG modes as main candidate. A detailed investigation of the turbulence driven by these modes will be the focus of the next chapter.

4.3.4. The impact of electromagnetic effects

We are now interested in characterizing the role played by electromagnetic (EM) effects induced by the nominal β_e across all scales. To this end, the linear spectra for the three discharges at the pedestal top positions with the nominal β_e values (EM) are compared with those obtained in the electrostatic limit (ES_l), i.e., by setting $\beta_{\mathrm{ref}} = 10^{-5}$ and neglecting the parallel magnetic field fluctuations $B_{1\parallel}$. The results are shown in Fig. 4.7.

Focusing first on the ion-scale modes in the range $0.1 \lesssim \hat{k}_y \lesssim 2.0$, a similar effect is observed across the three discharges. The largest scale modes, at $\hat{k}_y \lesssim 0.4$, are destabilized by electromagnetic effects. Indeed, the previous analysis in Fig. 4.7 also found a slightly destabilizing role of β_e on the instability at $\hat{k}_y = 0.1$ before reaching the KBM threshold. On the other hand, for $\hat{k}_y > 0.4$, around the growth rate peaks, an electromagnetic stabilization occurs. This mechanism is consistent with the electromagnetic stabilization of ITG and TEM modes [114, 176, 179, 180].

Regarding electron scales at $\hat{k}_y > 2.0$, EM effects have a negligible impact on discharges #97395-Type-I ELMs and #94442-BSE, mainly affecting the real frequency of toroidal-ETG branches in the range $3.0 \lesssim \hat{k}_y \lesssim 6.0$. However, for discharge #96994-BSE, EM effects play a dual role on the toroidal-ETG branch: reducing the growth rates and modifying the real frequency. Notably, the peak growth rates for the three discharges, occurring around $\hat{k}_y \sim 100$, correspond to slab-ETG modes, on which EM effects are negligible.

We have thus seen that linear electromagnetic effects do not determine the destabilization of electromagnetic modes such as the MTMs. The main effect can be summarized

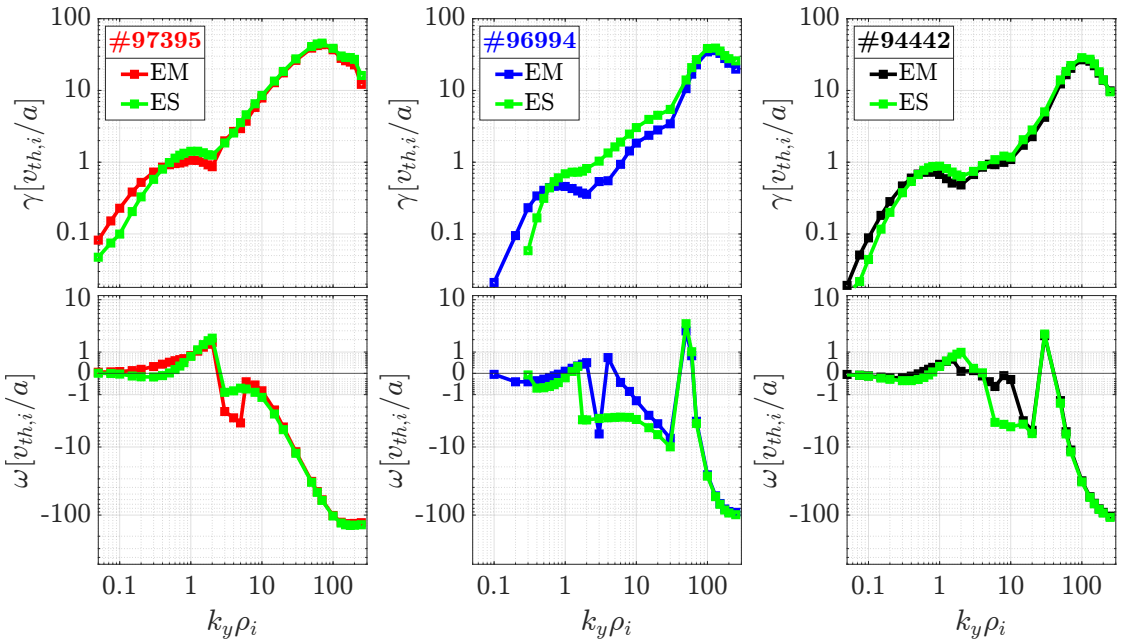

(a) #97395-Type-I ELMs (b) #96994-BSE (c) #94442-BSE

Figure 4.7.: Linear growth rates γ and real frequency ω as function of the binormal wavenumber $\hat{k}_y$ at the pedestal top of the three discharges: reference input parameters (EM) are compared with electrostatic-limit (ES_l).

as a slight destabilization of the largest scale modes and the stabilization of ITG modes, with a negligible role in the most unstable slab-ETG modes. In the next chapter, an extensive analysis will be dedicated to assessing the role played by EM effects in the nonlinear regime.

4.3.5. The impact of impurities

Particular attention has been dedicated to the characterization of the role played by impurities, representing one of the main differences between the type-I ELMs regime and the BSE regimes. As discussed in Chapter 2, impurities reach a higher concentration in the BSE regimes (for #94442, $Z_{\mathrm{eff}} = 3.1$, and for #96994, $Z_{\mathrm{eff}} = 2.4$, see Table 2.3) compared to the type-I ELMs regime ($Z_{\mathrm{eff}} = 1.4$). Generally, due to the proximity of the material walls to the plasma edge, impurity concentration can be significantly higher than in the plasma core, and thus their role in turbulent transport processes must be investigated. Impurities can specifically modify the linear modes through several mechanisms, such as ion dilution, inter-species collisions, or resonant kinetic effects. In particular, in Appendix B, the impact of kinetic impurity species on ITG and adiabatic ions on ETG is analytically studied. We will now proceed to evaluate the impact of impurities on the linear spectra for the three discharges.

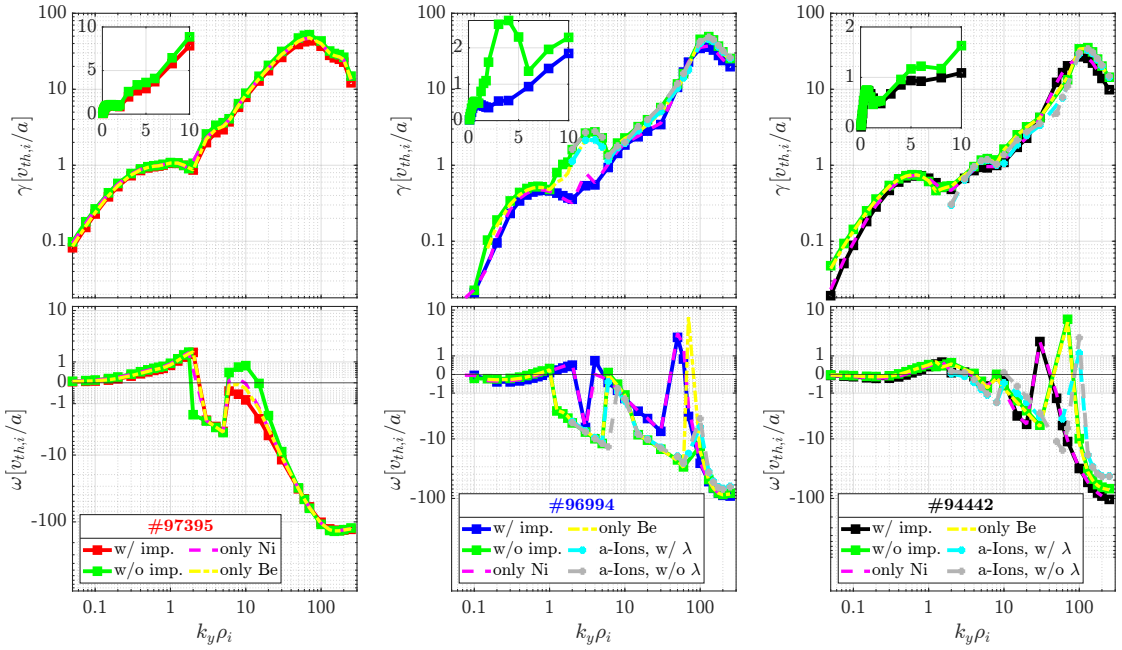

(a) #97395-Type-I ELMs (b) #96994-BSE (c) #94442-BSE

Figure 4.8.: Linear growth rates γ and real frequency ω as function of the binormal wavenumber $\hat{k}_y$ at the pedestal top of the three discharges. Spectra with reference input parameters (w/ imp.) are compared with spectra obtained: without kinetic impurities (w/o imp.), including only one kinetic impurity (only Ni or only Be), and for BSE discharges, electron-scale (from $\hat{k}_y \sim 2.0$) simulations with adiabatic ions (a-Ions) with/without $\lambda = Z_{\text{eff}}T_e/T_i$ parameter.

First, the impact of impurities on the instability spectra was assessed by conducting simulations without including impurities as kinetic species, and ensuring quasi-neutrality (see Sec. 2.2) by setting the deuterium density equal to the electron density. The spectra of growth rate and real frequency with impurities (w/ imp.) and without impurities (w/o imp.) are compared in Fig. 4.8 for the three discharges.

For discharge #97395-Type-I ELMs, we observe that due to their low concentration, impurities have a weak impact on the spectra, stabilizing the growth rates at all scales by approximately 10–15%. Additionally, with impurities included, the ETG branch starts around $\hat{k}_y \sim 3$, whereas without impurities, it starts around $\hat{k}_y \sim 2$, indicating an influence on the toroidal-ETG threshold. Finally, the presence of impurities also affects the frequency of slab-ETG modes in the range $7 \lesssim \hat{k}_y \lesssim 20$.

Turning our attention to the instability spectra in the BSE regimes, we observe that impurities play a significant role, especially for discharge #96994. Impurities have a stabilizing effect across all scales, reducing instability growth rates by at least 20%. The most significant impact is the stabilization of the toroidal-ETG branch in the range $2 \lesssim \hat{k}_y \lesssim 7$ for discharge #96994-BSE, leaving a positive frequency mode as the most unstable. The stabilizing impact of impurities on ETG modes has also been reported in Ref. [181]. It should also be noted that kinetic impurity effects on mode destabilization

can be expected in this range of binormal wavenumbers $2 \lesssim \hat{k}_y \lesssim 6$. For the main ions, finite Larmor radius (FLR) effects in the resonant response of the distribution function, represented by the Bessel function $J_0(k_\perp \rho_\sigma) \sim 1/\sqrt{k_\perp \rho_\sigma}$, make the adiabatic response a good approximation. However, for impurities, FLR effects do not cancel their response as $\rho_e < \rho_Z = (\sqrt{A_Z}/Z_Z)\rho_i < \rho_i$, where for Be, $\sqrt{A_{\mathrm{Be}}}/Z_{\mathrm{Be}} \sim 0.75$, and for Ni, $\sqrt{A_{\mathrm{Ni}}}/Z_{\mathrm{Ni}} \sim 0.27$, leading to a deviation from adiabaticity.

For the discharges in BSE regimes, spectra including only the Ni impurity (shown in magenta) are also presented, demonstrating that including Ni alone yields spectra similar to those with four species, while including only Be (in yellow) is not sufficient, resulting in spectra similar to those without impurities. This result justifies the setup of ion-scale $0 < \hat{k}_y < 1.41$ nonlinear simulations presented in the next chapter with three kinetic species, only retaining the Ni impurity.

Given the prominent role played by impurities on the toroidal ETG branches in the range $2 \lesssim \hat{k}_y \lesssim 7$ in BSE regimes, to further elucidate the underlying physical mechanism, and specifically to further determine if kinetic impurities are decisive, additional electron-scale simulations $\hat{k}_y > 2$ were conducted assuming adiabatic ions (for details, see Appendix B). In GENE, the adiabatic ion approximation modifies the Poisson equation, which becomes [151, 172]

$$\phi_1 = \frac{\pi Z_e \hat{n}_{0e} \int \mathrm{d}\hat{v}_\parallel \mathrm{d}\hat{\mu}\, J_0 \left(\frac{v_{Te}}{\Omega_e} k_\perp \sqrt{\mu B} \right) \hat{g}_{1e}}{k_\perp^2 \lambda_D^2 + \frac{\hat{n}_{0e}}{\hat{T}_{0e}} \left[\lambda + 1 - \Gamma_0 \left(\frac{T_e m_e k_\perp^2}{B^2} \right) \right]} \tag{4.1}$$

where the hat $\hat{\cdot}$ indicates normalized quantity (see Appendix A), $\hat{g}_{1e}$ is a combined modified perturbed distribution function that includes a term with $\hat{A}_{1\parallel}$, $\lambda_D = \sqrt{B_{\mathrm{ref}}^2/(4\pi c^2 n_{\mathrm{ref}} m_{\mathrm{ref}})}$ is the Debye length, $\Gamma_0(x) = I_0(x)e^{-x}$ with I_0 being the modified Bessel function of the first kind, and $\lambda = Z_{\mathrm{eff}} T_e/T_i$ is the parameter determined by the adiabatic approximation of ion species (assuming all ions have the same temperature). Note that for a pure hydrogen plasma with $T_e = T_i$, $\lambda = 1$. The effect of this parameter directly influences the feedback loop of the instability by decreasing the perturbed electrostatic potential response resulting from the electron density perturbation. Therefore, an increase in this parameter, determined by impurities via Z_{eff} and the temperature ratio T_e/T_i, is expected to weaken the ETG instabilities (see Appendix B) and the resulting turbulence.

In our case, at the pedestal top, the values are: for discharge #96994-BSE $Z_{\mathrm{eff}} = 2.4$ and $T_e/T_i = 0.53$, determining $\lambda = 1.27$, and for discharge #94442-BSE $Z_{\mathrm{eff}} = 3.1$ and $T_e/T_i = 0.44$, resulting in $\lambda = 1.36$. Note that the reduced temperature ratio, typical of this regime, partially compensates for the higher effective charge, leading to a slight increase of about 30% in λ compared to pure hydrogen. Additionally, the effect induced by Z_{eff} has been included in the collision operator, modifying the collision frequency [141].

The objective is to test whether modeling impurities through the inclusion of these effects is sufficient to retrieve the full-physics spectra. If not, the results would suggest a significant role of kinetic effects associated with kinetic impurities. The instability spectra for the BSE regimes are shown in Fig. 4.8, including and excluding the parameters λ and Z_{eff} (w/ λ and w/o λ).

Looking at the instability spectrum for discharge #96994-BSE, we observe that none of the models excluding kinetic impurities can capture the strong stabilization of the

toroidal-ETG branch in the wavenumber range $1 \lesssim \hat{k}_y \lesssim 6$. These results suggest that the impurity-induced stabilization mechanism on ETG is related to kinetic effects. For the ETG branches at the largest wavenumbers $\hat{k}_y > 7$, all models show the same trend and growth rate peak, while the mode frequencies are modified by the presence of kinetic impurities. Furthermore, the inclusion of the parameter λ results, as expected, in a reduction of all the ETG branch growth rates.

Turning to discharge #94442-BSE, we also observe the presence of the toroidal-ETG branch in the range $4 \lesssim \hat{k}_y \lesssim 7$, although much less pronounced than in the previous case. We observe the same trend for the slab-ETG branches, where the growth rate trends and peak are well captured by the models with adiabatic ions, while the mode frequencies are shifted. Here again, the inclusion of the parameter λ leads to a reduction in the ETG growth rate. Based on these results, it seems reasonable to conduct turbulence simulations driven by slab-ETG modes using the adiabatic ion approximation. These simulations will be presented in the next chapter.

As a final investigation, the role of the Debye shielding effect in the Poisson equation, represented by the term $k_\perp^2 \lambda_D^2$ in the denominator of Eq. 4.1, is compared in Fig. 4.9 by excluding this term. The wavelengths corresponding to the Debye length, $k_D \rho_i = 2\pi/\hat{\lambda}_D$, are shown as vertical lines. It is evident that the decay of the slab-ETG branches is determined by the inclusion of this effect [96]. Interestingly, a stabilizing effect when including the Laplacian is also observed at mid-range scales $5 < \hat{k}_y < 10$ for the two BSE discharges. This is suggested to be due to the extension of mode structures along the field line through the term $k_\perp^2$.

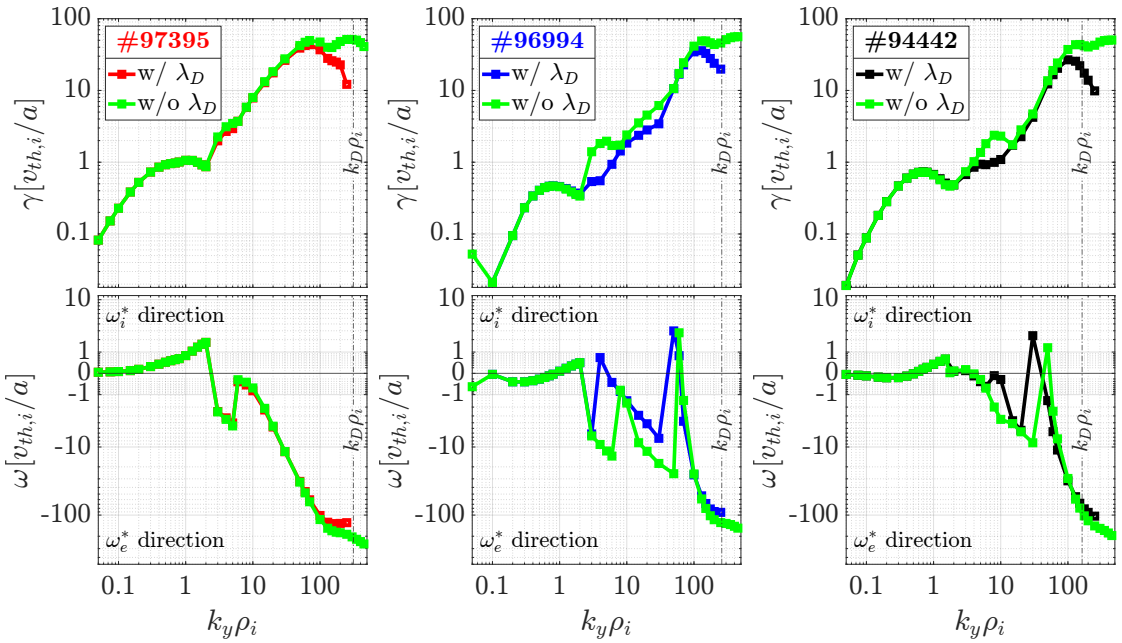

(a) #97395-Type-I ELMs (b) #96994-BSE (c) #94442-BSE

Figure 4.9.: Linear growth rates γ and real frequency ω as function of the binormal wavenumber $\hat{k}_y$ at the pedestal top of the three discharges: reference input parameters (w/ λ_D) are compared with neglecting the laplacian in the Poisson equation (w/o λ_D).

4.4. Linear insights for the importance of non-linear mechanisms

To conclude this chapter, before proceeding to the study of the nonlinear regime, some criteria derived from linear results that provide insights into the role of nonlinear mechanisms will be evaluated. First, the equilibrium shearing rate will be compared with the linear spectra to assess the stabilizing effect that can be expected nonlinearly (see Sec. 1.5.2 for further discussion). Second, since nonlinear simulations that include both ion and electron scales are not the focus of this thesis, the validity of scale separation will be tested.

4.4.1. Shearing rate comparison with linear spectra

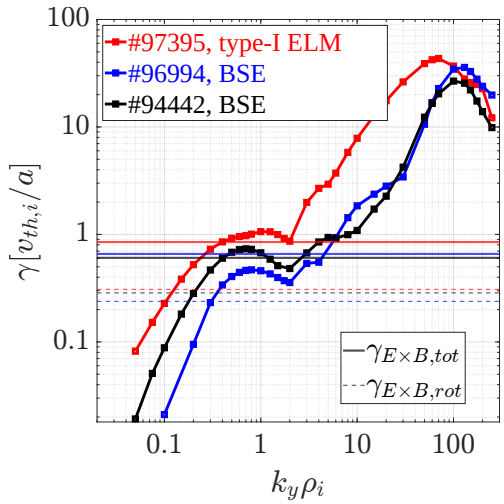

Figure 4.10.: Linear growth rates γ as function of the binormal wavenumber $\hat{k}_y$ at the pedestal top of the three discharges. The value of the total shearing rate $\gamma_{\boldsymbol{E}\times\boldsymbol{B},tot}$ (solid) and the one only due to the toroidal rotation $\gamma_{\boldsymbol{E}\times\boldsymbol{B},rot}$ (dashed) are shown as horizontal lines for comparison.

The spectra of growth rates at the pedestal top position for the three discharges are compared with the equilibrium $\boldsymbol{E}\times\boldsymbol{B}$ shearing rates in Fig. 4.10. This comparison allows for the evaluation of the heuristic Waltz criterion [35, 36, 182], which states that effective turbulence suppression can be expected when the $\boldsymbol{E}\times\boldsymbol{B}$ shearing rate is comparable to the maximum growth rate of the instability γ_{peak}. Specifically, both the total shearing rate due to toroidal rotation and the diamagnetic term, $\gamma_{\boldsymbol{E}\times\boldsymbol{B},\text{tot}}$, and the shearing rate due solely to toroidal rotation, $\gamma_{\boldsymbol{E}\times\boldsymbol{B},\text{rot}}$, are shown as horizontal lines (see Chapter 2 for details on these terms).

For all three discharges, we observe that while the shearing rate due only to toroidal rotation remains significantly below the peak growth rate of ion-scale microinstabilities, including the diamagnetic term provides a substantial contribution, bringing the total shearing rate closer to the peak values. Specifically, at ion scales up to $\hat{k}_y \sim 2$, both discharge #97395-Type-I ELMs and discharge #94442-BSE exhibit ratios of $\gamma_{\boldsymbol{E}\times\boldsymbol{B},\text{tot}}/\gamma_{\text{peak}} \sim 0.8$, while discharge #96994-BSE shows a ratio of $\gamma_{\boldsymbol{E}\times\boldsymbol{B},\text{tot}}/\gamma_{\text{peak}} \sim 1.4$. These values suggest a non-negligible stabilizing impact of the equilibrium $\boldsymbol{E}\times\boldsymbol{B}$ shear and confirm the importance of including the diamagnetic term when evaluating the radial electric field.

Conversely, at electron-scales, the shearing rate values remain well below the peak growth rates, indicating a negligible stabilizing role at these scales and highlighting the differing effectiveness of shear stabilization depending on the spatial scale considered. In the next chapter, targeted nonlinear simulations will be performed to assess the impact of equilibrium $\boldsymbol{E}\times\boldsymbol{B}$ shear on turbulence saturation more comprehensively.

4.4.2. Multi-scale criterion

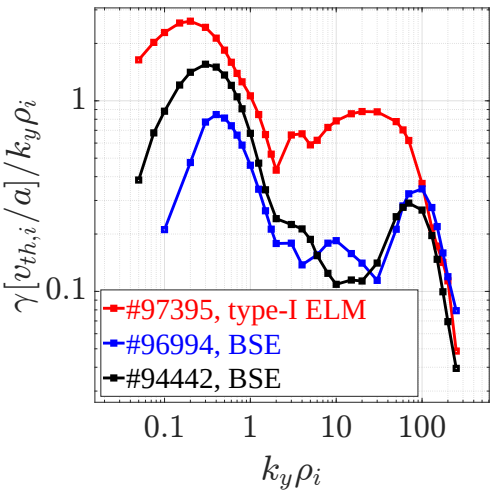

Figure 4.11.: Linear $\hat{k}_y$ spectra of $\gamma/k_y[v_{\mathrm{th},i}/a\rho_i]$ at the pedestal top for the three discharges.

We now aim to assess whether the approximation of scale separation between ion and electron scales—i.e., neglecting the cross-scale coupling between these scales—is adequate for determining turbulence saturation levels. It is important to note that multiscale turbulence simulations have shown that cross-scale interactions can influence turbulent transport saturation, particularly when ion-scale modes are close to marginal stability, for instance, through equilibrium flow stabilization [183] or electromagnetic stabilization [184]. These mechanisms will prove to be relevant in the context of this thesis, as will be found in the next chapter. Certainly, these are not the only possible mechanisms. Ion-scale turbulent eddies driven by ITG could also non-trivially impact the electron-scale ETG-driven eddies, for example, through shearing effects [185, 186]. Additionally, electron-scale eddies could undergo an inverse cascade process, thereby influencing ion-scale dynamics. Recent work on the interplay of $\boldsymbol{E}\times\boldsymbol{B}$ flow shearing with multi-scale turbulence has also demonstrated the destabilizing role of low flow shear values on ETG-driven turbulence, thereby determining an increase in electron transport compared to the absence of shearing rate [187].

Several studies [188–190] have proposed that the impact of ETG turbulence is significant in determining electron heat transport if $(\gamma/\hat{k}_y)_{\text{high-}k} > (\gamma/\hat{k}_y)_{\text{low-}k}$, where high(low)-$k$ represents electron(ion)-scale modes. The spectra of $\gamma/\hat{k}_y$ for the discharges at the pedestal top positions as a function of the binormal wavenumber $\hat{k}_y$ are shown in Fig. 4.11. Specifically, for discharge #97395-Type-I ELMs, we have $(\gamma/\hat{k}_y)_{\text{low-}k}/(\gamma/\hat{k}_y)_{\text{high-}k} \sim 3.0$, and for discharges #96994/#94442-BSE, we have $(\gamma/\hat{k}_y)_{\text{low-}k}/(\gamma/\hat{k}_y)_{\text{high-}k} \sim 2.5/5.3$, respectively. Thus, in all cases, the criterion for scale separation is satisfied, suggesting the validity of this approximation. Consequently, in the next chapter, ion and electron-scale simulations will be conducted separately to evaluate the turbulence saturation mechanisms and levels.

5. Turbulent transport at the pedestal top

Contents

5.1. Ion-scale turbulence: electromagnetic effects vs. equilibrium $\boldsymbol{E} \times \boldsymbol{B}$ shear flow . . . 107
5.1.1. Time traces of fluxes . . . 108
5.1.2. Comparison of turbulence regimes: Fourier spectra . . . 112
5.1.3. Assessing the importance of Zonal Flows vs. $\boldsymbol{E} \times \boldsymbol{B}$ flow shear in saturation . . . 113
5.1.4. Heat flux spectra . . . 116
5.1.5. Analysis of cross-phases . . . 118
5.2. Electron-scale turbulence: stiff ETG transport . . . 120
5.2.1. The role of electromagnetic effects and equilibrium $\boldsymbol{E} \times \boldsymbol{B}$ shear flow 122
5.2.2. The impact of adiabatic ions modelled with $\lambda = Z_{\text{eff}} T_e/T_i$ . . . 123
5.2.3. Stiffness study of ETG transport: comparison with experimental transport level . . . 124
5.3. Basic application of quasi-linear theory . . . 125
5.3.1. Quasi-linear expression of fluxes . . . 125
5.3.2. Heat flux spectra comparison: quasi-linear vs. non-linear . . . 130
5.3.3. Heat flux ratio Q_e/Q_i: sensitivity scan to input parameters . . . 132

The stability study around the pedestal top position conducted in the previous chapter revealed key differences between the two ELMy regimes analyzed in this thesis. The results showed that, at the ion-scale, while hybrid ITG-KBM and KBM are dominant in the type-I ELMy discharge, the BSE regimes are dominated by hybrid ITG-TEM. Additionally, weak electromagnetic effects have been found to influence the modes in BSE regimes. At the electron scale, we found that both plasma regimes are dominated by toroidal and slab ETG, the latter extending to very small scales.

The objective of this chapter is to characterize the turbulence regimes driven by the modes linearly found and, in particular, to get insights on the main physical mechanisms affecting turbulence saturation. The analysis will focus on discharge #94442, selected as the reference case for the BSE regime. The chapter is organized as follows: in Sec. 5.1, ion-scale turbulence simulations driven by hybrid ITG-TEM modes are presented, focusing on the interplay between electromagnetic effects and equilibrium $\boldsymbol{E} \times \boldsymbol{B}$ shear flow; in Sec. 5.2, electron-scale turbulence simulations driven by slab ETG modes are presented; in Sec. 5.3 an initial application of quasi-linear models to get turbulence heat flux spectra is discussed and employed for the validation with experimental results. Parts of the results presented in this chapter have been reported in Ref. [165].

Table 5.1.: Set of ion-scale simulations performed at the pedestal top positions.

Discharge	EM/ES$_l$	$\gamma_{\boldsymbol{E}\times\boldsymbol{B}}$
BSE – #94442	EM	0.3
	EM	0.45
	ES$_l$	0.3
	ES$_l$	0.45
Type-I ELMs – #97395	ES$_l$	0.6
	EM	0.6

5.1. Ion-scale turbulence: electromagnetic effects vs. equilibrium $\boldsymbol{E}\times\boldsymbol{B}$ shear flow

As an initial investigation, non-linear simulations have been performed taking into account the ion-scale portion (roughly up to $\hat{k}_y \sim 1.5$) of the linear spectrum discussed in Chapter 4. The analysis of the turbulence regime driven by the strong gradients typical of the pedestal region focused particularly on the impact of key mechanisms in edge turbulence: the electromagnetic effects [116–118, 191, 192], and the equilibrium $\boldsymbol{E}\times\boldsymbol{B}$ shear flow [35, 36]. The turbulence regimes thus obtained will be compared to disentangle the physical mechanisms at play and assess their impact on turbulence saturation.

Simulations setup The set of simulations performed is summarized in Table 5.1. Full electromagnetic (EM) simulations, including the perpendicular $A_{1\parallel}$ and parallel $B_{1\parallel}$ magnetic fluctuations, have been performed using the reference parameters at the ρ_{tor} corresponding to the pedestal top position for discharge #94442-BSE and #97395-type-I ELMs (see Chapter 2 for the input parameters). Specifically, for discharge #94442-BSE, two values of equilibrium $\boldsymbol{E}\times\boldsymbol{B}$ shearing rate, compatible with the experimental values, were tested to evaluate their impact. Note that in all subsequent simulations, the external equilibrium $\boldsymbol{E}\times\boldsymbol{B}$ shearing rate was included from the start of the simulation, at $t = 0$. In fact, tests without including it resulted in a strong increase in fluctuation levels during the initial phase of the simulation, consequently causing a drastic reduction in the adaptive time-step, making the simulation computationally infeasible. To assess the impact of electromagnetic fluctuations, the same simulations were performed in the electrostatic limit (ES$_l$), i.e., by reducing β_{ref} to 0.001% and without including $B_{1\parallel}$ fluctuations.

The simulations were set up according to extensive linear simulations conducted to: firstly, determine the physical terms to consider for including the effects that play a major role (see Chapter 4 for discussion); and secondly, to determine the required numerical grid setup. Thus, the simulations for discharge #94442-BSE consider three kinetic species (electrons, deuterium, and Ni impurity), while for #97395-type-I ELMs, impurities were neglected due to their negligible impact as found in linear analysis. Additionally, collisions were included using the linearized Landau-Boltzmann operator, and rotational effects (centrifugal, Coriolis, and parallel flow shear terms) has been accounted for.

Table 5.2.: Flux-tube resolutions for the non-linear simulations at the ion-scale. The parameters are: number of radial and bi-normal modes, parallel resolution, parallel-velocity resolution, magnetic-moment resolution, radial, bi-normal and velocity domain size.

n_{k_x}	n_{k_y}	n_z	$n_{v_\parallel}$	n_μ	L_x/ρ_i	L_y/ρ_i	$L_{v_\parallel}/v_{T_\sigma}$	$L_\mu/(T_{0\sigma}/B_{\mathrm{ref}})$
512	48	64	48	16	452	209	3.0	9.0

Regarding the numerical grid, targeted linear simulations were performed to optimize the parallel z grid resolution necessary to resolve the lowest $\hat{k}_y$ mode, considered the most challenging to numerically resolve. In this regard, multi-parameter linear scans were performed over the parallel resolution, $n_z = [64, 96, 128]$, parallel hyperdiffusion, `hyp_z` $= [1, 5, 10, 50, 100, 150, 200]$, and redistribution of parallel grid-points, `edge_opt` $= [0, 2, 3]$, to identify the combination of numerical parameters that ensures the ballooning structure of the electric potential, parallel vector potential, and parallel magnetic field without grid-scale oscillations, while also yielding growth rates and real frequencies consistent with the results obtained using the highest resolution and lowest numerical dissipation. We emphasize that for the numerical parameter values $n_z = [64, 95]$, `hyp_z` $= [1, 5, 10, 50]$, and `edge_opt` $= [0, 2, 3]$, only numerical instabilities were obtained, characterized by zig-zag oscillations of the ballooning structures along the field line coordinate z. Instead, once a physical solution is achieved, the ballooning structures result to be consistent across the different numerical settings, with growth rates and real frequencies in excellent agreement, thus suggesting robust numerical solutions. Consequently, a resolution of $n_z = 64$, combined with a poloidal redistribution of grid points concentrating on the outboard mid-plane using `edge_opt` $= 3.0$, and a relatively strong numerical parallel hyperdiffusion `hyp_z` $= 100$, were found to be sufficient and thus selected. Regarding the hyperdiffusion in x and y, the adaptive GyroLES scheme, as implemented in GENE [193], was chosen to mimic energy transfer to smaller, unresolved scales. For the velocity space, no numerical dissipation was included, since the inclusion of collisions already provides physical dissipation. The complete grid resolution for non-linear simulations is reported in Table 5.2. These simulations cover the radial and bi-normal wavenumbers in the range: $\hat{k}_y = 0.03 - 1.41$ (with the lowest corresponding to the toroidal mode number $n \approx 3$) and $\hat{k}_x = 0.013 - 3.5$. A quite large radial domain size L_x was necessary, particularly in the EM simulations, to accommodate the magnetic potential $A_{1\parallel}$ turbulent structures and thus avoid the appearance of radially elongated streamers (as also found in Ref. [119]). At the same time, a high radial resolution n_{k_x} was required to ensure a sufficient number of connected $\hat{k}_x$ modes through the parallel boundary condition (see Eq. 3.15), which encounter fewer connections due to the high magnetic shear $\hat{s}$ typical of the edge.

5.1.1. Time traces of fluxes

The time traces of the turbulent radial electron particle and heat fluxes for the ES$_l$ and EM simulations are shown in Fig. 5.1 for the #97395-type-I ELMy discharge and in Fig. 5.2 for the #94442-BSE discharge.

Focusing on the results obtained for the discharge #97395 with type-I ELMs, we note that in the ES_l case, after a fast-growing linear phase up to $\hat{t} \sim 90$, the time traces of the fluxes reach a robust steady state. In the saturation phase, the heat flux in the ion channel is approximately 65% higher than in the electron channel, and the electron particle flux is very low. These transport flux characteristics are typical of a turbulence regime driven by ITG. For reference, the time-averaged electron and ion heat fluxes in the turbulence-saturated phase are reported in Table 5.3.

On the other hand, the fluxes of the challenging EM simulation at nominal plasma β_e, driven by the ITG-KBM modes, encounter a flux blow-up, reaching unrealistically high values without saturating. This result necessitates further investigation to determine if it is a physical result, e.g., nonzonal transition/high-β runaway [194], or a numerical artifact. Notably, this behavior occurs in the presence of hybrid ITG-KBM modes rather than pure KBM modes in the corresponding linear spectra, suggesting that non-linearly, the threshold in β_e for the strong EM turbulence regime is reduced compared to the linear one. To achieve time-convergent EM simulations, one approach would be reducing the plasma β within an experimental compatible range to assess the distance to the non-linear β threshold for flux blow-up. This is left as future work.

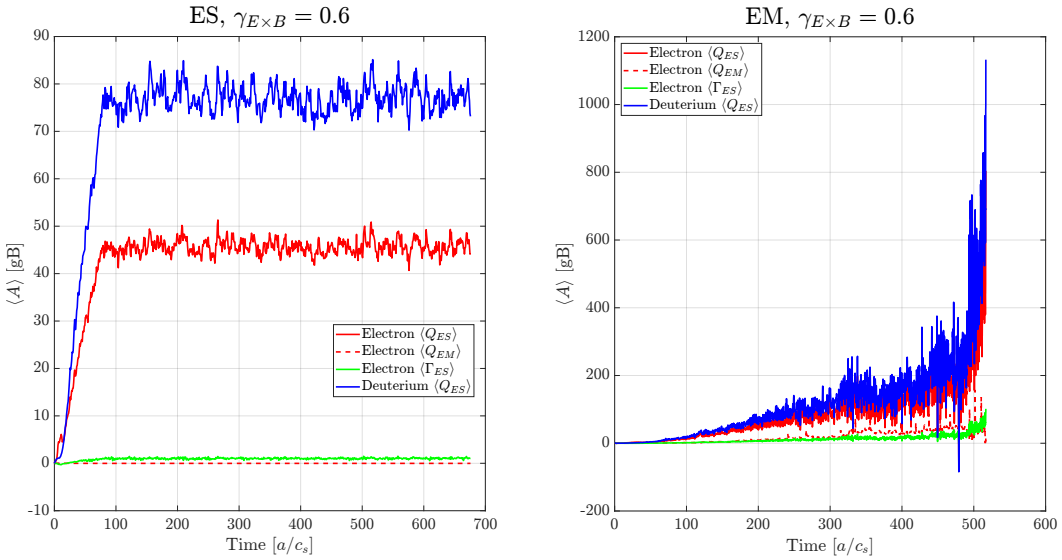

Figure 5.1.: Time traces of electron (red) and ion (blue) heat, and electron particle (green) fluxes in Gyro-Bohm units for the pedestal top parameters of #97395-Type-I ELM discharge. (a) ES_l with $\gamma_{\boldsymbol{E}\times\boldsymbol{B}} = 0.6$. (b) EM with $\gamma_{\boldsymbol{E}\times\boldsymbol{B}} = 0.6$.

For the simulations performed for the #94442-BSE discharge shown in Fig. 5.2, a turbulent saturated state is reached in both the ES_l and EM cases. Comparing the two ES_l cases with different shearing rates $\gamma_{\boldsymbol{E}\times\boldsymbol{B}} = 0.45$, slightly slower growth of the fluxes in the linear phase with the higher shearing rate is observed, consistent with its stabilizing role. Once the turbulence-saturated phase is reached, despite the different shearing rates, a very similar trend for the fluxes is obtained, suggesting a similar turbulence regime. The time-averaged electron and ion heat fluxes are reported in Table 5.3. Overall, the

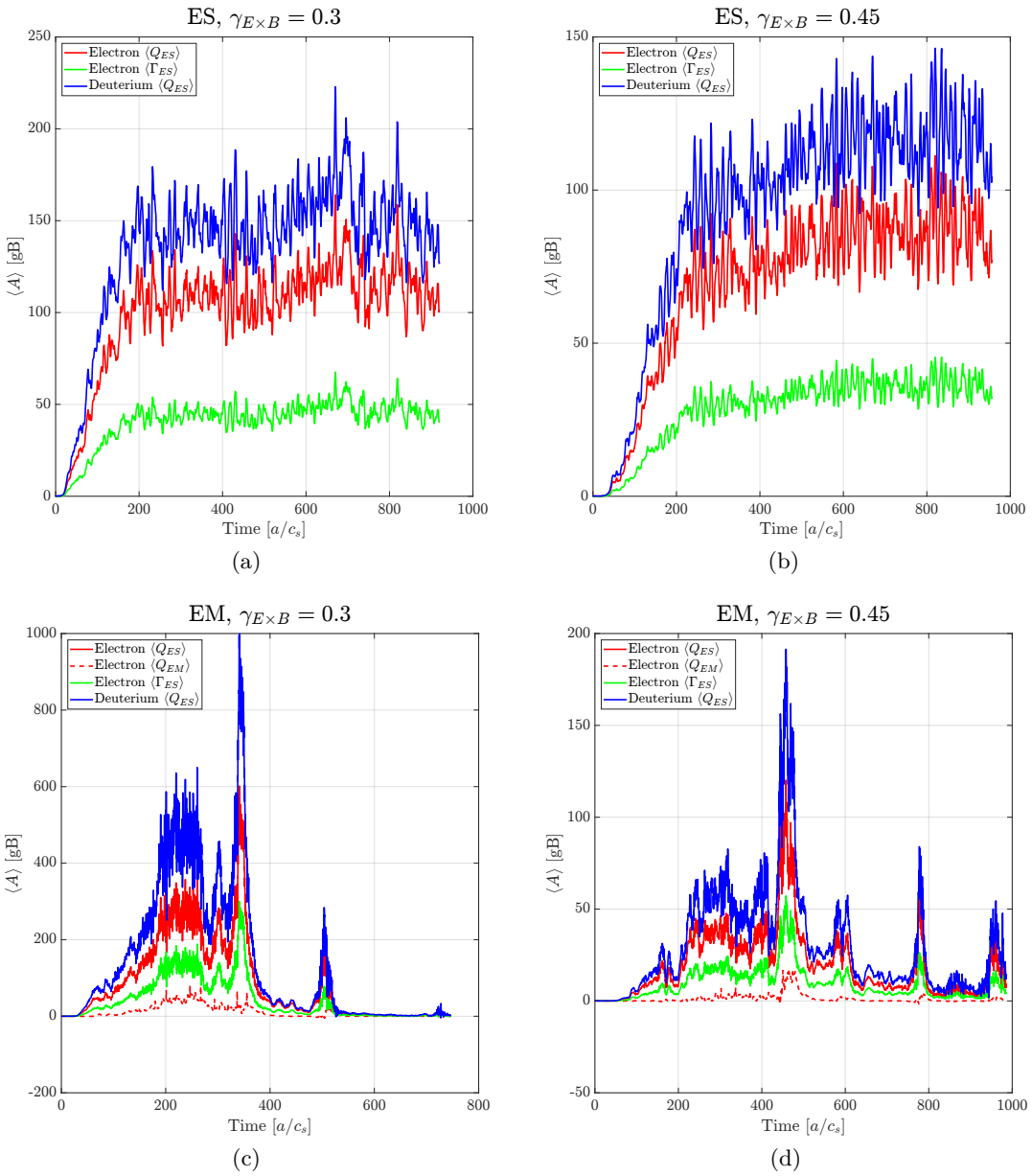

Figure 5.2.: Time traces of electron (red) and ion (blue) heat, and electron particle (green) fluxes in Gyro-Bohm units for the pedestal top parameters of #94442-BSE discharge. (a) ES$_l$ with $\gamma_{\boldsymbol{E\times B}} = 0.3$. (b) ES$_l$ with $\gamma_{\boldsymbol{E\times B}} = 0.45$. (c) EM with $\gamma_{\boldsymbol{E\times B}} = 0.3$. (d). EM with $\gamma_{\boldsymbol{E\times B}} = 0.45$

Table 5.3.: Averaged heat fluxes in the electron Q_e and ion Q_i channels in the time windows corresponding to turbulence saturated phases. For comparison, the experimentally inferred fluxes, calculated from power balance in TRANSP, are reported. Notice: N.C. indicates a not converged simulation. The flux surface area is $V' = 108.27\,\mathrm{m}^2$.

Discharge	EM/ES$_l$	$\gamma_{\boldsymbol{E}\times\boldsymbol{B}}$	time window	Q_e [MW/m^2]	Q_i [MW/m^2]	Q_e/Q_i
#94442	EM	0.3	[650 - 786]	0.037	0.063	0.59
	EM	0.45	[850 - 986]	0.096	0.144	0.67
	ES$_l$	0.3	[700 - 842]	1.105	1.457	0.77
	ES$_l$	0.45	[700 - 884]	0.832	1.117	0.75
	Exp.			0.0192	0.025	0.77
#97395	ES$_l$	0.6	[500 - 675]	0.2336	0.395	0.59
	EM	0.6	N.C.			
	Exp.			0.076	0.062	1.23

main effect of the higher shearing rate is to decrease the flux levels by approximately 25% in all the transport channels.

Compared to the ES$_l$ case of the type-I ELMs discharge, we note that in this case, the saturated ion-heat flux is only about 30% higher than the electron heat flux, and a non-negligible electron particle flux is also obtained. These results are consistent with the underlying modes driving the turbulence, i.e., the hybrid ITG-TEM found in the previous chapter.

Moving to the EM cases, where the nominal value of the plasma beta $\beta = 0.08\%$ is included, a strong effect is observed. Unlike the well-saturated regimes in the ES$_l$ cases, the EM turbulence is characterized by bursty behavior and different turbulence phases. Focusing on the dependence on the equilibrium $\boldsymbol{E}\times\boldsymbol{B}$ shear, we see that in the case with lower shearing rate, $\gamma_{\boldsymbol{E}\times\boldsymbol{B}} = 0.3$, after a linear phase up to $\hat{t} \sim 200$, a turbulence regime characterized by high transport fluxes in all channels is observed. In a second phase, around approximately $\hat{t} \sim 380$, a stabilization mechanism occurs, leading to a strong flux reduction in all channels. A very similar trend is also observed for the EM case with higher $\gamma_{\boldsymbol{E}\times\boldsymbol{B}} = 0.45$, where the electromagnetic stabilization mechanisms taking place in the second phase result in a less pronounced reduction in heat flux. This trend in the fluxes, characterized by intermittent behaviour and strong flux reduction, is reminiscent of the Dimits regime, i.e., turbulence regimes where zonal flows prevail and prevent turbulence from developing [195]. In the following section, the activity of zonal flows in these regimes will be analysed to assess their importance.

The negligible impact of electromagnetic effects observed in the linear simulations (see Sec. 4.3.4) indicates that the nature of the stabilization mechanism is determined by non-linear mechanisms that dominate during an advanced stage of turbulence development.

The time-averaged ion and electron heat fluxes of the set of simulations performed are summarized in Table 5.3, where the experimental fluxes obtained via power balance

calculations are also provided for comparison. For the simulations of discharge #94442-BSE, it is noted that the radial heat fluxes due to the ES_l turbulence regime, for both values of the shearing rate $\gamma_{\boldsymbol{E}\times\boldsymbol{B}}$, significantly exceed experimental values, suggesting that the electrostatic limit is not appropriate for describing the turbulent transport at the pedestal top of BSE regimes. Interestingly, the heat flux levels resulting from the EM turbulence regime are closer to the experimental ones, although still overestimating. In addition, neoclassical transport simulations have been conducted with GENE, revealing a negligible contribution to ion heat transport compared to the turbulent one.

These results suggest that for the pedestal top microturbulence in BSE plasma regimes, stabilization via equilibrium $\boldsymbol{E}\times\boldsymbol{B}$ shear, although essential, is not the dominant mechanism, as the ES_l cases result in fluxes about 50 times higher than the experimental values. Instead, the results obtained from the interplay of EM stabilization with equilibrium $\boldsymbol{E}\times\boldsymbol{B}$ shearing, being in better agreement, highlight the importance of the electromagnetic nature of turbulence affecting the pedestal top region. Additionally, the ambivalent role of the $\boldsymbol{E}\times\boldsymbol{B}$ shear emerges: while in the ES_l simulations a higher shearing rate results in reduced heat fluxes, in the EM case it results in enhanced fluxes.

In what follows, targeted analyses of the two turbulence regimes, ES_l and EM, just described will be conducted to distinguish and better understand the physical mechanisms that govern them.

5.1.2. Comparison of turbulence regimes: Fourier spectra

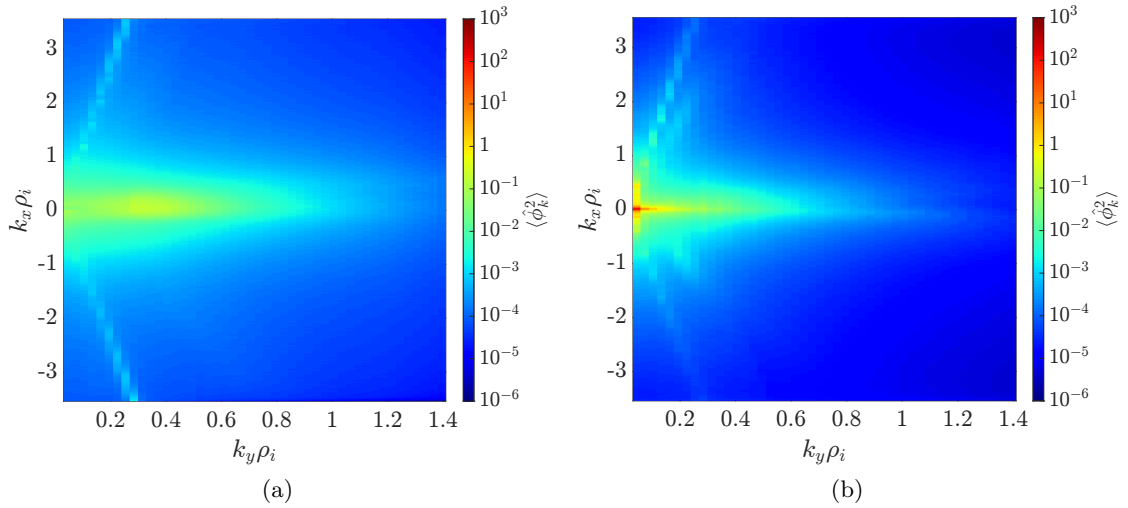

Figure 5.3.: Fourier spectra of field-line averaged, and time averaged electrostatic potential $\phi^2_{\hat{k}_x,\hat{k}_y}$ for discharge #94442-BSE: (a) ES_l case, (b) EM case.

As a first step, to characterize the turbulence regimes of the ES_l and EM simulations for discharge #94442-BSE, the Fourier spectra of the squared electrostatic potential $\phi^2_{\hat{k}_x,\hat{k}_y}$, obtained by performing the field-line average of each mode and time average over the turbulence saturated phases, are compared in Fig. 5.3, without including the zonal modes $\phi_{\hat{k}_x,\hat{k}_y=0}$, which will be analyzed in Sec. 5.1.3. The spectra reveal profound differences

between the ES$_l$ and EM cases. Specifically, the fluctuation spectrum in the ES$_l$ case peaks around $\hat{k}_x = 0, \hat{k}_y \sim 0.3$, typical of electrostatic turbulence driven by ITG modes. In contrast, the EM fluctuation spectrum shows a strong destabilization of mesoscale modes with low-$\hat{k}_y$ and low-$\hat{k}_x$. Interestingly, no large-scale modes were found to be strongly unstable linearly (see Fig 4.7), even at ballooning angles $\hat{k}_{x,0} \neq 0$, suggesting that energy transfer via turbulence drives these modes. Similar results obtained in δf gyrokinetic simulations for edge turbulence have been documented in Ref. [116, 118, 119], where the enhancement of *mesoscale MHD modes* with $\hat{k}_y < 0.1$ was attributed to the mechanism of inverse-cascade energy transfer. Moreover, also in those cases, the large-scale modes that developed did not correspond to the linearly dominant instability and were obtained with plasma β values well below the MHD limit. However, in those cases, the heat transport associated with these modes also increased dramatically, whereas in our cases, the heat spectra (see Sec. 5.1.4) do not peak on these modes. These results indicated the dominance of nonlinear mechanisms in the electromagnetic turbulence regime, suggesting that linear instability modeling alone is insufficient for understanding tokamak edge phenomenology. Additionally, the ES$_l$ turbulence spectrum reveals a broader extension in the $\hat{k}_x$ space compared to the EM spectrum. These distinct features indicate different turbulence regimes in the two cases, highlighting the importance of electromagnetic effects in plasma edge turbulence.

5.1.3. Assessing the importance of Zonal Flows vs. $E \times B$ flow shear in saturation

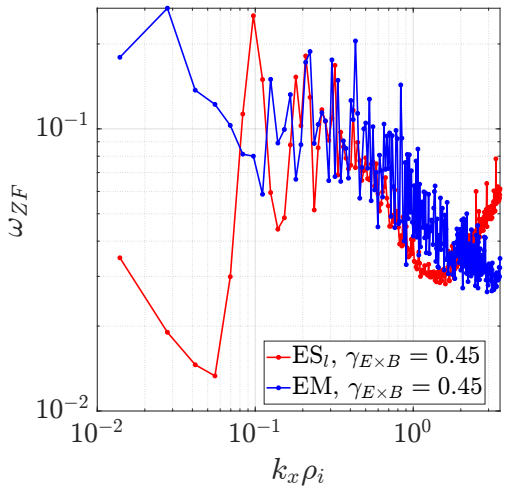

(a)

Figure 5.4.: Time averaged zonal flows shearing rate spectra: ES$_l$ (red) vs. EM (blue) for the simulations with $\gamma_{\boldsymbol{E}\times\boldsymbol{B}} = 0.45$.

As discussed in Chapter 1.5, the self-generated zonal flows $\phi_{\hat{k}_x,\hat{k}_y=0}$ represent one of the self-regulation mechanisms for turbulence. To discern their role in the ES$_l$ and EM turbulence regimes for discharge #94442-BSE and evaluate their impact on the electromagnetic stabilization mechanisms found, the zonal flow activity in the two cases is compared. In particular, it is quantified by computing the associated shearing rate

Table 5.4.: Shearing rate vs. equilibrium $\boldsymbol{E}\times\boldsymbol{B}$ shearing comparison. The ratio between the zonal flows shearing rate ω_{ZF} and the peak of growth rate at the ion-scale γ_{lin}, corresponding to the spectra discussed in Chapter 4.

Discharge	EM/ES$_l$	$\gamma_{\boldsymbol{E}\times\boldsymbol{B}}$	time window	ω_{ZF}	$\omega_{\mathrm{ZF}}/\gamma_{\mathrm{lin}}$
#94442	EM	0.30	[200 - 300]	1.64	2.23
			[450 - 650]	1.6	2.18
	EM	0.45	[250 - 400]	1.28	1.74
			[650 - 750]	1.55	2.10
			[800 - 950]	1.53	2.08
	ES$_l$	0.30	[500 - 700]	1.21	1.65
	ES$_l$	0.45	[500 - 700]	1.38	1.88
#97395	ES$_l$	0.6	[500 - 675]	0.94	0.89

spectrum defined as

$$\omega_{\mathrm{ZF}}(\hat{k}_x) = \left\langle -\hat{k}_x^2 \sqrt{\left|\langle\hat{\phi}_{\hat{k}_x,\hat{k}_y=0}\rangle_z\right|^2} \right\rangle_t$$

where $\langle\dots\rangle_z$ denotes the field-line average, and $\langle\dots\rangle_t$ denotes the time average over the saturated turbulence phase. The shearing rate spectra for the ES$_l$ and EM cases are compared in Fig. 5.4.

Interestingly, a remarkable difference is observed for the largest scale (low $\hat{k}_x$) zonal flows, which are the most effective in saturating turbulence. Indeed, they appear strongly enhanced in the EM case compared to the ES$_l$ case: while the shearing rate spectrum for the EM case reveals a peak at $\hat{k}_x = 0.028$, in the ES$_l$ case the peak is shifted to smaller scales at $\hat{k}_x = 0.097$. This enhancement of the large-scale zonal flows in the EM case compared to the ES$_l$ case could possibly play a role in the observed electromagnetic stabilization.

Starting from the ZFs spectrum, an effective $\hat{k}_x$-averaged ZFs shearing rate can be introduced as

$$\omega_{\mathrm{ZF}} = \left\langle \sqrt{\sum_{\hat{k}_x} \left| -\hat{k}_x^2 \sqrt{\left|\langle\hat{\phi}_{\hat{k}_x,\hat{k}_y=0}\rangle_z\right|^2} \right|^2} \right\rangle_t .$$

This definition allows for a quantitative evaluation of the effectiveness of the ZFs against the equilibrium $\boldsymbol{E}\times\boldsymbol{B}$ shearing in saturating the turbulence, by directly comparing ω_{ZF} with $\gamma_{\boldsymbol{E}\times\boldsymbol{B}}$. These comparisons are reported in Table 5.4.

Firstly, we observe that for discharge #94442-BSE, the effective ZFs shearing rate is always at least three times larger than the equilibrium $\boldsymbol{E}\times\boldsymbol{B}$ shearing rate, in both the ES$_l$ and EM simulations. Additionally, it is noted that in the latter phase of the EM simulations, ω_{ZF} is higher than in the ES$_l$ ones. Specifically, by comparing the values in the two cases with $\gamma_{\boldsymbol{E}\times\boldsymbol{B}} = 0.3$ and 0.45, we observe that in the first case, the ω_{ZF} in the EM simulation exceeds the corresponding in the ES$_l$ by approximately 30%, while in the

second case, it exceeds by about 10%. Finally, it is observed that in the EM simulations, the effective ZFs shearing rate is higher for the case with the lower equilibrium $\gamma_{\boldsymbol{E}\times\boldsymbol{B}}$. These results suggest that the equilibrium $\boldsymbol{E}\times\boldsymbol{B}$ shearing may play a significant role in affecting the dynamics of the self-regulation mechanisms of turbulence. Understanding the competition between these two mechanisms is an active area of research [196, 197].

Regarding discharge #97395-Type-I ELMs, we note that in this case, the effective ZFs shearing rate is only about 50% higher than the equilibrium $\boldsymbol{E}\times\boldsymbol{B}$ shearing, suggesting that both mechanisms are crucial in determining the saturation level.

In addition, the role of ZFs in saturating the linearly most unstable mode at the ion-scale is evaluated by computing the ratio $\omega_{\mathrm{ZF}}/\gamma_{\mathrm{lin}}$, with γ_{lin} the growth rate of the most unstable mode [182] (referring to the linear spectra discussed in Chapter 4), reported in Table 5.4. It is noted that for discharge #94442-BSE, the ratio $\omega_{\mathrm{ZF}}/\gamma_{\mathrm{lin}} > 1$ for all cases, indicating the dominant role of ZFs in saturating linear instabilities. Conversely, for discharge #97395-Type-I ELMs, $\omega_{\mathrm{ZF}}/\gamma_{\mathrm{lin}} < 1$, suggesting a less determinant role of ZFs in the saturation.

5.1.4. Heat flux spectra

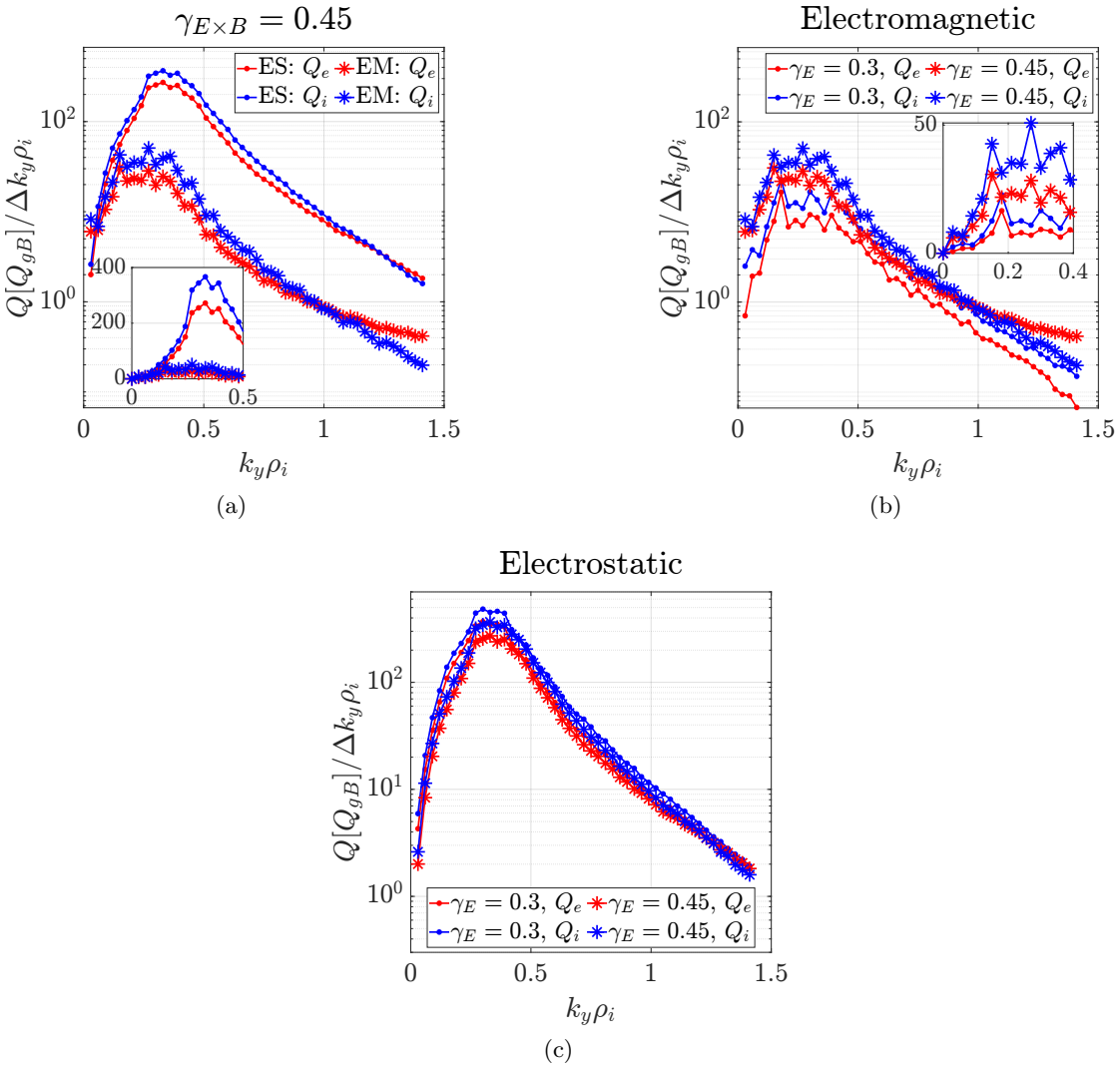

Figure 5.5.: Normalized ion (blue) and electron (red) heat flux spectra (lin-log scales) as a function of the binormal wavenumber $\hat{k}_y$ for the discharge #94442-BSE: (a) $\gamma_{\boldsymbol{E}\times\boldsymbol{B}} = 0.45$, ES$_l$ vs. EM; (b) EM, $\gamma_{\boldsymbol{E}\times\boldsymbol{B}} = 0.3/0.45$; (c) ES: $\gamma_{\boldsymbol{E}\times\boldsymbol{B}} = 0.3/0.45$. In (a) and (b) insets with a zoom at low $\hat{k}_y$ are shown (lin-lin scales).

We are now interested in characterizing the impact of the equilibrium $\boldsymbol{E}\times\boldsymbol{B}$ shearing and electromagnetic stabilization across the different scales by examining the turbulence heat flux spectra as a function of the binormal wavenumber $\hat{k}_y$. The normalized spectra of the electrostatic contribution to electron and deuterium heat flux, resulting from time-averaging across the time windows reported in Table 5.3, are shown in Fig. 5.5 for discharge #94442-BSE and in Fig. 5.6 for discharge #97395-Type-I ELMs.

Firstly, in Fig. 5.5a, the heat flux spectra of the ES$_l$ and EM simulations for discharge

#94442-BSE with $\gamma_{\boldsymbol{E}\times\boldsymbol{B}} = 0.45$ are compared. The reduction of the fluxes in the EM case is significant starting from $\hat{k}_y \sim 0.18$ in both the electron and ion channels. This reduction in the EM case particularly affects the flux peak, which is about seven times lower, and broader, developing several peaks compared to the ES$_l$ case.

In Fig. 5.5b, the role of varying equilibrium $\boldsymbol{E} \times \boldsymbol{B}$ shearing in the EM simulations is characterized. We first note that the flux spectra shapes are very similar. Remarkably, however, the heat fluxes are higher with higher $\gamma_{\boldsymbol{E}\times\boldsymbol{B}}$, contrary to what one would expect considering only its stabilizing role. This result suggests that the saturation level is determined by a competition between equilibrium $\boldsymbol{E}\times\boldsymbol{B}$ shearing and the electromagnetic turbulence self-organization mechanism leading to the observed stabilization. Additionally, although the Fourier spectrum of the electrostatic potential (see Fig. 5.3) in the EM case revealed a strong enhancement of low-$\hat{k}_x$ low-$\hat{k}_y$ modes, the heat flux peak still occurs around $\hat{k}_y \sim 0.2$. This indicates that the emerging mesoscale modes, although dominating the fluctuation spectra, contribution to heat transport is negligible (the mechanism behind this, is characterized in the next section by analyzing the cross-phases). These modes may play a role in the electromagnetic stabilization mechanism, acting as an energy reservoir.

Finally, in Fig. 5.5c, the spectra of the two ES$_l$ simulations with different $\gamma_{\boldsymbol{E}\times\boldsymbol{B}}$ are compared. In this case, we observe that higher $\boldsymbol{E} \times \boldsymbol{B}$ shearing results in a reduction of fluxes that is not uniform across all scales. It is particularly effective at the largest scales up to $\hat{k}_y \sim 0.4$, reducing fluxes by up to about 40%, while being less effective at finer scales. This result is consistent with the mechanism of $\boldsymbol{E} \times \boldsymbol{B}$ shearing acting more efficiently on the largest turbulence structures (see Chapter 1.5.2 for a discussion).

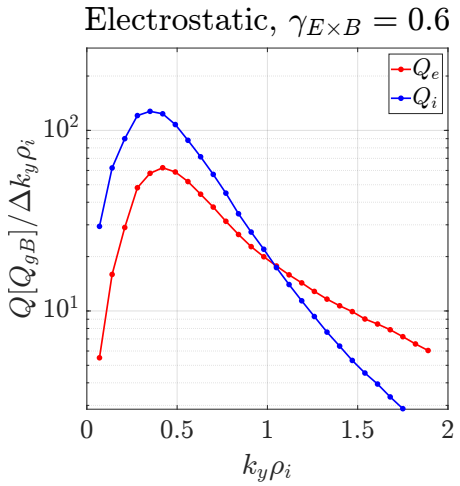

Figure 5.6.: Normalized ion (blue) and electron (red) heat flux spectra as a function of the binormal wavenumber $\hat{k}_y$ for the discharge #97395-Type-ELMs for the ES$_l$ case.

The normalized heat fluxes of the ES$_l$ simulation for discharge #97395-Type-I ELMs are shown in Fig. 5.6. In this case, we observe that, at the largest scales, the ion heat flux peak exceeds the electron heat flux by about a factor 2, indicative of a stronger ion-driven turbulence for this case. On the other hand, we notice that the trend reverses towards the smallest scales, where the electron heat flux surpasses the ion heat flux, suggesting that

ETG or TEM modes may already play a role. The differences observed here compared to the turbulence regime found in the ES_l simulations for discharge #94442-BSE add details on the potential differences in turbulent transport in the various channels (e.g., electron and ion heat) and its role in pedestals with different structures.

5.1.5. Analysis of cross-phases

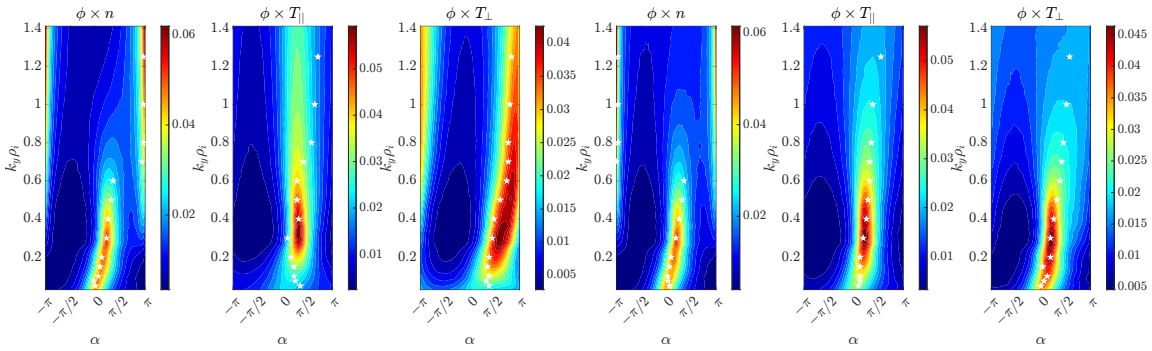

(a) ES_l, electrons.

(b) ES_l, deuterium.

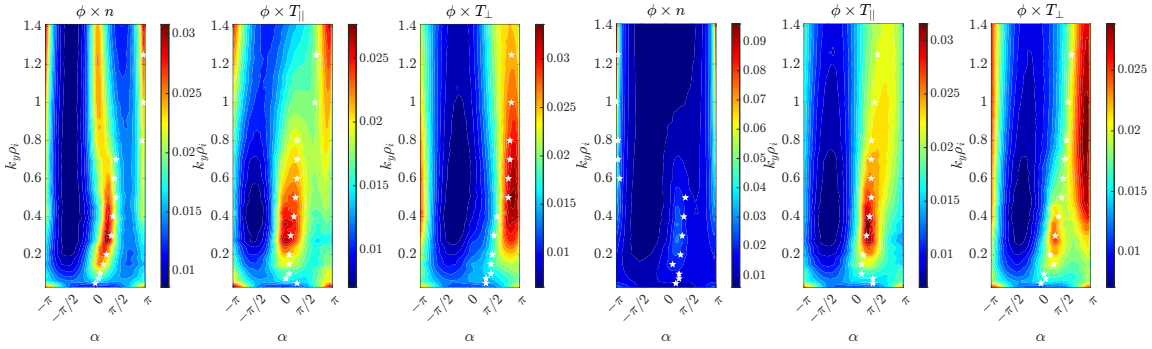

(c) EM, electrons.

(d) EM, deuterium.

Figure 5.7.: Time averaged histograms of cross-phases α between the electrostatic potential ϕ_1 and fluctuating quantities $(n_1, T_{\parallel 1}, T_{\perp 1})$ for each k_y mode: (a,b) for electrons and deuterium in the ES_l simulation; (b,c) for electrons and deuterium in the EM simulation. White stars indicate the dominant cross-phases for each $\hat{k}_y$ mode from linear simulations of discharge #94442-BSE with $\gamma_{\boldsymbol{E}\times\boldsymbol{B}} = 0$.

It is also interesting to characterize the two turbulence regimes, ES_l and EM, for simulations of discharge #94442-BSE with $\gamma_{\boldsymbol{E}\times\boldsymbol{B}} = 45.$ by analyzing the cross-phases between the fluctuating electrostatic potential ϕ_1 and fluctuations of density n_1, parallel temperature $T_{\parallel 1}$, and perpendicular temperature $T_{\perp 1}$. In fact, the transport fluxes are determined not only by the fluctuation levels but also by their relative phases. The radial

particle and heat fluxes can be expressed as (see Appendix A) [141, 159]:

$$\Gamma_\sigma^x = \frac{1}{V}\int_V \mathrm{d}^3x\, n_{1\sigma}(\boldsymbol{x},t)\boldsymbol{v}_\chi^x(\boldsymbol{x},t)$$
$$Q_\sigma^x = \frac{1}{V}\int_V \mathrm{d}^3x\, \left(\frac{3}{2}T_{0\sigma}n_{1\sigma}(\boldsymbol{x},t) + \frac{1}{2}n_{0\sigma}T_{\parallel 1\sigma}(\boldsymbol{x},t) + n_{0\sigma}T_{\perp 1\sigma}(\boldsymbol{x},t)\right)\boldsymbol{v}_\chi^x(\boldsymbol{x},t)$$

where the generalized $\boldsymbol{E}\times\boldsymbol{B}$ velocity, considering only the ϕ_1 contribution, is given by $\boldsymbol{v}_\chi^x(\boldsymbol{x},t) \propto ik_y\phi_1$. The cross-phases α between the electrostatic potential ϕ_1 and each of the fluctuating quantities $(n_1, T_{\parallel 1}, T_{\perp 1})$ are computed as follows

$$\alpha(k_x,k_y,z) = \arg\left(\frac{\phi_1(k_x,k_y,z)}{\left\{n_1,T_{\parallel 1},T_{\perp 1}\right\}(k_x,k_y,z)}\right)$$

where the arg function provides the argument (or phase) of the complex number. The cross-phases α associated with each k_y mode are evaluated by sampling the values for each (k_x, z) dimension into a histogram, and then normalizing by the total occurrences given by $n_{k_x} * n_z$. The fluxes are maximized for $\alpha = \pm\pi/2$, while they cancel out for $\alpha = 0, \pm\pi$.

The results obtained by averaging during the turbulence saturated phase over the time windows in Table 5.3 are shown in Fig. 5.7. Specifically, for the ES_l simulation, the cross-phases for the electron and deuterium species are shown in Figs. 5.7a 5.7b, respectively. In Figs. 5.7c 5.7d, the corresponding cross-phases for the EM simulation are displayed. For comparison, the maxima of the cross-phases for each $\hat{k}_y$ from linear simulations are indicated by white stars.

We first note that the cross-phases for the ES_l simulation for electrons and deuterium are qualitatively similar across all scales. A minor difference is observed in the cross-phase of $\phi_1 \times T_{\perp 1}$, where for electrons, it manifests as a slightly broader peak at $\alpha \gtrsim \pi/2$ extending to finer scales, while for deuterium, it assumes values of $0 < \alpha < \pi/2$. These results highlight the development of transport-favorable cross-phases in all channels for the largest scale modes with $0.15 < \hat{k}_y < 0.6$. For $\hat{k}_y > 0.6$, the cross-phases of $\phi_1 \times n_1$ develop peaks at $\pm\pi$, which are unfavorable for transport.

Comparing with the corresponding cross-phases obtained for the EM simulations, a striking difference is observed for the largest scale modes with $\hat{k}_y \lesssim 0.1$. Indeed, for both electrons and deuterium, the cross-phases spread out, peaking around $\alpha = \pm\pi$, indicating an unfavorable condition for transport. Given the strong electrostatic potential fluctuations observed in the EM turbulence Fourier spectra in Sec. 5.1.2, this result explains the moderated heat fluxes associated with these modes as characterized in Sec. 5.1.4. The mechanism active in the EM case, which involves the transfer of energy and enhancement of fluctuations towards the mesoscale modes while simultaneously modifying the cross-phases to make them transport-unfavorable, is suggested to contribute to the electromagnetic stabilization.

It is useful to compare the non-linear cross-phases with the dominant ones obtained from linear simulations to test whether the dominant linear microinstability features persist in the non-linear dynamics. This validation is particularly important to justify the use of quasi-linear reduced models (see Sec. 5.3) for edge plasma turbulence.

Comparing the non-linear and linear cross-phases for the ES_l turbulence regime in

Table 5.5.: Set of electron-scale simulations performed at the pedestal top position of discharge #94442-BSE.

	β_e	$\gamma_{\boldsymbol{E}\times\boldsymbol{B}}$	$1/L_{T_e}$
ref.	0.08%	0.6	14.94
scan β_e	$\beta_{e,\text{ref}} \times 0.75$ $\beta_{e,\text{ref}} \times 1.5$ $\beta_{e,\text{ref}} \times 2.0$		
scan $\gamma_{\boldsymbol{E}\times\boldsymbol{B}}$		0 0.30 0.45	
scan $1/L_{T_e}$			$1/L_{T_e,\text{ref}} \times 1.25$ $1/L_{T_e,\text{ref}} \times 1.5$

Figs. 5.7a 5.7b, we generally observe a fairly good agreement for both the electron and deuterium species. Specifically, this agreement is particularly satisfactory in the range of highest contribution to heat fluxes, $0.15 \lesssim \hat{k}_y \lesssim 0.6$, suggesting the potential validity of quasi-linear models.

Similarly, the comparison for the EM case (see Figs. 5.7a 5.7b) also reveals a general agreement between the non-linear and linear cross-phases, particularly in the range of highest heat flux, $0.15 \lesssim \hat{k}_y \lesssim 0.6$. A notable difference is found for the largest scale modes with $\hat{k}_y \lesssim 0.15$, where the linear cross-phases show transport-favorable phases, $0 < \alpha < \pi/2$, while the non-linear phases are unfavorable, peaking at $\alpha = \pm\pi$. This result provides additional evidence that the excitation mechanisms of these modes are due to mechanisms occurring during turbulence development.

These results are thus promising for the application of quasi-linear models in these turbulence regimes that develop with parameters compatible with the plasma edge. Therefore, an attempt to develop quasi-linear models starting from GENE linear simulations is carried out in Sec. 5.3. However, the non-linear electromagnetic stabilization mechanisms play a key role in fluxes and must be better understood to determine the physical conditions under which they manifest. Including this information in quasi-linear models would ensure greater reliability and robustness across different turbulence regimes. In a recent work [115], an extension of the quasi-linear model has been proposed for this purpose.

5.2. Electron-scale turbulence: stiff ETG transport

To evaluate the potential role of electron-scale induced turbulent transport in discharge #94442-BSE, simulations of microturbulence driven by electron-scale modes, starting from $\hat{k}_y \sim 2.5$ (refer to Chapter 4 for the detailed linear spectra), have been conducted. This analysis will first focus on the impact of the mechanisms already discussed for ion-scale turbulence, namely the finite-β and equilibrium $\boldsymbol{E} \times \boldsymbol{B}$. Secondly, the impact

Table 5.6.: Flux-tube resolutions for the converged non-linear simulations at the electron-scale for discharge #94442-BSE. The parameters are: number of radial and bi-normal modes, parallel resolution, parallel-velocity resolution, magnetic-moment resolution, radial, bi-normal, parallel velocity and magnetic moment domain size.

n_{k_x}	n_{k_y}	n_z	$n_{v_\parallel}$	n_μ	L_x/ρ_i	L_y/ρ_i	$L_{v_\parallel}/v_{T_e}$	$L_\mu/(T_{0e}/B_{\text{ref}})$
256/384	24/40/80	256	48	16	4.5	0.62/1.25/2.51	3.0	9.0

of the parameter $\lambda = \tau_e Z_{\text{eff}} = (T_e/T_i)Z_{\text{eff}}$ appearing in the ion-adiabatic response will be tested. Finally, a scan of the ETG driving parameter $1/L_{T_e}$ will be performed to evaluate the magnitude of turbulent electron heat transport and compare it to the experimentally inferred value for validation. We must recall that the scale separation between ions and electrons, justified by the analysis conducted in Sec. 4.4, has been assumed. This assumption excludes the cross-coupling dynamics of turbulence, which could affect the turbulence saturation level. Keeping this limitation in mind, it is still interesting to determine whether experimentally relevant transport can be obtained.

Simulations setup The set of simulations performed is summarized in Table 5.5. The analysis primarily focuses on extensive tests for discharge #94442-BSE. Due to limited computational resources, simulations for discharge #97395-Type-I ELMs were not conducted. The simulations include full electromagnetic effects, i.e. perpendicular $A_{1\parallel}$ and parallel $B_{1\parallel}$ magnetic fluctuations at the reference plasma β. Collisions are modeled using the linearized Landau-Boltzmann collision operator. Rotation effects considered include parallel and perpendicular $\boldsymbol{E} \times \boldsymbol{B}$ shear flow. To reduce computational costs, electrons are treated kinetically, while ions are assumed adiabatic. Based on extensive linear simulations described in Chapter 4, Sec. 4.3.5, this approximation is expected to provide a qualitatively accurate description of electron-scale dynamics.

The numerical grid resolution for the converged non-linear simulations is detailed in Table 5.6. A high resolution along the parallel coordinate z has been selected, with the poloidal grid redistribution coefficient of `edge_opt`= 2.0. This setting has proven more than sufficient to resolve the very narrow mode structures that emerge at the electron scale (see Sec. 4.2, Fig. 4.3 for details). Standard resolution in velocity space $(v_\parallel, \mu)$ has been employed. The wavenumber grids in the perpendicular directions span the ranges: $\hat{k}_x \sim 1.4 - 177/266$ in the radial direction, and $\hat{k}_y \sim 2.5/5/10 - 200$ in the binormal direction. In this configuration, the radial extension is sufficient to contain any radially elongated vortices (i.e. streamer structures) within the computational box. High values of $\hat{k}_{y,\text{min}}$ in the binormal grid were necessary at reference parameters to prevent flux spectra from peaking at the first mode. It should be noted that in these cases, only the slab-ETG portion of the spectrum is included (see Fig. 4.2).

5.2.1. The role of electromagnetic effects and equilibrium $E \times B$ shear flow

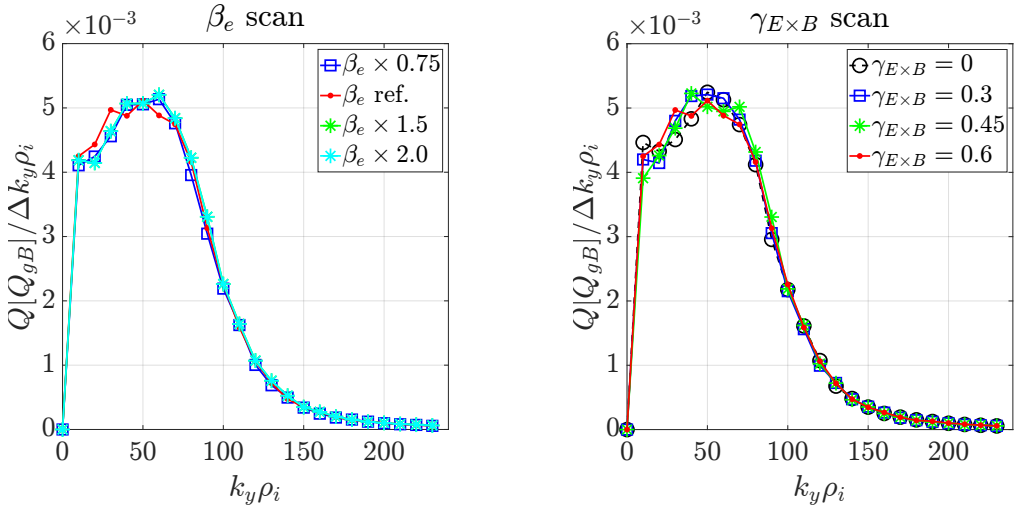

Figure 5.8.: Normalized electron heat flux spectra as a function of the binormal wavenumber $\hat{k}_y$ for the sensitivity scan: (a) $\beta = [0.75, 1, 1.5, 2.0]\beta_{\text{ref}}$, (b) $\gamma_{\boldsymbol{E}\times\boldsymbol{B}} = [0.3, 0.45, 0.6]$.

Firstly, the importance of electromagnetic effects via the finite-β, as well as the impact of the equilibrium $\boldsymbol{E} \times \boldsymbol{B}$ shearing rate on the heat flux saturation level of electron-scale turbulence has been assessed. The heat flux spectra from the sensitivity scans, with $\beta = [0.75, 1, 1.5, 2.0]\beta_{\text{ref}}$ and $\gamma_{\boldsymbol{E}\times\boldsymbol{B}} = [0, 0.3, 0.45, 0.6]$, are shown in Fig. 5.8. We observe that, in both cases, the electron heat flux spectra are almost unaffected, highlighting the negligible impact of these parameters within the sensitivity range tested.

Regarding the electromagnetic effects, this result is not surprising, given the negligible impact found in the linear analysis (see Sec. 4.3.4, Fig. 4.7), and confirms the predominantly electrostatic nature of slab-ETG-driven turbulence.

Concerning the equilibrium $\boldsymbol{E} \times \boldsymbol{B}$ shear flow, considering the much higher linear growth rates of ETG modes relative to the low values used in the sensitivity scan (see Sec. 4.4, Fig. 4.10), the negligible impact observed is consistent. However, it has been reported that ETG-driven turbulence with typical core plasma parameters can develop large streamer structures, which are considered responsible for enhanced electron transport from electron-scale modes [95, 96, 198]. In such cases, the $\boldsymbol{E} \times \boldsymbol{B}$ shearing could be effective in disrupting large turbulent structures. The independence of the results by varying $\gamma_{\boldsymbol{E}\times\boldsymbol{B}}$ indicate that slab-ETG turbulence at nominal parameters is not dominated by streamers. This finding is consistent with previous literature suggesting that ETG turbulence, with parameters compatible with the edge, does not develop streamers. For a recent and comprehensive review on ETG turbulent transport, see Ref. [199]. Additionally, we emphasize that the different efficacy of $\boldsymbol{E} \times \boldsymbol{B}$ shear flow across ion and electron scales, given that electron-scale turbulence mainly transports electron heat while ion-scale turbulence governs the ion heat channel, determines its varying effectiveness across the different transport channels.

Finally, we note that the heat flux peak occurs around $\hat{k}_y \sim 50$, significantly lower than the peak in the linear growth rate, which was found at $\hat{k}_y \sim 90$ (see Chapter 4). This suggests the importance of nonlinear energy transfer dynamics in determining energy redistribution across the involved scales.

5.2.2. The impact of adiabatic ions modelled with $\lambda = Z_{\text{eff}} T_e/T_i$

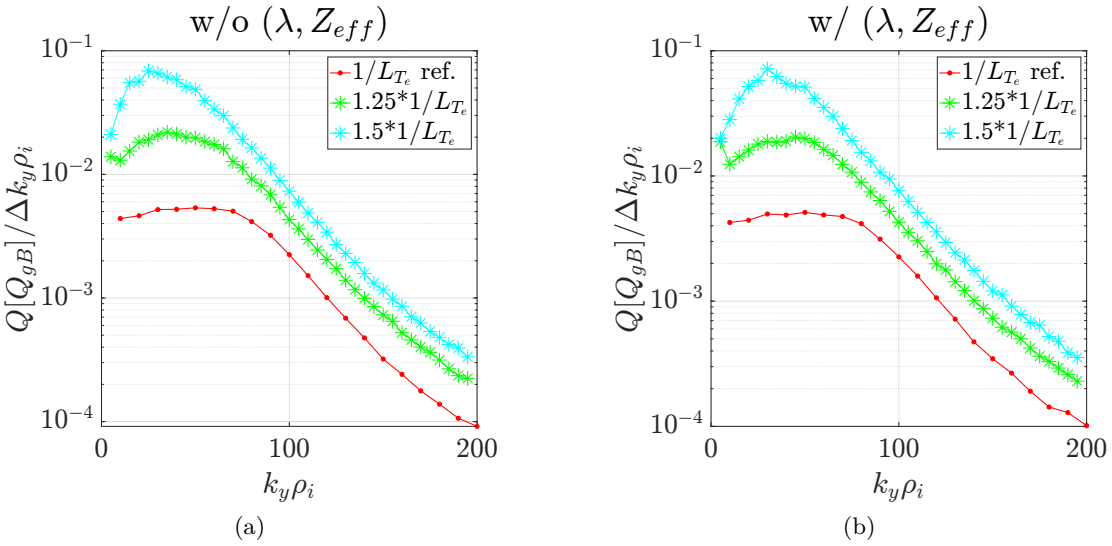

Figure 5.9.: Normalized electron heat flux spectra as a function of the binormal wavenumber $\hat{k}_y$ for different values of $1/L_{T_e}$: (a) [(b)] without [with] including the $\lambda = T_e/T_i Z_{\text{eff}}$ parameter in the ion adiabatic response, and Z_{eff} in the collisional operator.

We now proceed to characterize the impact of $\lambda = Z_{\text{eff}} T_e/T_i \approx 1.37$ in the adiabatic ion response, combined with $Z_{\text{eff}} \approx 3.14$ in the collisional operator, on the electron heat flux spectra. The results from a scan performed on the ETG driving parameter, the normalized logarithmic electron temperature gradient $1/L_{T_e}$, with/without including those effects, are shown in Fig. 5.9. A slight stabilizing effect on the ETG instability by including λ and Z_{eff} was documented in the linear analysis (see Sec. 4.3.5, Fig. 4.8). Now, examining the turbulence spectra of the electron heat flux, we observe that their effect is almost negligible.

Finally, by comparing the spectra from the $1/L_{T_e}$ scan for both cases, we note that increasing the drive leads to an increase in heat flux across all scales, with a more significant contribution at the largest scales. Simultaneously, the peak of the heat flux spectra is slightly shifted towards the larger scales, reaching $\hat{k}_y \sim 25$ in the strongest driven case with $1/L_{T_e} = 1.5 \cdot 1/L_{T_e,\text{ref}}$. On the other hand, in the turbulence inertial range between $90 \lesssim \hat{k}_y \lesssim 180$, we observe that the energy cascade power law remains the same, indicating that the same physical mechanisms dominate the various cases.

5.2.3. Stiffness study of ETG transport: comparison with experimental transport level

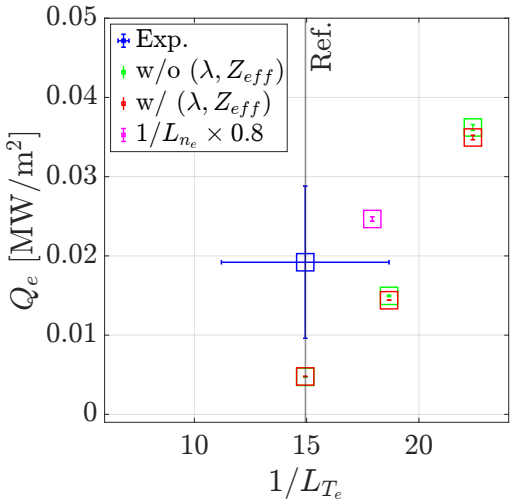

Figure 5.10.: Electron heat flux Q_e as function of the normalized logarithmic gradient $1/L_{T_e}$: including (and not) λ and Z_{eff} in red (green). One case with reduced normalized logarithmic density gradient $1/L_{n_e} = 0.8(1/L_{n_e})_{\text{ref}}$ is shown in magenta. The experimental inferred electron heat transport is shown in blue. For reference, the flux-surface area is $V' = 108.27\,\text{m}^2$.

The electron heat flux Q_e obtained from the previously discussed spectra is summarized in Fig. 5.10 to study its stiffness with respect to the normalized logarithmic gradient $1/L_{T_e}$. Additionally, the heat flux obtained by reducing the reference normalized logarithmic gradient of the electron density $1/L_{n_e}$ by 20% and increasing the reference $1/L_{T_e}$ by 20%, which are stabilizing and destabilizing parameters for ETG modes, respectively, is shown in magenta. We observe that stiff electron heat transport driven by slab-ETG modes is achieved by varying $1/L_{n_e}$ and $1/L_{T_e}$ within a reasonable range around the reference parameters. Although the stiff Q_e transport obtained under nominal parameters underestimates the experimentally derived value, it reaches experimentally relevant levels by slightly varying the input parameters.

However, we note that these transport values are lower than those obtained from ion-scale turbulence (see Table 5.3). Nonetheless, those values were subject to significant uncertainty due to the limited number of sensitivity scans around the nominal parameters and the only near-steady state reached during the saturation phase. Given this, and assuming that the ion-scale level may yield results in better agreement with experimental data, the stiff electron heat transport identified from slab-ETG turbulence may be responsible for the resilience of the electron temperature pedestal in discharge #94442-BSE.

5.3. Basic application of quasi-linear theory

The results of ion-scale turbulence simulations obtained so far have revealed a significant difference between the electrostatic potential spectra ϕ_1 in the ES$_l$ and EM regimes, with the latter indicating that nonlinear mechanisms are crucial for the enhancement of mesoscale modes. At the same time, when comparing the heat spectra between the ES$_l$ and EM cases, despite the different saturation levels and a broader peak in the EM case, it was found that mesoscale modes do not contribute significantly to the flux, resulting in overall qualitatively similar spectra in both cases. The cross-phase analysis also suggested that, excluding the mesoscale modes in the EM simulation, a qualitative agreement between the nonlinear and dominant linear modes is retrieved for both the ES$_l$ and EM simulations.

Motivated by these results, we now aim to test the validity of quasi-linear estimates of heat fluxes obtained from GENE linear simulations, focusing on the ion-scale. The quasi-linear approximation is based on two assumptions: (1) the cross-phases between the quantities appearing in the transport fluxes (see Sec. 5.1.5) are determined by linear modes [200]; (2) the ratio between the lifetime of turbulent eddies of the electrostatic potential and the transit time of a test particle around an eddy, i.e., the Kubo number [201], must be less than unity. The validity and applicability of this approximation have been demonstrated in various applications involving flux-tube gyrokinetic simulations of turbulence regimes typical of the plasma core, characterized by weak mode coupling [202–204], although there are counterexamples near marginal stability [205]. The current objective is to verify whether a basic application of quasi-linear theory with plasma parameters typical of the edge can provide satisfactory results compared to those from nonlinear simulations. Recent studies suggest that this application may be valid in low-power plasma regimes [119, 206, 207], while in other regimes, it may not be [208]. Once validated, the quasi-linear model will be used to compute the heat flux ratio Q_e/Q_i across a broader range of parameters than what is computationally feasible with nonlinear simulations. The results obtained will be compared with the experimentally inferred value. This analysis will thus provide qualitative estimates on the dependence of transport fluxes on varying driving normalized gradients, offering insights for experimental interpretation.

5.3.1. Quasi-linear expression of fluxes

Assuming that the quasi-linear approximation holds, the quasi-linear fluxes F_σ^{QL}, such as the particle flux Γ_σ or the heat flux Q_σ for a species σ, are computed as follows [209–214]:

$$F_\sigma^{\mathrm{QL}} = A_0 \sum_{k_y} w^{\mathrm{QL}}(k_y) F^{\mathrm{L}}_{\sigma,\mathrm{norm}}(k_y) \; . \tag{5.1}$$

Here, A_0 is a scaling factor associated with the absolute amplitude of fluctuations, calibrated with nonlinear simulations. The term $w^{\mathrm{QL}}(k_y)$ is the spectral amplitude weighting (or saturation rule), which depends on the chosen model. Finally, $F^{\mathrm{L}}_{\sigma,\mathrm{norm}} = F^{\mathrm{L}}_\sigma/\mathcal{A}^2$ represents the normalized *linear flux*, calculated for the most unstable mode at each k_y from linear GENE's simulations. This latter term is related to the cross-phases analyzed in Sec. 5.1.5. We emphasize that the terms in this expression are dimensionless, as they represent normalized quantities. Accordingly, the fluxes will be expressed in

gyro-Bohm units (see Appendix A), which can be converted into physical units. The terms involved are discussed in detail below.

Saturation rules We now move on to the description of the saturation rules w^{QL} tested in this thesis work. The goal of these models is to provide an approximation of the spectra of the fluctuation amplitude $|\phi|^2$ in the saturated turbulence regime. As previously mentioned, these are a critical component of quasi-linear theory, and for this reason, three saturation models have been compared to assess the sensitivity of the results.

1. *Mixing-length model (ML).* The first saturation rule, historically motivated by the scaling of turbulent diffusivity with the scale length $1/\langle k_\perp^2 \rangle$ and the time-scale $1/\gamma$ set by the most unstable mode, is given by [209, 210, 215]:

$$w^{\mathrm{QL}}(k_y) = \frac{\gamma(k_y)}{\langle k_\perp^2 \rangle(k_y)}$$

where the average squared perpendicular wavenumber in the denominator is given by

$$\langle k_\perp^2 \rangle(k_y) = \frac{\sum_{k_x} \int_{-\pi}^{\pi} \mathrm{d}z \left(g^{xx}(z) k_x^2 + 2 g^{xy}(z) k_x k_y + g^{yy}(z) k_y^2 \right) \left| \phi_{k_x,k_y}(z) \right|^2 J(z)}{\sum_{k_x} \int_{-\pi}^{\pi} \mathrm{d}z \left| \phi_{k_x,k_y}(z) \right|^2 J(z)} . \tag{5.2}$$

Note that all the coupled k_x modes ($n_{k_x} = 48$, as discussed in Sec. 4.1) have been taken into account in evaluating this average. It is possible to extend this weighting over the mode structures by including the contributions from the fields $A_\parallel(z)$ and $B_\parallel(z)$. The impact of these terms will be tested later.

2. *Mixing-length model modified (ML-mod).* A modified mixing-length saturation rule has been proposed in Ref. [211–214] to better match the nonlinear spectra by introducing an exponent to the standard ML model, resulting in:

$$w^{\mathrm{QL}}(k_y) = \left(\frac{\gamma(k_y)}{\langle k_\perp^2 \rangle(k_y)} \right)^{\zeta} .$$

In this thesis, the exponent was varied between $\zeta = 2$ and $\zeta = 3$. By comparing the quasi-linear heat spectra with the nonlinear ones, $\zeta = 3$ was chosen as the optimal value.

3. *QuaLiKiz.* The last model tested is the one implemented in the QuaLiKiz [215, 216] transport code, given by:

$$w^{\mathrm{QL}}(k_y) = \mathcal{S}(k_y) \max_{k_y} \left[\frac{\gamma(k_y)}{\langle k_\perp^2 \rangle(k_y)} \right] \frac{1}{(k_y)_{\max}}$$

with the spectral shape $\mathcal{S}(k_y)$ defined as

$$\begin{cases} \mathcal{S}(k_y) = \dfrac{k_y}{(k_y)_{\max}} & \text{for} \quad k_y < (k_y)_{\max} \\ \mathcal{S}(k_y) = \left(\dfrac{k_y}{(k_y)_{\max}}\right)^{-3} & \text{for} \quad k_y > (k_y)_{\max} \end{cases}$$

where $(k_y)_{\max}$ is the wavenumber corresponding to the maximum of $\gamma/\langle k_\perp^2 \rangle$.

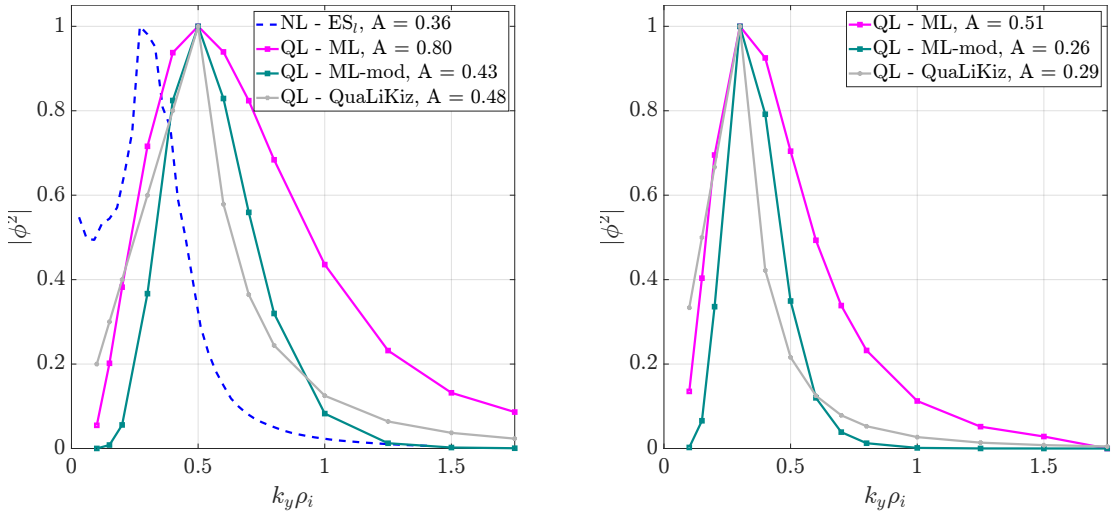

(a) ES$_l$ (b) EM

Figure 5.11.: Comparison of the three saturation rules ML (magenta), ML-mod (green), and QuaLiKiz (grey) computed from linear GENE simulations. For each spectrum, the area below the curve is reported in the legend. (a) For the ES$_l$ settings the non-linear $|\phi|^2$ spectrum is shown in dashed blue for discharge #94442-BSE with $\gamma_{\boldsymbol{E}\times\boldsymbol{B}} = 0.45$.

The saturation rules calculated from GENE linear simulations at the ion-scale, $0 < \hat{k}_y < 1.75$, for discharge #94442-BSE are shown in Fig. 5.11. Specifically, they were computed for the linear spectra of the ES$_l$ and EM cases discussed in Sec. 4.3.4. Since the A_0 factor was not calibrated, the spectra have been normalized to their peak value.

In the ES$_l$ case, a direct comparison is made with the nonlinear spectrum $\sum_{k_x} \left\langle \left| \hat{\phi}_{k_x,k_y} \right|^2 (z) \right\rangle_{z,t}$. We observe that all the quasi-linear models tested peak at $\hat{k}_y = 0.5$, which disagrees with the nonlinear spectrum peak, being shifted to larger scales at $\hat{k}_y \sim 0.3$. Regarding the general shape, the standard ML model provides a spectrum that is too broad compared to the nonlinear one, decaying too slowly. In contrast, the ML-mod with $\zeta = 3$ and QuaLiKiz models are similar to each other and better capture the trends both before and after the peak, more accurately representing the spectral decays. A more quantitative comparison can be made by examining the areas under the curves, as reported in the legend of the figure. However, it is important to note that, given the arbitrary choice to

normalize the non-linear and quasi-linear spectra by their peak values, the comparison of areas does not provide a fully meaningful metric. Instead, it offers insights into the impact of the different spectral decays employed in the saturation rules tested, on the area under the curve. While the standard ML model overestimates the area under the nonlinear spectrum by more than a factor of 2, the other two models are in better agreement, overestimating by at most around 60%.

In the EM case, a direct comparison with the nonlinear spectrum is not insightful due to the presence of mesoscale modes. Regarding the general shape, the same trend as in the ES_l case is observed: the standard ML model results in a broader spectrum with a larger area below it compared to the other two models, which instead show similar trends and very similar areas. Interestingly, in this case, the spectrum peaks at $\hat{k}_y \sim 0.3$, shifted to a lower value compared to the ES_l case. We also note that the spectral shapes in the EM case decay earlier than those in the ES_l case. These results already highlight the sensitivity of the quasi-linear model to the physical terms taken into account in the linear simulations. To better understand the origin of these differences, recalling that the growth rate spectra were qualitatively similar in both cases (see Sec. 4.3.4, Fig. 4.7), we focused on the role of the effective perpendicular wavenumber.

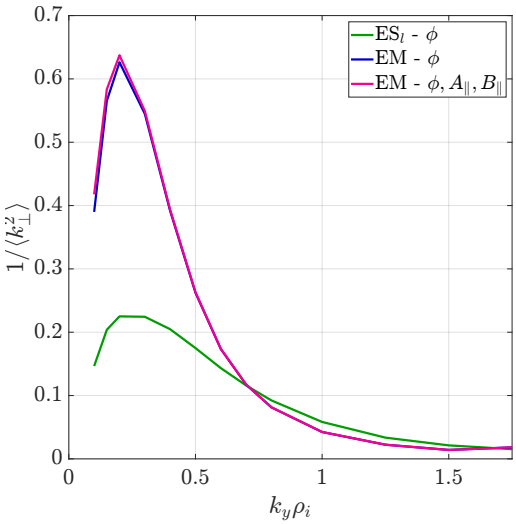

Figure 5.12.: Comparison of the inverse effective perpendicular wavenumber $1/\langle k_\perp^2 \rangle$ from linear GENE simulations as function of $\hat{k}_y$: ES_l (green), EM considering only ϕ_1 (blue), and EM considering the three fields $(\phi_1, A_{1\parallel}, B_{1\parallel})$ (magenta).

In Fig. 5.12, the behavior of the inverse effective perpendicular wavenumber $1/\langle k_\perp^2 \rangle$ for the ES_l and EM cases is shown. For the EM case, the results including the magnetic fields in Eq. 5.2 are also presented, demonstrating that in this case, they play a negligible role. Interestingly, within the range of the spectrum peaks, $0 \lesssim \hat{k}_y \lesssim 0.6$, a significant difference emerges. Specifically, the largest scales in the EM case are enhanced, while the smaller scales remain similar to those in the ES_l case. As a result, the decay of $1/\langle k_\perp^2 \rangle$ is quite different between the two cases. These differences are attributed to the modification of the linear mode structures, even of the electric potential ϕ_1, when electromagnetic effects are included.

Linear fluxes (or quasi-linear weights) We now turn to the second factor that appears in the definition of the quasi-linear fluxes in Eq. 5.1. In the case of the heat flux $F_\sigma^{\mathrm{L}} \equiv Q_\sigma^{\mathrm{L}}$, starting from the fluxes calculated in GENE, as reported in Appendix A, the calculation of the contribution from ϕ_1 of the generalized $\boldsymbol{E} \times \boldsymbol{B}$ is explicitly given by [141, 214]:

$$Q_\sigma^{\mathrm{L}}(k_y) = \left\langle \frac{1}{C} \sum_{k_x} 2\Re \left[ik_y \phi_1^* \int \mathrm{d}^3 v \, \frac{1}{2} m_\sigma v^2 f_{1\sigma} \right] \right\rangle_z$$

where $C = B_0 / \sqrt{g^{xx} g^{yy} - (g^{xy})^2}$, with B_0 being the background magnetic field, $\Re$ takes the real part of a complex number, and $\langle A \rangle_z = \int \mathrm{d}z \, J(z) A(z) / \int \mathrm{d}z \, J(z)$ is the field-line average, with $J(z)$ being the Jacobian of the (x, y, z) coordinate system. This will be the only contribution considered in what follows, given the negligible contributions of the other components previously found. The linear fluxes must thus be normalized, as their amplitude is physically irrelevant (it grows exponentially). The normalizing factor $\mathcal{A}^2$ chosen here is given by:

$$\mathcal{A}^2(k_y) = \sum_{k_x} \left\langle |\phi_1|^2 \right\rangle_z$$

which differs from the one used in most of the aforementioned works, where the normalization is given by $|\phi(k_x = 0, k_y, z = 0)|^2$. The choice adopted here is partially motivated by its validity even in the case of modes with ϕ_1 exhibiting tearing parity, which are not uncommon in simulations with steep gradients [175].

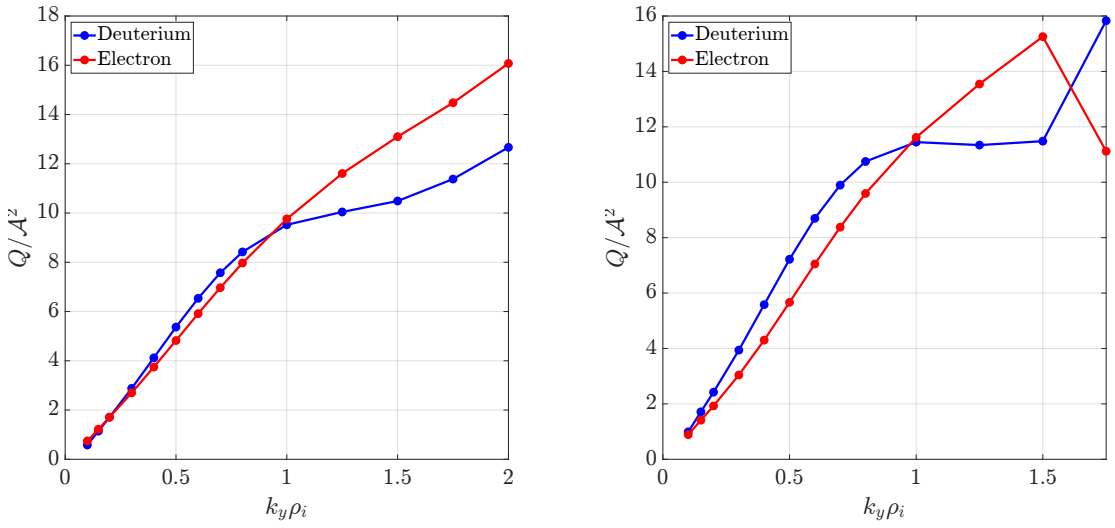

(a) ES_l (b) EM

Figure 5.13.: Normalized linear heat fluxes for the electron (red) and deuterium (blue) as function of the binormal wavenumber $\hat{k}_y$ for: (a) ES_l, and (b) EM.

The normalized linear fluxes for the electron and deuterium species, calculated from GENE linear simulations for discharge #94442-BSE, are shown in Fig. 5.13 for the ES_l

and EM cases. A similar trend is observed in both cases: up to $\hat{k}_y \sim 1.0$, the ion heat flux associated with each $\hat{k}_y$ exceeds the electron heat flux, while the trend reverses between $1.0 < \hat{k}_y < 1.5$. In the EM case, we note that Q_i is up to approximately 30% higher than Q_e, while in the ES$_l$ case, it never exceeds Q_e by more than about 10%. These factors will be important in determining the relative heat flux levels in the two channels, as calculated in the following sections.

5.3.2. Heat flux spectra comparison: quasi-linear vs. non-linear

We proceed with the direct comparison of the nonlinear and quasi-linear heat flux spectra. This comparison is a necessary step to validate the quasi-linear model in preparation for its more extensive use. Note that the validation performed is quite limited given the small number of available non-linear simulations. The nonlinear heat flux spectra correspond to the cases with $\gamma_{\boldsymbol{E}\times\boldsymbol{B}} = 0.45$, chosen as the reference. The comparison for the ES$_l$ case is shown in Fig. 5.14, while the comparison for the EM case is shown in Fig. 5.15. The spectra for Q_i and Q_e are shown separately to facilitate the comparison with the quasi-linear models. Note that the spectra are normalized to the peak of the Q_i spectrum to preserve the information related to the Q_e/Q_i ratio which will be compared in Sec 5.3.3.

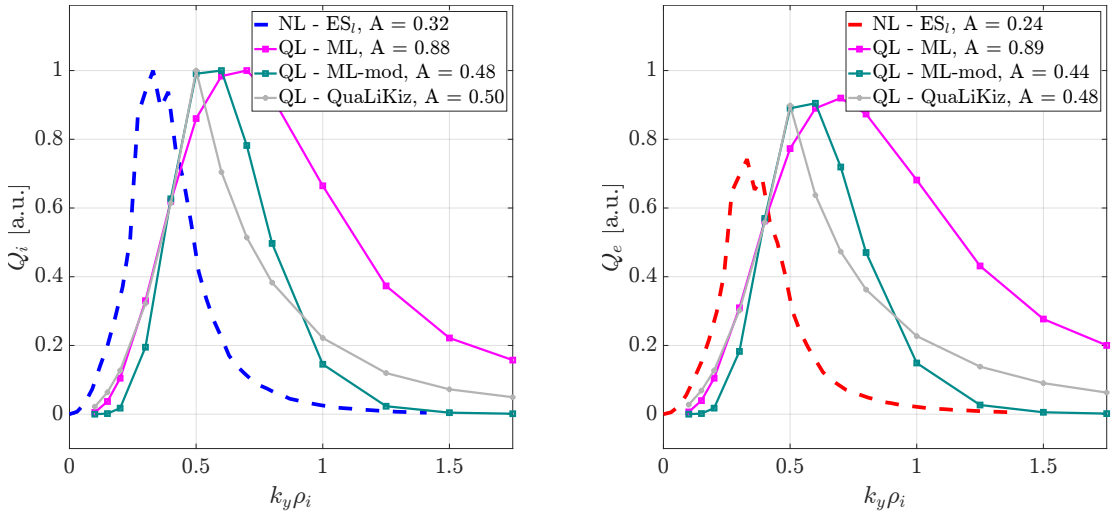

(a) Ion (b) Electron

Figure 5.14.: Comparison of non-linear (with $\gamma_{\boldsymbol{E}\times\boldsymbol{B}} = 0.45$) and quasi-linear (using the three saturation rules) heat flux spectra as function of $\hat{k}_y$ from ES$_l$ GENE simulations: (a) ion, and (b) electron heat flux. The spectra are normalized with the peak of the ion heat flux. For each spectrum, the area below the curve is reported in the legend.

Looking at the spectra for the ES$_l$ case in Fig. 5.14, we observe, unsurprisingly, that the peak of the spectra is not well captured by any quasi-linear model. This is due to the inaccuracies of the saturation rules w^{QL} previously described (see Fig. 5.11). For a more quantitative comparison, the areas under the spectra are reported in the legends.

We emphasize that the purpose of this analysis, although the areas under the normalized spectra are not entirely meaningful, is to compare the impact of the different quasi-linear saturation rules tested on the final flux spectra and to provide indications regarding the quasi-linear spectra that best approximate the non-linear ones. For the Q_i spectrum, we note that all quasi-linear models overestimate the nonlinear one, with the ML-mod model being the most accurate, overestimating by 50%. Examining the normalized Q_e spectra, we observe that the quasi-linear models consistently overestimate the nonlinear Q_e spectrum by at least a factor 2. This may be partly due to the peak of the spectra not being well represented by the quasi-linear models, or it may indicate that the linear fluxes (or cross-phases) are not in perfect agreement with the nonlinear ones. As a result, the nonlinear ratio $Q_e/Q_i = 0.75$ (see Table 5.3) is not well reproduced by any quasi-linear model, with the best result being $Q_e/Q_i = 0.92$.

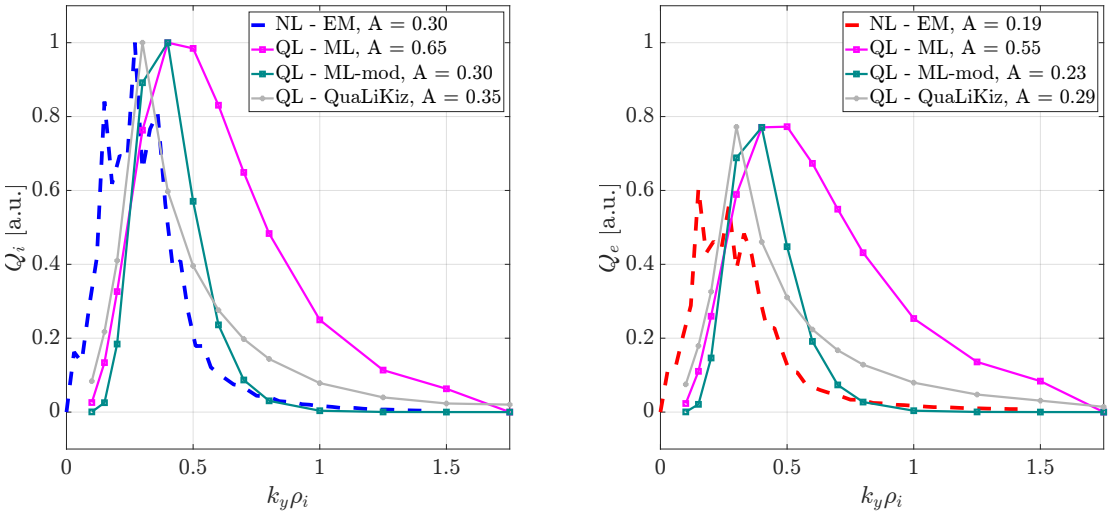

(a) Ion (b) Electron

Figure 5.15.: Comparison of non-linear (with $\gamma_{\boldsymbol{E}\times\boldsymbol{B}} = 0.45$) and quasi-linear (using the three saturation rules) heat flux spectra as function of $\hat{k}_y$ from EM GENE simulations: (a) ion, and (b) electron heat flux. The spectra are normalized with the peak of the ion heat flux. For each spectrum, the area below the curve is reported in the legend.

Now, looking at the comparison of spectra for the EM case in Fig. 5.15, we observe that the shift towards the larger scales in the saturation rules w^{QL} previously found allows for a better agreement between the non-linear and quasi-linear peaks of the spectra for both Q_i and Q_e. Comparing the areas below the spectra, once again the standard ML model overestimates the nonlinear one, while the ML-mod model provides estimates in better agreement. In particular, the ML-mod model is able to capture the rapid decay of the nonlinear spectrum at smaller scales. However, as with the ES_l case, the Q_e spectra still slightly overestimate the nonlinear result. Nevertheless, the quasi-linear estimates using the ML-mod model yield a flux ratio of $Q_e/Q_i = 0.77$, which is in agreement with the experimental value, and approximates the corresponding nonlinear value of $Q_e/Q_i = 0.63$. Considering these results more than satisfactory, in the next section, the quasi-linear

ML-mod model will be extensively used in a parameter scan to characterize the flux ratio dependencies on relevant input parameters.

It should be noted that these results are quite promising given the simplicity of the quasi-linear model adopted, which does not, for example, model the electromagnetic stabilization or the $\boldsymbol{E} \times \boldsymbol{B}$ shearing effects. Certainly, if one were to calibrate the factor A_0, these physical effects would need to be included in the model to capture the saturation level of the turbulence. However, for our application, we will compare the flux ratios Q_e/Q_i, so the calibration of A_0 is not necessary.

5.3.3. Heat flux ratio Q_e/Q_i: sensitivity scan to input parameters

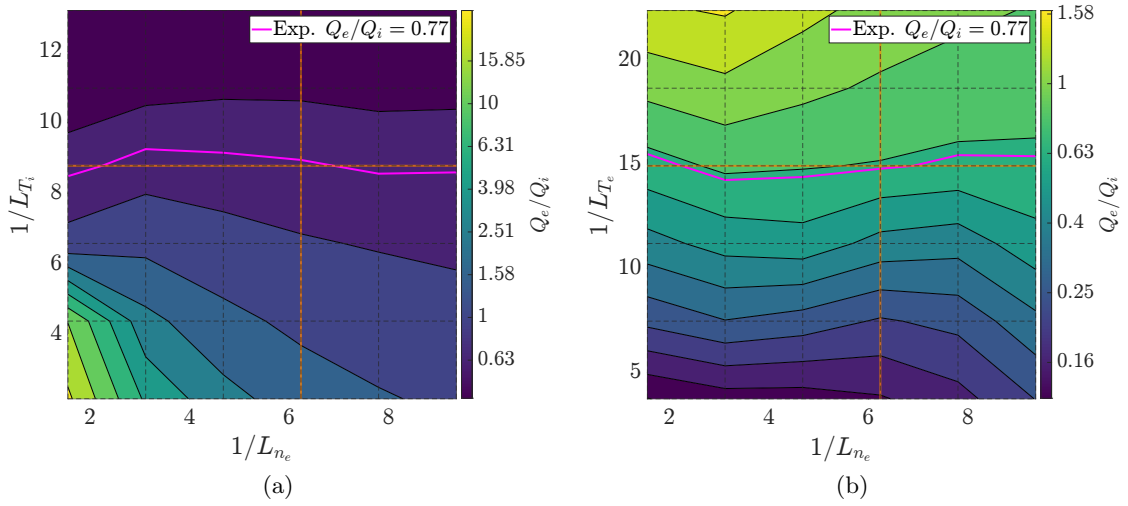

Figure 5.16.: Contours of electron to ion heat flux ratio Q_e/Q_i from quasi-linear calculations using ML-mod saturation rule and GENE EM linear simulations: (a) $(1/L_{n_e}, 1/L_{T_i})$, and (b) $(1/L_{n_e}, 1/L_{T_e})$ parameters scan. The solid magenta line corresponds to the experimental value of Q_e/Q_i. The vertical and horizontal orange lines are in correspondence of the reference values of $(1/L_{n_e}, 1/L_{T_i})$ (see Table 2.5).

Finally, we aim to obtain quasi-linear estimates of the heat flux ratio Q_e/Q_i as a function of the driving parameters of the underlying linear modes, i.e., the hybrid ITG-TEM modes found in Chapter 4. This will allow us to characterize the turbulent transport regimes and their dependence on driving parameters. Keeping in mind that both the quasi-linear model and the experimental power balance provide estimates, comparing the simulation results with the experimentally inferred flux ratio can yield insights for experimental interpretation. However, it is important to emphasize that electron-scale induced transport has been neglected and could play a significant role.

The quasi-linear model used will be the ML-mod, which, according to previous analyses, provided the best results at the reference parameters when compared with nonlinear simulations. We specifically focused on the impact of the most relevant parameters for hybrid ITG-TEM modes, namely $(1/L_{T_i}, 1/L_{T_e}, 1/L_{n_e})$. In particular, we first conducted a double scan with the parameters $1/L_{T_i} = [0.25, 0.5, 0.75, 1, 1.25, 1.5] \times 1/(L_{T_i})_{\text{ref}}$ and

$1/L_{n_e} = [0.25, 0.5, 0.75, 1, 1.25, 1.5] \times 1/(L_{n_e})_{\text{ref}}$ at fixed $1/(L_{T_e}) = 1/(L_{T_e})_{\text{ref}}$, defining a grid of 6×6 pairs of values. For each point on the grid, the heat flux spectra were computed from linear spectra with 14 $\hat{k}_y$ in the range $[0.1, 1.4]$, resulting in a total of 504 linear simulations. The same analysis was conducted by substituting $1/L_{T_i}$ with $1/L_{T_e}$ at fixed $1/(L_{T_i}) = 1/(L_{T_i})_{\text{ref}}$, thus requiring another set of 504 linear simulations. It should be noted that in this broad input parameter scan, it is not guaranteed that the most unstable modes remain the hybrid ITG-TEM. The results obtained for the heat flux ratio Q_e/Q_i are reported in Fig. 5.16. The nominal values of input parameters are indicated with orange horizontal and vertical lines. The experimental heat flux ratio Q_e/Q_i is shown in magenta. Note the different ranges in the colormaps.

We first focus on the results obtained from the $(1/L_{T_i}, 1/L_{n_e})$ scan shown in Fig. 5.16a. Moving vertically in the contour plot, i.e., at fixed $1/L_{n_e}$, we observe that progressively increasing $1/L_{T_i}$ leads to a decrease in the heat flux ratio Q_e/Q_i. This is consistent with the fact that $1/L_{T_i}$ drives the flux in the ion heat flux channel. This effect is less pronounced as $1/L_{n_e}$ increases. Moving horizontally, i.e., at fixed $1/L_{T_i}$, two different trends are observed. For low values of $1/L_{T_i}$, an increase in $1/L_{n_e}$ results in a decrease in the heat flux ratio towards unity, consistently with the stabilization of ITG with increasing $1/L_{n_e}$. In contrast, for high values of $1/L_{T_i}$, the heat flux ratio is approximately one, and almost insensitive to variations in $1/L_{n_e}$. This is the case for the nominal $1/L_{T_i}$ value. We note that the experimental heat flux ratio is matched around the nominal $1/L_{T_i}$ and is almost insensitive to variations in $1/L_{n_e}$.

The results from the $(1/L_{T_e}, 1/L_{n_e})$ scan are shown in Fig. 5.16b. In this case, we observe that the range of heat flux ratio values is narrower than in the previous scan. Specifically, moving vertically in the contour plot, i.e., at fixed $1/L_{n_e}$, we observe that progressively increasing $1/L_{T_e}$ leads to an increase in the heat flux ratio Q_e/Q_i. This is consistent with the fact that $1/L_{T_e}$ drives the flux in the electron heat flux channel. This effect is practically constant with varying $1/L_{n_e}$. Moving horizontally, i.e., at fixed $1/L_{T_e}$, the heat flux ratio appears less sensitive to variations in $1/L_{n_e}$. Again, the experimental heat flux ratio is matched around the nominal $1/L_{T_e}$.

These results indicate that while heat transport is strongly regulated by the steep normalized gradients of the ion and electron temperatures, the normalized density gradient plays a less decisive role in determining the heat flux ratio. It is most likely crucial in regulating the particle flux. However, the particle flux constraint was not considered in this analysis due to the limited knowledge of particle flux balance in the edge region. Recent advances in pedestal particle balance modeling, as reported in Ref. [217], could provide valuable constraints in the future for the validation of reduced quasi-linear models in the pedestal region.

6. Conclusions

Contents

6.1. Results summary 135
6.2. Discussion and future work 137

One of the primary concerns for the operation of future fusion reactors is the development of integrated core-edge plasma regimes that ensure high confinement, compatible with fusion performance requirements, while simultaneously maintaining edge dynamics that meet the constraints imposed by plasma-facing components tolerances for heat and particle loads. In particular, the mechanisms regulating edge dynamics are crucial, as they define the boundary for the stiff core plasma profiles and determine the fluxes on plasma-facing components depending on the type of potentially triggered edge-localized modes (ELMs). In this context, the EPED model is the most widely used model to predict pedestal pressure height relying on combined constraints from MHD limits imposed by coupled peeling-ballooning (P-B) modes and transport limits imposed by kinetic-ballooning modes (KBM). Despite progress in understanding the physical processes determining the pedestal structure, the role of turbulent transport mechanisms, driven by instabilities (e.g., ion and electron-temperature gradient (ITG and ETG) modes, and trapped-electron modes (TEM)), remains one of the least understood.

The starting point of this thesis is the discovery during the 2019-2020 experimental campaigns at the JET tokamak of new H-mode regimes featuring small-ELM dynamics, referred to as baseline small-ELMs (BSE). These regimes are of interest due to their combination of high confinement and the small-ELMs edge dynamics that may be sustainable in reactor-scale devices. Despite significant progress in understanding the physical mechanisms regulating the pedestal, the distinctive pedestal structures observed in BSE regimes, as compared to those in type-I ELM regimes, remain unexplained by the EPED model, indicating potentially missing physical insights that require further study.

The aim of this thesis is to better understand transport mechanisms in the pedestal of BSE regimes through a comparative analysis with a standard H-mode discharge featuring type-I ELMs. This investigation is carried out using interpretive gyrokinetic modeling, beginning with stability studies presented in Chapter 4 and followed by turbulence studies in Chapter 5, focusing on the region near the pedestal top in both ELMy regimes. An overview of the gyrokinetic theoretical framework and the numerical resolution using the GENE code is provided in Chapter 3.

In this concluding chapter, the main findings and contributions of this thesis are summarized, and potential directions for future research are discussed in light of the remaining and emerging open questions.

6.1. Results summary

The main experimental conditions of the two discharges in BSE regimes are compared with a reference standard H-mode with type-I ELMs in Chapter 2, where the role of particle fueling in accessing these regimes is highlighted. Analyses of the MHD stability of the pedestal are presented, revealing that while the type-I ELM regime pedestal is P-B unstable, the BSE pedestals remain stable, not reaching the critical pressure and current gradients required for P-B onset. In light of these results, the pedestal structure of BSE regimes remains unexplained within the framework of EPED model assumptions. The measured pedestal plasma profiles across the different regimes are analyzed, revealing distinctive structures: while the electron temperature pedestals are similar, ion temperatures are higher in BSE regimes compared to type-I ELMs, and electron density is significantly lower. This latter feature determines a higher normalized logarithmic density gradient, $1/L_n$, and a lower electron plasma β_e for BSE compared to the type-I ELM regime. Moreover, higher impurity concentrations are observed in BSE regimes compared to type-I ELMs. These distinctive features already suggest that different transport mechanisms may govern the two ELMy regimes pedestals. Finally, the radial electric field is reconstructed from the radial profiles of toroidal velocity and pressure, enabling estimates of the equilibrium $\boldsymbol{E} \times \boldsymbol{B}$ shearing rate, a key factor in turbulence regulation.

To assess the impact of differences in the pedestal top structure across the different ELMy regimes on the stability, local linear gyrokinetic simulations are conducted and presented in Chapter 4. Analyses performed at three closely spaced radial locations around the pedestal top reveal that at ion-scales, while the type-I ELMs regime is dominated by hybrid ITG-KBM and KBM modes, the BSE discharges are characterized by hybrid ITG-TEM modes. In the former case, the results are consistent with the current understanding that KBM limits combined with P-B limits play a determining role in the pedestals of type-I ELMy H-mode. A dedicated investigation is then conducted to determine the origin of this difference by performing a scan of the KBM driving parameters, i.e. plasma beta (i.e., the ratio of thermal pressure to magnetic pressure) and normalized logarithmic ion temperature gradient, $(\beta_e, 1/L_{T_i})$. The origin is identified: KBMs are stable at the pedestal top in BSE regimes due to the lower plasma β_e, a characteristic of these regimes. Furthermore, the destabilization of KBMs is found to be incompatible with experimental uncertainties in the KBM driving parameters. Interestingly, the destabilization of micro-tearing modes (MTM), one of the mechanisms recently considered key for transport in JET-ILW pedestals, is excluded in these discharges, even in the sub-dominant mode analyses, indicating that other mechanisms are responsible for electron heat transport. However, given the sensitivity of the results to the radial location of the analysis, this mechanism cannot be excluded in the whole pedestal. In addition, spectra of microinstabilities at reference parameters are compared with simulations in the electrostatic limit, showing weak electromagnetic effects. Finally, simulations are performed beyond the ion scale, revealing the destabilization of several toroidal and slab ETG mode branches in both regimes, consistent with other studies of JET-ILW pedestals. Notably, the toroidal-ETG branches in BSE regimes, unlike those in type-I ELMy, are found to be sensitive to impurity stabilization. The stability analysis has thus provided evidence of different ion-scale instabilities at the pedestal top of the two ELMy regimes, possibly indicating distinct roles of turbulent transport processes.

In Chapter 5, to gain insights into the main mechanisms responsible for turbulence saturation, very challenging local nonlinear gyrokinetic simulations are conducted, focusing on the BSE discharge. Building upon available studies of edge turbulent transport, the role of two key mechanisms in edge turbulent transport is considered: electromagnetic effects and their interplay with equilibrium $\boldsymbol{E} \times \boldsymbol{B}$ shearing. Turbulence simulations at ion-scale reveal significantly higher heat flux levels in the electrostatic ES_l regime compared to the electromagnetic EM regime, indicating an electromagnetic stabilization mechanism at play. These results extend the observation of electromagnetic stabilization, typically found in core turbulence simulations, to edge turbulence characterized by steep gradients and the low-β of BSE regimes. The analysis of the turbulence Fourier spectra of the electrostatic potential shows the presence of mesoscale modes in the EM case, consistent with previous studies, which are absent in the ES_l case. Given the weak electromagnetic effects observed in linear simulations, the destabilization of mesoscale modes is attributed to nonlinear mechanisms, supporting evidence of dominant nonlinear processes in electromagnetic turbulence. Zonal flow activity in the ES_l and EM cases is compared to evaluate its role in electromagnetic stabilization. A remarkable difference in the zonal shearing rate spectra is observed, with large-scale enhancement in the EM case. Although evidence suggests that zonal flow self-regulation plays a more significant role in the EM case compared to ES_l, a conclusive statement on its decisive role in electromagnetic stabilization cannot be made. A comparison of heat flux spectra allows for an evaluation of the effectiveness of the equilibrium $\boldsymbol{E} \times \boldsymbol{B}$ shearing across the different scales, and highlights its ambivalent role in the EM case, where the higher shearing rate results in higher heat fluxes. The underlying mechanisms are not identified, but a competition between self-organization mechanisms and equilibrium shearing is suggested. Additionally, it is demonstrated that mesoscale modes, although strongly excited in the Fourier spectra, do not significantly transport heat. This mechanism is further explored by examining the cross-phases of potential fluctuations with density and temperature, showing that the mesoscale modes exhibit cross-phases unfavorable for transport. The nonlinear mechanism in the EM case, involving the transfer of energy and the enhancement of mesoscale mode fluctuations while simultaneously modifying the cross-phases to make them transport-unfavorable, is suggested to contribute to electromagnetic stabilization, with these modes potentially acting as energy reservoirs.

Despite evidence of strong nonlinear mechanisms at play, good agreement is found for the cross-phases between the nonlinear and the dominant linear, for modes with the most favorable cross-phases for transport. This result motivates the application of quasi-linear theory to reproduce the ion-scale nonlinear heat flux. Spectra are constructed by testing different saturation rules and using the linear fluxes from GENE simulations. Promising results are obtained regarding the agreement between the nonlinear heat flux spectra and the basic quasi-linear models tested, suggesting their potential applicability while also highlighting critical areas requiring further development, such as capturing flux spectra with multiple peaks.

Finally, simulations of ETG-driven turbulence, retaining the slab-ETG branch of the BSE regime, are conducted to quantitatively assess the electron heat transport. The results demonstrate their insensitivity to EM effects and equilibrium $\boldsymbol{E} \times \boldsymbol{B}$ shearing, and stiff electron heat transport with respect to the normalized logarithmic electron temperature gradient, $1/L_{T_e}$. These results emphasize the role of electron-scale turbulence

in heat transport in the electron channel for BSE regimes, potentially representing a mechanism that limits the electron temperature pedestal height.

The findings contribute to extending our understanding of the key transport mechanisms at the pedestal top of the new BSE regimes, particularly highlighting the importance of the competition between stabilizing electromagnetic effects and equilibrium $\boldsymbol{E} \times \boldsymbol{B}$ shearing for hybrid ITG-TEM driven turbulence, as well as the role of electron-scale transport from ETG-driven turbulence. These results confirm that turbulent transport in the pedestal is electromagnetic and multi-scale, with underlying turbulence mechanisms having a nontrivial influence on the different transport channels.

6.2. Discussion and future work

We now aim to discuss some of the limitations of the present work and suggest possible directions for further development.

First, it is important to note that the simulations conducted in this thesis employ the local version of the GENE code, which simulates only a flux-tube of the whole plasma, thus neglecting global effects. As discussed in Chapter 4, the validity of the local approximation in the steepest pedestal region becomes questionable. For this reason, global simulations, retaining the variations in radial profiles, should be performed to quantify the expected stabilization induced by finite ρ^* effects and further validate the results obtained in this thesis. In this context, the recently GPU-accelerated version of the GENE code is promising for making these simulations more computationally affordable. Additionally, recent advancements in numerical implementation have enabled numerically stable global electromagnetic simulations, opening new avenues for further studies. Another possible extension involves increasing the resolution by retaining more modes in turbulence development. In this thesis, a scale separation between ion and electron scales is assumed, supported by linear arguments. This assumption allows to reduce the computational cost, which for the electromagnetic simulations at the ion scale were already quite expensive, requiring approximately 2MCPUh. To account for cross-scale interactions, multi-scale simulations are needed. Indeed, several mechanisms could potentially play a role, such as the damping of ion-scale driven zonal flows due to electron-scale effects, or the coupling between electron-scale and ion-scale modes, leading to additional damping.

Beyond the limitations of the model used, more effort should be directed toward assessing the sensitivity of nonlinear simulation results to experimental uncertainty. The pedestal region, due to edge dynamics, is characterized by fast temporal variations within a very narrow region, making it subject to significant experimental uncertainties. Improvements in plasma diagnostics, providing higher-quality diagnosed plasmas, would be highly desirable for more accessible validation of simulation results against experimental measurements.

Going beyond the results obtained in this thesis, intriguing features of electromagnetic turbulence have been revealed, potentially pointing to mechanisms that deserve further investigation, both theoretically and experimentally. Specifically, the excitation mechanisms of the mesoscale modes observed in the electromagnetic turbulence regime have not been fully explored, nor has their role in electromagnetic stabilization been completely understood. From a theoretical and simulation perspective, detailed analyses

of turbulence energy transfer across modes could provide valuable insights. A detailed characterization of mesoscale mode features may also provide parameters directly comparable to experimental measurements, such as modes number and frequency obtained with correlated magnetic coil measurements with fast electron cyclotron emission diagnostics. Similar comparative analyses have already been performed, allowing for example for direct comparison of experimental cross-phases with numerical simulations. These should continue to be developed and provide test assumptions for turbulent transport theories.

The combination of theoretical and experimental insights could potentially guide the development and refinement of transport coefficients for the pedestal region to be included in predictive models for pedestal structure, such as EPED, possibly accounting for the different ELMy regimes. Testing and validating these models could help advance our understanding of the pedestal and enable the extrapolation of the performance of future fusion devices, which is an active area of research.

Finally, further development of both theory and simulation codes beyond current approaches is necessary. Edge dynamics and transport are inherently multi-scale, spanning from pedestal-scale modes like ELMs to electron-scale turbulence driven by ETG modes, and multi-channel, affecting particle and heat transport in both ion and electron channels. While an initial approach, as used in this thesis for turbulent transport, is to treat these dynamics separately, future progress would highly benefit from approaches integrating all these dynamics, such as recent coupled core-edge and full-f codes.

In conclusion, a deeper understanding of the contribution of turbulent transport processes to plasma edge dynamics would ultimately provide valuable insights for controlling and developing operational regimes compatible with future fusion reactors. The combination of advances in modeling capabilities, supported by high-performance computing, and plasma operations in magnetically confined plasma experiments with advanced diagnostics and novel data analysis techniques, are essential for improving our understanding of edge plasma physics. Progress in these research areas will be key to the success of magnetic confinement fusion as a viable energy source.

Bibliography

[1] J. Garcia, E. de la Luna, M. Sertoli, et al. "New H-mode regimes with small ELMs and high thermal confinement in the Joint European Torus". en. In: *Physics of Plasmas* 29.3 (Mar. 2022), p. 032505. ISSN: 1070-664X, 1089-7674. DOI: 10.1063/5.0072236. URL: https://pubs.aip.org/pop/article/29/3/032505/2847797/New-H-mode-regimes-with-small-ELMs-and-high (cit. on pp. 9, 41, 43, 55, 58).

[2] J. G. Lambert, C. A. S. Hall, S. Balogh, et al. "Energy, EROI and quality of life". In: *Energy Policy* 64 (Jan. 2014), pp. 153–167. ISSN: 0301-4215. DOI: 10.1016/j.enpol.2013.07.001. URL: https://www.sciencedirect.com/science/article/pii/S0301421513006447 (cit. on p. 30).

[3] H. Ritchie, P. Rosado, and M. Roser. "Energy Production and Consumption". In: *Our World in Data* (2020). URL: https://ourworldindata.org/energy-production-consumption (cit. on p. 31).

[4] Intergovernmental Panel on Climate Change (IPCC). *Climate Change 2021 – The Physical Science Basis: Working Group I Contribution to the Sixth Assessment Report of the Intergovernmental Panel on Climate Change*. Cambridge University Press, 2023. URL: https://doi.org/10.1017/9781009157896 (cit. on p. 31).

[5] A. S. Eddington. "The Internal Constitution of the Stars". In: *The Scientific Monthly* 11.4 (1920). Publisher: American Association for the Advancement of Science, pp. 297–303. ISSN: 0096-3771. URL: https://www.jstor.org/stable/6491 (cit. on p. 32).

[6] M. L. E. Oliphant, P. Harteck, and E. Rutherford. "Transmutation effects observed with heavy hydrogen". In: *Proceedings of the Royal Society of London. Series A, Containing Papers of a Mathematical and Physical Character* 144.853 (Jan. 1997). Publisher: Royal Society, pp. 692–703. DOI: 10.1098/rspa.1934.0077. URL: https://royalsocietypublishing.org/doi/10.1098/rspa.1934.0077 (cit. on p. 32).

[7] M. L. E. Oliphant and E. Rutherford. "Experiments on the transmutation of elements by protons". In: *Proceedings of the Royal Society of London. Series A, Containing Papers of a Mathematical and Physical Character* 141.843 (Jan. 1997). Publisher: Royal Society, pp. 259–281. DOI: 10.1098/rspa.1933.0117. URL: https://royalsocietypublishing.org/doi/10.1098/rspa.1933.0117 (cit. on p. 32).

[8] H. A. Bethe. "Energy Production in Stars". In: *Physical Review* 55.5 (Mar. 1939). Publisher: American Physical Society, pp. 434–456. DOI: 10.1103/PhysRev.55.434. URL: https://link.aps.org/doi/10.1103/PhysRev.55.434 (cit. on p. 32).

[9] J. P. Freidberg. *Plasma physics and fusion energy*. OCLC: ocm71808136. Cambridge: Cambridge University Press, 2007. ISBN: 978-0-521-85107-7 978-0-521-73317-5 (cit. on pp. 32, 33, 36).

[10] A. Fasoli. "Essay: Overcoming the Obstacles to a Magnetic Fusion Power Plant". In: *Physical Review Letters* 130.22 (May 2023). Publisher: American Physical Society, p. 220001. DOI: 10.1103/PhysRevLett.130.220001. URL: https://link.aps.org/doi/10.1103/PhysRevLett.130.220001 (cit. on p. 32).

[11] J. Wesson and D. J. Campbell. *Tokamaks*. en. Clarendon Press, 2004. ISBN: 978-0-19-850922-6 (cit. on pp. 33, 36, 39, 40, 42, 48).

[12] J. D. Huba, D. L. Book, and Naval Research Laboratory (U.S.) *NRL Plasma Formulary*. NRL publication. Naval Research Laboratory, 1998. URL: https://books.google.fr/books?id=19HvAAAAMAAJ (cit. on p. 33).

[13] J. M. Dawson. "16 - Advanced Fusion Reactors". In: *Fusion*. Ed. by E. Teller. Academic Press, 1981, pp. 453–501. ISBN: 978-0-12-685241-7. DOI: https://doi.org/10.1016/B978-0-12-685241-7.50013-X. URL: https://www.sciencedirect.com/science/article/pii/B978012685241750013X (cit. on p. 34).

[14] R. M. Magee, K. Ogawa, T. Tajima, et al. "First measurements of p11B fusion in a magnetically confined plasma". In: *Nature Communications* 14.1 (Feb. 2023). ISSN: 2041-1723. DOI: 10.1038/s41467-023-36655-1. URL: http://dx.doi.org/10.1038/s41467-023-36655-1 (cit. on p. 34).

[15] S. Atzeni and J. Meyer-ter-Vehn. *The Physics of Inertial Fusion: BeamPlasma Interaction, Hydrodynamics, Hot Dense Matter*. International Series of Monographs on Physics. Oxford, New York: Oxford University Press, June 2004. ISBN: 978-0-19-856264-1 (cit. on p. 35).

[16] J. D. Lawson. "Some Criteria for a Power Producing Thermonuclear Reactor". en. In: *Proceedings of the Physical Society. Section B* 70.1 (Jan. 1957), p. 6. ISSN: 0370-1301. DOI: 10.1088/0370-1301/70/1/303. URL: https://dx.doi.org/10.1088/0370-1301/70/1/303 (cit. on p. 36).

[17] W. M. Stacey. *Fusion Plasma Physics*. en. 1st ed. Wiley, Aug. 2012. ISBN: 978-3-527-41134-4 978-3-527-66951-6. DOI: 10.1002/9783527669516. URL: https://onlinelibrary.wiley.com/doi/book/10.1002/9783527669516 (cit. on pp. 36, 39).

[18] R. J. Goldston. *Introduction to Plasma Physics*. Boca Raton: CRC Press. ISBN: 978-0-367-80695-8. DOI: 10.1201/9780367806958 (cit. on pp. 36, 38, 39).

[19] F. F. Chen. *Introduction to Plasma Physics and Controlled Fusion*. en. URL: https://link.springer.com/book/10.1007/978-3-319-22309-4 (cit. on p. 36).

[20] W. D. D'haeseleer, W. N. G. Hitchon, J. D. Callen, et al. *Flux Coordinates and Magnetic Field Structure*. Berlin, Heidelberg: Springer Berlin Heidelberg, 1991. ISBN: 978-3-642-75597-2 978-3-642-75595-8. DOI: 10.1007/978-3-642-75595-8. URL: http://link.springer.com/10.1007/978-3-642-75595-8 (cit. on pp. 39, 81, 82).

[21] J. P. Freidberg. *Ideal MHD*. Cambridge: Cambridge University Press, 2014. ISBN: 978-1-107-00625-6 (cit. on pp. 40, 44).

[22] H. Zohm, ed. *Magnetohydrodynamic Stability of Tokamaks*. en. 1st ed. Wiley, Dec. 2014. ISBN: 978-3-527-41232-7 978-3-527-67737-5. DOI: 10.1002/9783527677375. URL: https://onlinelibrary.wiley.com/doi/book/10.1002/9783527677375 (cit. on p. 40).

[23] X. Garbet. "Introduction to Drift Wave Turbulence Modelling". en. In: *Fusion Science and Technology* 61.2T (Feb. 2012), pp. 161–168. ISSN: 1536-1055, 1943-7641. DOI: 10.13182/FST12-A13503. URL: https://www.tandfonline.com/doi/full/10.13182/FST12-A13503 (cit. on p. 40).

[24] X. Litaudon, S. Abduallev, M. Abhangi, et al. "Overview of the JET results in support to ITER". In: *Nuclear Fusion* 57.10 (June 2017), p. 102001. DOI: 10.1088/1741-4326/aa5e28. URL: https://dx.doi.org/10.1088/1741-4326/aa5e28 (cit. on p. 41).

[25] J. Mailloux, N. Abid, K. Abraham, et al. "Overview of JET results for optimising ITER operation". In: *Nuclear Fusion* 62.4 (June 2022), p. 042026. DOI: 10.1088/1741-4326/ac47b4. URL: https://dx.doi.org/10.1088/1741-4326/ac47b4 (cit. on p. 41).

[26] C. F. Maggi, D. Abate, N. Abid, et al. "Overview of T and D–T results in JET with ITER-like wall". In: *Nuclear Fusion* 64.11 (Aug. 2024), p. 112012. DOI: 10.1088/1741-4326/ad3e16. URL: https://dx.doi.org/10.1088/1741-4326/ad3e16 (cit. on p. 41).

[27] E. de la Luna, J. Garcia, M. Sertoli, et al. "Exploring the physics of a high-performance H-mode scenario with small ELMs at low collisionality in JET with Be/W wall". In: *Nuclear Fusion* 64.9 (July 2024), p. 096014. DOI: 10.1088/1741-4326/ad5fa0. URL: https://dx.doi.org/10.1088/1741-4326/ad5fa0 (cit. on pp. 41, 55).

[28] ITER Physics Expert Group on Confinement, Transport, ITER Physics Expert Group on Confinement Modelling, et al. "Chapter 2: Plasma confinement and transport". en. In: *Nuclear Fusion* 39.12 (Dec. 1999), p. 2175. ISSN: 0029-5515. DOI: 10.1088/0029-5515/39/12/302. URL: https://dx.doi.org/10.1088/0029-5515/39/12/302 (cit. on pp. 41, 56).

[29] F. Wagner, G. Becker, K. Behringer, et al. "Regime of Improved Confinement and High Beta in Neutral-Beam-Heated Divertor Discharges of the ASDEX Tokamak". en. In: *Physical Review Letters* 49.19 (Nov. 1982), pp. 1408–1412. ISSN: 0031-9007. DOI: 10.1103/PhysRevLett.49.1408. URL: https://link.aps.org/doi/10.1103/PhysRevLett.49.1408 (cit. on p. 42).

[30] F. Wagner. "A quarter-century of H-mode studies". In: *Plasma Physics and Controlled Fusion* 49.12B (Nov. 2007), B1. DOI: 10.1088/0741-3335/49/12B/S01. URL: https://dx.doi.org/10.1088/0741-3335/49/12B/S01 (cit. on p. 42).

[31] P. Gohil. "Edge transport barriers in magnetic fusion plasmas". en. In: *Comptes Rendus. Physique* 7.6 (July 2006), pp. 606–621. ISSN: 1878-1535. DOI: 10.1016/j.crhy.2006.06.006. URL: https://comptes-rendus.academie-sciences.fr/physique/articles/10.1016/j.crhy.2006.06.006/ (cit. on p. 42).

[32] R. J. Groebner and T. N. Carlstrom. "Critical edge parameters for H-mode transition in DIII-D". In: *Plasma Physics and Controlled Fusion* 40.5 (May 1998), p. 673. DOI: 10.1088/0741-3335/40/5/021. URL: https://dx.doi.org/10.1088/0741-3335/40/5/021 (cit. on p. 42).

[33] R. J. Groebner, D. R. Baker, K. H. Burrell, et al. "Progress in quantifying the edge physics of the H mode regime in DIII-D". en. In: *Nuclear Fusion* 41.12 (Dec. 2001), p. 1789. ISSN: 0029-5515. DOI: 10.1088/0029-5515/41/12/306. URL: https://dx.doi.org/10.1088/0029-5515/41/12/306 (cit. on pp. 42, 68).

[34] T. Carter. *Drift waves, turbulence and transport in the laboratory*. en (cit. on p. 43).

[35] P. W. Terry. "Suppression of turbulence and transport by sheared flow". en. In: *Reviews of Modern Physics* 72.1 (Jan. 2000), pp. 109–165. ISSN: 0034-6861, 1539-0756. DOI: 10.1103/RevModPhys.72.109. URL: https://link.aps.org/doi/10.1103/RevModPhys.72.109 (cit. on pp. 42, 52, 104, 107).

[36] K. H. Burrell. "Role of sheared $E \times B$ flow in self-organized, improved confinement states in magnetized plasmas". en. In: *Physics of Plasmas* 27.6 (June 2020), p. 060501. ISSN: 1070-664X, 1089-7674. DOI: 10.1063/1.5142734. URL: https://pubs.aip.org/pop/article/27/6/060501/153617/Role-of-sheared-E-B-flow-in-self-organized (cit. on pp. 42, 52, 80, 104, 107).

[37] H. Zohm. "Edge localized modes (ELMs)". en. In: *Plasma Physics and Controlled Fusion* 38.2 (Feb. 1996), pp. 105–128. ISSN: 0741-3335, 1361-6587. DOI: 10.1088/0741-3335/38/2/001. URL: https://iopscience.iop.org/article/10.1088/0741-3335/38/2/001 (cit. on p. 43).

[38] J. W. Connor. "Edge-localized modes - physics and theory". en. In: *Plasma Physics and Controlled Fusion* 40.5 (May 1998), pp. 531–542. ISSN: 0741-3335, 1361-6587. DOI: 10.1088/0741-3335/40/5/002. URL: https://iopscience.iop.org/article/10.1088/0741-3335/40/5/002 (cit. on p. 43).

[39] A. W. Leonard. "Edge-localized-modes in tokamaks". en. In: *Physics of Plasmas* 21.9 (Sept. 2014), p. 090501. ISSN: 1070-664X, 1089-7674. DOI: 10.1063/1.4894742. URL: https://pubs.aip.org/pop/article/21/9/090501/625104/Edge-localized-modes-in-tokamaksa (cit. on p. 43).

[40] E. Viezzer. "Access and sustainment of naturally ELM-free and small-ELM regimes". en. In: *Nuclear Fusion* 58.11 (Sept. 2018). Publisher: IOP Publishing, p. 115002. ISSN: 0029-5515. DOI: 10.1088/1741-4326/aac222. URL: https://dx.doi.org/10.1088/1741-4326/aac222 (cit. on p. 43).

[41] E. Viezzer, M.E. Austin, M. Bernert, et al. "Prospects of core–edge integrated no-ELM and small-ELM scenarios for future fusion devices". en. In: *Nuclear Materials and Energy* 34 (Mar. 2023), p. 101308. ISSN: 23521791. DOI: 10.1016/j.nme.2022.101308. URL: https://linkinghub.elsevier.com/retrieve/pii/S2352179122001892 (cit. on p. 43).

[42] L. Frassinetti, S. Saarelma, G. Verdoolaege, et al. “Pedestal structure, stability and scalings in JET-ILW: the EUROfusion JET-ILW pedestal database”. en. In: *Nuclear Fusion* 61.1 (Jan. 2021), p. 016001. ISSN: 0029-5515, 1741-4326. DOI: 10.1088/1741-4326/abb79e. URL: https://iopscience.iop.org/article/10.1088/1741-4326/abb79e (cit. on pp. 44, 68).

[43] E. Wolfrum, M. Beurskens, M.G. Dunne, et al. “Impact of wall materials and seeding gases on the pedestal and on core plasma performance”. In: *Nuclear Materials and Energy* 12 (2017). Proceedings of the 22nd International Conference on Plasma Surface Interactions 2016, 22nd PSI, pp. 18–27. ISSN: 2352-1791. DOI: https://doi.org/10.1016/j.nme.2017.01.002. URL: https://www.sciencedirect.com/science/article/pii/S2352179116302290 (cit. on p. 44).

[44] D. Lortz. “The general “peeling” instability”. In: *Nuclear Fusion* 15.1 (Feb. 1975), p. 49. DOI: 10.1088/0029-5515/15/1/007. URL: https://dx.doi.org/10.1088/0029-5515/15/1/007 (cit. on p. 44).

[45] J. W. Connor, R. J. Hastie, H. R. Wilson, et al. “Magnetohydrodynamic stability of tokamak edge plasmas”. In: *Physics of Plasmas* 5.7 (July 1998), pp. 2687–2700. ISSN: 1070-664X. DOI: 10.1063/1.872956. URL: https://doi.org/10.1063/1.872956 (cit. on p. 44).

[46] P. B. Snyder, R. J. Groebner, A. W. Leonard, et al. “Development and validation of a predictive model for the pedestal height”. en. In: *Physics of Plasmas* 16.5 (May 2009), p. 056118. ISSN: 1070-664X, 1089-7674. DOI: 10.1063/1.3122146. URL: https://pubs.aip.org/pop/article/16/5/056118/677838/Development-and-validation-of-a-predictive-model (cit. on p. 44).

[47] P. B. Snyder, N. Aiba, M. Beurskens, et al. “Pedestal stability comparison and ITER pedestal prediction”. en. In: *Nuclear Fusion* 49.8 (July 2009), p. 085035. ISSN: 0029-5515. DOI: 10.1088/0029-5515/49/8/085035. URL: https://dx.doi.org/10.1088/0029-5515/49/8/085035 (cit. on p. 44).

[48] P. B. Snyder, R. J. Groebner, J. W. Hughes, et al. “A first-principles predictive model of the pedestal height and width: development, testing and ITER optimization with the EPED model”. en. In: *Nuclear Fusion* 51.10 (Oct. 2011), p. 103016. ISSN: 0029-5515, 1741-4326. DOI: 10.1088/0029-5515/51/10/103016. URL: https://iopscience.iop.org/article/10.1088/0029-5515/51/10/103016 (cit. on p. 44).

[49] P. Helander and D. J. Sigmar. *Collisional Transport in Magnetized Plasmas*. en. Cambridge University Press, Oct. 2005. ISBN: 978-0-521-02098-5 (cit. on pp. 44, 45, 70, 71).

[50] R. J. Groebner and S. Saarelma. “Elements of H-mode pedestal structure”. en. In: *Plasma Physics and Controlled Fusion* 65.7 (May 2023). Publisher: IOP Publishing, p. 073001. ISSN: 0741-3335. DOI: 10.1088/1361-6587/acd478. URL: https://dx.doi.org/10.1088/1361-6587/acd478 (cit. on p. 44).

[51] C. F. Maggi, S. Saarelma, F. J. Casson, et al. “Pedestal confinement and stability in JET-ILW ELMy H-modes”. In: *Nuclear Fusion* 55.11 (Oct. 2015), p. 113031. DOI: 10.1088/0029-5515/55/11/113031. URL: https://dx.doi.org/10.1088/0029-5515/55/11/113031 (cit. on p. 44).

[52] A. E. Hubbard. “Physics and scaling of the H-mode pedestal”. In: *Plasma Physics and Controlled Fusion* 42.5A (May 2000), A15. DOI: 10.1088/0741-3335/42/5A/302. URL: https://dx.doi.org/10.1088/0741-3335/42/5A/302 (cit. on p. 44).

[53] T. Fujita. “Spatial structure of internal and edge transport barriers”. In: *Plasma Physics and Controlled Fusion* 44.5A (Apr. 2002), A19. DOI: 10.1088/0741-3335/44/5A/302. URL: https://dx.doi.org/10.1088/0741-3335/44/5A/302 (cit. on p. 44).

[54] A. W. Leonard. “Progress in characterization of the H-mode pedestal”. In: *Journal of Physics: Conference Series* 123.1 (July 2008), p. 012001. DOI: 10.1088/1742-6596/123/1/012001. URL: https://dx.doi.org/10.1088/1742-6596/123/1/012001 (cit. on p. 44).

[55] C. F. Maggi. “Progress in understanding the physics of the H-mode pedestal and ELM dynamics”. In: *Nuclear Fusion* 50.6 (May 2010), p. 066001. DOI: 10.1088/0029-5515/50/6/066001. URL: https://dx.doi.org/10.1088/0029-5515/50/6/066001 (cit. on p. 44).

[56] H. Urano. “Pedestal structure in H-mode plasmas”. en. In: *Nuclear Fusion* 54.11 (Nov. 2014). Publisher: IOP Publishing, p. 116001. ISSN: 0029-5515. DOI: 10.1088/0029-5515/54/11/116001. URL: https://dx.doi.org/10.1088/0029-5515/54/11/116001 (cit. on p. 44).

[57] F. L. Hinton and R. D. Hazeltine. “Theory of plasma transport in toroidal confinement systems”. In: *Reviews of Modern Physics* 48.2 (Apr. 1976). Publisher: American Physical Society, pp. 239–308. DOI: 10.1103/RevModPhys.48.239. URL: https://link.aps.org/doi/10.1103/RevModPhys.48.239 (cit. on p. 45).

[58] X. Garbet. “Turbulence in fusion plasmas: key issues and impact on transport modelling”. en. In: *Plasma Physics and Controlled Fusion* 43.12A (Nov. 2001), A251. ISSN: 0741-3335. DOI: 10.1088/0741-3335/43/12A/319. URL: https://dx.doi.org/10.1088/0741-3335/43/12A/319 (cit. on p. 45).

[59] X. Garbet, P. Mantica, C. Angioni, et al. “Physics of transport in tokamaks”. en. In: *Plasma Physics and Controlled Fusion* 46.12B (Nov. 2004), B557. ISSN: 0741-3335. DOI: 10.1088/0741-3335/46/12B/045. URL: https://dx.doi.org/10.1088/0741-3335/46/12B/045 (cit. on p. 45).

[60] E. J. Doyle, W. A. Houlberg, Y. Kamada, et al. “Chapter 2: Plasma confinement and transport”. en. In: *Nuclear Fusion* 47.6 (June 2007), S18. ISSN: 0029-5515. DOI: 10.1088/0029-5515/47/6/S02. URL: https://dx.doi.org/10.1088/0029-5515/47/6/S02 (cit. on p. 45).

[61] W. M. Tang. “Microinstability theory in tokamaks”. In: *Nuclear Fusion* 18.8 (Aug. 1978), p. 1089. DOI: 10.1088/0029-5515/18/8/006. URL: https://dx.doi.org/10.1088/0029-5515/18/8/006 (cit. on p. 45).

[62] W. Horton. “Drift waves and transport”. en. In: *Reviews of Modern Physics* 71.3 (Apr. 1999), pp. 735–778. ISSN: 0034-6861, 1539-0756. DOI: 10.1103/RevModPhys.71.735. URL: https://link.aps.org/doi/10.1103/RevModPhys.71.735 (cit. on pp. 45, 46, 48).

[63] A. Dinklage, T. Klinger, G. Marx, et al., eds. *Plasma Physics: Confinement, Transport and Collective Effects*. en. Vol. 670. Lecture Notes in Physics. Berlin, Heidelberg: Springer, 2005. ISBN: 978-3-540-25274-0 978-3-540-31521-6. DOI: 10.1007/b103882. URL: http://link.springer.com/10.1007/b103882 (cit. on p. 46).

[64] L. I. Rudakov and R. Z. Sagdeev. “On the Instability of a Nonuniform Rarefied Plasma in a Strong Magnetic Field”. In: *Soviet Physics Doklady* 6 (Nov. 1961), p. 415 (cit. on p. 46).

[65] B. Coppi, M. N. Rosenbluth, and R. Z. Sagdeev. “Instabilities due to Temperature Gradients in Complex Magnetic Field Configurations”. In: *The Physics of Fluids* 10.3 (Mar. 1967), pp. 582–587. ISSN: 0031-9171. DOI: 10.1063/1.1762151. URL: https://doi.org/10.1063/1.1762151 (cit. on pp. 46, 48).

[66] F. Romanelli. “Ion temperature-gradient-driven modes and anomalous ion transport in tokamaks”. en. In: *Physics of Fluids B: Plasma Physics* 1.5 (May 1989), pp. 1018–1025. ISSN: 0899-8221. DOI: 10.1063/1.859023. URL: https://pubs.aip.org/pfb/article/1/5/1018/894288/Ion-temperature-gradient-driven-modes-and (cit. on pp. 47, 48, 175).

[67] W. Horton, B. G. Hong, and W. M. Tang. “Toroidal electron temperature gradient driven drift modes”. In: *The Physics of Fluids* 31.10 (Oct. 1988), pp. 2971–2983. ISSN: 0031-9171. DOI: 10.1063/1.866954. URL: https://doi.org/10.1063/1.866954 (cit. on pp. 47, 49).

[68] Richard Fitzpatrick. *Plasma Physics: An Introduction*. Boca Raton: CRC Press, Aug. 2014. ISBN: 978-0-429-16906-9. DOI: 10.1201/b17263 (cit. on p. 47).

[69] P. J. Catto, M. N. Rosenbluth, and C. S. Liu. “Parallel velocity shear instabilities in an inhomogeneous plasma with a sheared magnetic field”. In: *The Physics of Fluids* 16.10 (Oct. 1973), pp. 1719–1729. ISSN: 0031-9171. DOI: 10.1063/1.1694200. URL: https://doi.org/10.1063/1.1694200 (cit. on p. 48).

[70] N. D’Angelo. “Kelvin—Helmholtz Instability in a Fully Ionized Plasma in a Magnetic Field”. In: *The Physics of Fluids* 8.9 (Sept. 1965), pp. 1748–1750. ISSN: 0031-9171. DOI: 10.1063/1.1761496. URL: https://doi.org/10.1063/1.1761496 (cit. on p. 48).

[71] R. D. Hazeltine, D. Dobrott, and T. S. Wang. “Kinetic theory of tearing instability”. In: *The Physics of Fluids* 18.12 (Dec. 1975), pp. 1778–1786. ISSN: 0031-9171. DOI: 10.1063/1.861097. eprint: https://pubs.aip.org/aip/pfl/article-pdf/18/12/1778/12677837/1778_1_online.pdf. URL: https://doi.org/10.1063/1.861097 (cit. on pp. 48, 49).

[72] J. F. Drake and Y. C. Lee. "Kinetic theory of tearing instabilities". In: *The Physics of Fluids* 20.8 (Aug. 1977), pp. 1341–1353. ISSN: 0031-9171. DOI: 10.1063/1.862017. eprint: https://pubs.aip.org/aip/pfl/article-pdf/20/8/1341/12612734/1341_1_online.pdf. URL: https://doi.org/10.1063/1.862017 (cit. on pp. 48, 49).

[73] D. R. Hatch, M. Kotschenreuther, S. Mahajan, et al. "A gyrokinetic perspective on the JET-ILW pedestal". en. In: *Nuclear Fusion* 57.3 (Jan. 2017). Publisher: IOP Publishing, p. 036020. ISSN: 0029-5515. DOI: 10.1088/1741-4326/aa51e1. URL: https://dx.doi.org/10.1088/1741-4326/aa51e1 (cit. on p. 49).

[74] D. R. Hatch, M. Kotschenreuther, S. M. Mahajan, et al. "Direct gyrokinetic comparison of pedestal transport in JET with carbon and ITER-like walls". en. In: *Nuclear Fusion* 59.8 (July 2019). Publisher: IOP Publishing, p. 086056. ISSN: 0029-5515. DOI: 10.1088/1741-4326/ab25bd. URL: https://dx.doi.org/10.1088/1741-4326/ab25bd (cit. on p. 49).

[75] I. Predebon, D. R. Hatch, L. Frassinetti, et al. "Isotope mass dependence of pedestal transport in JET H-mode plasmas". In: *Nuclear Fusion* 63.3 (Feb. 2023), p. 036010. DOI: 10.1088/1741-4326/acb44f. URL: https://dx.doi.org/10.1088/1741-4326/acb44f (cit. on p. 49).

[76] M. Kotschenreuther, X. Liu, D. R. Hatch, et al. "Gyrokinetic analysis and simulation of pedestals to identify the culprits for energy losses using 'fingerprints'". In: *Nuclear Fusion* 59.9 (July 2019), p. 096001. DOI: 10.1088/1741-4326/ab1fa2. URL: https://dx.doi.org/10.1088/1741-4326/ab1fa2 (cit. on pp. 49, 94–96).

[77] B. Coppi and G. Rewoldt. "New Trapped-Electron Instability". In: *Phys. Rev. Lett.* 33 (22 Nov. 1974), pp. 1329–1332. DOI: 10.1103/PhysRevLett.33.1329. URL: https://link.aps.org/doi/10.1103/PhysRevLett.33.1329 (cit. on p. 49).

[78] B. B. Kadomtsev and O. P. Pogutse. "Turbulence in Toroidal Systems". en. In: *Reviews of Plasma Physics: Volume 5*. Ed. by M. A. Leontovich. Boston, MA: Springer US, 1995, pp. 249–400. ISBN: 978-1-4615-7793-5. DOI: 10.1007/978-1-4615-7793-5_2. URL: https://doi.org/10.1007/978-1-4615-7793-5_2 (cit. on p. 49).

[79] D. Told, F. Jenko, P. Xanthopoulos, et al. "Gyrokinetic microinstabilities in ASDEX Upgrade edge plasmas". en. In: *Physics of Plasmas* 15.10 (Oct. 2008), p. 102306. ISSN: 1070-664X, 1089-7674. DOI: 10.1063/1.3000132. URL: https://pubs.aip.org/pop/article/15/10/102306/262416/Gyrokinetic-microinstabilities-in-ASDEX-Upgrade (cit. on pp. 49, 92).

[80] D. R. Hatch, D. Told, F. Jenko, et al. "Gyrokinetic study of ASDEX Upgrade inter-ELM pedestal profile evolution". en. In: *Nuclear Fusion* 55.6 (May 2015). Publisher: IOP Publishing, p. 063028. ISSN: 0029-5515. DOI: 10.1088/0029-5515/55/6/063028. URL: https://dx.doi.org/10.1088/0029-5515/55/6/063028 (cit. on p. 49).

[81] W. M. Tang, J. W. Connor, and R. J. Hastie. "Kinetic-ballooning-mode theory in general geometry". en. In: *Nuclear Fusion* 20.11 (Nov. 1980), pp. 1439–1453. ISSN: 0029-5515, 1741-4326. DOI: 10.1088/0029-5515/20/11/011. URL: https://iopscience.iop.org/article/10.1088/0029-5515/20/11/011 (cit. on p. 49).

[82] W. M. Tang, G. Rewoldt, C. Z. Cheng, et al. "Kinetic analysis of MHD ballooning modes in tokamaks". In: *Nuclear Fusion* 25.2 (Feb. 1985), p. 151. DOI: 10.1088/0029-5515/25/2/003. URL: https://dx.doi.org/10.1088/0029-5515/25/2/003 (cit. on pp. 49, 95).

[83] Z. Yan, G. R. McKee, R. J. Groebner, et al. "High-Frequency Coherent Edge Fluctuations in a High-Pedestal-Pressure Quiescent H-Mode Plasma". In: *Phys. Rev. Lett.* 107 (5 July 2011), p. 055004. DOI: 10.1103/PhysRevLett.107.055004. URL: https://link.aps.org/doi/10.1103/PhysRevLett.107.055004 (cit. on p. 49).

[84] D. Dickinson, C. M. Roach, S. Saarelma, et al. "Kinetic Instabilities that Limit β in the Edge of a Tokamak Plasma: A Picture of an H-Mode Pedestal". In: *Phys. Rev. Lett.* 108 (13 Mar. 2012), p. 135002. DOI: 10.1103/PhysRevLett.108.135002. URL: https://link.aps.org/doi/10.1103/PhysRevLett.108.135002 (cit. on p. 49).

[85] D. J. Applegate, C. M. Roach, J. W. Connor, et al. "Micro-tearing modes in the mega ampere spherical tokamak". In: *Plasma Physics and Controlled Fusion* 49.8 (July 2007), p. 1113. DOI: 10.1088/0741-3335/49/8/001. URL: https://dx.doi.org/10.1088/0741-3335/49/8/001 (cit. on p. 49).

[86] K. L. Wong, S. Kaye, D. R. Mikkelsen, et al. "Microtearing Instabilities and Electron Transport in the NSTX Spherical Tokamak". In: *Phys. Rev. Lett.* 99 (13 Sept. 2007), p. 135003. DOI: 10.1103/PhysRevLett.99.135003. URL: https://link.aps.org/doi/10.1103/PhysRevLett.99.135003 (cit. on p. 49).

[87] W. Guttenfelder, J. Candy, S. M. Kaye, et al. "Electromagnetic Transport from Microtearing Mode Turbulence". In: *Phys. Rev. Lett.* 106 (15 Apr. 2011), p. 155004. DOI: 10.1103/PhysRevLett.106.155004. URL: https://link.aps.org/doi/10.1103/PhysRevLett.106.155004 (cit. on p. 49).

[88] H. Doerk, F. Jenko, M. J. Pueschel, et al. "Gyrokinetic Microtearing Turbulence". In: *Phys. Rev. Lett.* 106 (15 Apr. 2011), p. 155003. DOI: 10.1103/PhysRevLett.106.155003. URL: https://link.aps.org/doi/10.1103/PhysRevLett.106.155003 (cit. on p. 49).

[89] S. Maeyama, T.-H. Watanabe, and A. Ishizawa. "Suppression of Ion-Scale Microtearing Modes by Electron-Scale Turbulence via Cross-Scale Nonlinear Interactions in Tokamak Plasmas". In: *Phys. Rev. Lett.* 119 (19 Nov. 2017), p. 195002. DOI: 10.1103/PhysRevLett.119.195002. URL: https://link.aps.org/doi/10.1103/PhysRevLett.119.195002 (cit. on p. 49).

[90] M. J. Pueschel, D. R. Hatch, M. Kotschenreuther, et al. "Multi-scale interactions of microtearing turbulence in the tokamak pedestal". In: *Nuclear Fusion* 60.12 (Oct. 2020), p. 124005. DOI: 10.1088/1741-4326/abba49. URL: https://dx.doi.org/10.1088/1741-4326/abba49 (cit. on p. 49).

[91] D. R. Hatch, M. Kotschenreuther, S. Mahajan, et al. “Microtearing turbulence limiting the JET-ILW pedestal”. en. In: *Nuclear Fusion* 56.10 (Aug. 2016). Publisher: IOP Publishing, p. 104003. ISSN: 0029-5515. DOI: 10.1088/0029-5515/56/10/104003. URL: https://dx.doi.org/10.1088/0029-5515/56/10/104003 (cit. on pp. 49, 91, 95).

[92] D. Dickinson, C. M. Roach, S. Saarelma, et al. “Microtearing modes at the top of the pedestal”. In: *Plasma Physics and Controlled Fusion* 55.7 (June 2013), p. 074006. DOI: 10.1088/0741-3335/55/7/074006. URL: https://dx.doi.org/10.1088/0741-3335/55/7/074006 (cit. on p. 49).

[93] C. S. Liu, M. N. Rosenbluth, and C. W. Horton. “Electron Temperature-Gradient Instability and Anomalous Skin Effect in Tokamaks”. In: *Phys. Rev. Lett.* 29 (22 Nov. 1972), pp. 1489–1492. DOI: 10.1103/PhysRevLett.29.1489. URL: https://link.aps.org/doi/10.1103/PhysRevLett.29.1489 (cit. on p. 49).

[94] Y. C. Lee, J. Q. Dong, P. N. Guzdar, et al. “Collisionless electron temperature gradient instability”. In: *The Physics of Fluids* 30.5 (May 1987), pp. 1331–1339. ISSN: 0031-9171. DOI: 10.1063/1.866248. eprint: https://pubs.aip.org/aip/pfl/article-pdf/30/5/1331/12781080/1331_1_online.pdf. URL: https://doi.org/10.1063/1.866248 (cit. on p. 49).

[95] F. Jenko, W. Dorland, M. Kotschenreuther, et al. “Electron temperature gradient driven turbulence”. In: *Physics of Plasmas* 7.5 (May 2000), pp. 1904–1910. ISSN: 1070-664X. DOI: 10.1063/1.874014. URL: https://doi.org/10.1063/1.874014 (cit. on pp. 50, 122).

[96] F. Jenko, W. Dorland, and G. W. Hammett. “Critical gradient formula for toroidal electron temperature gradient modes”. en. In: *Physics of Plasmas* 8.9 (Sept. 2001), pp. 4096–4104. ISSN: 1070-664X, 1089-7674. DOI: 10.1063/1.1391261. URL: https://pubs.aip.org/pop/article/8/9/4096/265245/Critical-gradient-formula-for-toroidal-electron (cit. on pp. 50, 102, 122).

[97] J. F. Parisi, F.x I. Parra, C. M. Roach, et al. “Toroidal and slab ETG instability dominance in the linear spectrum of JET-ILW pedestals”. en. In: *Nuclear Fusion* 60.12 (Oct. 2020). Publisher: IOP Publishing, p. 126045. ISSN: 0029-5515. DOI: 10.1088/1741-4326/abb891. URL: https://dx.doi.org/10.1088/1741-4326/abb891 (cit. on pp. 50, 92).

[98] B. Chapman-Oplopoiou, D. R. Hatch, A. R. Field, et al. “The role of ETG modes in JET–ILW pedestals with varying levels of power and fuelling”. en. In: *Nuclear Fusion* 62.8 (June 2022). Publisher: IOP Publishing, p. 086028. ISSN: 0029-5515. DOI: 10.1088/1741-4326/ac7476. URL: https://dx.doi.org/10.1088/1741-4326/ac7476 (cit. on p. 50).

[99] W. Guttenfelder, R. J. Groebner, J. M. Canik, et al. “Testing predictions of electron scale turbulent pedestal transport in two DIII-D ELMy H-modes”. In: *Nuclear Fusion* 61.5 (Apr. 2021), p. 056005. DOI: 10.1088/1741-4326/abecc7. URL: https://dx.doi.org/10.1088/1741-4326/abecc7 (cit. on p. 50).

[100] E. Mazzucato, D. R. Smith, R. E. Bell, et al. "Short-Scale Turbulent Fluctuations Driven by the Electron-Temperature Gradient in the National Spherical Torus Experiment". In: *Phys. Rev. Lett.* 101 (7 Aug. 2008), p. 075001. DOI: 10.1103/PhysRevLett.101.075001. URL: https://link.aps.org/doi/10.1103/PhysRevLett.101.075001 (cit. on p. 50).

[101] S. Ichimaru. *Statistical Plasma Physics, Volume I.* ISBN: 978-0-8133-4178-1 (cit. on pp. 50, 73).

[102] P. H. Diamond, Sanae-I. Itoh, and K. Itoh. *Modern Plasma Physics: Volume 1: Physical Kinetics of Turbulent Plasmas*. Vol. 1. Cambridge: Cambridge University Press, 2010. ISBN: 978-0-521-86920-1. DOI: 10.1017/CBO9780511780875. URL: https://www.cambridge.org/core/books/modern-plasma-physics/862295AFE870A506FAD95E409B6045E8 (cit. on p. 50).

[103] E. Viezzer. "Radial electric field studies in the plasma edge of ASDEX Upgrade". PhD thesis. 2012 (cit. on pp. 51, 52).

[104] R. D. Hazeltine and J. D. Meiss. *Plasma Confinement*. en. Courier Corporation, Jan. 2003. ISBN: 978-0-486-43242-7 (cit. on pp. 51, 73).

[105] T. S. Hahm and K. H. Burrell. "Flow shear induced fluctuation suppression in finite aspect ratio shaped tokamak plasma". In: *Physics of Plasmas* 2.5 (May 1995), pp. 1648–1651. ISSN: 1070-664X. DOI: 10.1063/1.871313. eprint: https://pubs.aip.org/aip/pop/article-pdf/2/5/1648/19155960/1648_1_online.pdf. URL: https://doi.org/10.1063/1.871313 (cit. on p. 52).

[106] H. Biglari, P. H. Diamond, and P. W. Terry. "Influence of sheared poloidal rotation on edge turbulence". In: *Physics of Fluids B: Plasma Physics* 2.1 (Jan. 1990), pp. 1–4. ISSN: 0899-8221. DOI: 10.1063/1.859529. eprint: https://pubs.aip.org/aip/pfb/article-pdf/2/1/1/12784369/1_1_online.pdf. URL: https://doi.org/10.1063/1.859529 (cit. on p. 52).

[107] P. H. Diamond, S.-I. Itoh, K. Itoh, et al. "Zonal flows in plasma—a review". en. In: *Plasma Physics and Controlled Fusion* 47.5 (May 2005), R35–R161. ISSN: 0741-3335, 1361-6587. DOI: 10.1088/0741-3335/47/5/R01. URL: https://iopscience.iop.org/article/10.1088/0741-3335/47/5/R01 (cit. on pp. 52, 80).

[108] B. G. Hong, W. Horton, and Duk-In Choi. "Pressure gradient-driven modes in finite beta toroidal plasmas". In: *Plasma Physics and Controlled Fusion* 31.8 (July 1989), p. 1291. DOI: 10.1088/0741-3335/31/8/006. URL: https://dx.doi.org/10.1088/0741-3335/31/8/006 (cit. on p. 53).

[109] J. Y. Kim, W. Horton, and J. Q. Dong. "Electromagnetic effect on the toroidal ion temperature gradient mode". In: *Physics of Fluids B: Plasma Physics* 5.11 (Nov. 1993), pp. 4030–4039. ISSN: 0899-8221. DOI: 10.1063/1.860623. eprint: https://pubs.aip.org/aip/pfb/article-pdf/5/11/4030/12653101/4030_1_online.pdf. URL: https://doi.org/10.1063/1.860623 (cit. on p. 53).

[110] J. Y. Kim and W. Horton. "Electromagnetic effect on the toroidal electron temperature gradient mode". In: *Physics of Fluids B: Plasma Physics* 3.11 (Nov. 1991), pp. 3194–3197. ISSN: 0899-8221. DOI: 10.1063/1.859800. eprint: https://pubs.aip.org/aip/pfb/article-pdf/3/11/3194/12317441/3194_1_online.pdf. URL: https://doi.org/10.1063/1.859800 (cit. on p. 53).

[111] P. W. Terry, D. Carmody, H. Doerk, et al. "Overview of gyrokinetic studies of finite-β microturbulence". en. In: *Nuclear Fusion* 55.10 (Oct. 2015), p. 104011. ISSN: 0029-5515, 1741-4326. DOI: 10.1088/0029-5515/55/10/104011. URL: https://iopscience.iop.org/article/10.1088/0029-5515/55/10/104011 (cit. on p. 53).

[112] J. Citrin and P. Mantica. "Overview of tokamak turbulence stabilization by fast ions". en. In: *Plasma Physics and Controlled Fusion* 65.3 (Mar. 2023), p. 033001. ISSN: 0741-3335, 1361-6587. DOI: 10.1088/1361-6587/acab2b. URL: https://iopscience.iop.org/article/10.1088/1361-6587/acab2b (cit. on p. 53).

[113] M. J. Pueschel, M. Kammerer, and F. Jenko. "Gyrokinetic turbulence simulations at high plasma beta". en. In: *Physics of Plasmas* 15.10 (Oct. 2008), p. 102310. ISSN: 1070-664X, 1089-7674. DOI: 10.1063/1.3005380. URL: https://pubs.aip.org/pop/article/15/10/102310/262261/Gyrokinetic-turbulence-simulations-at-high-plasma (cit. on p. 53).

[114] M. J. Pueschel and F. Jenko. "Transport properties of finite-β microturbulence". en. In: *Physics of Plasmas* 17.6 (June 2010), p. 062307. ISSN: 1070-664X, 1089-7674. DOI: 10.1063/1.3435280. URL: https://pubs.aip.org/pop/article/17/6/062307/262476/Transport-properties-of-finite-microturbulence (cit. on pp. 53, 98).

[115] G. G. Whelan, M. J. Pueschel, and P. W. Terry. "Nonlinear Electromagnetic Stabilization of Plasma Microturbulence". In: *Physical Review Letters* 120.17 (Apr. 2018). Publisher: American Physical Society, p. 175002. DOI: 10.1103/PhysRevLett.120.175002. URL: https://link.aps.org/doi/10.1103/PhysRevLett.120.175002 (cit. on pp. 53, 120).

[116] B. D. Scott. "Drift wave versus interchange turbulence in tokamak geometry: Linear versus nonlinear mode structure". en. In: *Physics of Plasmas* 12.6 (June 2005), p. 062314. ISSN: 1070-664X, 1089-7674. DOI: 10.1063/1.1917866. URL: https://pubs.aip.org/pop/article/12/6/062314/762231/Drift-wave-versus-interchange-turbulence-in (cit. on pp. 53, 107, 113).

[117] B. D. Scott. "Tokamak edge turbulence: background theory and computation". en. In: *Plasma Physics and Controlled Fusion* 49.7 (July 2007), S25–S41. ISSN: 0741-3335, 1361-6587. DOI: 10.1088/0741-3335/49/7/S02. URL: https://iopscience.iop.org/article/10.1088/0741-3335/49/7/S02 (cit. on pp. 53, 107).

[118] B. D. Scott, A. Kendl, and T. Ribeiro. "Nonlinear Dynamics in the Tokamak Edge". en. In: *Contributions to Plasma Physics* 50.3-5 (2010), pp. 228–241. ISSN: 1521-3986. DOI: 10.1002/ctpp.201010039. URL: https://onlinelibrary.wiley.com/doi/abs/10.1002/ctpp.201010039 (cit. on pp. 53, 107, 113).

[119] N. Bonanomi, C. Angioni, P. C. Crandall, et al. "Effect of the isotope mass on the turbulent transport at the edge of L-mode plasmas in ASDEX Upgrade and JET-ILW". en. In: *Nuclear Fusion* 59.12 (Oct. 2019). Publisher: IOP Publishing, p. 126025. ISSN: 0029-5515. DOI: 10.1088/1741-4326/ab3ecc. URL: https://dx.doi.org/10.1088/1741-4326/ab3ecc (cit. on pp. 53, 85, 108, 113, 125).

[120] A. C. C. Sips, J. Schweinzer, T. C. Luce, et al. "Assessment of the baseline scenario at q95 3 for ITER". In: *Nuclear Fusion* 58.12 (Sept. 2018), p. 126010. DOI: 10.1088/1741-4326/aade57. URL: https://dx.doi.org/10.1088/1741-4326/aade57 (cit. on p. 55).

[121] N. Aiba, M. Honda, and K. Kamiya. "Impact of ion diamagnetic drift on MHD stability at edge pedestal in JT-60U rotating plasmas". In: *Nuclear Fusion* 57.2 (Sept. 2016), p. 022011. DOI: 10.1088/0029-5515/57/2/022011. URL: https://dx.doi.org/10.1088/0029-5515/57/2/022011 (cit. on p. 58).

[122] O. Sauter, C. Angioni, and Y. R. Lin-Liu. "Neoclassical conductivity and bootstrap current formulas for general axisymmetric equilibria and arbitrary collisionality regime". In: *Physics of Plasmas* 6.7 (July 1999), pp. 2834–2839. ISSN: 1070-664X. DOI: 10.1063/1.873240. URL: https://doi.org/10.1063/1.873240 (cit. on p. 58).

[123] O. Sauter, C. Angioni, and Y. R. Lin-Liu. "Erratum: "Neoclassical conductivity and bootstrap current formulas for general axisymmetric equilibria and arbitrary collisionality regime" [Phys. Plasmas 6, 2834 (1999)]". In: *Physics of Plasmas* 9.12 (Dec. 2002), pp. 5140–5140. ISSN: 1070-664X. DOI: 10.1063/1.1517052. URL: https://doi.org/10.1063/1.1517052 (cit. on p. 58).

[124] P. B. Snyder, R. J. Groebner, J. W. Hughes, et al. "A first-principles predictive model of the pedestal height and width: development, testing and ITER optimization with the EPED model". In: *Nuclear Fusion* 51.10 (Aug. 2011), p. 103016. DOI: 10.1088/0029-5515/51/10/103016. URL: https://dx.doi.org/10.1088/0029-5515/51/10/103016 (cit. on pp. 59, 97).

[125] R. J. Hawryluk. "An empirical approach to tokamak transport". In: *Physics of Plasmas Close to Thermonuclear Conditions*. Ed. by B. Coppi, G.G. Leotta, D. Pfirsch, et al. Pergamon, 1981, pp. 19–46. ISBN: 978-1-4832-8385-2. DOI: https://doi.org/10.1016/B978-1-4832-8385-2.50009-1. URL: https://www.sciencedirect.com/science/article/pii/B9781483283852500091 (cit. on p. 59).

[126] J. P. H. E. Ongena, I. Voitsekhovitch, M. Evrard, et al. "Numerical Transport Codes". In: *Fusion Science and Technology* 61.2T (Feb. 2012). Publisher: American Nuclear Society _eprint: https://doi.org/10.13182/FST12-A13505, pp. 180–189. ISSN: 1536-1055. DOI: 10.13182/FST12-A13505. URL: https://doi.org/10.13182/FST12-A13505 (cit. on p. 59).

[127] L. Frassinetti, M. N. A. Beurskens, R. Scannell, et al. "Spatial resolution of the JET Thomson scattering system". In: *Review of Scientific Instruments* 83.1 (Jan. 2012), p. 013506. ISSN: 0034-6748. DOI: 10.1063/1.3673467. URL: https://doi.org/10.1063/1.3673467 (cit. on p. 59).

[128] E. Delabie, N. Hawkes, T. M. Biewer, et al. “In situ wavelength calibration of the edge CXS spectrometers on JET”. In: *Review of Scientific Instruments* 87.11 (Aug. 2016), 11E525. ISSN: 0034-6748. DOI: 10.1063/1.4960306. URL: https://doi.org/10.1063/1.4960306 (cit. on p. 59).

[129] N. C. Hawkes, E. Delabie, S. Menmuir, et al. “Instrumentation for the upgrade to the JET core charge-exchange spectrometers”. In: *Review of Scientific Instruments* 89.10 (Aug. 2018), p. 10D113. ISSN: 0034-6748. DOI: 10.1063/1.5037639. URL: https://doi.org/10.1063/1.5037639 (cit. on p. 59).

[130] A. Thorman, E. Litherland-Smith, S. Menmuir, et al. “Visible spectroscopy of highly charged tungsten ions with the JET charge exchange diagnostic”. en. In: *Physica Scripta* 96.12 (Dec. 2021). Publisher: IOP Publishing, p. 125631. ISSN: 1402-4896. DOI: 10.1088/1402-4896/ac387b. URL: https://dx.doi.org/10.1088/1402-4896/ac387b (cit. on p. 59).

[131] Ž. Štancar, K.K. Kirov, F. Auriemma, et al. “Overview of interpretive modelling of fusion performance in JET DTE2 discharges with TRANSP”. In: *Nuclear Fusion* 63.12 (Nov. 2023), p. 126058. DOI: 10.1088/1741-4326/ad0310. URL: https://dx.doi.org/10.1088/1741-4326/ad0310 (cit. on pp. 60, 65).

[132] O. Sauter and SPC-EPFL. *INTERPOS*. Private communication (a publication is under development) (cit. on p. 63).

[133] A. Kramida, Yu. Ralchenko, J. Reader, et al. NIST Atomic Spectra Database (ver. 5.11), [Online]. Available: https://physics.nist.gov/asd. National Institute of Standards and Technology, Gaithersburg, MD. 2023 (cit. on p. 65).

[134] E. A. Belli, G. W. Hammett, and W. Dorland. “Effects of plasma shaping on nonlinear gyrokinetic turbulence”. In: *Physics of Plasmas* 15.9 (Sept. 2008), p. 092303. ISSN: 1070-664X. DOI: 10.1063/1.2972160. URL: https://doi.org/10.1063/1.2972160 (cit. on p. 65).

[135] L. L. Lao, H. St. John, R. D. Stambaugh, et al. “Reconstruction of current profile parameters and plasma shapes in tokamaks”. In: *Nuclear Fusion* 25.11 (Nov. 1985), p. 1611. DOI: 10.1088/0029-5515/25/11/007. URL: https://dx.doi.org/10.1088/0029-5515/25/11/007 (cit. on p. 65).

[136] L. C. Appel and I. Lupelli. “Equilibrium reconstruction in an iron core tokamak using a deterministic magnetisation model”. In: *Computer Physics Communications* 223 (2018), pp. 1–17. ISSN: 0010-4655. DOI: https://doi.org/10.1016/j.cpc.2017.09.016. URL: https://www.sciencedirect.com/science/article/pii/S001046551730303X (cit. on p. 65).

[137] V. D. Shafranov. “Plasma Equilibrium in a Magnetic Field”. In: *Reviews of Plasma Physics* 2 (Jan. 1966), p. 103 (cit. on p. 65).

[138] P. Xanthopoulos and F. Jenko. “Clebsch-type coordinates for nonlinear gyrokinetics in generic toroidal configurations”. In: *Physics of Plasmas* 13.9 (Sept. 2006), p. 092301. ISSN: 1070-664X. DOI: 10.1063/1.2338818. eprint: https://pubs.aip.org/aip/pop/article-pdf/doi/10.1063/1.2338818/14748399/092301_1_online.pdf. URL: https://doi.org/10.1063/1.2338818 (cit. on p. 65).

[139] J. D. Callen, A. J. Cole, and C. C. Hegna. "Toroidal rotation in tokamak plasmas". en. In: *Nuclear Fusion* 49.8 (July 2009), p. 085021. ISSN: 0029-5515. DOI: 10.1088/0029-5515/49/8/085021. URL: https://dx.doi.org/10.1088/0029-5515/49/8/085021 (cit. on pp. 69, 80).

[140] M. Landreman and D. R. Ernst. "Local and global Fokker–Planck neoclassical calculations showing flow and bootstrap current modification in a pedestal". en. In: *Plasma Physics and Controlled Fusion* 54.11 (Oct. 2012). Publisher: IOP Publishing, p. 115006. ISSN: 0741-3335. DOI: 10.1088/0741-3335/54/11/115006. URL: https://dx.doi.org/10.1088/0741-3335/54/11/115006 (cit. on pp. 70, 71).

[141] Gene Development Team. *The Gyrokinetic Plasma Turbulence Code Gene: User Manual* (cit. on pp. 71, 83, 101, 119, 129).

[142] F. Jenko, W. Dorland, M. Kotschenreuther, et al. "Electron temperature gradient driven turbulence". In: *Physics of Plasmas* 7.5 (May 2000), pp. 1904–1910. ISSN: 1070-664X. DOI: 10.1063/1.874014. URL: https://doi.org/10.1063/1.874014 (cit. on pp. 73, 81, 83).

[143] A. J. Brizard and T. S. Hahm. "Foundations of nonlinear gyrokinetic theory". In: *Reviews of Modern Physics* 79.2 (Apr. 2007). Publisher: American Physical Society, pp. 421–468. DOI: 10.1103/RevModPhys.79.421. URL: https://link.aps.org/doi/10.1103/RevModPhys.79.421 (cit. on pp. 74–76, 79).

[144] P. J. Catto. "Linearized gyro-kinetics". en. In: *Plasma Physics* 20.7 (July 1978), pp. 719–722. ISSN: 0032-1028. DOI: 10.1088/0032-1028/20/7/011. URL: https://iopscience.iop.org/article/10.1088/0032-1028/20/7/011 (cit. on p. 75).

[145] E. A. Frieman and L. Chen. "Nonlinear gyrokinetic equations for low-frequency electromagnetic waves in general plasma equilibria". en. In: *The Physics of Fluids* 25.3 (Mar. 1982), pp. 502–508. ISSN: 0031-9171. DOI: 10.1063/1.863762. URL: https://pubs.aip.org/pfl/article/25/3/502/830619/Nonlinear-gyrokinetic-equations-for-low-frequency (cit. on p. 75).

[146] I. G. Abel, G. G. Plunk, E. Wang, et al. "Multiscale gyrokinetics for rotating tokamak plasmas: fluctuations, transport and energy flows". en. In: *Reports on Progress in Physics* 76.11 (Nov. 2013), p. 116201. ISSN: 0034-4885, 1361-6633. DOI: 10.1088/0034-4885/76/11/116201. URL: https://iopscience.iop.org/article/10.1088/0034-4885/76/11/116201 (cit. on p. 75).

[147] R. G. Littlejohn. "A guiding center Hamiltonian: A new approach". en. In: *Journal of Mathematical Physics* 20.12 (Dec. 1979), pp. 2445–2458. ISSN: 0022-2488, 1089-7658. DOI: 10.1063/1.524053. URL: https://pubs.aip.org/jmp/article/20/12/2445/894195/A-guiding-center-Hamiltonian-A-new-approach (cit. on p. 75).

[148] J. R. Cary and A. J. Brizard. "Hamiltonian theory of guiding-center motion". In: *Reviews of Modern Physics* 81.2 (May 2009). Publisher: American Physical Society, pp. 693–738. DOI: 10.1103/RevModPhys.81.693. URL: https://link.aps.org/doi/10.1103/RevModPhys.81.693 (cit. on p. 75).

[149] E. Mazzucato. “Spectrum of Small-Scale Density Fluctuations in Tokamaks”. en. In: *Physical Review Letters* 48.26 (June 1982), pp. 1828–1830. ISSN: 0031-9007. DOI: 10.1103/PhysRevLett.48.1828. URL: https://link.aps.org/doi/10.1103/PhysRevLett.48.1828 (cit. on p. 76).

[150] D. Told. “Gyrokinetic Microturbulence in Transport Barriers”. PhD thesis (cit. on pp. 77, 79, 164).

[151] F. Merz. “Gyrokinetic simulation of multimode plasma turbulence”. PhD thesis (cit. on pp. 77, 79, 80, 82, 83, 86, 101, 164).

[152] J. Candy, R. E. Waltz, S. E. Parker, et al. “Relevance of the parallel nonlinearity in gyrokinetic simulations of tokamak plasmas”. en. In: *Physics of Plasmas* 13.7 (July 2006), p. 074501. ISSN: 1070-664X, 1089-7674. DOI: 10.1063/1.2220536. URL: https://pubs.aip.org/pop/article/13/7/074501/915222/Relevance-of-the-parallel-nonlinearity-in (cit. on p. 78).

[153] B. F. McMillan, J. Ball, and S. Brunner. “Simulating background shear flow in local gyrokinetic simulations”. en. In: *Plasma Physics and Controlled Fusion* 61.5 (Mar. 2019). Publisher: IOP Publishing, p. 055006. ISSN: 0741-3335. DOI: 10.1088/1361-6587/ab06a4. URL: https://dx.doi.org/10.1088/1361-6587/ab06a4 (cit. on p. 80).

[154] G. W. Hammett, W. Dorland, U. Maryland, et al. “Implementation of Large Scale E x B Shear Flow in the GS2 Gyrokinetic Turbulence Code”. en. In: () (cit. on p. 80).

[155] *gkw / gkw / wiki / Home — Bitbucket*. URL: https://bitbucket.org/gkw/gkw/wiki/Home (cit. on p. 81).

[156] M. A. Beer, S. C. Cowley, and G. W. Hammett. “Field-aligned coordinates for nonlinear simulations of tokamak turbulence”. en. In: *Physics of Plasmas* 2.7 (July 1995), pp. 2687–2700. ISSN: 1070-664X, 1089-7674. DOI: 10.1063/1.871232. URL: https://pubs.aip.org/pop/article/2/7/2687/261544/Field-aligned-coordinates-for-nonlinear (cit. on pp. 81, 84, 89, 164, 166, 167).

[157] X. Garbet. *Ballooning representation: an introduction* (cit. on p. 81).

[158] G. Merlo. “Flux-tube and global grid-based gyrokinetic simulations of plasma microturbulence and comparisons with experimental TCV measurements”. eng. PhD thesis. Lausanne: EPFL, 2016. DOI: 10.5075/epfl-thesis-7065 (cit. on pp. 81, 82).

[159] T. Goerler. “Multiscale effects in plasma microturbulence”. PhD thesis (cit. on pp. 82, 119, 165).

[160] S. Balay, S. Abhyankar, M. F. Adams, et al. *PETSc Web page*. 2024. URL: https://petsc.org/ (cit. on p. 83).

[161] V. Hernandez, J. E. Roman, and V. Vidal. “SLEPc: A scalable and flexible toolkit for the solution of eigenvalue problems”. In: *ACM Transactions on Mathematical Software* 31.3 (Sept. 2005), pp. 351–362. ISSN: 0098-3500. DOI: 10.1145/1089014.1089019. URL: https://doi.org/10.1145/1089014.1089019 (cit. on p. 83).

[162] J. E. Roman, M. Kammerer, F. Merz, et al. "Fast eigenvalue calculations in a massively parallel plasma turbulence code". In: *Parallel Computing*. Parallel Matrix Algorithms and Applications 36.5 (June 2010), pp. 339–358. ISSN: 0167-8191. DOI: 10.1016/j.parco.2009.12.001. URL: https://www.sciencedirect.com/science/article/pii/S0167819109001239 (cit. on p. 83).

[163] M. Dicorato, M. Muraglia, Y. Camenen, et al. "Gyrokinetic Stability Analysis of JET Pedestal Top Plasmas with Small-ELMs". In: *Journal of Physics: Conference Series* 2397.1 (Dec. 2022). Publisher: IOP Publishing, p. 012007. ISSN: 1742-6596. DOI: 10.1088/1742-6596/2397/1/012007. URL: https://dx.doi.org/10.1088/1742-6596/2397/1/012007 (cit. on p. 89).

[164] A. G. Peeters, Y. Camenen, F. J. Casson, et al. "The nonlinear gyro-kinetic flux tube code GKW". In: *Computer Physics Communications*. 40 YEARS OF CPC: A celebratory issue focused on quality software for high performance, grid and novel computing architectures 180.12 (Dec. 2009), pp. 2650–2672. ISSN: 0010-4655. DOI: 10.1016/j.cpc.2009.07.001. URL: https://www.sciencedirect.com/science/article/pii/S0010465509002112 (cit. on p. 89).

[165] M. Dicorato, M. Muraglia, Y. Camenen, et al. "Turbulent transport mechanisms and their impact on the pedestal top of JET plasmas with small-ELMs". In: *Plasma Physics and Controlled Fusion* 66.12 (Oct. 2024), p. 125002. DOI: 10.1088/1361-6587/ad867b. URL: https://dx.doi.org/10.1088/1361-6587/ad867b (cit. on pp. 89, 106).

[166] A. J. Wootton, B. A. Carreras, H. Matsumoto, et al. "Fluctuations and anomalous transport in tokamaks". In: *Physics of Fluids B: Plasma Physics* 2.12 (Dec. 1990), pp. 2879–2903. ISSN: 0899-8221. DOI: 10.1063/1.859358. URL: https://doi.org/10.1063/1.859358 (cit. on p. 89).

[167] J. Candy, R. E. Waltz, and W. Dorland. "The local limit of global gyrokinetic simulations". en. In: *Physics of Plasmas* 11.5 (May 2004), pp. L25–L28. ISSN: 1070-664X, 1089-7674. DOI: 10.1063/1.1695358. URL: https://pubs.aip.org/pop/article/11/5/L25/980304/The-local-limit-of-global-gyrokinetic-simulations (cit. on p. 89).

[168] B. F. McMillan, X. Lapillonne, S. Brunner, et al. "System Size Effects on Gyrokinetic Turbulence". en. In: *Physical Review Letters* 105.15 (Oct. 2010), p. 155001. ISSN: 0031-9007, 1079-7114. DOI: 10.1103/PhysRevLett.105.155001. URL: https://link.aps.org/doi/10.1103/PhysRevLett.105.155001 (cit. on p. 89).

[169] M. J. Pueschel, T. Dannert, and F. Jenko. "On the role of numerical dissipation in gyrokinetic Vlasov simulations of plasma microturbulence". en. In: *Computer Physics Communications* 181.8 (Aug. 2010), pp. 1428–1437. ISSN: 00104655. DOI: 10.1016/j.cpc.2010.04.010. URL: https://linkinghub.elsevier.com/retrieve/pii/S0010465510001219 (cit. on p. 90).

[170] E. A. Belli and J. Candy. "Fully electromagnetic gyrokinetic eigenmode analysis of high-beta shaped plasmas". en. In: *Physics of Plasmas* 17.11 (Nov. 2010), p. 112314. ISSN: 1070-664X, 1089-7674. DOI: 10.1063/1.3495976. URL: https://

pubs.aip.org/pop/article/17/11/112314/108414/Fully-electromagnetic-gyrokinetic-eigenmode (cit. on p. 92).

[171] M. Kammerer, F. Merz, and F. Jenko. "Exceptional points in linear gyrokinetics". en. In: *Physics of Plasmas* 15.5 (May 2008), p. 052102. ISSN: 1070-664X, 1089-7674. DOI: 10.1063/1.2909618. URL: https://pubs.aip.org/pop/article/15/5/052102/1015702/Exceptional-points-in-linear-gyrokinetics (cit. on p. 92).

[172] D. Told, F. Jenko, T. Görler, et al. "Characterizing turbulent transport in ASDEX Upgrade L-mode plasmas via nonlinear gyrokinetic simulations". In: *Physics of Plasmas* 20.12 (Dec. 2013), p. 122312. ISSN: 1070-664X. DOI: 10.1063/1.4858899. URL: https://doi.org/10.1063/1.4858899 (cit. on pp. 92, 101).

[173] T. F. Neiser, F. Jenko, T. A. Carter, et al. "Gyrokinetic GENE simulations of DIII-D near-edge L-mode plasmas". en. In: *Physics of Plasmas* 26.9 (Sept. 2019), p. 092510. ISSN: 1070-664X, 1089-7674. DOI: 10.1063/1.5052047. URL: https://pubs.aip.org/pop/article/26/9/092510/263664/Gyrokinetic-GENE-simulations-of-DIII-D-near-edge-L (cit. on p. 92).

[174] W. Guttenfelder, J. L. Peterson, J. Candy, et al. "Progress in simulating turbulent electron thermal transport in NSTX". en. In: *Nuclear Fusion* 53.9 (Sept. 2013), p. 093022. ISSN: 0029-5515, 1741-4326. DOI: 10.1088/0029-5515/53/9/093022. URL: https://iopscience.iop.org/article/10.1088/0029-5515/53/9/093022 (cit. on p. 92).

[175] M. J. Pueschel, D. R. Hatch, D. R. Ernst, et al. "On microinstabilities and turbulence in steep-gradient regions of fusion devices". en. In: *Plasma Physics and Controlled Fusion* 61.3 (Feb. 2019). Publisher: IOP Publishing, p. 034002. ISSN: 0741-3335. DOI: 10.1088/1361-6587/aaf8c1. URL: https://dx.doi.org/10.1088/1361-6587/aaf8c1 (cit. on pp. 92, 129).

[176] P. B. Snyder and G. W. Hammett. "Electromagnetic effects on plasma microturbulence and transport". en. In: *Physics of Plasmas* 8.3 (Mar. 2001), pp. 744–749. ISSN: 1070-664X, 1089-7674. DOI: 10.1063/1.1342029. URL: https://pubs.aip.org/pop/article/8/3/744/265128/Electromagnetic-effects-on-plasma-microturbulence (cit. on pp. 95, 98).

[177] G. Rewoldt, W. M. Tang, and M. S. Chance. "Electromagnetic kinetic toroidal eigenmodes for general magnetohydrodynamic equilibria". en. In: *The Physics of Fluids* 25.3 (Mar. 1982), pp. 480–490. ISSN: 0031-9171. DOI: 10.1063/1.863760. URL: https://pubs.aip.org/pfl/article/25/3/480/830593/Electromagnetic-kinetic-toroidal-eigenmodes-for (cit. on p. 95).

[178] P. B. Snyder, N. Aiba, M. Beurskens, et al. "Pedestal stability comparison and ITER pedestal prediction". In: *Nuclear Fusion* 49.8 (July 2009), p. 085035. DOI: 10.1088/0029-5515/49/8/085035. URL: https://dx.doi.org/10.1088/0029-5515/49/8/085035 (cit. on p. 97).

[179] J. Weiland and A. Hirose. "Electromagnetic and kinetic effects on the ion temperature gradient mode". In: *Nuclear Fusion* 32.1 (Jan. 1992), p. 151. DOI: 10.1088/0029-5515/32/1/I13. URL: https://dx.doi.org/10.1088/0029-5515/32/1/I13 (cit. on p. 98).

[180] A. Hirose. "On finite β stabilization of the toroidal ion temperature gradient mode". In: *Physics of Plasmas* 7.2 (Feb. 2000), pp. 433–436. ISSN: 1070-664X. DOI: 10.1063/1.873866. URL: https://doi.org/10.1063/1.873866 (cit. on p. 98).

[181] M. Reshko, C. M. Roach, and the MAST Team. "Effects of impurities on electron temperature gradient modes". en. In: *Plasma Physics and Controlled Fusion* 50.11 (Sept. 2008), p. 115002. ISSN: 0741-3335. DOI: 10.1088/0741-3335/50/11/115002. URL: https://dx.doi.org/10.1088/0741-3335/50/11/115002 (cit. on p. 100).

[182] R. E. Waltz, R. L. Dewar, and X. Garbet. "Theory and simulation of rotational shear stabilization of turbulence". en. In: *Physics of Plasmas* 5.5 (May 1998), pp. 1784–1792. ISSN: 1070-664X, 1089-7674. DOI: 10.1063/1.872847. URL: https://pubs.aip.org/pop/article/5/5/1784/1069037/Theory-and-simulation-of-rotational-shear (cit. on pp. 104, 115).

[183] R. E. Waltz, J. Candy, and M. Fahey. "Coupled ion temperature gradient and trapped electron mode to electron temperature gradient mode gyrokinetic simulationsa)". In: *Physics of Plasmas* 14.5 (May 2007), p. 056116. ISSN: 1070-664X. DOI: 10.1063/1.2436851. URL: https://doi.org/10.1063/1.2436851 (cit. on p. 105).

[184] S. Maeyama, Y. Idomura, T.-H. Watanabe, et al. "Cross-Scale Interactions between Electron and Ion Scale Turbulence in a Tokamak Plasma". In: *Phys. Rev. Lett.* 114 (25 June 2015), p. 255002. DOI: 10.1103/PhysRevLett.114.255002. URL: https://link.aps.org/doi/10.1103/PhysRevLett.114.255002 (cit. on p. 105).

[185] N. T. Howard, C. Holland, A. E. White, et al. "Synergistic cross-scale coupling of turbulence in a tokamak plasma". In: *Physics of Plasmas* 21.11 (Nov. 2014), p. 112510. ISSN: 1070-664X. DOI: 10.1063/1.4902366. URL: https://doi.org/10.1063/1.4902366 (cit. on p. 105).

[186] N. T. Howard, C. Holland, A. E. White, et al. "Multi-scale gyrokinetic simulation of tokamak plasmas: enhanced heat loss due to cross-scale coupling of plasma turbulence". In: *Nuclear Fusion* 56.1 (Dec. 2015), p. 014004. DOI: 10.1088/0029-5515/56/1/014004. URL: https://dx.doi.org/10.1088/0029-5515/56/1/014004 (cit. on p. 105).

[187] E. A. Belli, J. Candy, and I. Sfiligoi. "Flow-shear destabilization of multiscale electron turbulence". en. In: *Plasma Physics and Controlled Fusion* 66.4 (Mar. 2024). Publisher: IOP Publishing, p. 045019. ISSN: 0741-3335. DOI: 10.1088/1361-6587/ad2c28. URL: https://dx.doi.org/10.1088/1361-6587/ad2c28 (cit. on p. 105).

[188] G. M. Staebler, N. T. Howard, J. Candy, et al. "A model of the saturation of coupled electron and ion scale gyrokinetic turbulence". en. In: *Nuclear Fusion* 57.6 (May 2017). Publisher: IOP Publishing, p. 066046. ISSN: 0029-5515. DOI: 10.1088/1741-4326/aa6bee. URL: https://dx.doi.org/10.1088/1741-4326/aa6bee (cit. on p. 105).

[189] A. J. Creely, P. Rodriguez-Fernandez, G. D. Conway, et al. “Criteria for the importance of multi-scale interactions in turbulent transport simulations”. en. In: *Plasma Physics and Controlled Fusion* 61.8 (June 2019). Publisher: IOP Publishing, p. 085022. ISSN: 0741-3335. DOI: 10.1088/1361-6587/ab24ae. URL: https://dx.doi.org/10.1088/1361-6587/ab24ae (cit. on p. 105).

[190] S. Maeyama, N. T. Howard, J. Citrin, et al. “Overview of multiscale turbulence studies covering ion-to-electron scales in magnetically confined fusion plasma”. In: *Nuclear Fusion* 64.11 (Aug. 2024), p. 112007. DOI: 10.1088/1741-4326/ad34e1. URL: https://dx.doi.org/10.1088/1741-4326/ad34e1 (cit. on p. 105).

[191] B. D. Scott. “Computation of electromagnetic turbulence and anomalous transport mechanisms in tokamak plasmas”. en. In: *Plasma Physics and Controlled Fusion* 45.12A (Nov. 2003), A385. ISSN: 0741-3335. DOI: 10.1088/0741-3335/45/12A/025. URL: https://dx.doi.org/10.1088/0741-3335/45/12A/025 (cit. on p. 107).

[192] B. D. Scott. “Computation of turbulence in magnetically confined plasmas”. en. In: *Plasma Physics and Controlled Fusion* 48.12B (Dec. 2006), B277–B293. ISSN: 0741-3335, 1361-6587. DOI: 10.1088/0741-3335/48/12B/S27. URL: https://iopscience.iop.org/article/10.1088/0741-3335/48/12B/S27 (cit. on p. 107).

[193] P. Morel, A. Bañón Navarro, M. Albrecht-Marc, et al. “Gyrokinetic large eddy simulations”. In: *Physics of Plasmas* 18.7 (July 2011), p. 072301. ISSN: 1070-664X. DOI: 10.1063/1.3601053. URL: https://doi.org/10.1063/1.3601053 (cit. on p. 108).

[194] M. J. Pueschel, P. W. Terry, F. Jenko, et al. “Extreme Heat Fluxes in Gyrokinetic Simulations: A New Critical β”. en. In: *Physical Review Letters* 110.15 (Apr. 2013), p. 155005. ISSN: 0031-9007, 1079-7114. DOI: 10.1103/PhysRevLett.110.155005. URL: https://link.aps.org/doi/10.1103/PhysRevLett.110.155005 (cit. on p. 109).

[195] A. M. Dimits, G. Bateman, M. A. Beer, et al. “Comparisons and physics basis of tokamak transport models and turbulence simulations”. en. In: *Physics of Plasmas* 7.3 (Mar. 2000), pp. 969–983. ISSN: 1070-664X, 1089-7674. DOI: 10.1063/1.873896. URL: https://pubs.aip.org/pop/article/7/3/969/1029781/Comparisons-and-physics-basis-of-tokamak-transport (cit. on p. 111).

[196] K. Miki, P. H. Diamond, Ö. D. Gürcan, et al. “Spatio-temporal evolution of the L $\rightarrow$ I $\rightarrow$ H transition”. en. In: *Physics of Plasmas* 19.9 (Sept. 2012), p. 092306. ISSN: 1070-664X, 1089-7674. DOI: 10.1063/1.4753931. URL: https://pubs.aip.org/pop/article/19/9/092306/909312/Spatio-temporal-evolution-of-the-L-I-H-transition (cit. on p. 115).

[197] Pei-Chun Hsu and P. H. Diamond. “Zonal flow formation in the presence of ambient mean shear”. In: *Physics of Plasmas* 22.2 (Feb. 2015), p. 022306. ISSN: 1070-664X. DOI: 10.1063/1.4907905. URL: https://doi.org/10.1063/1.4907905 (cit. on p. 115).

[198] W. Dorland, F. Jenko, M. Kotschenreuther, et al. “Electron Temperature Gradient Turbulence”. In: *Phys. Rev. Lett.* 85 (26 Dec. 2000), pp. 5579–5582. DOI: 10.1103/PhysRevLett.85.5579. URL: https://link.aps.org/doi/10.1103/PhysRevLett.85.5579 (cit. on p. 122).

[199] Y. Ren, W. Guttenfelder, S. M. Kaye, et al. “Transport from electron-scale turbulence in toroidal magnetic confinement devices”. en. In: *Reviews of Modern Plasma Physics* 8.1 (Mar. 2024), p. 5. ISSN: 2367-3192. DOI: 10.1007/s41614-023-00138-z. URL: https://doi.org/10.1007/s41614-023-00138-z (cit. on p. 122).

[200] J. Weiland, A. B. Jarmén, and H. Nordman. “Diffusive particle and heat pinch effects in toroidal plasmas”. In: *Nuclear Fusion* 29.10 (Oct. 1989), p. 1810. DOI: 10.1088/0029-5515/29/10/015. URL: https://dx.doi.org/10.1088/0029-5515/29/10/015 (cit. on p. 125).

[201] R. Kubo. “Stochastic Liouville Equations”. In: *Journal of Mathematical Physics* 4.2 (Feb. 1963), pp. 174–183. ISSN: 0022-2488. DOI: 10.1063/1.1703941. URL: https://doi.org/10.1063/1.1703941 (cit. on p. 125).

[202] A. Casati, C. Bourdelle, X. Garbet, et al. “Validating a quasi-linear transport model versus nonlinear simulations”. In: *Nuclear Fusion* 49.8 (July 2009), p. 085012. DOI: 10.1088/0029-5515/49/8/085012. URL: https://dx.doi.org/10.1088/0029-5515/49/8/085012 (cit. on p. 125).

[203] R. E. Waltz, A. Casati, and G. M. Staebler. “Gyrokinetic simulation tests of quasi-linear and tracer transport”. In: *Physics of Plasmas* 16.7 (July 2009), p. 072303. ISSN: 1070-664X. DOI: 10.1063/1.3167391. URL: https://doi.org/10.1063/1.3167391 (cit. on p. 125).

[204] G. M. Staebler, E. A. Belli, J. Candy, et al. “Verification of a quasi-linear model for gyrokinetic turbulent transport”. In: *Nuclear Fusion* 61.11 (Sept. 2021), p. 116007. DOI: 10.1088/1741-4326/ac243a. URL: https://dx.doi.org/10.1088/1741-4326/ac243a (cit. on p. 125).

[205] C. Gillot, G. Dif-Pradalier, Y. Sarazin, et al. “The problem of capturing marginality in model reductions of turbulence”. In: *Plasma Physics and Controlled Fusion* 65.5 (Mar. 2023), p. 055012. DOI: 10.1088/1361-6587/acc276. URL: https://dx.doi.org/10.1088/1361-6587/acc276 (cit. on p. 125).

[206] T. F. Neiser, F. Jenko, T. A. Carter, et al. “Gyrokinetic GENE simulations of DIII-D near-edge L-mode plasmas”. In: *Physics of Plasmas* 26.9 (Sept. 2019), p. 092510. ISSN: 1070-664X. DOI: 10.1063/1.5052047. URL: https://doi.org/10.1063/1.5052047 (cit. on p. 125).

[207] K. Stimmel, A. Bañón Navarro, T. Happel, et al. “Gyrokinetic investigation of the ASDEX Upgrade I-mode pedestal”. In: *Physics of Plasmas* 26.12 (Dec. 2019), p. 122504. ISSN: 1070-664X. DOI: 10.1063/1.5124986. URL: https://doi.org/10.1063/1.5124986 (cit. on p. 125).

[208] K. Stimmel, L. Gil, T. Goerler, et al. “Gyrokinetic analysis of an argon-seeded EDA H-mode in ASDEX Upgrade”. In: *Journal of Plasma Physics* 88.3 (2022), p. 905880315. DOI: 10.1017/S0022377822000484 (cit. on p. 125).

[209] T. Dannert and F. Jenko. “Gyrokinetic simulation of collisionless trapped-electron mode turbulence”. In: *Physics of Plasmas* 12.7 (July 2005), p. 072309 (cit. on pp. 125, 126).

[210] F. Jenko, T. Dannert, and C. Angioni. “Heat and particle transport in a tokamak: advances in nonlinear gyrokinetics”. In: *Plasma Physics and Controlled Fusion* 47.12B (Nov. 2005), B195. DOI: 10.1088/0741-3335/47/12B/S15. URL: https://dx.doi.org/10.1088/0741-3335/47/12B/S15 (cit. on pp. 125, 126).

[211] E. Fable, C. Angioni, and O. Sauter. “The role of ion and electron electrostatic turbulence in characterizing stationary particle transport in the core of tokamak plasmas”. en. In: *Plasma Physics and Controlled Fusion* 52.1 (Dec. 2009), p. 015007. ISSN: 0741-3335. DOI: 10.1088/0741-3335/52/1/015007. URL: https://dx.doi.org/10.1088/0741-3335/52/1/015007 (cit. on pp. 125, 126).

[212] X. Lapillonne, S. Brunner, O. Sauter, et al. “Non-linear gyrokinetic simulations of microturbulence in TCV electron internal transport barriers”. In: *Plasma Physics and Controlled Fusion* 53.5 (Apr. 2011), p. 054011. DOI: 10.1088/0741-3335/53/5/054011. URL: https://dx.doi.org/10.1088/0741-3335/53/5/054011 (cit. on pp. 125, 126).

[213] A. Mariani, G. Merlo, S. Brunner, et al. “Characterization with microturbulence simulations of the zero particle flux condition in case of a TCV discharge showing toroidal rotation reversal”. en. In: *Journal of Physics: Conference Series* 775 (Nov. 2016), p. 012007. ISSN: 1742-6588, 1742-6596. DOI: 10.1088/1742-6596/775/1/012007. URL: https://iopscience.iop.org/article/10.1088/1742-6596/775/1/012007 (cit. on pp. 125, 126).

[214] A. Mariani, S. Brunner, J. Dominski, et al. “Identifying microturbulence regimes in a TCV discharge making use of physical constraints on particle and heat fluxes”. en. In: *Physics of Plasmas* 25.1 (Jan. 2018), p. 012313. ISSN: 1070-664X, 1089-7674. DOI: 10.1063/1.5006408. URL: https://pubs.aip.org/pop/article/25/1/012313/128810/Identifying-microturbulence-regimes-in-a-TCV (cit. on pp. 125, 126, 129).

[215] C. Bourdelle, X. Garbet, F. Imbeaux, et al. “A new gyrokinetic quasilinear transport model applied to particle transport in tokamak plasmas”. In: *Physics of Plasmas* 14.11 (Nov. 2007), p. 112501. ISSN: 1070-664X. DOI: 10.1063/1.2800869. URL: https://doi.org/10.1063/1.2800869 (cit. on p. 126).

[216] J. Citrin, C. Bourdelle, F. J. Casson, et al. “Tractable flux-driven temperature, density, and rotation profile evolution with the quasilinear gyrokinetic transport model QuaLiKiz”. In: *Plasma Physics and Controlled Fusion* 59.12 (Nov. 2017), p. 124005. DOI: 10.1088/1361-6587/aa8aeb. URL: https://dx.doi.org/10.1088/1361-6587/aa8aeb (cit. on p. 126).

[217] L. Horvath, B. Lomanowski, J. Karhunen, et al. “Pedestal particle balance studies in JET-ILW H-mode plasmas”. en. In: *Plasma Physics and Controlled Fusion* 65.4 (Mar. 2023). Publisher: IOP Publishing, p. 044003. ISSN: 0741-3335. DOI: 10.1088/1361-6587/acbb23. URL: https://dx.doi.org/10.1088/1361-6587/acbb23 (cit. on p. 133).

[218] X. Lapillonne. “Local and Global Eulerian Gyrokinetic Simulations of Microturbulence in Realistic Geometry with Applications to the TCV Tokamak”. PhD thesis (cit. on p. 164).

[219] J. W. Connor, R. J. Hastie, and J. B. Taylor. “Shear, Periodicity, and Plasma Ballooning Modes”. en. In: *Physical Review Letters* 40.6 (Feb. 1978), pp. 396–399. ISSN: 0031-9007. DOI: 10.1103/PhysRevLett.40.396. URL: https://link.aps.org/doi/10.1103/PhysRevLett.40.396 (cit. on p. 164).

[220] J. Candy and R. E. Waltz. “Velocity-space resolution, entropy production, and upwind dissipation in Eulerian gyrokinetic simulations”. In: *Physics of Plasmas* 13.3 (Mar. 2006), p. 032310. ISSN: 1070-664X. DOI: 10.1063/1.2184069. URL: https://doi.org/10.1063/1.2184069 (cit. on p. 166).

Appendix

A. Normalization and diagnostics in GENE

The purpose of this appendix is to provide additional details regarding the gyrokinetic code GENE. In particular, the normalizations used and the main diagnostics are described.

A.1. Normalization

The set of gyrokinetic equations is implemented in GENEin dimensionless form, requiring proper normalization of the quantities appearing in the equations. In this section, we introduce these normalizations, chosen such that the normalized quantities are all approximately of the same order of magnitude, $\mathcal{O}(1)$. In particular, all the appearing quantities can be properly normalized by combining the base reference quantities, given by the density n_{ref}, temperature T_{ref}, mass m_{ref}, length L_{ref}, magnetic field strength B_{ref}, charge q_{ref}, and toroidal angular velocity $\Omega_{\mathrm{tor,ref}}$. Typical choices for reference quantities are $n_{\mathrm{ref}} = n_e$, $T_{\mathrm{ref}} = T_i$, $m_{\mathrm{ref}} = m_i$, and L_{ref} is typically the major radius R or minor radius a. From these quantities, other reference physical quantities can be derived, such as velocity c_{ref}, the Larmor frequency Ω_{ref}, and Larmor radius ρ_{ref} given by

$$c_{\mathrm{ref}} = \sqrt{\frac{T_{\mathrm{ref}}}{m_{\mathrm{ref}}}}, \quad \Omega_{\mathrm{ref}} = \frac{eB_{\mathrm{ref}}}{m_{\mathrm{ref}}}, \quad \rho_{\mathrm{ref}} = \frac{c_{\mathrm{ref}}}{\Omega_{\mathrm{ref}}}\,.$$

Additional plasma physical parameters depending on the reference quantities can be derived, such as beta β_{ref}, collisionality $\nu_{c,\mathrm{ref}}$, and ρ^*_{ref} given by

$$\beta_{\mathrm{ref}} = \frac{8\pi n_{\mathrm{ref}} T_{\mathrm{ref}}}{B^2_{\mathrm{ref}}}, \quad \nu_{c,\mathrm{ref}} = \frac{\pi e^4 n_{\mathrm{ref}} L_{\mathrm{ref}} \ln(\Lambda)}{2^{3/2} T^2_{\mathrm{ref}}}, \quad \rho^*_{\mathrm{ref}} = \frac{\rho_{\mathrm{ref}}}{L_{\mathrm{ref}}}\,.$$

Then, time and phase space coordinates are normalized as follows

$$\hat{t} = t\frac{c_{\mathrm{ref}}}{L_{\mathrm{ref}}}, \quad \hat{x} = \frac{x}{\rho_{\mathrm{ref}}}, \quad \hat{y} = \frac{y}{\rho_{\mathrm{ref}}}, \quad \hat{z} = z, \quad \hat{v}_{\parallel\sigma} = \frac{v_\parallel}{c_{\mathrm{ref}}}\frac{1}{\hat{v}_{\mathrm{th}\sigma}}, \quad \hat{\mu}_\sigma = \mu\frac{B_{\mathrm{ref}}}{T_{\mathrm{ref}}\hat{T}_{0\sigma}}$$

where the normalized thermal velocity $\hat{v}_{\mathrm{th}\sigma} = v_{\mathrm{th}\sigma}/c_{\mathrm{ref}} = \sqrt{2\hat{T}_{0\sigma}/\hat{m}_\sigma}$ is introduced. Note that velocity normalization are species-dependent, motivated by the significant variation in thermal velocities between species. The background and perturbed distribution functions are then normalized as follows

$$\hat{F}_{0\sigma} = F_{0\sigma}\frac{c^3_{\mathrm{ref}}}{n_{\mathrm{ref}}}\frac{\hat{v}^3_{\mathrm{th}\sigma}}{\hat{n}_{0\sigma}}, \quad \hat{f}_{1\sigma} = f_{1\sigma}\frac{c^3_{\mathrm{ref}}}{n_{\mathrm{ref}}}\frac{\hat{v}^3_{\mathrm{th}\sigma}}{\hat{n}_{0\sigma}}\frac{1}{\rho^*}$$

and the electromagnetic fields as

$$\hat{\phi}_1 = \frac{e}{T_{\mathrm{ref}}}\frac{1}{\rho^*}, \quad \hat{A}_{1\parallel} = \frac{A_{1\parallel}}{B_{\mathrm{ref}}\rho_{\mathrm{ref}}\rho^*}, \quad \hat{B}_{1\parallel} = \frac{B_{1\parallel}}{B_{\mathrm{ref}}\rho^*}\,.$$

Note that in normalizing the perturbed quantities, the factor ρ^* is introduced, to reflect their ordering compared to the background quantities (see Sec. 3.2). Finally, the background logarithmic density and temperature gradients are normalized as follows

$$\frac{1}{L_{n\sigma}} = -L_{\text{ref}} \frac{\mathrm{d}\log n_{0\sigma}}{\mathrm{d}x}, \quad \frac{1}{L_{T\sigma}} = -L_{\text{ref}} \frac{\mathrm{d}\log T_{0\sigma}}{\mathrm{d}x}\,.$$

Applying these normalizations to the gyrokinetic equation set allows deriving the normalized equations solved in GENE. For a comprehensive list of equations, the reader is referred to [150, 151, 218].

A.2. Diagnostics

We now introduce the definitions of quantities that will be thoroughly examined in this dissertation. The complete information from the numerical resolution of the gyrokinetic system includes the temporal evolution of the perturbed distribution function $f_{1\sigma}$ in the 5D phase space. However, accessing this information is unfeasible due to constraints in data storage capacity. Nonetheless, the physical quantities of typical interest are represented by the electromagnetic fields and appropriate moments in the phase space of the distribution function, thus allowing for data reduction.

Ballooning structures The temporal evolution of the normalized electromagnetic fields $\hat{\phi}_1$, $\hat{A}_{1\parallel}$, and $\hat{B}_{1\parallel}$ constitutes one of the outputs of major interest. These fields are complex-valued, and at each time step, they have the three physical space dimensions (k_x, k_y, z). For example, from the temporal evolution of the fields in linear simulations, it is possible to calculate the growth rate γ and the real frequency ω of the instability.

From the Fourier coefficients of the electromagnetic fields, it is also possible to reconstruct the associated *ballooning envelope*, in the same fashion as in the ballooning representation [219]. As discussed in Ref. [156], the combination of field-aligned coordinates (x, y, z), spectral representation in (x, y), and the parallel boundary condition given by Eq. 3.15, provides an equivalent representation to that of ballooning. The ballooning envelope for a selected k_y of a generic field $\mathcal{A}(\zeta)$, over the extended domain $\zeta \in [-\infty, +\infty]$, is thus given by appropriately appending at the boundary of z domain, i.e. at $z = [-\pi, +\pi]$, the connected k_x modes

$$\mathcal{A}(\zeta) = \sum_{p\in\mathbb{Z}} \mathcal{A}(z + p2\pi)$$

$$\text{where} \qquad \mathcal{A}(z + p2\pi) = \hat{f}_{k_x + p2\pi\hat{s}k_{y,\min}}(z) \exp(ik_y 2\pi x_0)\,.$$

This representation of the fields is physically useful for characterizing modes based on their parity according to the features introduced in Sec. 1.5.1. Moreover, it is particularly helpful for verifying the correctness and quality of the numerical solution, in order to identify potential numerical artifacts.

Turbulent fluxes Radial particle and heat fluxes constitute other quantities of particular interest as they can be directly compared with those deduced from experiments via power balance analysis. Generally, particle and heat fluxes for each plasma species, at the

particle position $\boldsymbol{x}$, are given by

$$\Gamma_\sigma(\boldsymbol{x}) = \int \mathrm{d}^3 v\, \boldsymbol{v} f_{1\sigma}\,,$$
$$Q_\sigma(\boldsymbol{x}) = \int \mathrm{d}^3 v\, \frac{1}{2} m_\sigma v^2 \boldsymbol{v} f_{1\sigma}\,.$$

Note that to express the fluxes in terms of particle coordinates, it is necessary to employ the pull-back operator introduced in Eq. 3.11 on the perturbed distribution function. These fluxes are due to the advection of particles and energy via the velocity $\boldsymbol{v}$, which is generally due to the sum of drift velocities in Eq. 3.6. In GENE, this velocity is approximated by only considering the term due to the generalized $\boldsymbol{E} \times \boldsymbol{B}$ velocity $\boldsymbol{v}_\chi$, which is the dominant contribution in the case of flux-surfaces with weak up-down asymmetry [159]. Thus, radial fluxes are obtained by taking the radial projection of the velocity $\boldsymbol{v}_\chi^x = \boldsymbol{v}_\chi \cdot \boldsymbol{\nabla} x$, resulting in

$$\Gamma_\sigma^x = \left\langle \int \mathrm{d}^3 v\, \boldsymbol{v}_\chi^x f_{1\sigma} \right\rangle$$
$$Q_\sigma^x = \left\langle \int \mathrm{d}^3 v\, \frac{1}{2} m_\sigma v^2 \boldsymbol{v}_\chi^x f_{1\sigma} \right\rangle$$

where $\langle \dots \rangle$ indicates the field-line average. Recall that the generalized $\boldsymbol{E} \times \boldsymbol{B}$ velocity $\boldsymbol{v}_\chi$ is given by the sum of terms due to fluctuations of the electrostatic potential ϕ_1 and of the parallel vector potential $A_{1\parallel}$ and magnetic field $B_{1\parallel}$. Accordingly, particle and heat fluxes can be decomposed into the so-called electrostatic component, which includes only the contribution from ϕ_1, and electromagnetic, which includes contributions from $A_{1\parallel}$ and $B_{1\parallel}$. According to the previously introduced units, the fluxes are normalized using gyro-Bohm units, given by $\Gamma_{\mathrm{gb}} = c_{\mathrm{ref}} n_{\mathrm{ref}} (\rho^*_{\mathrm{ref}})^2$ and $Q_{\mathrm{gb}} = c_{\mathrm{ref}} p_{\mathrm{ref}} (\rho^*_{\mathrm{ref}})^2$.

B. Dispersion relations of ITG and ETG modes with impurities

B.1. Linear electrostatic gyrokinetic equation

We start from the linear electrostatic gyrokinetic equation, in coordinate-free form, for the evolution of the non-adiabatic part g_σ of the perturbed distribution function $f_{1\sigma}$ [220]

$$\partial_t g_\sigma + (v_\parallel \hat{\boldsymbol{b}} + \boldsymbol{v}_\mathrm{d}) \cdot \boldsymbol{\nabla} g_\sigma = \frac{Z_\sigma e}{T_{0,\sigma}} J_{0,\sigma} F_{M,\sigma} \partial_t \phi - \boldsymbol{v}_\mathrm{E} \cdot \boldsymbol{\nabla} F_{M,\sigma} \tag{B.1}$$

We make the notation explicit

$$g_\sigma = f_{1\sigma} + \frac{Z_\sigma e \phi}{T_\sigma} F_{M,\sigma} \tag{B.2}$$

$$\boldsymbol{v}_\mathrm{d} = \frac{m_\sigma}{Z_\sigma e B^2} \left(v_\parallel^2 + \frac{v_\perp^2}{2} \right) \hat{\boldsymbol{b}} \times \boldsymbol{\nabla} B \tag{B.3}$$

$$\boldsymbol{v}_\mathrm{E} = J_{0,\sigma} \frac{\boldsymbol{b} \times \boldsymbol{\nabla} \phi}{B} \tag{B.4}$$

$$J_{0,\sigma} = J_0 \left(\frac{k_\perp v_\perp}{\Omega_{c,\sigma}} \right) = J_0 \left(k_\perp \rho_{\mathrm{L},\sigma} \right) \tag{B.5}$$

$$F_{M,\sigma} = \frac{n_{0,\sigma}}{\left(2\pi \frac{T_{0,\sigma}}{m_\sigma} \right)^{\frac{3}{2}}} e^{-\left(\frac{m_\sigma (v_\parallel^2 + v_\perp^2)}{2 T_{0,\sigma}} \right)} \tag{B.6}$$

where J_0 is the zeroth-order Bessel function of the first kind, and the cyclotron frequency and Larmor radius are respectively $\Omega_{c,\sigma} = Z_\sigma e B / m_\sigma$ and $\rho_{\mathrm{L},\sigma} = m_\sigma v_\perp / (Z_\sigma e B)$.

B.1.1. Field-aligned coordinates

We now adopt the field-aligned coordinate system [156] and rewrite the operators that appear in the Eq. B.1 in this coordinate system.

$$\begin{cases} \rho &= \psi - \psi_0 \\ \alpha &= \varphi - q(\psi) \theta \\ \eta &= \theta \end{cases} \tag{B.7}$$

where (ψ, θ, φ) is a right-handed coordinate system with respectively ψ radial coordinate, θ poloidal angle, and φ toroidal angle. In this system the magnetic field can be written in Clebsch representation as $\boldsymbol{B} = \boldsymbol{\nabla} \alpha \times \boldsymbol{\nabla} \psi$.

So, the operators become [156]

$$\hat{\boldsymbol{b}} \cdot \boldsymbol{\nabla} = \frac{1}{Rq}\partial_\eta \tag{B.8}$$

$$\boldsymbol{v}_\mathrm{d} \cdot \boldsymbol{\nabla} = -ik_\theta \frac{m_\sigma}{Z_\sigma eBR}\left(v_\parallel^2 + \frac{v_\perp^2}{2}\right)[\hat{s}(\eta - \theta_k)\sin\eta + \cos\eta] \tag{B.9}$$

$$\boldsymbol{v}_\mathrm{E} \cdot \boldsymbol{\nabla} F_{M,\sigma} = -ik_\theta \frac{J_{0,\sigma}\phi}{B} F_{M,\sigma} \frac{\mathrm{d}\log n_{0,\sigma}}{\mathrm{d}\psi}\left[1 + \frac{\mathrm{d}\log T_{0,\sigma}}{\mathrm{d}\log n_{0,\sigma}}\left(\frac{m_\sigma v^2}{2T_{0,\sigma}} - \frac{3}{2}\right)\right] \tag{B.10}$$

By inserting these operators in the gyrokinetic equation, Eq. B.1, we obtain

$$(\omega - k_\parallel v_\parallel - \omega_{\mathrm{d},\sigma})g_\sigma = \frac{Z_\sigma e}{T_{0,\sigma}} J_{0,\sigma}\phi\left[\omega - \omega^*_{n,\sigma} - \omega^*_{T,\sigma}\left(\frac{m_\sigma v^2}{2T_{0,\sigma}} - \frac{3}{2}\right)\right] F_{M,\sigma} \tag{B.11}$$

where we have expanded in time as $e^{-i(\omega_r + i\gamma)t}$ giving $\partial_t = -i\omega$ and introduced the definitions

$$\frac{\partial_\eta}{Rq} = ik_\parallel \tag{B.12}$$

$$\omega_{\mathrm{d},\sigma} = k_\theta \frac{m_\sigma}{Z_\sigma eBR}\left(v_\parallel^2 + \frac{v_\perp^2}{2}\right)[\hat{s}(\eta - \theta_k)\sin\eta + \cos\eta] \tag{B.13}$$

$$\omega^*_{n,\sigma} = k_\theta \frac{T_{0,\sigma}}{Z_\sigma eB}\frac{\mathrm{d}\log n_{0,\sigma}}{\mathrm{d}\psi} = -k_\theta \frac{T_{0,\sigma}}{Z_\sigma eB}\frac{1}{L_{n,\sigma}} \tag{B.14}$$

$$\omega^*_{T,\sigma} = k_\theta \frac{T_{0,\sigma}}{Z_\sigma eB}\frac{\mathrm{d}\log T_{0,\sigma}}{\mathrm{d}\psi} = -k_\theta \frac{T_{0,\sigma}}{Z_\sigma eB}\frac{1}{L_{T,\sigma}} \tag{B.15}$$

For completeness, we also provide standard definitions which may be useful in what follows; in particular, the diamagnetic drift frequency is defined as

$$\begin{aligned}
\omega^*_\sigma &= \omega^*_{n,\sigma} + \omega^*_{T,\sigma}\left(\frac{m_\sigma v^2}{2T_{0,\sigma}} - \frac{3}{2}\right) = \\
&= \omega^*_{T,\sigma}\left(\frac{\omega^*_{n,\sigma}}{\omega^*_{T,\sigma}} + \frac{m_\sigma v^2}{2T_{0,\sigma}} - \frac{3}{2}\right) = \\
&= \omega^*_{T,\sigma}\left(\frac{1}{\eta_\sigma} + \frac{m_\sigma v^2}{2T_{0,\sigma}} - \frac{3}{2}\right)
\end{aligned}$$

where $\eta_\sigma = \mathrm{d}\log T_{0,\sigma}/\mathrm{d}\log n_{0,\sigma} = L_{n,\sigma}/L_{T,\sigma}$; and we define the factor

$$\omega_{\mathrm{d},T_\sigma} = -k_\theta \frac{T_{0,\sigma}}{Z_\sigma eBR} \tag{B.16}$$

B.1.2. Linear response

From the gyrokinetic equation in the form Eq. B.11, it is straightforward to get the linear response

$$g_\sigma = \frac{Z_\sigma e}{T_{0,\sigma}} J_{0,\sigma}\phi \frac{\omega - \omega^*_{n,\sigma} - \omega^*_{T,\sigma}\left(\frac{m_\sigma v^2}{2T_{0,\sigma}} - \frac{3}{2}\right)}{\omega - k_\parallel v_\parallel - \omega_{\mathrm{d},\sigma}} F_{M,\sigma} =$$
$$= \frac{Z_\sigma e}{T_{0,\sigma}} J_{0,\sigma}\phi \frac{\omega - \omega^*_{T,\sigma}\left(\frac{m_\sigma v^2}{2T_{0,\sigma}} - \frac{3}{2} + \eta_e^{-1}\right)}{\omega - k_\parallel v_\parallel - \omega_{\mathrm{d},\sigma}} F_{M,\sigma} \tag{B.17}$$

B.2. Quasi-neutrality

The system of equations is closed by the quasi-neutrality equation

$$\sum_\sigma Z_\sigma n_\sigma = 0 \tag{B.18}$$

where the density fluctuations is given by

$$n_\sigma = -\frac{n_{0,\sigma} Z_\sigma e}{T_{0,\sigma}}\phi + \int \mathrm{d}^3 v\, g_\sigma J_{0,\sigma} \tag{B.19}$$

with $\mathrm{d}^3 v = \mathrm{d}\theta v_\perp \mathrm{d}v_\perp \mathrm{d}v_\parallel$, and the linear response g_σ from Eq B.17. We here notice that, the adiabatic response is

$$n_\sigma = -\frac{n_{0,\sigma} Z_\sigma e}{T_{0,\sigma}}\phi \tag{B.20}$$

B.3. Dispersion relations

In this section, the dispersion relation for the ETG and ITG instabilities taking into account impurity species are derived.

B.3.1. ETG with impurity

We start from the dispersion relation for ETG modes, considering kinetic electrons and an arbitrary number of adiabatic ionic species. And so, we have

$$n_e = \frac{n_{0,e} e}{T_{0,e}}\phi \left[1 - \frac{1}{n_{0,e}} \int \mathrm{d}^3 v \, \frac{\omega - \omega^*_{T,e}\left(\frac{m_e v^2}{2T_{0,e}} - \frac{3}{2} + \eta_e^{-1}\right)}{\omega - k_\parallel v_\parallel - \omega_{\mathrm{d},e}} J^2_{0,e} F_{M,e}\right]$$
$$n_i = -\frac{n_{0,i} Z_i e}{T_{0,i}}\phi$$

which, inserted into the quasi-neutrality equation Eq. B.18, yield the dispersion relation

$$\mathcal{D}(\boldsymbol{k}, \omega) = \mathcal{C} + 1 - \frac{1}{n_{0,e}} \int \mathrm{d}^3 v \, \frac{\omega - \omega^*_{T,e}\left(\frac{m_e v^2}{2T_{0,e}} - \frac{3}{2} + \eta_e^{-1}\right)}{\omega - k_\parallel v_\parallel - \omega_{\mathrm{d},e}} J^2_{0,e} F_{M,e} = 0 \tag{B.21}$$

where we have introduced the definitions

$$\mathcal{C} = \frac{T_e}{T_i} Z_{\text{eff}}$$
$$Z_{\text{eff}} = \frac{\sum_i Z_i^2 n_{0,i}}{n_{0,e}}$$

B.3.1.1. Analytical limits: marginal stability and fluid limit

We now introduce some physical assumptions that will allow us to analytically solve the dispersion relation. In particular, at the resonant denominator we assume:

1. the mode frequency is much higher than the frequency associated with the free streaming motion along the field line: $\omega \gg k_\parallel v_\parallel$, with $v_\parallel \sim v_{\text{th},e}$
2. $v_\perp \gg v_\parallel$.

Then, the dispersion relation becomes

$$\mathcal{D}(\boldsymbol{k},\omega) = \mathcal{C} + 1 - \frac{1}{n_{0,e}} \int \mathrm{d}^3 v \, \frac{\omega - \omega^*_{T,e}\left(\frac{m_e v^2}{2T_{0,e}} - \frac{3}{2} + \eta_e^{-1}\right)}{\omega - \omega_{\mathrm{d},T_e} \frac{m_e v_\perp^2}{2T_{0,e}}} J_{0,e}^2 F_{M,e} = 0$$

We further simplify by assuming $J_{0,e}^2 \sim 1$, considering the stability at the outer mid-plane, and neglecting the the trapped particle , giving $\int \mathrm{d}\theta = 2\pi$. Finally, we explicit the Maxwellian and introduce in the integral a change of variables[1], and we obtain

$$\mathcal{D}(\boldsymbol{k},\omega) = \mathcal{C} + 1 - \frac{1}{\sqrt{2\pi}} \int \mathrm{d}\zeta \mathrm{d}u \, \frac{\omega - \omega^*_{T,e}\left(u + \frac{\zeta^2}{2} - \frac{3}{2} + \eta_e^{-1}\right)}{\omega - \omega_{\mathrm{d},T_e} u} e^{-\left(u + \frac{\zeta^2}{2}\right)} = 0 \qquad \text{(B.22)}$$

[1] To make the derivation more agile, we decide to make here explicit the changes of variables that we use to carry out the integral involving the linear response g_σ appearing in Eq. B.19. In particular, we use two different changes of variables:

1.
$$\begin{cases} \zeta = v_\parallel \sqrt{\frac{m_\sigma}{T_{0,\sigma}}} & \Rightarrow \quad \mathrm{d}\zeta = \mathrm{d}v_\parallel \sqrt{\frac{m_\sigma}{T_{0,\sigma}}} \\ u = \frac{m_\sigma v_\perp^2}{2T_{0,\sigma}} & \Rightarrow \quad \mathrm{d}u = v_\perp \mathrm{d}v_\perp \frac{m_\sigma}{T_{0,\sigma}} \end{cases}$$

such that

$$\int \mathrm{d}^3 v = 2\pi \int_{-\infty}^{\infty} \mathrm{d}v_\parallel \int_0^{\infty} v_\perp \mathrm{d}v_\perp \quad \rightarrow \quad 2\pi \left(\frac{T_{0,\sigma}}{m_\sigma}\right)^{3/2} \int_{-\infty}^{\infty} \mathrm{d}\zeta \int_0^{\infty} \mathrm{d}u$$

2.
$$\begin{cases} \zeta = v_\parallel \sqrt{\frac{m_\sigma}{T_{0,\sigma}}} & \Rightarrow \quad \mathrm{d}\zeta = \mathrm{d}v_\parallel \sqrt{\frac{m_\sigma}{T_{0,\sigma}}} \\ w = v_\perp \sqrt{\frac{m_\sigma}{T_{0,\sigma}}} & \Rightarrow \quad \mathrm{d}w = \mathrm{d}v_\perp \sqrt{\frac{m_\sigma}{T_{0,\sigma}}} \end{cases}$$

such that

$$\int \mathrm{d}^3 v = 2\pi \int_{-\infty}^{\infty} \mathrm{d}v_\parallel \int_0^{\infty} v_\perp \mathrm{d}v_\perp \quad \rightarrow \quad 2\pi \left(\frac{T_{0,\sigma}}{m_\sigma}\right)^{3/2} \int_{-\infty}^{\infty} \mathrm{d}\zeta \int_0^{\infty} w \mathrm{d}w$$

and by performing the integral in $\mathrm{d}\zeta$ we get

$$\mathcal{D} = \mathcal{C} + 1 - \int_0^\infty \mathrm{d}u \, \frac{\omega - \omega^*_{T,e}\left(u - 1 + \eta_e^{-1}\right)}{\omega - \omega_{\mathrm{d},T_e} u} e^{-u} = 0 \tag{B.23}$$

Marginal stability

First, let's study the issue of stability. In particular, we are interested in finding an expression for the critical gradient of the logarithmic electron temperature above which the ETG instability is destabilized, i.e. the instability threshold, and its dependence on impurity parameters Z_{eff} and $T_{0,e}/T_{0,i}$.

To do so, we solve the dispersion relation for zero growth rate, $\gamma = 0$, such that the frequency is purely real $\omega = \omega_r$. So, we solve the dispersion relation for the unknowns ω_r and $1/L_{T,e}$ (or, with our notation, $\omega^*_{T,e}$). Then, the dispersion relation

$$\mathcal{D} = \mathcal{D}_r + i\mathcal{D}_i = 0$$

gives the system of equation (as long as all the other plasma parameters are provided)

$$\begin{cases} \mathcal{D}_r(\omega_r, \omega^*_{T,e}) &= 0 \\ \mathcal{D}_i(\omega_r, \omega^*_{T,e}) &= 0 \end{cases} \tag{B.24}$$

We start by rearranging the dispersion relation Eq. B.23

$$\mathcal{D} = \mathcal{C} + 1 + \frac{1}{\omega_{\mathrm{d},T_e}} \int_0^\infty \mathrm{d}u \, \frac{\omega - \omega^*_{T,e}\left(u - \frac{\omega}{\omega_{\mathrm{d},T_e}} + \frac{\omega}{\omega_{\mathrm{d},T_e}} - 1 + \eta_e^{-1}\right)}{u - \frac{\omega}{\omega_{\mathrm{d},T_e}}} e^{-u} = 0$$

and by expanding the sum at the numerator we finally get

$$\mathcal{D} = \mathcal{C} + 1 - \frac{\omega^*_{T,e}}{\omega_{\mathrm{d},T_e}} + \frac{1}{\omega_{\mathrm{d},T_e}} \left[\omega - \omega^*_{T,e}\left(\frac{\omega}{\omega_{\mathrm{d},T_e}} - 1 + \eta_e^{-1}\right)\right] \int_0^\infty \mathrm{d}u \, \frac{e^{-u}}{u - \frac{\omega}{\omega_{\mathrm{d},T_e}}} = 0$$

Having assumed $\gamma = 0$, we can evaluate the integral by using the *Plemelj's formula*

$$\lim_{\gamma \to 0^+} \int_a^b \mathrm{d}x \frac{f(x)}{x - \omega_r \pm i\gamma} = \mathcal{P}\int_a^b \mathrm{d}x \frac{f(x)}{x - \omega_r} \mp i\pi f(\omega_r) \quad \text{if} \quad a < \omega_r < b$$

such that the dispersion relation takes the form

$$\mathcal{D} = \mathcal{C} + 1 - \frac{\omega^*_{T,e}}{\omega_{\mathrm{d},T_e}} + \frac{1}{\omega_{\mathrm{d},T_e}} \left[\omega - \omega^*_{T,e}\left(\frac{\omega}{\omega_{\mathrm{d},T_e}} - 1 + \eta_e^{-1}\right)\right] \left[\mathcal{F}\left(\frac{\omega_r}{\omega_{\mathrm{d},T_e}}\right) - i\pi e^{-\frac{\omega_r}{\omega_{\mathrm{d},T_e}}}\right] = 0$$

where $\mathcal{F}$ is a real valued function. It is now straightforward to evaluate the system of equation Eq. B.24.

1. The imaginary part is zero if the first parenthesis is zero

$$\mathcal{D}_i(\omega_r, \omega^*_{T,e}) = 0 \quad \Rightarrow \quad \omega_r = \omega^*_{T,e}\left(1 - \eta_e^{-1}\right) \frac{1}{\frac{\omega^*_{T,e}}{\omega_{\mathrm{d},T_e}} - 1}$$

2. Then, by inserting this result into the full dispersion relation we get

$$\mathcal{C} + 1 - \frac{\omega^*_{T,e}}{\omega_{\mathrm{d},T_e}} = 0 \quad \Rightarrow \quad \frac{\omega^*_{T,e}}{\omega_{\mathrm{d},T_e}} = \frac{R}{L_{T_e}} = 1 + \frac{T_{0,e}}{T_{0,i}} Z_{\mathrm{eff}}$$

So, we found that the ETG instability threshold R/L_{T_e} increases with Z_{eff} and $T_{0,e}/T_{0,i}$, indicating that these two factors have a stabilising effect. We also notice that these results are valid if u at the resonance is strictly positive, that implies $\omega/\omega_{\mathrm{d},T_e} > 0$ and $\eta_e < 0$ or $\eta_e > 1$.

Fluid limit

We now address the study of the dispersion relation in the limit

$$\omega \gg \omega_{\mathrm{d},T_e} \tag{B.25}$$

known as *fluid limit*, because it lets neglecting the role of kinetic processes like the *Landau damping*.

We rearrange the dispersion relation Eq. B.23 as follows, by dividing and multiplying the integral argument by ω

$$\mathcal{D} = \mathcal{C} + 1 - \int_0^\infty \mathrm{d}u \, \frac{1 - \frac{\omega^*_{T,e}}{\omega}\left(u - 1 + \eta_e^{-1}\right)}{1 - \frac{\omega_{\mathrm{d},T_e}}{\omega} u} e^{-u} = 0 \tag{B.26}$$

Given the fluid limit assumption Eq. B.25, we are now able to Taylor develop the argument of the integral as follows

$$\frac{1}{1-x} \approx 1 + x + x^2 + \dots \tag{B.27}$$

and by taking the first two terms of the development, we write the integral argument as

$$\left[1 - \frac{\omega^*_{T,e}}{\omega}\left(u - 1 + \eta_e^{-1}\right)\right]\left[1 + \frac{\omega_{\mathrm{d},T_e}}{\omega} u\right]$$

Now, by performing the integrals, remembering that $\int_0^\infty \mathrm{d}u \, u e^{-u} = 1$ and $\int_0^\infty \mathrm{d}u \, u^2 e^{-u} = 2$, we obtain the dispersion relation

$$\mathcal{D} = \mathcal{C} + \frac{\omega^*_{T,e}\eta_e^{-1} - \omega_{\mathrm{d},T_e}}{\omega} + \frac{\omega_{\mathrm{d},T_e}\omega^*_{T,e}(1 + \eta_e^{-1})}{\omega^2} = 0$$

The solution of this second order polynomial equation is

$$\omega = -\frac{\omega^*_{T,e}\eta_e^{-1} - \omega_{\mathrm{d},T_e} \pm \sqrt{(\omega^*_{T,e}\eta_e^{-1} - \omega_{\mathrm{d},T_e})^2 - 4\mathcal{C}\omega_{\mathrm{d},T_e}\omega^*_{T,e}(1 + \eta_e^{-1})}}{2\mathcal{C}}$$

whose solution is imaginary if the argument of the square root is negative

$$4\mathcal{C}\omega_{\mathrm{d},T_e}\omega^*_{T,e}(1 + \eta_e^{-1}) > (\omega^*_{T,e}\eta_e^{-1} - \omega_{\mathrm{d},T_e})^2$$

that provides the condition on $\omega^*_{T,e}$ such that there is an instability.

An estimate of the instability growth rate far above the threshold, i.e. for the argument of the square root being dominated by the second term, is

$$\boxed{\gamma \sim \sqrt{\frac{\omega_{\mathrm{d},T_e}\omega^*_{T,e}(1+\eta_e^{-1})}{\mathcal{C}}}}$$

and so, also in this case we obtain that Z_{eff} and $T_{0,e}/T_{0,i}$ are stabilizing.

B.3.2. ITG with impurity

Here we derive the dispersion relation for ITG modes, considering kinetic ions and adiabatic electrons

$$n_i = -\frac{n_{0,i}Z_i e}{T_{0,i}}\phi\left[1 - \frac{1}{n_{0,i}}\int \mathrm{d}^3 v\, \frac{\omega - \omega^*_{T,i}\left(\frac{m_i v^2}{2T_{0,i}} - \frac{3}{2} + \eta_i^{-1}\right)}{\omega - k_\parallel v_\parallel - \omega_{\mathrm{d},i}} J^2_{0,i} F_{M,i}\right]$$
$$n_e = \frac{n_{0,e}e}{T_{0,e}}\phi$$

which, inserted into the quasi-neutrality equation Eq. B.18, and considering an arbitrary number of ion species, yield the dispersion relation

$$\mathcal{D}(\boldsymbol{k},\omega) = \frac{n_{0,e}}{T_{0,e}} + \sum_i \frac{n_{0,i}Z_i^2}{T_{0,i}}\left[1 - \frac{1}{n_{0,i}}\int \mathrm{d}^3 v\, \frac{\omega - \omega^*_{T,i}\left(\frac{m_i v^2}{2T_{0,i}} - \frac{3}{2} + \eta_i^{-1}\right)}{\omega - k_\parallel v_\parallel - \omega_{\mathrm{d},i}} J^2_{0,i} F_{M,i}\right] = 0 \tag{B.28}$$

At this point, we explicit the standard notation by using the first change of variables previously introduced. The magnetic and diamagnetic drift frequencies for the ions are:

$$\begin{aligned}
\omega_{\mathrm{d},i} &= \omega_{\mathrm{d},T_i}\left(u + \zeta^2\right) \\
\omega^*_i &= \omega^*_{n,i} + \omega^*_{T,i}\left(u + \frac{\zeta^2}{2} - \frac{3}{2}\right) \\
&= \omega^*_{T,i}\left(u + \frac{\zeta^2}{2} - \frac{3}{2} + \eta_i^{-1}\right)
\end{aligned}$$

Finally, the dispersion relation is

$$\mathcal{D}(\boldsymbol{k},\omega) = \frac{n_{0,e}}{T_{0,e}} + \sum_i \frac{n_{0,i}Z_i^2}{T_{0,i}}\left[1 - \frac{1}{\sqrt{2\pi}}\int \mathrm{d}u\mathrm{d}\zeta\, \frac{\omega - \omega^*_{T,i}\left(u + \frac{\zeta^2}{2} - \frac{3}{2} + \eta_i^{-1}\right)}{\omega - k_\parallel \zeta v_{\mathrm{th},i} - \omega_{\mathrm{d},i}} J^2_{0,i} e^{-\left(u + \frac{\zeta^2}{2}\right)}\right] = 0 \tag{B.29}$$

Since we will include different ionic species, and therefore different impurities, it is useful to rewrite the characteristic quantities of a generic ion species i, in terms of the proton p ones knowing that $Z_p = 1$, and $m_i = Am_p$

$$\omega^*_{n,i} = \frac{\omega^*_{n,p}}{Z_i}, \qquad \omega^*_{T,i} = \frac{\omega^*_{T,p}}{Z_i}, \qquad \rho_{\mathrm{L},i} = \rho_{\mathrm{t},p}\frac{\sqrt{A}}{Z_i}\sqrt{u} \tag{B.30}$$

where the thermal gyro-radius is defined as $\rho_{\mathrm{t},p} = \sqrt{m_p T_{0,p}}/(Z_p e B)$, and A is the mass number.

B.3.2.1. Analytical limits: marginal stability and fluid limit

Again we neglect parallel dynamics in order to carry out the threshold calculation analytically, albeit approximately.

We assume that there are an arbitrary number of ion species divided between the main ion i and impurities z; but we assume that the ITG mode is driven by the main ion species, such that $\omega \sim \omega_{\mathrm{d},i}$ and thus from the Eq. B.30 we have that, if the impurity charge Z_z is large enough

$$\omega \gg \omega_{\mathrm{d},z}, \quad \omega_z^*$$

With these assumptions, and assuming again $\omega \gg k_\parallel v_\parallel$, the integrals in the dispersion relation for impurities species are simplified to

$$\int \mathrm{d}u\mathrm{d}\zeta \, \frac{\omega - \omega_{T,i}^* \left(u + \frac{\zeta^2}{2} - \frac{3}{2} + \eta_z^{-1}\right)}{\omega - \omega_{\mathrm{d},z}} J_{0,z}^2 e^{-\left(u+\frac{\zeta^2}{2}\right)} \approx \int \mathrm{d}u\mathrm{d}\zeta \, J_{0,z}^2 e^{-\left(u+\frac{\zeta^2}{2}\right)}$$

and the dispersion relation Eq. B.29 becomes

$$\begin{aligned}
\mathcal{D}(\boldsymbol{k},\omega) = {} & \frac{n_{0,e}}{T_{0,e}} + \\
& + \sum_z \frac{n_{0,z} Z_z^2}{T_{0,z}} \left[1 - \frac{1}{\sqrt{2\pi}} \int \mathrm{d}u\mathrm{d}\zeta \, J_{0,z}^2 e^{-\left(u+\frac{\zeta^2}{2}\right)}\right] + \\
& + \frac{n_{0,i} Z_i^2}{T_{0,i}} \left[1 - \frac{1}{\sqrt{2\pi}} \int \mathrm{d}u\mathrm{d}\zeta \, \frac{\omega - \omega_{T,i}^* \left(u + \frac{\zeta^2}{2} - \frac{3}{2} + \eta_i^{-1}\right)}{\omega - \omega_{\mathrm{d},i}} J_{0,i}^2 e^{-\left(u+\frac{\zeta^2}{2}\right)}\right] = 0
\end{aligned}$$

Marginal stability

We here address the calculation for the threshold by introducing the *strong* assumption that for all the ion species $k_\perp \rho_{\mathrm{L},i} \ll 1$ holds, which allows to Taylor expand the Bessel function as $J_{0,i}^2 \approx 1$, such that the dispersion relation is further simplified and becomes formally equivalent to that found for the ETG modes

$$\mathcal{D} = \frac{n_{0,e}}{n_{0,i} Z_i^2} \frac{T_{0,i}}{T_{0,e}} + 1 - \frac{\omega_{T,i}^*}{\omega_{\mathrm{d},T_i}} + \frac{1}{\omega_{\mathrm{d},T_i}} \left[\omega - \omega_{T,i}^* \left(\frac{\omega}{\omega_{\mathrm{d},T_i}} - 1 + \eta_i^{-1}\right)\right] \int_0^\infty \mathrm{d}u \frac{e^{-u}}{u - \frac{\omega}{\omega_{\mathrm{d},T_i}}} = 0$$

Repeating the steps already seen above, we derive the threshold for ITG modes

$$\frac{\omega_{T,i}^*}{\omega_{\mathrm{d},T_i}} = 1 + \frac{n_{0,e}}{n_{0,i}} \frac{T_{0,i}}{T_{0,e}} \frac{1}{Z_i^2} \tag{B.31}$$

in which, the densities at equilibrium satisfy the quasi-neutrality, such that the main ion density with an arbitrary number of impurities is given by

$$n_{0,i} = \frac{n_{0,e}}{Z_i} - \sum_z \frac{Z_z}{Z_i} n_{0,z}$$

By inserting this last relation into the ITG threshold Eq. B.31, we get

$$\frac{\omega^*_{T,i}}{\omega_{\mathrm{d},T_i}} = 1 + \frac{T_{0,i}}{T_{0,e}} \frac{1}{Z_i \left(1 - \sum_z Z_z \frac{n_{0,z}}{n_{0,e}}\right)}$$

where we notice that the threshold for ITGs increases, as the densities of impurities increase. This effect is known as the *dilution effect*. Instead, we notice that the effect of main ion charge Z_i is destabilizing.

Fluid limit

We address now the study of the so-called *fluid limit*, i.e. we consider the system to be far above the instability threshold. The limit is so named in the literature because it will give the same results as those obtained in the framework of the fluid theory.

Let's start again from the dispersion relation Eq. B.29 that, for convenience, we rewrite it here in the form

$$\mathcal{D}(\boldsymbol{k},\omega) = \frac{n_{0,e}}{T_{0,e}} + \sum_i \frac{n_{0,i} Z_i^2}{T_{0,i}} \left[1 - \frac{1}{\sqrt{2\pi}} \int \mathrm{d}u \mathrm{d}\zeta \, \frac{1 - \frac{\omega^*_{T,i}}{\omega}\left(u + \frac{\zeta^2}{2} - \frac{3}{2} + \eta_i^{-1}\right)}{1 - \frac{k_\parallel v_{\mathrm{th},i}}{\omega}\zeta - \frac{\omega_{\mathrm{d},i}}{\omega}} J_{0,i}^2 e^{-\left(u + \frac{\zeta^2}{2}\right)}\right] = 0$$

We thus consider the limits:

$$\omega \gg \omega_i^*, \quad \omega_{\mathrm{d},i}, \quad k_\parallel v_\parallel$$

allowing us to Taylor develop the following terms appearing in the integrand as

$$J_0^2(k_\perp \rho_{\mathrm{t},i}\sqrt{u}) \approx 1 - \frac{k_\perp^2 \rho_{\mathrm{t},i}^2}{2} u + \dots$$

$$\left[1 - \left(\frac{k_\parallel v_{\mathrm{th},i}}{\omega}\zeta + \frac{\omega_{\mathrm{d},i}}{\omega}\right)\right] \approx 1 + \left(\frac{k_\parallel v_{\mathrm{th},i}}{\omega}\zeta + \frac{\omega_{\mathrm{d},i}}{\omega}\right) + \left(\frac{k_\parallel v_{\mathrm{th},i}}{\omega}\zeta + \frac{\omega_{\mathrm{d},i}}{\omega}\right)^2 + \dots$$

By inserting these developments, we obtain the integrand

$$\left(1 - \frac{\omega_i^*}{\omega}\right)\left[\left(1 + \cancel{\frac{k_\parallel v_{\mathrm{th},i}}{\omega}\zeta} + \frac{\omega_{\mathrm{d},i}}{\omega} + \left(\frac{k_\parallel v_{\mathrm{th},i}}{\omega}\right)^2 \zeta^2 + \left(\frac{\omega_{\mathrm{d},i}}{\omega}\right)^2 + \cancel{2\frac{k_\parallel v_{\mathrm{th},i}\omega_{\mathrm{d},i}}{\omega^2}\zeta}\right)\left(1 - \frac{k_\perp^2 \rho_{\mathrm{t},i}^2}{2} u\right)\right]$$

where we have removed the odd terms in ζ, given that their integral over the even domain is zero. In order to compare the different terms appearing in the integrand, we introduce the expansion parameter δ

$$\left(\frac{k_\parallel v_{\mathrm{th},i}}{\omega}\right)^2 \zeta^2 \sim \frac{\omega_{\mathrm{d},i}}{\omega} \sim k_\perp \rho_{\mathrm{t},i}^2 \sim \delta \ll 1$$

By expanding the calculations and retaining only the first order terms in δ, we finally obtain the integrand

$$\left(1 - \frac{\omega_i^*}{\omega}\right)\left[1 + \frac{\omega_{\mathrm{d},i}}{\omega} + \left(\frac{k_\parallel v_{\mathrm{th},i}}{\omega}\right)^2 \zeta^2 - \frac{k_\perp^2 \rho_{\mathrm{t},i}^2}{2} u\right]$$

such that the integral to be solved is

$$I = \frac{1}{\sqrt{2\pi}} \int \mathrm{d}u\mathrm{d}\zeta \left[1 - \frac{\omega^*_{T,i}}{\omega} \left(u + \frac{\zeta^2}{2} - \frac{3}{2} + \eta_i^{-1} \right) + \left(\frac{\omega_{\mathrm{d},i}}{\omega} + \left(\frac{k_\parallel v_{\mathrm{th},i}}{\omega} \right)^2 \zeta^2 - \frac{k_\perp^2 \rho_{\mathrm{t},i}^2}{2} u \right) \right.$$
$$\left. - \frac{\omega^*_{T,i}}{\omega} \left(u + \frac{\zeta^2}{2} - \frac{3}{2} + \eta_i^{-1} \right) \left(\frac{\omega_{\mathrm{d},i}}{\omega} + \left(\frac{k_\parallel v_{\mathrm{th},i}}{\omega} \right)^2 \zeta^2 - \frac{k_\perp^2 \rho_{\mathrm{t},i}^2}{2} u \right) \right] e^{-\left(u + \frac{\zeta^2}{2} \right)}$$

where we explicitly recall the term $\omega_{\mathrm{d},i} = \omega_{\mathrm{d},T_i} \left(\zeta^2 + u \right)$.

Performing all the integrals, we obtain

$$I = 1 - \frac{\omega^*_{n,i}}{\omega} + \left(2\frac{\omega_{\mathrm{d},T_i}}{\omega} + \left(\frac{k_\parallel v_{\mathrm{th},i}}{\omega} \right)^2 - \frac{k_\perp^2 \rho_{\mathrm{t},i}^2}{2} \right) +$$
$$- \frac{\omega^*_{T,i}}{\omega} \left(1 + \eta_i^{-1} \right) \left(2\frac{\omega_{\mathrm{d},T_i}}{\omega} + \left(\frac{k_\parallel v_{\mathrm{th},i}}{\omega} \right)^2 - \frac{k_\perp^2 \rho_{\mathrm{t},i}^2}{2} \right)$$

So, in the end, we obtain the dispersion relation

$$\mathcal{D} = \frac{n_{0,e}}{T_{0,e}} + \sum_i \frac{n_{0,i} Z_i^2}{T_{0,i}} \left[\cancel{1} - \cancel{1} + \frac{\omega^*_{n,i}}{\omega} - \left(2\frac{\omega_{\mathrm{d},T_i}}{\omega} + \left(\frac{k_\parallel v_{\mathrm{th},i}}{\omega} \right)^2 - \frac{k_\perp^2 \rho_{\mathrm{t},i}^2}{2} \right) + \right.$$
$$\left. + \frac{\omega^*_{T,i}}{\omega} \left(1 + \eta_i^{-1} \right) \left(2\frac{\omega_{\mathrm{d},T_i}}{\omega} + \left(\frac{k_\parallel v_{\mathrm{th},i}}{\omega} \right)^2 - \frac{k_\perp^2 \rho_{\mathrm{t},i}^2}{2} \right) \right] = 0$$

which, by introducing the definition

$$\frac{\omega^*_{T,i}}{\omega} \left(1 + \eta_i^{-1} \right) = \frac{1}{\omega} \left(\omega^*_{T,i} + \omega^*_{n,i} \right) \equiv \frac{\omega^*_{p,i}}{\omega}$$

we rewrite as

$$\mathcal{D} = \frac{n_{0,e}}{T_{0,e}} + \sum_i \frac{n_{0,i} Z_i^2}{T_{0,i}} \left[\frac{\omega^*_{n,i}}{\omega} - \left(1 - \frac{\omega^*_{p,i}}{\omega} \right) \left(2\frac{\omega_{\mathrm{d},T_i}}{\omega} + \left(\frac{k_\parallel v_{\mathrm{th},i}}{\omega} \right)^2 - \frac{k_\perp^2 \rho_{\mathrm{t},i}^2}{2} \right) \right] \tag{B.32}$$

Example. Romanelli ITG dispersion relation [66]
To derive the dispersion relation for ITGs obtained in Ref. [66], let's consider a single ion species, $T_{0,e} = T_{0,i}$, $Z_i = 1$ and $n_{0,e} = n_{0,i}$. Then we obtain

$$\boxed{\frac{\omega + \omega^*_{n,i}}{\omega - \omega^*_{p,i}} - 2\frac{\omega_{\mathrm{d},T_i}}{\omega} - \left(\frac{k_\parallel v_{\mathrm{th},i}}{\omega} \right)^2 + \frac{k_\perp^2 \rho_{\mathrm{t},i}^2}{2} = 0}$$

In the general case, let's rewrite some terms in the dispersion relation by invoking the quasi-neutrality constraint

$$\sum_\sigma q_\sigma n_{0,\sigma} = 0 \quad \rightarrow \quad \sum_i Z_i n_{0,i} - n_{0,e} = 0$$

and by taking the radial derivative we get the relation

$$\sum_\sigma q_\sigma \frac{\partial n_{0,\sigma}}{\partial r} = 0 \quad \rightarrow \quad \sum_i Z_i \frac{\partial n_{0,i}}{\partial r} - \frac{\partial n_{0,e}}{\partial r} = 0$$

Now, we use these relations to rewrite the second term of the dispersion relation Eq. B.32, making explicit the definition of $\omega^*_{n,i}$

$$\begin{aligned}
\sum_i \frac{n_{0,i} Z_i^2}{T_{0,i}} \frac{\omega^*_{n,i}}{\omega} &= \sum_i \frac{\cancel{n_{0,i}} Z_i^2}{\cancel{T_{0,i}}} \frac{1}{\omega} k_\theta \frac{\cancel{T_{0,i}}}{\cancel{Z_i} eB} \frac{\partial n_{0,i}}{\partial r} \frac{1}{\cancel{n_{0,i}}} = \\
&= \frac{k_\theta}{eB} \frac{1}{\omega} \sum_i Z_i \frac{\partial n_{0,i}}{\partial r} = \\
&= \frac{k_\theta}{eB} \frac{1}{\omega} \frac{\partial n_{0,e}}{\partial r} \frac{T_{0,e}}{T_{0,e}} \frac{n_{0,e}}{n_{0,e}} = \\
&= -\frac{n_{0,e}}{T_{0,e}} \frac{\omega^*_{n,e}}{\omega}
\end{aligned}$$

so the dispersion relation becomes

$$\mathcal{D} = \frac{n_{0,e}}{T_{0,e}} \left(1 - \frac{\omega^*_{n,e}}{\omega}\right) - \sum_i \frac{n_{0,i} Z_i^2}{T_{0,i}} \left[\left(1 - \frac{\omega^*_{p,i}}{\omega}\right) \left(2 \frac{\omega_{\mathrm{d},T_i}}{\omega} + \left(\frac{k_\parallel v_{\mathrm{th},i}}{\omega}\right)^2 - \frac{k_\perp^2 \rho_{\mathrm{t},i}^2}{2}\right)\right] = 0$$

Finally, by rewriting the quantities associated with the ions in terms of those of the proton ($Z_p = 1$, $m_i = A_i m_p$) using Eq. B.30, and assuming $T_{0,i}$ equal for all ions, we obtain the following local dispersion relation, by furthermore considering the approximation $k_\parallel v_{\mathrm{th}}/\omega \sim k_\perp \rho_{\mathrm{t}} \to 0$

$$\mathcal{D} = 1 - \frac{\omega^*_{n,e}}{\omega} - \sum_i \frac{n_{0,i} Z_i}{n_{0,e}} \frac{T_{0,e}}{T_{0,i}} 2 \frac{\omega_{\mathrm{d},T_p}}{\omega} + \sum_i \frac{n_{0,i}}{n_{0,e}} \frac{T_{0,e}}{T_{0,i}} 2 \frac{\omega^*_{p,p} \omega_{\mathrm{d},T_p}}{\omega^2} = 0$$

where the third term can be rewritten as

$$\begin{aligned}
-\frac{1}{\omega} \sum_i \frac{n_{0,i} Z_i}{n_{0,e}} \frac{T_{0,e}}{T_{0,i}} 2\omega_{\mathrm{d},T_p} &= -\frac{1}{\omega} \sum_i \frac{n_{0,i} Z_i}{n_{0,e}} \frac{T_{0,e}}{\cancel{T_{0,i}}} 2k_\theta \frac{\cancel{T_{0,p}}}{eBR} = \\
&= -\frac{1}{\omega} 2k_\theta \frac{T_{0,e}}{eBR} \frac{\sum_i n_{0,i} Z_i}{n_{0,e}} = \\
&= +\frac{2\omega_{\mathrm{d},T_e}}{\omega}
\end{aligned}$$

such that the dispersion relation simplifies to

$$\mathcal{D} = 1 - \frac{\omega^*_{n,e}}{\omega} + \frac{2\omega_{\mathrm{d},T_e}}{\omega} + \frac{1}{\omega^2} \sum_i \frac{n_{0,i}}{n_{0,e}} \frac{T_{0,e}}{T_{0,i}} 2\omega^*_{p,p} \omega_{\mathrm{d},T_p} = 0$$

The solution of this second order equation in ω of the form

$$1 - \frac{A}{\omega} + \frac{B}{\omega^2} = 0$$

is imaginary, i.e. instability, if $4B > A^2$. In particular, far above the threshold we get

$$\gamma \sim \sqrt{B} = \sqrt{\sum_i \frac{n_{0,i}}{n_{0,e}} \frac{T_{0,e}}{T_{0,i}} 2\omega^*_{p,p}\omega_{\mathrm{d},T_p}}$$

where we can notice the effects:

1. dilution: the growth rate decreases by increasing the impurity density
2. $T_{0,e}/T_{0,i}$ stabilization
3. role of the impurity pressure gradient